

**PHYSICAL MECHANISMS
CONTROLLING THE
STRENGTH-DEFORMATION
BEHAVIOR OF FROZEN SAND: PART II**

FINAL REPORT

by
**Christopher W. Swan
Charles C. Ladd
John T. Germaine
Glen R. Andersen**

April, 1995



**U.S. ARMY RESEARCH OFFICE
Contract Number DAAL03-92-G-0226**

**Dept. of Civil and Environmental Engineering
Henry L. Pierce Laboratory
Massachusetts Institute of Technology
Cambridge, MA 02139-4307**

**APPROVED FOR PUBLIC RELEASE;
DISTRIBUTION UNLIMITED**

MIT

**DEPARTMENT
OF CIVIL &
ENVIRONMENTAL
ENGINEERING**

**SCHOOL OF ENGINEERING
MASSACHUSETTS INSTITUTE OF TECHNOLOGY
Cambridge, Massachusetts 02139**

19950703 245

THE VIEWS, OPINIONS, AND/OR
FINDINGS CONTAINED IN THIS RE-
PORT ARE THOSE OF THE AUTHORS
AND SHOULD NOT BE CONSTRUED
AS AN OFFICIAL DEPARTMENT OF
THE ARMY POSITION, POLICY OR
DECISION, UNLESS SO DESIGNATED
BY OTHER DOCUMENTATION.

REPORT DOCUMENTATION PAGE			Form Approved OMB No. 0704-0188	
Public reporting burden for this collection of information is estimated to average 1 hour per response, including the time for reviewing instructions, searching existing data sources, gathering and maintaining the data needed, and completing and reviewing the collection of information. Send comments regarding this burden estimate or any other aspect of this collection of information, including suggestions for reducing this burden, to Washington Headquarters Services, Directorate for Information Operations and Reports, 1215 Jefferson Davis Highway, Suite 1204, Arlington, VA 22202-4302, and to the Office of Management and Budget, Paperwork Reduction Project (0704-0188), Washington, DC 20503.				
1. AGENCY USE ONLY (Leave blank)	2. REPORT DATE April, 1995	3. REPORT TYPE AND DATES COVERED		
4. TITLE AND SUBTITLE Physical Mechanisms Controlling the Strength-Deformation Behavior of Frozen Sand: Part II		5. FUNDING NUMBERS DAAL 03-92-G-0226		
6. AUTHOR(S) Christopher W. Swan, Charles C. Ladd, John T. Germaine, and Glen R. Andersen				
7. PERFORMING ORGANIZATION NAME(S) AND ADDRESS(ES) Dept. of Civil and Environmental Engineering Henry L. Pierce Laboratory Massachusetts Institute of Technology Cambridge, MA 02139-4307		8. PERFORMING ORGANIZATION REPORT NUMBER		
9. SPONSORING/MONITORING AGENCY NAME(S) AND ADDRESS(ES) U. S. Army Research Office P. O. Box 12211 Research Triangle Park, NC 27709-2211		10. SPONSORING/MONITORING AGENCY REPORT NUMBER ARO 29781.3-GS		
11. SUPPLEMENTARY NOTES The view, opinions and/or findings contained in this report are those of the author(s) and should not be construed as an official Department of the Army position, policy, or decision, unless so designated by other documentation.				
12a. DISTRIBUTION/AVAILABILITY STATEMENT Approved for public release; distribution unlimited.			12b. DISTRIBUTION CODE	
13. ABSTRACT (Maximum 200 words) A high-pressure low-temperature triaxial compression testing system with on-specimen axial strain (ϵ_a) measurements and lubricated end platens was used to measure the stress-strain-volume change behavior of pluviated Manchester Fine Sand (MFS) from $\epsilon_a = 0.001\%$ to 25%. Three types of tests were performed: 1) 99 conventional tests on frozen MFS having four testing variables—relative density (D_r), confining pressure ($\sigma_c = 0.1$ to 10 MPa), three strain rates ($\dot{\epsilon} = 3 \times 10^{-6}/s$ to $5 \times 10^{-4}/s$), and four temperatures ($T = -10^\circ C$ to $-25^\circ C$); 2) 10 tests on dense MFS that was frozen after consolidation to effective stresses (σ'_c) up to 10 MPa; and 3) 49 undrained and drained triaxial tests on unfrozen MFS at varying D_r and σ'_c . For ice-saturated, frozen MFS, <ul style="list-style-type: none"> • Young's modulus is independent of σ_c, $\dot{\epsilon}$, and T, as predicted by an isostrain composite materials model; • all specimens have a distinct upper yield stress (Q_{uy}) that varies only with $\dot{\epsilon}$ and T (unless frozen under a high σ'_c) and probably reflects a greatly enhanced ice matrix strength, compared to bulk granular ice; and • the normalized peak strength ratio (Q_p/Q_{uy}) varies in a complex manner with D_r, σ_c, $\dot{\epsilon}$, and T. However, the normalized rate of post-peak strain softening is uniquely related to the amount of volumetric expansion. 				
14. SUBJECT TERMS Cold Regions, confining pressure, deformation, dilatancy, frozen soil, modulus, permafrost, sand, shear strength, strain rate, temperature, triaxial tests, yield stress			15. NUMBER OF PAGES 253	
			16. PRICE CODE	
17. SECURITY CLASSIFICATION OF REPORT UNCLASSIFIED	18. SECURITY CLASSIFICATION OF THIS PAGE UNCLASSIFIED	19. SECURITY CLASSIFICATION OF ABSTRACT UNCLASSIFIED	20. LIMITATION OF ABSTRACT UL	

FOREWORD

The research described in the report involves presentation and evaluation of results from some 150 triaxial compression tests run on specimens of unfrozen and frozen sand at varying densities, levels of confinement, rates of axial strain and temperatures. The authors had planned to prepare a very brief report that summarized the principal findings and conclusions from three papers: one on the behavior of frozen sand at small strains (from 0.001% to about 1% axial strain); a second on the behavior of frozen sand at large strains (where fracturing of the ice matrix and the frictional resistance of the sand skeleton play major roles); and a third on quantitative analysis of the peak strength of frozen sand using a dilatancy-hardening model. Whereas the first paper was written last spring and has been accepted for publication, it became obvious that considerably more analysis of the data was required, in order to submit the other two papers. Consequently, the first two authors devoted several hundred hours since last July to further evaluation of the data and on preparation of this report. But in spite of their effort, the report is less polished than desired, which explains the many hand-drafted figures in the appendices, and why the text on large strain behavior sometimes reads like a mystery novel. However, we hope the final section provides a coherent summary and set of conclusions.

For	
A&I	<input checked="" type="checkbox"/>
3	<input type="checkbox"/>
ced	<input type="checkbox"/>
Justification	
By	
Distribution /	
Availability Codes	
Dist	Avail and/or Special
A-1	

TABLE OF CONTENTS

	Page No.
TITLE PAGE AND DISCLAIMER CLAUSE	
REPORT DOCUMENTATION PAGE (Form 298).....	i
FOREWORD.....	ii
TABLE OF CONTENTS.....	iii
LIST OF TABLES.....	vii
LIST OF FIGURES.....	vii
 I. INTRODUCTION	
1.1 Background.....	1
1.2 Research Objectives and Scope.....	3
1.3 Organization of this Report.....	6
1.4 Publications and Reports.....	7
1.5 Staff and Advanced Degrees.....	8
1.6 Acknowledgments.....	9
 2. EXPERIMENTAL PROGRAM AND PROCEDURES	
2.1 Description of Manchester Fine Sand.....	10
2.2 Scope of Experimental Program.....	11
2.3 Cold Room Facility and Triaxial Testing System.....	12
2.4 Testing Procedures.....	15
2.4.1 Conventional tests on frozen sand.....	15
2.4.2 Tests on unfrozen sand.....	16
2.4.3 Consolidate-freeze tests on frozen sand.....	17
2.5 Overview of Stress-Strain Behavior and Definition of Stress-Strain Parameters.....	18
2.5.1 Overview of stress-strain behavior.....	18
2.5.2 Definition of parameters.....	20

3. SMALL STRAIN BEHAVIOR OF FROZEN SAND

3.1	Background.....	29
3.2	Young's Modulus.....	30
3.2.1	Data on Manchester Fine Sand.....	30
3.2.2	Comparisons with prior data.....	30
3.2.3	Prediction of Young's modulus.....	32
3.3	Yield Offset Stress.....	34
3.4	Upper Yield Stress.....	35
3.4.1	Data on Manchester Fine Sand.....	35
3.4.2	Comparisons with prior data.....	37
3.4.3	Discussion of mechanisms and analogy with peak ice strength.....	39
3.5	Summary and Conclusions.....	42

4. LARGE STRAIN BEHAVIOR OF FROZEN SAND

4.1	Background.....	52
4.2	Overview of Stress-Strain Behavior at Large Strains.....	54
4.3	Post-Upper Yield Strengthening and Peak Strength.....	56
4.3.1	Comparison of peak strengths with prior data.....	56
4.3.2	Effects of relative density and confining pressure.....	57
4.3.3	Effects of strain rate and temperature.....	63
4.3.4	Summary and conclusions.....	64
4.4	Volumetric Behavior.....	67
4.4.1	Background.....	67
4.4.2	Maximum rate of dilation.....	68
4.4.3	Volumetric expansion at 20% axial strains.....	68
4.5	Post-Peak Strain Softening.....	69
4.5.1	Objective.....	69
4.5.2	Results of analyses.....	69
4.5.3	Summary and conclusions.....	72
4.6	Conceptual Model of Physical Mechanisms Governing the Large-Strain Behavior of Frozen Sand.....	74
4.6.1	Introduction.....	74
4.6.2	Ice behavior and upper yield strength of frozen sand.....	75
4.6.3	Post-upper yield weakening and strengthening mechanisms.....	76
4.6.4	Post-upper yield behavior of frozen MFS.....	79

5. QUANTITATIVE ANALYSIS OF THE STRENGTH OF FROZEN SAND

5.1	Introduction.....	104
5.2	Dilatancy-Hardening Model.....	104
5.2.1	Assumptions and development.....	104
5.2.2	Prior experimental validation.....	109
5.3	Triaxial Compression Behavior of Unfrozen MFS.....	110
5.3.1	Scope of test program.....	110
5.3.2	Stress-strain-effective stress behavior.....	111
5.3.3	Steady-state analysis and critical confining pressure.....	114
5.4	Results from Consolidate-Freeze Tests on MFS.....	116
5.4.1	Objectives and scope.....	116
5.4.2	Experimental results and comparison with conventional frozen tests.....	118
5.4.3	Summary and discussion.....	121
5.5	Application of Dilatancy-Hardening Model to Frozen MFS.....	123
5.5.1	Selection of model parameters.....	123
5.5.2	Results of analyses.....	126
5.5.3	Collective comparison and revised model predictions.....	130
5.5.4	Summary and conclusions.....	136

6. SUMMARY AND CONCLUSIONS

6.1	Research Objectives and Scope.....	158
6.2	Overview and Definition of Stress-Strain Behavior.....	162
6.2.1	Overview of stress-strain behavior.....	162
6.2.2	Definition of stress-strain behavior.....	163
6.3	Small-Strain Behavior of Frozen Sand.....	165
6.3.1	Young's modulus.....	165
6.3.2	Yield offset stress.....	166
6.3.3	Upper yield stress.....	166
6.4	Large-Strain Behavior of Frozen Sand.....	169
6.4.1	Volumetric behavior.....	169
6.4.2	Post-upper yield behavior: curve types and conceptual model.....	170
6.4.3	Peak strength: background.....	174
6.4.4	Peak strength: dilatancy-hardening model.....	176
6.4.5	Peak strength: effect of testing variables.....	180
6.4.6	Post-peak strain softening behavior.....	185

7.	REFERENCES.....	187
----	-----------------	-----

3. SMALL STRAIN BEHAVIOR OF FROZEN SAND

3.1	Background.....	29
3.2	Young's Modulus.....	30
3.2.1	Data on Manchester Fine Sand.....	30
3.2.2	Comparisons with prior data.....	30
3.2.3	Prediction of Young's modulus.....	32
3.3	Yield Offset Stress.....	34
3.4	Upper Yield Stress.....	35
3.4.1	Data on Manchester Fine Sand.....	35
3.4.2	Comparisons with prior data.....	37
3.4.3	Discussion of mechanisms and analogy with peak ice strength.....	39
3.5	Summary and Conclusions.....	42

4. LARGE STRAIN BEHAVIOR OF FROZEN SAND

4.1	Background.....	52
4.2	Overview of Stress-Strain Behavior at Large Strains.....	54
4.3	Post-Upper Yield Strengthening and Peak Strength.....	56
4.3.1	Comparison of peak strengths with prior data.....	56
4.3.2	Effects of relative density and confining pressure.....	57
4.3.3	Effects of strain rate and temperature.....	63
4.3.4	Summary and conclusions.....	64
4.4	Volumetric Behavior.....	67
4.4.1	Background.....	67
4.4.2	Maximum rate of dilation.....	68
4.4.3	Volumetric expansion at 20% axial strains.....	68
4.5	Post-Peak Strain Softening.....	69
4.5.1	Objective.....	69
4.5.2	Results of analyses.....	69
4.5.3	Summary and conclusions.....	72
4.6	Conceptual Model of Physical Mechanisms Governing the Large-Strain Behavior of Frozen Sand.....	74
4.6.1	Introduction.....	74
4.6.2	Ice behavior and upper yield strength of frozen sand.....	75
4.6.3	Post-upper yield weakening and strengthening mechanisms.....	76
4.6.4	Post-upper yield behavior of frozen MFS.....	79

LIST OF TABLES

		Page
Table 2.1	Scope of Conventional Triaxial Tests on Frozen Manchester Fine Sand.....	23
Table 2.2	Definition of Characteristic Curve Types Describing the Large Strain Behavior of Frozen Manchester Fine Sand.....	24

LIST OF FIGURES

		Page
Fig. 2.1	Schematic of High-Pressure Triaxial Cell.....	25
Fig. 2.2	Effect of Relative Density and Confining Pressure on Stress-Strain Curves for Frozen MFS at	
	a) Varying strain rate.....	26
	b) Varying temperatures.....	26
Fig. 2.3	Definition of Small Strain Parameters	
	a) Modulus and yield offset stress.....	27
	b) Upper yield stress.....	27
Fig. 2.4	Types of Stress-Strain Curves Describing Large-Large Behavior.....	28
Fig. 3.1	Comparison of Measured and Predicted Young's Modulus vs. Relative Density for Frozen MFS at All Testing Conditions.....	45
Fig. 3.2	Yield Offset Stress vs. Temperature at Varying Strain Rate and All Relative Densities for Frozen MFS at	
	a) Low Confinement.....	46
	b) High Confinement.....	46
Fig. 3.3	Upper Yield Stress vs. Relative Density for Slow, Moderate and Fast Strain Rates at $T = -10^{\circ}\text{C}$ for Frozen MFS.....	47
Fig. 3.4	Upper Yield Stress vs. Strain Rate at Varying Temperatures for All Relative Densities and Confining Pressures for Frozen MFS.....	48

Fig. 3.5	Upper Yield Stress vs. Temperature at Varying Strain Rate for All Relative Densities and Confining Pressures for Frozen MFS.....	49
Fig. 3.6	Comparison of Effect of Confining Pressure on Upper Yield Stress with Prior Data on Frozen Ottawa Sands.....	50
Fig. 3.7	Comparison of Upper Yield Stress of Frozen MFS and Peak Strength of Polycrystalline Ice vs. Strain Rate.....	51
Fig. 4.1	Normalized Stress-Strain Data for Frozen MFS Showing the Effect of Relative Density at Low Confinement ($\sigma_c = 0.1$ MPa): (a) Moderate Strain Rate and $T = -10^\circ\text{C}$; (b) Moderate Strain Rate and $T = -20^\circ\text{C}$ [---questionable data; x = peak stress ratio].....	81
Fig. 4.2	Normalized Stress-Strain Data for Frozen MFS Showing the Effect of Confinement for Dense Specimens at Moderate Strain Rate and $T = -10^\circ\text{C}$ [x = peak stress ratio].....	82
Fig. 4.3	Normalized Stress-Strain Data for Frozen MFS Showing the Effect of Relative Density at High Confinement ($\sigma_c = 10$ MPa): (a) Moderate strain rate and $T = -10^\circ\text{C}$ (b) Fast strain rate and $T = -15^\circ\text{C}$ [x = peak stress ratio].....	83 83
Fig. 4.4	(a) Comparison of Peak Strength vs. Strain Rate of Dense MFS with Other Dense Sands at Zero or Low Confinement (letter designations for Table B)..... (b) Comparison of Peak Strength vs. Strain Rate of Dense MFS with Other Dense Sands at High Confinement (letter designations for Table B).....	84 85
Fig. 4.5	Peak Strength vs. Relative Density for Frozen MFS at Moderate Strain Rate, Low Confinement and Different Temperatures.....	86
Fig. 4.6	Strength Increase vs. Relative Density of Frozen MFS at Varying Strain Rates and Temperatures: (a) At $\sigma_c = 0.1$ Mpa..... (b) At $\sigma_c = 10$ MPa.....	87 87
Fig. 4.7	Effect of Confining Pressure on Value of dQ/dDr for Frozen MFS at Varying Temperatures: (a) At moderate strain rate..... (b) At slow and fast strain rates.....	88 88

Fig. 4.8	Peak Strength and Stress Increase vs. Confining Pressure for Dense, Moderate and Loose Frozen MFS at Moderate Strain Rate and $T = -10^{\circ}\text{C}$ (data points from linear regression).....	89
Fig. 4.9	Effect of Relative Density on Strength Gain with Confinement vs. Temperature for Frozen MFS at Slow and Moderate Strain Rates (mean values from linear regression analyses on Q_p and ΔQ data at $\sigma_c = 0.1$ and 10 MPa).....	90
Fig. 4.10	Effect on Confining Pressure on Peak Strength of Dense Sands from Prior Programs at $T \approx -10^{\circ}\text{C}$	91
Fig. 4.11	Relative Density Producing $Q_p = Q_{uy}$ at $\sigma_c = 0.1 \text{ MPa}$: (a) vs. temperature; (b) vs. strain rate.....	92
Fig. 4.12	Peak Strength and Upper Yield Stress vs. Strain Rate for Frozen MFS at (a) Low density and low confinement..... (b) High density and high confinement.....	93 93
Fig. 4.13	Strength Increases vs. Strain Rate for Loose and Dense Specimens of Frozen MFS at Varying Temperature: (a) $\sigma_c = 0.1 \text{ MPa}$; and (b) $\sigma_c = 10 \text{ MPa}$ (values from linear regression on data in Figure 4.6).....	94
Fig. 4.14	Maximum Rate of Dilation of Frozen MFS: (a) vs. confining pressure at moderate strain rate and $T = -10^{\circ}\text{C}$; and (b) and (c) vs. relative density at $\sigma_c = 0.1$ and 10 MPa , respectively, at varying strain rates and temperatures.....	95
Fig. 4.15	Volumetric Strain at 20% Axial Strain vs. Relative Density at Varying Strain Rates and Temperatures for Frozen MFS: (a) at $\sigma_c = 0.1 \text{ MPa}$; (b) at $\sigma_c = 10 \text{ MPa}$	96
Fig. 4.16	Normalized Rate of Strain Softening vs. Relative Density at Varying Strain Rates and Temperatures for Frozen MFS (Type C curves at $\sigma_c = 0.1 \text{ MPa}$).....	97
Fig. 4.17	Normalized Peak Strength Ratio vs. Relative Density at Varying Strain Rates and Temperatures for Frozen MFS (Type C curves at $\sigma_c = 0.1 \text{ MPa}$).....	98

Fig. 4.18	Normalized Strength at 20% Axial Strain vs. Strain Rate at Varying Temperatures for Frozen MFS (Type A and C curves at $\sigma_c = 0.1$ MPa).....	99
Fig. 4.19	Rate of Strain Softening vs. Maximum Rate of Dilation of Frozen MFS as a Function of Curve Type for All Testing Conditions.....	100
Fig. 4.20	Stress Ratio vs. Volumetric Strain of Frozen MFS as a Function of Curve Type for all Testing Conditions.....	101
Fig. 4.21	Normalized Rate of Strain Softening vs. Volumetric Strain at Varying Relative Density, Strain Rate and Temperature for Frozen MFS (Type A and C curves at $\sigma_c = 0.1$ MPa).....	102
Fig. 4.22	Typical Stress-Strain Curves for Polycrystalline Ice.....	103
Fig. 5.1	Schematic Representation of Total and Effective Stress Paths for Ladanyi's Dilatancy-Hardening Model.....	140
Fig. 5.2	Effect of Consolidation Stress on Undrained Stress-Strain and Pore Pressure Behavior from CU Triaxial Compression Tests on Unfrozen Dense MFS.....	141
Fig. 5.3	Effect of Consolidation Stress on Effective Stress Paths from CU Triaxial Compression Tests on Unfrozen Dense MFS.....	142
Fig. 5.4	Effect of Consolidation Stress on Drained Stress-Strain and Volumetric Strain Behavior from CD Triaxial Compression Tests on Unfrozen Dense MFS.....	143
Fig. 5.5	Effect of Relative Density on Undrained Stress-Strain and Pore Pressure Behavior from CU Triaxial Compression Tests at Low Confinement on Unfrozen MFS.....	144
Fig. 5.6	Effect of Relative Density on Undrained Stress-Strain and Pore Pressure Behavior from CU Triaxial Compression Tests at Moderate Confinement on Unfrozen MFS.....	145
Fig. 5.7	Mobilized Friction Angle at Maximum Obliquity from CU Triaxial Compression Tests on Unfrozen MFS.....	146
Fig. 5.8	Steady State and Critical Confining Pressure Lines for Unfrozen MFS Based on Steady State Analysis of CIUC Tests.....	147

Fig. 5.9	A_f vs. State Parameter from CIUC Tests on Unfrozen MFS.....	148
Fig. 5.10	Effect of Specimen Preparation Technique on Stress-Strain Curves from Conventional Tests on Frozen Dense MFS.....	149
Fig. 5.11	Initial Stress-Strain Curves Showing the Upper Yield Region for Consolidate-Freeze and Conventional Tests on Dense MFS at Moderate Strain Rate and $T = -10^{\circ}\text{C}$	150
Fig. 5.12	Comparison of Stress-Strain Curves for Consolidate-Freeze and Conventional Frozen Tests on Dense MFS at Moderate Strain Rate and $T = -10^{\circ}\text{C}$	151
Fig. 5.13	Comparison of Stress-Strain Curves for Consolidate-Freeze Tests on MSP Specimens and Conventional Frozen Tests on Wet Tamped Specimens of Dense MFS at Moderate Strain Rate and $T = -10^{\circ}\text{C}$	152
Fig. 5.14	Comparison of Measured vs. Predicted Effect of Confinement on Peak Strength of Conventional and Consolidate-Freeze Tests on Dense MFS at Moderate Strain Rate and $T = -10^{\circ}\text{C}$	153
Fig. 5.15	Peak Strength vs. Strain Rate Comparing Measured Results from Conventional and Consolidate-Freeze Tests on Dense MFS at Low Confinement with Predicted Results from Dilatancy- Hardening Model.....	154
Fig. 5.16	Peak Strength vs. Strain Rate Comparing Measured Results from Conventional and Consolidate-Freeze Tests on Dense MFS at High Confinement with Predicted Results from Dilatancy- Hardening Model.....	155
Fig. 5.17	Peak Strength vs. Strain Rate Comparing Measured Results from Conventional Frozen Tests on Loose MFS at Low Confinement with Predicted Results from Dilatancy-Hardening Model.....	156
Fig. 5.18	Peak Strength vs. Strain Rate Comparing Measured Results from Conventional Frozen Tests on Loose MFS at High Confinement with Predicted Results from Dilatancy-Hardening Model.....	157

1. INTRODUCTION

1.1 BACKGROUND

Frozen soils exist in Arctic regions as perennially frozen soil (permafrost) that underlies nearly 20% of the land surface of the earth. Of all geomaterials, the mechanical properties of frozen soil are perhaps the most variable and difficult to understand and model. Consequently, the placement of structures on frozen soil poses unique design problems because of uncertainties regarding the time and temperature dependence of the frozen soil response. Similar problems also arise when artificial soil freezing is used as a method of ground improvement for underpinning foundations and for strengthening soil around excavations (tunnels, shafts, etc.).

Even the simplest form of frozen soil (sand with ice-filled pores) entails a highly complex interaction between the skeleton of solid particles and the pore matrix (composed of ice and unfrozen water) that changes continuously with time as a function of temperature and stress/strain level. Consequently, the development of reliable constitutive relationships to model the stress-strain-time-temperature behavior of frozen soils lags far behind modeling capabilities for other geomaterials such as soil and ice. Long-term progress in modeling requires research in at least three principal areas:

- 1) experimental studies to completely define the strength-deformation properties of representative frozen natural soils as a function of the major variables thought to affect their behavior at the macrolevel;

- 2) coupled experimental and theoretical studies to test hypotheses regarding the physical mechanisms controlling the behavior of frozen soils at various stages of deformation; and
- 3) theoretical studies which absorb the insight from research areas 1) and 2) and lead to the development of physically based constitutive relationships for frozen soils.

Regarding the first area, the major variables thought to affect the behavior of frozen soils can be divided into three categories. Their description and the scope of experimental data that existed prior to this research are summarized below.

- The *soil type* that will be frozen. In general, this means the particle size, shape and gradation of granular soils and the plasticity characteristics of cohesive soils. *Most experimental data are restricted to uniform sands, such as commercially available Ottawa sand.*
- The *initial state* during freezing. This refers to the initial density (granular) or stress history (cohesive) of the specimen, the nature of the pore fluid, the magnitude of the applied **effective** confining stress, and the freezing temperature. *Most existing data are for sand specimens having one density, and all specimens were frozen under zero-confining stress.*
- *The conditions during shear.* The major variables include the confining pressure, the rate of straining or the creep stress, the

temperature, and the mode of shearing. *Essentially all existing tests have been restricted to monotonic loading in triaxial compression with external measurement of axial strain (which precludes reliable data at small strains) and only one program varied confining pressure, strain rate and temperature.*

This review of prior research indicates that no test program has produced stress-strain data from very small to very large strains for any frozen soil as a function of the four principal variables that affect its response, namely specimen density, confining pressure, strain rate and temperature.

1.2 RESEARCH OBJECTIVES AND SCOPE

The long-term objective of MIT's research is to develop physically based constitutive relations to describe the stress-strain-time-temperature behavior of frozen soils, which in turn first requires a better understanding of their fundamental behavior. Consequently, the near-term objective is the identification of the principal physical mechanisms that control the stress-strain behavior of frozen soils and a quantitative (or at least qualitative) assessment of their relative importance. The approach used by MIT to achieve this near-term objective has three components:

- 1) conduct a comprehensive experimental program to precisely measure the behavior of a frozen natural sand over a wide range of testing conditions;

- 2) from a knowledge of the general behavior of polycrystalline ice and of the measured stress-strain behavior of the same sand in an unfrozen state, attempt to deduce the relative importance of
 - the ice matrix *per se*
 - the frictional resistance of the sand skeleton *per se*, and
 - the interaction between the ice matrix and the sand skeleton;
- 3) where possible, employ models for composite materials to quantify the physical mechanisms responsible for the macro-behavior of frozen sands.

Detailed results from the preceding ARO contract (DAAL03-89-K0023) for the period January, 1989, through December, 1991, are contained in Andersen (1991) and Andersen *et al.* (1992). The principal experimental component of that research used a high-pressure, low-temperature triaxial compression testing system with on-specimen axial strain measurements and lubricated end platens to characterize the stress-strain-volume change characteristics of frozen Manchester Fine Sand (MFS) at a temperature of $T = 9.5^{\circ}\text{C}$ from very small (0.001%) to very large (25%) axial strains. The program varied the relative density of the sand from $D_r = 20$ to 100%, the confining pressure from $\sigma_c = 0.1$ to 10 MPa, and the strain rate from $\dot{\epsilon} = 3 \times 10^{-6}/\text{s}$ (slow) to $5 \times 10^{-4}/\text{s}$ (fast). A similar triaxial system was used to perform an initial series of undrained and drained shear tests on unfrozen MFS. The research also used a model developed for composite materials (concrete) to evaluate the Young's modulus of frozen MFS.

The experimental research conducted under this ARO contract extended the prior data on frozen MFS to lower temperatures (nominal values of $T = -15^{\circ}\text{C}$, -20°C and -25°C), completed the shear testing program on unfrozen MFS, and conducted preliminary tests on MFS wherein specimens of dense sand were frozen at $T = -9.5^{\circ}\text{C}$ after being consolidated to stresses ranging from $\sigma'_c = 0.1$ to 10 MPa. This research also evaluated a dilatancy-hardening model developed by Ladanyi (1985) for predicting the strength of frozen sand.

Unique aspects of the triaxial compression shear testing program on MFS include the following features:

- the first set of data on any frozen soil to fully characterize behavior as a function of sand density, confining stress, strain rate and temperature;
- the first set of data to reliably measure axial stress vs. axial strain behavior from very small (0.001%) to very large (25%) axial strains, along with reasonably accurate measurements of volumetric strains;
- the first set of data wherein specimens were consolidated to varying pressures prior to freezing, although the results are rather surprising and should be checked;
- the first program to measure the shear behavior of a soil in both its frozen and its unfrozen states.

Consequently, even if some of the conclusions drawn by the authors from their analyses of the data prove to be questionable, other researchers can still benefit from their own interpretation of a unique set of experimental data.

1.3 ORGANIZATION OF THIS REPORT

The objective of this report is to provide a detailed summary of the most important experimental results and of the authors' conclusions regarding the relative importance of the physical mechanisms controlling the strength-deformation behavior of frozen sands. The technical summary includes research conducted under both ARO contracts, i.e., support during calendar years 1989 to 1991 and from June, 1992, through May, 1994.

Section 2 presents an overview of the scope of the experimental program on Manchester Fine Sand (MFS) and of the experimental procedures since the details are contained in two doctoral theses (Andersen, 1991 and Swan, 1994) and the Final Report for the preceding contract (Andersen *et al.*, 1992). Section 3 describes the behavior of frozen MFS at small strains ($\epsilon_a < 1\%$), where sand density and confining pressure are seen to play a minor role in the observed behavior. Section 4 then describes the large strain behavior, wherein the fracturing of the ice matrix (as inferred from dilatant volumetric strains) and the frictional resistance of the sand skeleton now play a major role in the observed behavior. Section 5 summarizes results from the consolidate-freeze tests on MFS, i.e., influence of effective confining stress during freezing on subsequent behavior. Section 5 also applies Ladanyi's

dilatancy-hardening model to frozen MFS, which incorporates results from triaxial compression shear tests on unfrozen sand specimens.

1.4 PUBLICATIONS AND REPORTS

Three publications and reports on frozen sand were sent to ARO in 1994: on January 31, a Technical Progress Report was submitted; in August, a copy of the doctoral thesis by Swan (1994) was submitted; and in May, we sent a copy of the paper titled, "Small-Strain Behavior of Frozen Sand in Triaxial Compression," by Andersen *et al.* (1994) that was submitted to the *Canadian Geotechnical Journal*. Although accepted for publication, the Andersen *et al.* paper was expanded and improved in response to detailed comments by two reviewers; ARO was sent a copy of the revised paper. Two other papers are planned for submittal to the to the *Canadian Geotechnical Journal* in 1995; their status is as follows:

- "Large-Strain Behavior of Frozen Sand in Triaxial Compression" by C.C. Ladd, G.R. Andersen, C.W. Swan and J.T. Germaine. Rough drafts of text, tables and figures were prepared by Ladd that extend the scope of analyses contained in the theses by Andersen (1991) and Swan (1994). Section 4 of this report presents the principal results and conclusions.
- "Application of a Dilatancy-Hardening Model to the Strength of Frozen Sand in Triaxial Compression" (tentative title) by C.W. Swan, C.C. Ladd, J.T. Germaine and G.R. Andersen. The selection of parameters and results of preliminary analyses are contained in

Swan (1994); these are summarized in Section 5 of this report, along with results of additional analyses.

1.5 STAFF AND ADVANCED DEGREES

Dr. Charles C. Ladd, Edmund K. Turner Professor, and Dr. John T. Germaine, Principal Research Associate, served as co-principal investigators for the two-year project. Both are members of the Henry L. Pierce Laboratory in MIT's Department of Civil and Environmental Engineering. In simplified terms, Dr. Germaine was mainly responsible for supervision of the equipment development and experimental work, while Professor Ladd administered the contract and was mainly responsible for supervising the analyses and reporting the results.

Christopher W. Swan was a full-time graduate Research Assistant on the project; in May, 1994, he received the Doctor of Science Degree in Civil and Environmental Engineering. He is now an Assistant Professor in the Department of Civil and Environmental Engineering at Tufts University in Medford, Massachusetts.

The project involved three undergraduate students under MIT's Undergraduate Research Opportunities Program (UROP). They were Victor Salvador during the summer of 1992, Munera Abdur-Rahim during the summer of 1993, and Adrian Maung for one year starting September, 1992.

1.6 ACKNOWLEDGMENTS

The authors appreciate the support of Dr. Walter D. Bach, Dr. John J. Bowders, Jr., and Dr. Russell S. Harmon who acted as technical monitors. The authors are specially indebted to Dr. David M. Cole of CRREL who was Scientific Liaison representative on the project; besides making several visits to MIT during both contracts to help guide our experimental techniques and research directions (most notably, the extension of the testing program to lower temperatures), he was always available by phone for technical assistance in explaining the complex aspects of ice behavior.

2. EXPERIMENTAL PROGRAM AND PROCEDURES

2.1 DESCRIPTION OF MANCHESTER FINE SAND

A large supply of Manchester Fine Sand (MFS) was obtained from the banks of the Merrimack River, Manchester, New Hampshire, and processed to reduce the non-plastic fines content (portion passing No. 200 sieve) from 20% to 7%. Pertinent characteristics of the MFS abstracted from Andersen *et al.* (1992, 1994) and Swan (1994) follow:

- composition—mainly subangular quartz and feldspar with some mica flakes (Martin *et al.*, 1981)
- gradation—mean particle size, $d_{50} = 0.18$ mm; 99% passing No. 45 sieve (0.35 mm); 7.2% passing No. 200 sieve (0.074 mm); uniformity coefficient, $C_u = \frac{d_{60}}{d_{10}} = 2.35$
- specific gravity— $G_s = 2.688 \pm 0.003$
- minimum dry density— $\gamma_d = 1408$ kg/m³;
maximum void ratio, $e_{\max} = 0.909$
- maximum dry density— $\gamma_d = 1701$ kg/m³;
minimum void ratio, $e_{\min} = 0.580$
- particle crushing after undrained shearing at 10 MPa confining pressure—negligible for frozen sand; moderate for unfrozen sand

for intermediate size particles, e.g., percent finer than 0.125 mm

increases from about 25% to 35%

- unfrozen water content—less than 0.14% at $T = 9.5^{\circ}\text{C}$

2.2 SCOPE OF EXPERIMENTAL PROGRAM

The experimental program involved triaxial compression tests performed on three types of specimens: 1) specimens that were frozen in a mold before being placed in the triaxial cell, i.e., the **conventional** method for testing frozen soil; 2) specimens that were frozen **after** being consolidated to varying effective stress levels in the triaxial cell, which are called **consolidate-freeze** tests; and 3) specimens that were not frozen.

Table 2.1 summarizes the testing matrix for the parametric study in terms of the number of conventional frozen sand tests at each condition. The four variables were

- the relative density of the sand specimens, which varied from $D_r = 20$ to 100% , where $D_r = (e_{\max} - e)/(e_{\max} - e_{\min})$;
- the confining pressure during shearing, which varied from $\sigma_c = 0.1$ to 10 MPa ;
- the nominal testing temperature, which varied in 5°C increments from $T = -10$ to -25°C ;
- the nominal axial strain rate, which varied from $\dot{\epsilon} = 3 \times 10^{-6}/\text{s}$ (slow) to $\dot{\epsilon} = 5 \times 10^{-4}/\text{s}$ (fast)

Andersen (1991) and Andersen *et al.* (1992) presented results from the tests at $T = -10^{\circ}\text{C}$, which included the most detailed study of the influence of sand density and confining pressure at the moderate strain rate of $\dot{\epsilon} = 3.5 \times 10^{-5}/\text{s}$. The current contract performed the tests at the lower temperatures and typically included loose and dense specimens at low and high confining pressures ($\sigma_c = 0.1$ and 10 MPa, respectively).

Ten consolidate-freeze tests were run on dense MFS consolidated to effective stresses of $\sigma'_c = 0.1, 2, 5$ and 10 MPa, frozen at $T = -10^{\circ}\text{C}$ and then sheared at the moderate strain rate. Section 5.3 describes the general scope of the 49 undrained and drained triaxial compression tests run on *unfrozen* MFS for qualitative comparison with results for frozen sand and to obtain parameters required for application of Ladanyi's dilatancy-hardening model.

2.3 COLD ROOM FACILITY AND TRIAXIAL TESTING SYSTEM

2.3.1 Cold Room Facility

Pertinent aspects of this facility include the following features (abstracted from Andersen, 1991; Andersen *et al.*, 1992; and Swan, 1994):

- a growth room (at $T = 0^{\circ}\text{C}$) for specimen freezing; a staging room (at $T \approx -4$ to -5°C) for preparing triaxial specimens; and a testing room maintained a few degrees colder than the desired testing temperature; and

- an environmental chamber to maintain the air temperature surrounding the triaxial cell to within $\pm 0.17^\circ\text{C}$.

2.3.2 Triaxial Testing System

Figure 2.1 shows a schematic of a Wykeham Farrance high-pressure triaxial cell that was modified for conventional frozen soil testing to accommodate lubricated end platens, on-specimen axial strain measurements, an internal load cell to measure the axial force, and thermistors to record temperatures in the silicone oil cell fluid near the top and bottom of the test specimens (nominal dimensions of 38 mm diameter by 75 mm long). Confining pressures were generated using a closed-loop pressure/volume control system consisting of a DC servomotor attached to a hydraulic piston acting on a reservoir of fluid. For tests on unfrozen sand, a similar system provided back pressure saturation and volume changes during consolidation and drained shear. For the consolidate-freeze tests, the top cap was modified to allow drainage of water as the specimen was frozen by circulating a freezing fluid at -8°C through the base pedestal.

For conventional tests on frozen sand, the axial strain rate was applied by a screw-driven variable-speed 45kN Wykeham Farrance (T-57) loading frame. As a result of the use of lubricated end-platens and compliance of the triaxial system, the actual strain rate experienced by the specimen increased during shear.

Compared to the maximum rate, which was usually achieved after about one percent axial strain, the initial secant value (up to $\epsilon_a \approx 0.03\%$) was about one tenth of the maximum rate, and the tangent value at the upper yield stress (defined in Section 2.5 and occurring at $\epsilon_a \approx 0.6 \pm 0.3\%$) was typically $10 \pm 5\%$ lower than the

maximum rate. These actual rates are used for presentation of the data. The consolidate-freeze tests and most of the tests on unfrozen sand used hydraulically-driven loading frames that also required several tenths percent strain before reaching the maximum (nominal) strain rate.

Three experimental aspects of the program of conventional tests on frozen sand are especially noteworthy:

- The use of enlarged, lubricated (via ice caps and silicone grease) end platens to facilitate lateral straining of the specimen. Although constrained by a pin at each end, data at large strains were discounted for some tests, because of very poor stability due to excessive lateral sliding (as observed after shearing).
- Measurement of on-specimen axial strains via specially designed yokes holding two AC-type linear variable differential transformers on opposite sides of the specimen (see Fig. 2.1). These can resolve axial strains to 0.001% and eliminate the initially S-shaped stress-strain curves commonly reported in the literature based on displacement of the two end platens or the loading piston. Initial stress-strain data were discounted when the two ACDT's showed poor agreement. Note: displacement of the loading piston was used at $\epsilon_a > 2.5\%$.
- Measurement of volumetric strains. These were computed from motions of the cell pressure/volume controller piston and the axial loading piston; then they were corrected to account for cell fluid

leakage, compressibility of the cell fluid and triaxial chamber, and flexure of the base of the triaxial cell (Andersen, 1991). This technique has a maximum volumetric strain error of $\pm 0.2\%$, which is small compared to the computed volumetric strains at large axial strains and low-to-moderate confining pressures.

2.4 TESTING PROCEDURES

(Abstracted from Andersen, 1991; Andersen *et al.*, 1992, 1994; Swan, 1994)

2.4.1 Conventional Tests on Frozen Sand

The molds used for preparation and freezing had been used by Martin *et al.* (1981) and were obtained from CRREL. All but seven specimens were prepared using multiple sieve pluviation (MSP), which produced specimens of very uniform density (as verified by radiography). The other seven used wet tamping, as did Martin *et al.* (1981) and many other experimental programs. As demonstrated by Baker and Konrad (1985), this technique causes non-uniform densities and significant scatter in measured behavior. All specimens were frozen from the top (at -15°C) down in about four hours, with resultant degrees of ice saturation equal to $99.2\% \pm 1.4\%$ SD, and stored at -25°C prior to being carefully trimmed for testing, usually with ice end caps of 1- to 3-mm thickness. All specimens had a prophylactic membrane and were maintained under the cell pressure prior to shearing for at least 12 hours or the expected shearing duration, in order to allow temperature stabilization and measurement of the cell fluid leakage rate. Calculation of the specimen dry density was based on the volume of the trimmed specimen and

weights measured before and after shearing. The reported values of relative density have an estimated standard deviation of $\pm 2\%$.

Measurement of temperature within the triaxial cell produced the following results (± 1 std. dev.).

Nominal Temp. ($^{\circ}\text{C}$)	Mean Temp. ($^{\circ}\text{C}$)	Temperature Gradient ($^{\circ}\text{C}$)
-10	-9.55 ± 0.05	0.35 ± 0.05
-15	-15.60 ± 0.10	0.40 ± 0.10
-20	-20.50 ± 0.20	0.55 ± 0.20
-25	-25.35 ± 0.20	0.30 ± 0.15

The temperature gradient is thought to be caused by heat generated from the on-specimen axial strain device, since the top of the specimen was always warmer than the bottom. Note: MIT would like to construct a slightly larger cell with an internal mixer to eliminate the temperature gradient and enable testing at $T = -5^{\circ}\text{C}$.

2.4.2 Tests on Unfrozen Sand

Most tests were either isotropically or anisotropically consolidated after back pressure saturation (usually with a computer-automated system) and then sheared undrained in triaxial compression with pore pressure measurements at a strain rate of about $10^{-5}/\text{s}$ (i.e., the moderate rate for frozen sand testing) and are designated as CIUC and CAUC tests, respectively. Some tests were sheared with drainage at constant mean effective stress (CIDC tests). As with the frozen tests, the program employed multiple sieve pluviation (with the mold sitting on the base pedestal), lubricated end platens (usually greased latex rubber) and on-specimen axial strain measurements.

2.4.3 Consolidate-Freeze Tests

The consolidate-freeze test procedures combined those of the unfrozen and conventional frozen testing programs, but also required development of a technique for freezing the specimen in the triaxial cell while under a consolidation stress that ranged from $\sigma'_c = 0.1$ to 10 MPa. Note: since the program wanted specimens having the same pre-shear relative density ($D_r \approx 95\%$), the initial relative density was progressively reduced with increasing consolidation stress. After several attempts, the freezing process used the following procedure:

- saturate and consolidate specimens at $T = +3^\circ\text{C}$;
- circulate freezing fluid at $T = -8^\circ\text{C}$ through a redesigned base pedestal to cause freezing from the bottom to the top of the specimen (see Sheet D5 in Appendix D);
- during freezing, which took about four hours, measure the volume of water flow out of the top cap via a drainage line connected to the back pressure/volume change controller;
- also monitor the temperature via three thermistors located in the cell fluid adjacent to the bottom, middle and top of the specimen;
- note that the freezing process ends when there is no measured outflow of water and/or the top thermistor registers zero $^\circ\text{C}$; and
- reduce the temperature in the testing room and the environmental chamber to $T = -13$ and -10°C , respectively, and equilibrate for at least 12 hours prior to shearing.

Although Swan (1994) and Section 5.4 report results from ten consolidate-freeze tests, the data should be regarded as preliminary for two reasons: first, three tests developed oil leaks into the top drainage line (hence, questionable estimates of the volume of expelled water); and second, the volume of expelled water for all specimens was typically less than 85% of the theoretical volume increase due to freezing of the pore water (taken as a 9% volume increase).

2.5 OVERVIEW OF STRESS-STRAIN BEHAVIOR AND DEFINITION OF STRESS-STRAIN PARAMETERS

2.5.1 Overview of Stress-Strain Behavior

Figure 2.2 plots deviator stress ($Q = \sigma_1 - \sigma_3$) versus engineering axial strain (ϵ_a) in order to illustrate the range in types of stress-strain curves measured during the conventional testing program on frozen MFS. Two stress-strain curves are plotted at each strain rate and temperature. One corresponds to specimens having a low relative density ($D_r \approx 35\%$) and low confining pressure ($\sigma_c = 0.1$ MPa) and hence presumably reflecting the minimum frictional resistance of the sand skeleton. The other corresponds to specimens having a high relative density ($D_r \approx 95\%$) and high confining pressure ($\sigma_c = 10$ MPa) and presumably reflecting the maximum frictional resistance of the sand skeleton. Figure 2.2a shows the effect of increasing the strain rate ($\dot{\epsilon}$) by two orders of magnitude from slow to fast for specimens sheared at $T = -10^\circ\text{C}$; Figure 2.2b shows the effect of decreasing the temperature by 10°C for specimens sheared at the moderate strain rate.

All of the stress-strain curves in Figure 2.2 exhibit a very distinctive yield point (the knee of the curve) at levels of axial strain ranging from 0.3 to 1.0%, as shown by the circles in the figure. This point represents the onset of highly non-linear behavior and the development of very significant plastic deformations; it is termed the *upper yield* point.

A qualitative assessment of the data in Figure 2.2 shows that the behavior in the small-strain region is largely unaffected by changes in relative density and confining pressure, both of which affect the frictional resistance of the sand skeleton. The results in Figure 2.2 also clearly demonstrate that strain rate and temperature, which affect ice behavior, have a tremendous influence on the magnitude of the deviator stress at the upper yield point, termed the *upper yield stress* (Q_{uy}). Section 3 will evaluate the behavior of frozen sand in the small-strain region where the measured volumetric strains were essentially zero.

At larger strains beyond the upper yield region, the data in Figure 2.2 show that changes in relative density and confining pressure obviously have a tremendous influence on stress-strain behavior. These two variables also affect the frictional resistance of the sand skeleton. Moreover, at large strains, all of the test specimens exhibited varying degrees of dilation (volumetric expansion) that depended mainly on sand density and confining pressure. Section 4 will evaluate the behavior of frozen sand in the large-strain region.

2.5.2 Definition of Parameters

Small-Strain Behavior

Figure 2.3 presents actual stress-strain curves drawn to two different strain scales in terms of the deviator stress ($Q = \sigma_1 - \sigma_3$) and the axial strain (ϵ_a). The parameters that have been selected for the evaluation of the small-strain behavior are the Young's modulus, the yield offset at 0.01% strain, and the upper yield stress. The graphical construction techniques used to obtain these parameters are summarized on the figure and explained as follows:

- The Young's modulus (E). The initial slope of the stress-strain curve determined visually from the average of the ACDT's (Fig. 2.3a) at levels of axial strain less than 0.01%.
- The yield offset stress at 0.01% strain (Q_{yo}). The intersection point of the stress-strain curve and a line with a slope of the Young's modulus translated by 0.01% strain (Fig. 2.3a).
- The upper yield stress (Q_{uy}). The first point on the stress-strain curve where the slope ($dQ/d\epsilon_a$) either becomes zero or reaches its minimum positive value before significant strain hardening (Fig. 2.3b).

Tables 5 to 8 in Andersen *et al.* (1994) and Sheets A1 to A5 in Appendix A present these three parameters and the strain at the upper yield stress (ϵ_{uy}) measured from

the stress-strain curves for all tests in Table 2.1. However, values of E , Q_{y0} and ϵ_{uy} from tests with poor ACDT agreement are excluded from the subsequent analysis in Section 3.

Large-Strain Behavior

The deviator stress versus axial strain curves in Figure 2.2 have different characteristics regarding the degree of post-upper yield strain softening or strain hardening, i.e., whether Q decreases or increases after reaching Q_{uy} ; and whether or not strain softening occurs after the specimen reaches its peak strength (Q_p). These different characteristics, which depend mainly on sand density and confining pressure, are illustrated in the upper portion of Figure 2.4 for tests conducted at low and high confining pressures ($\sigma_c = 0.1$ and 10 MPa). Note that the deviator stress is normalized by the upper yield stress, since Q_{uy} does not vary with D_r and σ_c . Figure 2.4 also summarizes characteristic volumetric behavior measured at low and high confining pressures.

Figure 2.4 labels four curve types, and Table 2.2 describes their characteristics and the typical testing conditions leading to each type. In way of summary, **Type C curves predominate at low confining pressures** ($\sigma_c = 0.1$ MPa) and are characterized by post-yield strain hardening to give a peak strength (Q_p) at moderate strains, followed by significant strain softening and significant dilation. For loose sand sheared at higher strain rates and/or lower temperatures, this behavior switches to **Type A curves**, i.e., $Q_p = Q_{uy}$ followed by significant strain

softening and volumetric expansion. In contrast, **Type D curves**, predominate at **high confining pressures** ($\sigma_c = 10$ MPa) and are characterized by significant post-yield strain hardening to give a peak strength at large strains, all with minimal dilation. For loose sand sheared at higher strain rates and/or lower temperatures, this behavior switches to **Type B curves**, i.e., initial strain softening followed by strain hardening to produce $Q_p \approx Q_{uy}$, again with minimal dilation.

The above qualitative trends are quantified in Section 4 by analyzing the influence of the four testing variables (D_r , σ_c , $\dot{\epsilon}$ and T) on the following parameters:

- the amount of post-upper yield strengthening ($\Delta Q = Q_p - Q_{uy}$) and the axial strain at peak strength (ϵ_p);
- the volumetric behavior in terms of the maximum rate of dilation ($d\epsilon_v/d\epsilon_a \text{ max} = \text{maximum slope of the } \epsilon_v \text{ versus } \epsilon_a \text{ curve}$) and the amount of dilation at $\epsilon_a = 20\%$ (ϵ_{v20}); and
- the amount and rate of post-peak strain softening, both of which will be related to the volumetric behavior.

Section 4 also presents a conceptual explanation for the above behavior in terms of strengthening mechanisms related to the frictional resistance of the sand skeleton-ice matrix and weakening mechanisms related to damage (fracture) of the ice matrix.

Table 2.1 Scope of Conventional Triaxial Tests on Frozen Manchester Fine Sand

Nominal Temperature (°C)	Confining Pressure σ_c (MPa)	SLOW (3 X 10 ⁻⁶ /s)				MODERATE (3.5 x 10 ⁻⁵ /s)				FAST (5 x 10 ⁻⁴ /s)				Total Number of tests
		Range in D _r (%)				Range in D _r (%)				Range in D _r (%)				
		20-40	40-60	60-80	80-100	20-40	40-60	60-80	80-100	20-40	40-60	60-80	80-100	
-10	0.1	1			2	5	1	1	6	1			3	50
	2				1	2		3					2	
	5					1	2	2	4					
	10	1	1		2	1	3	3	4	1				
-15	0.1						1	1	2					17
	10	2			3		2	1	2		2		1	
-20	0.1	1			1	1	3	1	2	2			1	19
	10	2			1	1			1	1		1		
-25	0.1	1			1	1	1	1	1	1	2			13
	10		1		1	1				1				

Table 2.2 Definition of Characteristic Curve Types Describing the Large-Strain Behavior of Frozen Manchester Fine Sand

CURVE TYPE	CHARACTERISTICS	TESTING CONDITIONS
A	<ul style="list-style-type: none"> • Peak strength occurs at upper yield stress, $Q_p = Q_{uy}$ • Significant post-yield strain softening (low Q_{20}/Q_{uy}) • Significant dilation (large ϵ_{v20}) 	<ul style="list-style-type: none"> • Low D_r and low σ_c • Higher $\dot{\epsilon}$ and lower T
B	<ul style="list-style-type: none"> • Slight to moderate post-yield strain softening, followed by zero to slight strain hardening • Hence, $Q_{uy} \approx Q_p \approx Q_{20}$ • Small dilation (small ϵ_{v20}) 	<ul style="list-style-type: none"> • Low to moderate D_r and high σ_c • Higher $\dot{\epsilon}$ and lower T
C	<ul style="list-style-type: none"> • Slight to significant post-yield strain hardening, with Q_p occurring at moderate strains ($\epsilon_a \approx 5\%$) • Moderate to significant post-peak strain softening • Hence, $Q_p > Q_{uy} > Q_{20}$ • Significant dilation (large ϵ_{v20}) 	<ul style="list-style-type: none"> • Dominant behavior at low σ_c • Degrees of strain hardening/softening both increase with increasing D_r • Switches to Type A at lower D_r for high $\dot{\epsilon}$/low T
D	<ul style="list-style-type: none"> • Significant post-yield strain hardening, with Q_p occurring at large strains • No post-peak strain softening • Small dilation (small ϵ_{v20}) 	<ul style="list-style-type: none"> • Dominant behavior at high σ_c independent of D_r • Switches to Type B at lower D_r for high $\dot{\epsilon}$/low T

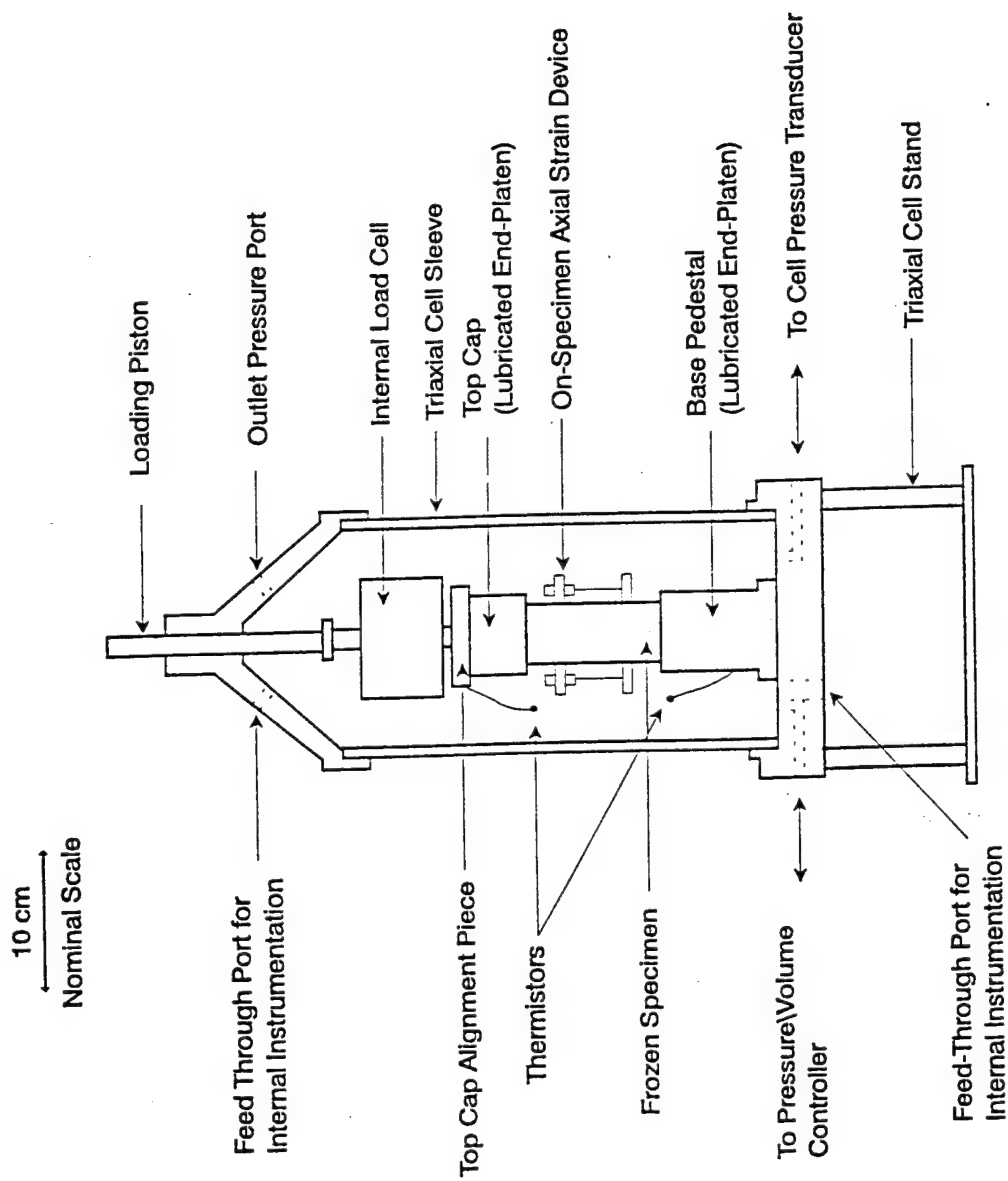


Fig. 2.1 Schematic of High Pressure Triaxial Cell

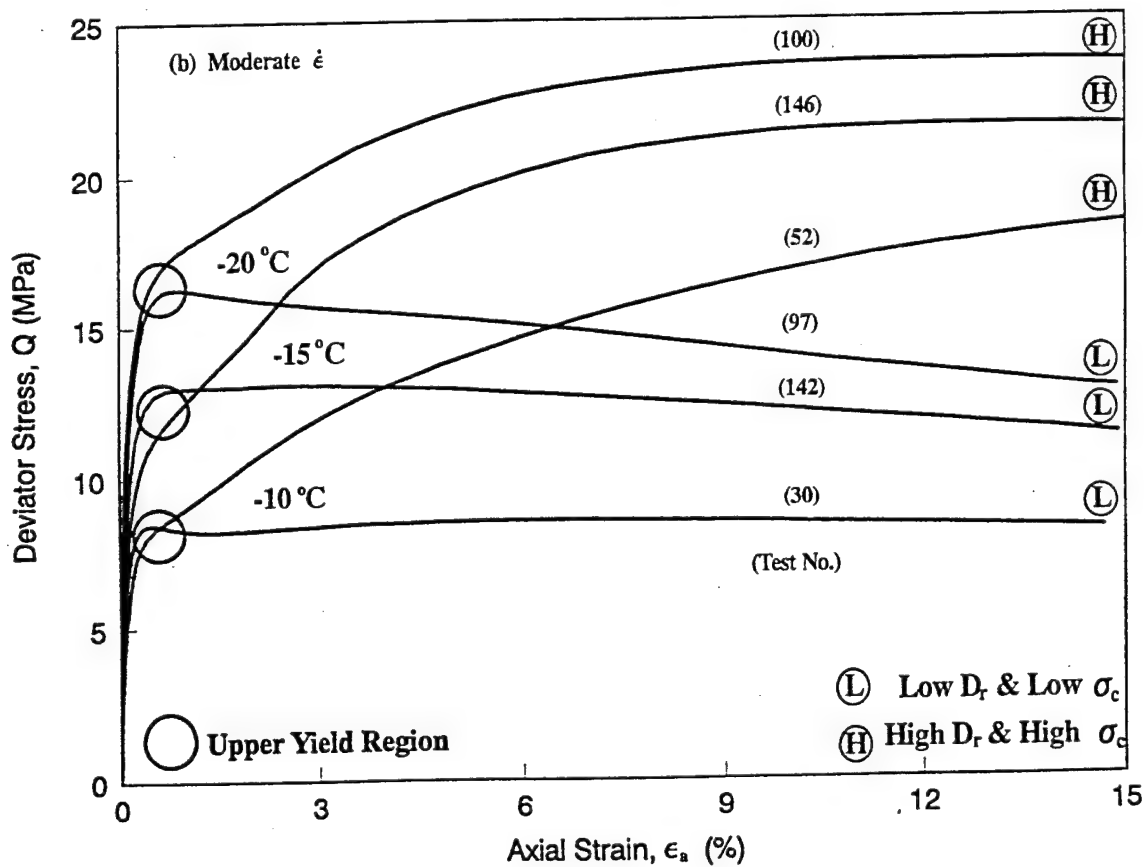
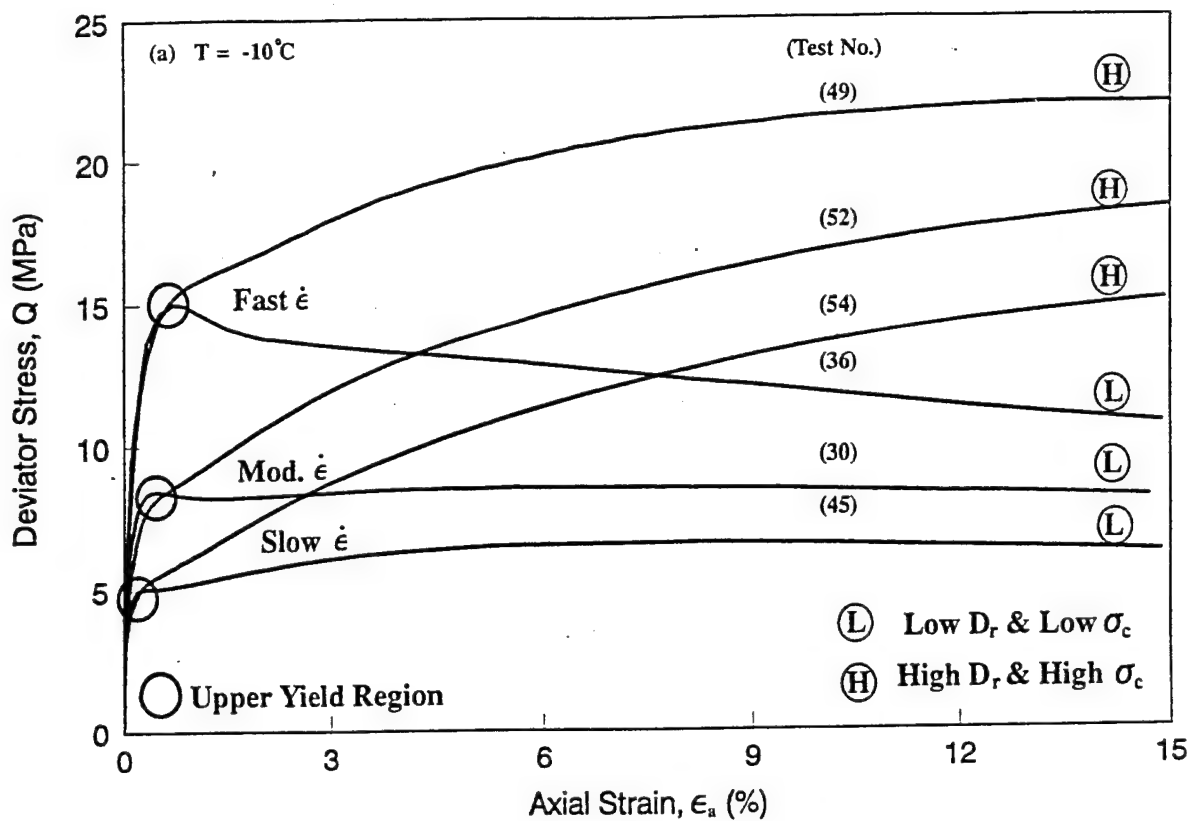


Fig. 2.2 Effect of Relative Density and Confining Pressure on Stress-Strain Curves for Frozen MFS: a) At Varying Strain Rates; b) At Varying Temperature

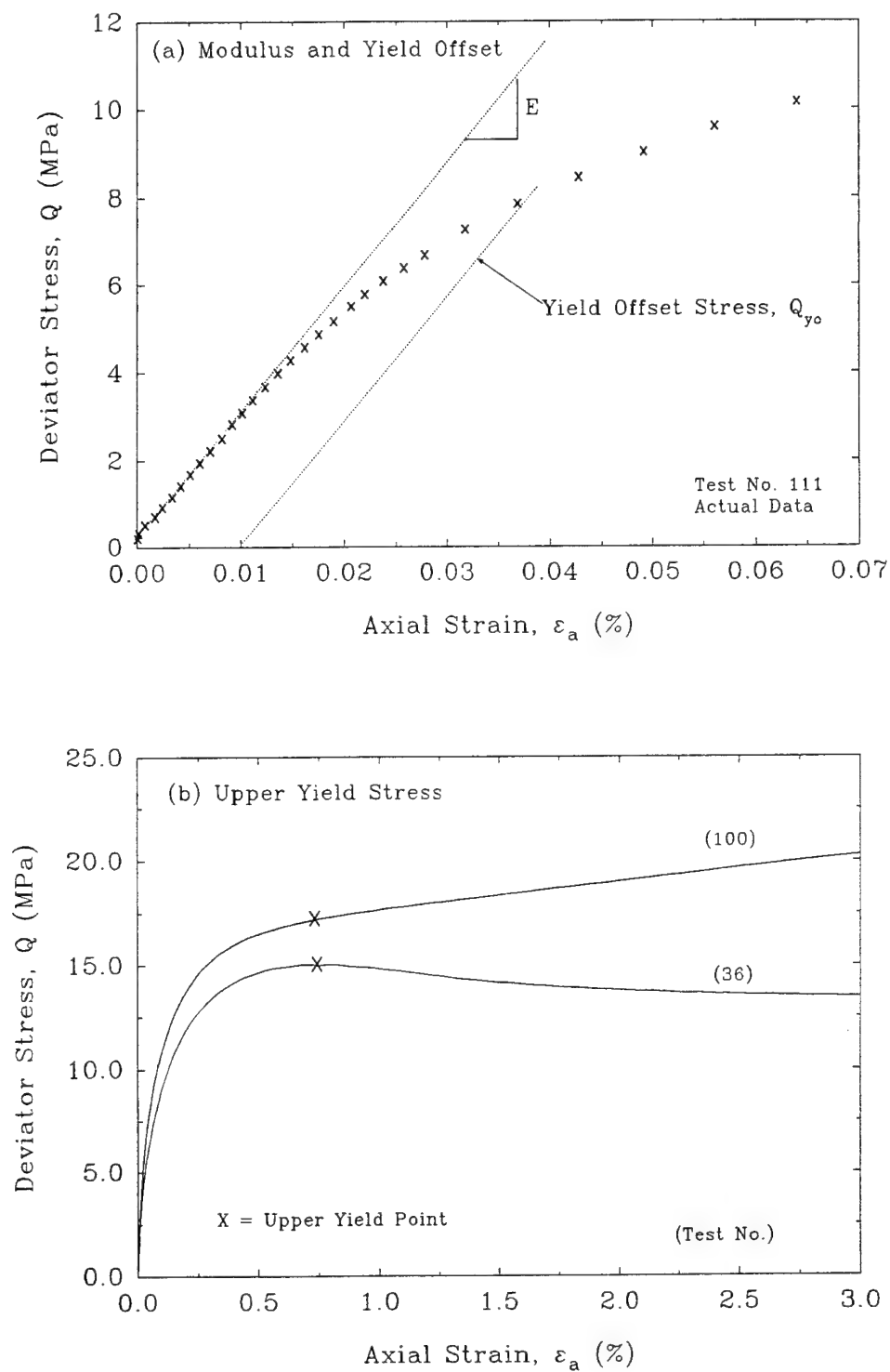


Fig. 2.3 Definition of Small Strain Parameters: (a) Modulus and Yield Offset Stress; (b) Upper Yield Stress

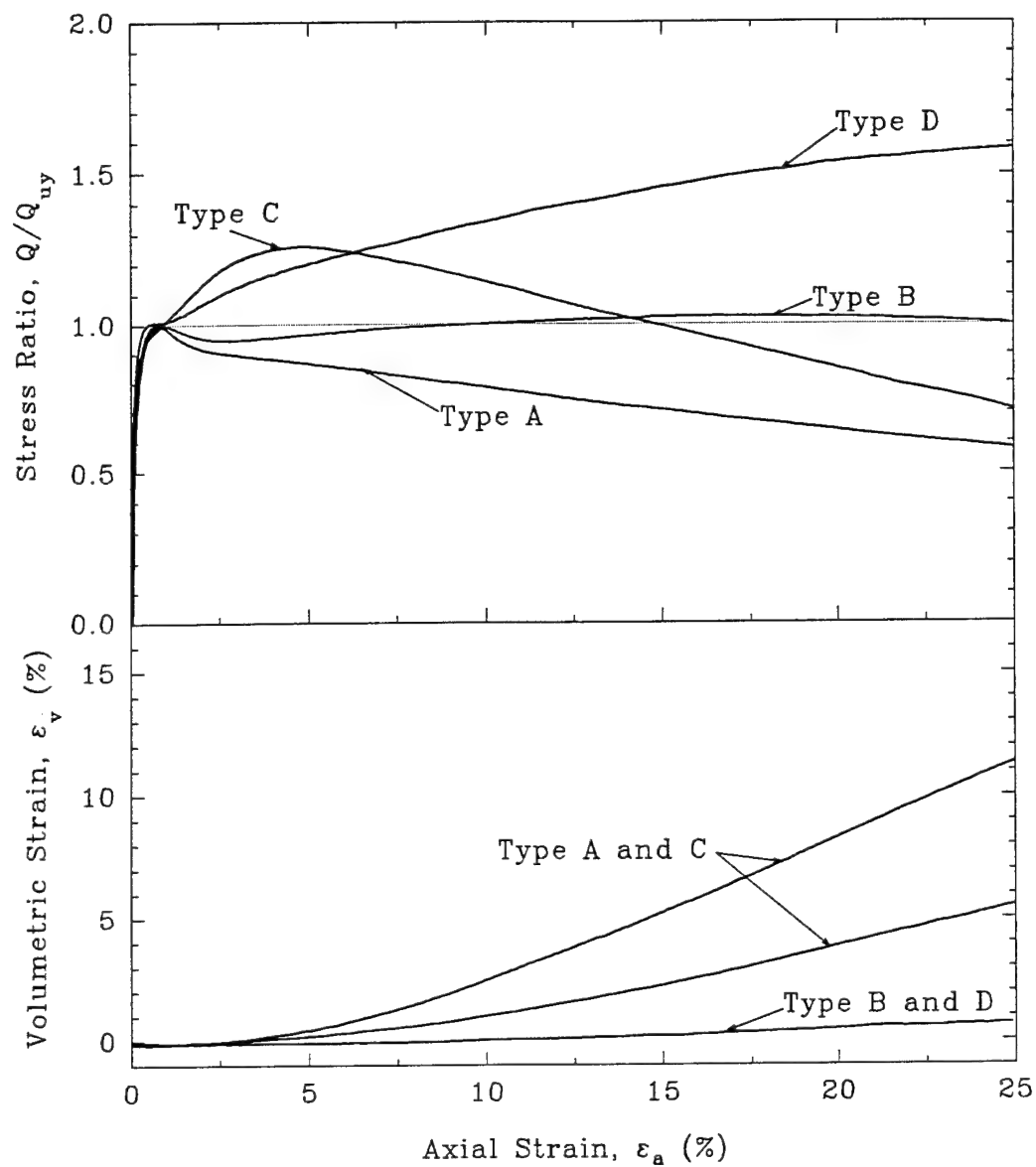


Fig. 2.4 Types of Stress-Strain Curves Describing Large Strain Behavior
 (Note: The magnitude of Q_p/Q_{uy} and/or the rates of strain hardening/
 softening and dilation vary for each curve type)

3. SMALL-STRAIN BEHAVIOR OF FROZEN SAND

3.1 BACKGROUND

The small-strain region refers to behavior measured up to the upper yield region (see Fig. 2.2), which typically occurs at axial strain levels of less than one percent. Section 3 summarizes data on Manchester Fine Sand (MFS) in terms of three parameters (E = Young's modulus; Q_{yo} = yield offset stress; and Q_{uy} = upper yield stress) and compares these results with information reported in the literature for other frozen sands. However, a review of the literature by Andersen *et al.* (1994) shows the following:

- Of the ten programs that report modulus data (tangent, secant, shear, etc.), only two used small-strain measurement techniques capable of obtaining reliable values of Young's modulus, i.e., within the linear range of stress-strain behavior corresponding to axial strains less than 0.01%.
- Of the 15 programs that present stress-strain curves with an upper yield stress (commonly referred to as the initial, first or lower yield or the first peak), none have investigated the combined effects of sand density, confining pressure, strain rate and temperature. Moreover, only two studied the effect of sand density, and only five evaluated the effect of confining pressure at varying strain rate or temperature.

Sheets A1 to A5 of Appendix A tabulate the specimen properties, testing conditions and measured small strain parameters for all conventional tests on frozen MFS.

3.2 YOUNG'S MODULUS

3.2.1 Data on Manchester Fine Sand

Figure 3.1 plots Young's modulus (E) versus relative density from all tests having good or fair ACDT agreement and shows the nominal temperature for each test. Mean and standard deviation values of modulus in GPa at each temperature are 26.6 ± 4.4 at -10°C ; 23.9 ± 2.5 at -15°C ; 28.1 ± 4.0 at -20°C , and 27.1 ± 1.3 at -25°C . This variation is not statistically significant. Andersen *et al.* (1994) conclude that modulus does not vary with strain rate, but does show a slight decrease with higher confinement. The collective data for all tests indicate that E decreases by about 10 to 15% as σ_c increases from 0.1 to 10 MPa. This is considered to be a second-order effect.

Linear regression on the data in Figure 3.1 predicts a slight increase in E with increasing relative density, but with very low correlation coefficient ($r^2 = 0.06$). Nevertheless, the authors conclude that the trend is real, based on the analysis presented in Section 3.2.3. But from a practical viewpoint, E for this frozen sand is independent of the four testing variables ($\dot{\epsilon}$, σ_c , D_r , and T) and equals 26.5 ± 4 GPa.

3.2.2 Comparisons with Prior Data

The Young's modulus of saturated, frozen sand has been measured reliably in two programs. Kaplar (1963) used the resonant beam technique to test two sands over a temperature range of $T = -1.1$ to -27.8°C . He recorded $E = 34.5$ to 42.4 GPa for Peabody Gravelly Sand and $E = 28.3$ to 34.5 GPa for McNamara Concrete

Sand. For both soils, E increased with decreasing temperature, but tended to level off below about -10°C . Baker and Kurfurst (1985) used two techniques for testing 16-100 Ottawa Sand. They recorded $E = 23 \pm 9$ GPa from on-specimen extensometer tests at $T = -10^{\circ}\text{C}$ and $E = 27 \pm 3$ GPa from acoustic wave propagation tests at $T = -3.2$ and -10°C (no influence of temperature). In both test series, E increased with increasing sand density, which varied between 1550 and 1780 kg/m^3 . Note: these authors also showed a substantial drop in E with slight increases in the salinity of the pore fluid, especially at -3.2°C .

The Young's modulus of frozen MFS agrees well with the Kaplar (1963) data and very well with the Baker and Kurfurst (1985) data. Hence, the actual sand type has a relatively minor effect on Young's modulus. In contrast, values of "initial modulus" reported in the literature from numerous programs that did not use on-specimen strain devices or acoustic wave propagation techniques are much lower, e.g., typically in the range of only 0.1 to 8 GPa. These modulus determinations were made at strain levels much higher than the $\epsilon_a < 0.01\%$ used for frozen MFS. These collective data also indicate a tendency for modulus to increase with decreasing confining pressure, increasing strain rate and decreasing temperature. As shown in Section 3.3, these trends are consistent with those observed for the yield offset stress (Q_{y0}) of frozen MFS; therefore, they undoubtedly include some nonlinear plastic deformations.

3.2.3 Prediction of Young's Modulus

The Young's modulus of frozen MFS is about three times larger than that reported for polycrystalline ice (i.e., 9 GPa by Sinha 1989) and one to two orders of magnitude larger than measured in consolidated-undrained triaxial compression tests on unfrozen MFS having consolidation stresses ranging from 0.1 to 10 MPa (i.e., 0.2 to 4 GPa by Swan 1994). A logical explanation for why E of frozen sand is larger than either of its components is that frozen sand acts as a composite material consisting of a stiff aggregate (sand particles) within a soft matrix (ice). That is, it is the stiffness of the sand particles, and not that of the sand skeleton, that dominates the overall stiffness of the frozen sand system at small strains.

Andersen (1991) and Andersen *et al.* (1992, 1994) applied Counto's (1964) isostrain composite material model, which was developed for concrete, to frozen MFS. His model can be visualized as a prism of a solid aggregate material (silicate mineral representing the sand phase) embedded in a cube of matrix material (polycrystalline ice representing the ice phase), with perfect bonding between the sand particles and the pore ice. The resulting equation for the composite Young's modulus is

$$\frac{1}{E_c} = \frac{1 - \sqrt{V_s}}{E_i} + \frac{1}{\left[\frac{1 - \sqrt{V_s}}{\sqrt{V_s}} \right] E_i + E_s} \quad \dots\dots\dots[3.1]$$

where E_c is the composite modulus; E_i and E_s are the Young's moduli for the ice matrix and the sand grains, respectively; and V_s is the volume fraction of the sand grains.

Using a Young's modulus for sand particles of 90 GPa (from Table 12.5 of Lambe and Whitman 1969, assuming an average value for Quartzite) and 9 GPa for polycrystalline ice from Sinha (1989), the estimated composite Young's modulus for frozen MFS ranges from 24.0 to 29.6 GPa for volume fractions ranging from 0.52 ($D_r = 0\%$) to 0.63 ($D_r = 100\%$). Figure 3.1 compares the predicted and measured Young's modulus for frozen MFS having relative densities varying from 20 to 100%.

The excellent agreement between the predicted and measured Young's modulus in Figure 3.1 and the agreement with prior reliable measurements indicates that the Counto isostrain model can offer insight as to why the Young's modulus of frozen sand is so much greater than either of its two components. It also helps to explain why the type of sand has little effect on Young's modulus of a frozen cohesionless soil (Section 3.2.2). The silicate/ice interface of frozen MFS in the range of temperatures and strain rates studied herein appears capable of transmitting the shear stresses necessary to allow the silicate particles to reinforce the ice matrix in composite action, thus causing the frozen sand to behave as a composite material at very small strains. The mineralogy of the silicate particles (governing their elastic properties) is much more important to the initial stress-strain response than is the structure of the sand skeleton. Additionally, the dry density of the sand is important insofar as it affects the volume fraction of the silicate minerals in the frozen composite material.

3.3 YIELD OFFSET STRESS

The yield offset stress is considered in order to include a parameter lying between the truly elastic region (Young's modulus) and the onset of highly non-linear and plastic behavior at the upper yield stress. Figure 3.2 plots the yield offset stress (Q_{yo}) versus temperature as a function of strain rate for the two extremes of confining pressure ($\sigma_c = 0.1$ and 10 MPa). Analysis of the extensive data at $T = -10^\circ\text{C}$ shows no effect of sand density. For the other three variables, the results in Figure 3.2 and similar analysis for Q_{yo} versus strain rate indicate the following:

- Q_{yo} is strongly dependent on temperature (increasing with decreasing temperature), with dQ_{yo}/dT (MPa/ $^\circ\text{C}$) decreasing consistently from about -0.02 at the slow strain rate to about -0.25 at the fast strain rate.
- Q_{yo} is also strongly dependent on initial secant strain rate. Using a power law relationship of the form (Glenn 1955, Sayles 1973)

$$Q_{yo} = B \left(\dot{\epsilon} \right)^{\frac{1}{n}} \quad \dots\dots\dots[3.2]$$

where B is a temperature-dependent constant, the power law coefficient (n) has values of 13.2 ± 5.2 (and $r^2 = 0.49 \pm 0.19$) with no consistent variation as a function of temperature and confining pressure.

- Q_{yo} decreases with increasing confining pressure. Although this pressure sensitivity cannot be defined as a function of strain rate and temperature,

the collective data suggests that the $dQ_{yo}/d\sigma_c \approx -0.1 \pm 0.05$ and perhaps tending towards zero at the lowest temperature.

3.4 UPPER YIELD STRESS

3.4.1 Data on Manchester Fine Sand

Definition of the upper yield stress (Q_{uy}) as a function of the testing variables is considered to be one of the most important contributions of this research. Figure 3.3 illustrates the fact that relative density does not affect Q_{uy} for specimens sheared at varying strain rates and $T = -10^\circ\text{C}$. For tests sheared at the moderate strain rate and a temperature of -10°C , the data in Figure 3.3 and the tabulated results in Appendix A show a fairly consistent decrease in Q_{uy} with increasing confining pressure, i.e., $dQ_{uy}/d\sigma_c = -0.06$ with $r^2 = 0.2$. However, the pressure sensitivity of the upper yield stress is considered a second order effect since the collective data at the other strain rates and lower temperatures do not show the same consistent change in Q_{uy} with confining pressure. Therefore, Figures 3.4 and 3.5 can be used to define Q_{uy} as a function of strain rate and temperature, respectively, independent of sand density and confining pressure. The strain rate used in Figure 3.4 is the tangent (instantaneous) strain rate at the upper yield stress, which typically was $10 \pm 5\%$ less than the nominal (maximum) strain rate.

For the data in Figure 3.4, a power law relationship for the strain rate dependency can be used of the form

$$Q_{uy} = A \left(\dot{\epsilon} \right)^{\frac{1}{n}} \quad \dots\dots\dots [3.3]$$

where A is a constant for a given temperature. For the data in Figure 3.5, the temperature dependency can be expressed using a linear relationship of the form

$$Q_{uy} = C + DT \quad \dots\dots\dots [3.4]$$

where C and D are constants for a given strain rate.

Sheet A6 presents the results of linear regression analyses on the data, which show the following trends:

- For the data in Figure 3.4, n increases in a very consistent fashion from about 4.6 to 6.6 as the temperature decreases from -10 to -25°C. That is, the upper yield stress becomes less strain rate dependent at lower temperatures.
- For the data in Figure 3.5, $D = dQ_{uy}/dT$ varies in a very consistent fashion from -0.58 at the slow strain rate to -0.97 at the fast strain rate. That is, the upper yield stress becomes more temperature dependent with increasing strain rate.

Appendix A lists the values of axial strain (ϵ_{uy}) at the upper yield stress, which range from 0.25 to 1.1% over all testing conditions. For shearing at the slow and moderate strain rates, mean values of ϵ_{uy} and Q_{uy} at each $\dot{\epsilon}$ and T give the relationship ($r^2 = 0.85$)

$$\epsilon_{uy}(\%) = 0.12 + 0.04 Q_{uy}(\text{MPa}) \quad \dots\dots\dots[3.5]$$

where the mean Q_{uy} ranged from 5.1 to 20.7 MPa.

3.4.2 Comparisons with Prior Data

Baker and Konrad (1985) represent the only other program to measure upper yield stress versus sand density. Their results show no change in Q_{uy} for pluviated 30-100 Ottawa sand with D_r ranging from 30 to 100% and tested in unconfined compression with on-specimen axial strain measurements at $\dot{\epsilon} = 1.7 \times 10^{-4}/\text{sec}$ and $T = -10^\circ\text{C}$. This behavior is consistent with the frozen MFS data in Figure 3.3. Their mean value of Q_{uy} also is within about 15% of that predicted for MFS at the same strain rate and temperature.

The primary focus of other programs reported in the literature was on peak strength; they contained relatively little discussion of upper yield behavior. The fact that these programs did not employ on-specimen axial strain measurements and usually tested "compacted" specimens also prevented reliable detection of the upper yield stress in a consistent fashion. These limitations should be born in mind when comparing prior data with results from this research.

Figure 3.6 plots the upper yield stress as a function of confining pressure for frozen Ottawa sands tested by Sayles (1973), Chamberlain *et al.* (1972) and Parameswaran and Jones (1981). The mesh sizes for the three sands were 20-30, 100-200 and 30-100, respectively. The Sayles tests were conducted at -3.85°C ; the others were conducted at $T \approx -10^\circ\text{C}$. The current data at the moderate strain rate for

all relative densities and a temperature of -10°C are also plotted. Although the Parameswaran and Jones (1981) test program produced a higher upper yield stress than expected for Manchester Fine Sand at the same strain rate (i.e., $Q_{uy} = 10 \text{ MPa}$ from Figure 3.4), the modest pressure sensitivity is consistent with the collective data on MFS which showed $dQ_{uy}/d\sigma_c \approx 0 \pm 0.1$ from nine sets of data (albeit that the Parameswaran and Jones data exhibit a consistent increase with confinement). Note that the confining pressure in the Parameswaran and Jones tests was not constant, but increased during each test (the confining pressure used in Figure 3.6 is that reported at the upper yield stress).

Two of the three tests by Chamberlain *et al.* (1972) produced values of significantly lower than expected for Manchester Fine Sand at the same strain rate (i.e., 18 MPa for Figure 3.4). Both the Sayles (1973) data at lower confining pressures and the Chamberlain *et al.* (1972) data have much larger pressure sensitivities than observed for MFS. Perhaps coarse-grained sands and higher strain rates cause earlier fracturing of the ice matrix, leading to a pressure sensitivity similar to that reported by Jones (1978, 1982) for polycrystalline ice. At higher confining pressures, the Sayles data indicated less pressure sensitivity in a manner consistent with the Parameswaran and Jones (1981) results and those in the current testing program.

Parameswaran and Roy (1982) present strain rate data ($\dot{\epsilon} = 5 \times 10^{-7}$ to $6 \times 10^{-3}/\text{sec}$) on upper yield stress for a compacted, saturated Ottawa 30-100 sand in unconfined compression at -30°C . They reported a power law coefficient of 10.6, which means a lower rate sensitivity than for frozen MFS. However, a direct

comparison with the power law coefficients of the present data may not be valid, since they did not have the true strain rate (and their initial stress-strain curves were S-shaped) and they used compacted rather than pluviated specimens.

3.4.3 Discussion of Mechanisms and Analogy with Peak Ice Strength

Various researchers have presented short discussions of possible mechanisms that may operate within the upper yield region during the shearing of frozen soils. These are focused on drawing an analogy between the upper yield behavior of frozen soil and the peak strength behavior of polycrystalline ice, e.g., Chamberlain *et al.* (1972), Bragg and Andersland (1980), Parameswaran and Jones (1981), and Sayles (1989), among others. Brief excerpts from these discussions follow:

Chamberlain et al. (1972) "The distinct yield points in the stress-strain curves for the OWS 'Ottawa sand' samples tested in the range of $\sigma_c = 0.5 - 5.0 \text{ kip/in}^2$ are most probably related to breaking of the ice-sand bonds and shearing of ice crystals."

Bragg and Andersland (1980) "The initial yield occurs as the pore ice reaches its final yield stress and as interparticle friction and dilatancy begin to contribute to the shear strength....With increasing strain rates the ice matrix strength increases giving a higher initial yield stress."

Parameswaran and Jones (1981) "This indicates that deformation behavior in the early elastic region is governed mainly by the ice matrix....The larger value of the yield strength for frozen sand as compared to ice is due to the mobilization of soil grain friction, in addition to cohesion of ice. As in ice, an initial

increase in yield stress with pressure can be explained by the closure of voids in the sand-ice specimens, thereby allowing the ice matrix to deform plastically."

Sayles (1989) "It should be noticed that yield (initial sharp bending of the curve) occurs at less than 1% strain, even though the maximum stress is not reached. There is evidence to suggest that initial cracking of the ice matrix occurs at this point....That the initial yield represents the domination of the ice matrix cohesive component...is reinforced by the shape of the Mohr's strength envelope....The envelope for the initial yield (i.e., first peak)...is curved at lower values of confining pressures, indicating that some internal friction is involved at these lower levels of confining pressures. This 'first peak' envelope approaches a constant value at the higher confining pressures, suggesting that ice cohesion provides nearly all the initial yield resistance at these confining pressures and small strains."

Thus, there is general consensus that the upper yield behavior of frozen sand is dominated by the ice matrix.

Figure 3.7 compares the upper yield stress as a function of strain rate for frozen MFS (from Fig. 3.4) and the peak strength of polycrystalline ice at temperatures ranging from -7 to -12°C, confining pressures up to 10 MPa and grain sizes of 0.7 and 1.0 mm. These ice data were reported by Hawkes and Mellor (1972) and Jones (1982). The power law coefficients (n) for ice range from 4.3 to 5.4 and correspond well to those of the Q_{uy} of frozen MFS. This suggests that the behavior of the frozen sand in the upper yield region is qualitatively similar to that of polycrystalline ice. However, the magnitude of the upper yield stress at comparable

temperatures is approximately double that of the strength of polycrystalline ice in unconfined compression. Apparently, the presence of the sand particles causes a strengthening effect, even though the frictional characteristics of the sand skeleton seem to be unimportant as evidenced by the insensitivity to changes in D_r and σ_c (Fig. 3.3). It is also important to note that the ice peak strength data of Jones (1982) show a confining pressure sensitivity unlike the upper yield stress of frozen Manchester Fine Sand.

The strong dependence of the upper yield behavior on the applied strain rate and temperature, its independence of the relative density and its very slight dependence on the confining pressure (considered a second-order effect) all indicate that the structure of the sand skeleton (i.e., its frictional resistance and tendency to dilate or contract) probably does not play a significant role in controlling the behavior of frozen sand in the upper yield region. On the other hand, the close agreement between the power law coefficients for the peak strength of polycrystalline ice and the upper yield stress of frozen sand over a wide range in strain rates and temperatures suggests that the principal physical mechanisms occurring within the upper yield region are probably similar to those controlling the behavior of polycrystalline ice at its peak strength.

Unfortunately, the ice data in Figure 3.7 are at strain rates beyond the ductile (i.e., flow or creep) range wherein the effects of strain rate and temperature can be modeled by a combination of the Norton-type power law and the Arrhenius temperature equation according to Glen(1955), i.e., the constant power law coefficient and activation energy. Consequently, an understanding of the physical

mechanisms controlling the upper yield behavior of frozen sand (in the deformational regime investigated in this research) will first require an improved knowledge of the physical mechanisms controlling the behavior of ice within the ductile-to-brittle transition region.

It is interesting to note that the initial shapes of the stress-strain curves presented in Figure 2.2 are qualitatively similar to those reported by Baker *et al.* (1982), Chamberlain *et al.* (1972), and Parameswaran and Jones (1981). Additionally, they are remarkably similar to the stress-strain curves presented by Mellor and Cole (1982) for polycrystalline ice.

The authors concur with prior researchers that the upper yield behavior is attributable to the pore ice, but have seen no evidence of a frictional contribution as suggested by Sayles (1973, 1989) and Parameswaran and Jones (1981) for frozen Manchester Fine Sand in the ranges of temperature and strain rate investigated in this program.

3.5 SUMMARY AND CONCLUSIONS

The measured small-strain response of frozen Manchester Fine Sand (MFS) is reported in terms of the Young's modulus, the yield offset stress at 0.01% strain, and the upper yield stress (first point on the stress-strain curve where the slope either becomes zero or reaches its minimum positive value before significant strain hardening). Figures 2.2 and 2.3 present stress-strain curves that show the upper yield region.

Figure 3.1 demonstrates that the Young's modulus (E) is nearly independent of testing variables. There is a slight (10-15%) decrease in E with σ_c increasing from 0.1 to 10 MPa (considered a second-order effect), and a slight increase (15%) with D_r increasing from 20 to 100%. The measured modulus equals 26.5 ± 4.0 GPa over all the testing variables. This value agrees well with reliable measurements on three other frozen sands.

The mineralogy of the sand grains, the sand density, and the ice/silicate bond strength are considered to be the most significant factors that contribute to the initial stiffness properties of frozen MFS in the ranges of temperature and strain rate investigated in this program. A composite materials model developed by Counto (1964) for concrete has been extended to frozen sands. The excellent agreement between predicted and measured data in Figure 3.1 indicates that composite action between the pore ice and silicate particles is the mechanism responsible for a Young's modulus that is several times greater than that of polycrystalline ice and up to two orders of magnitude greater than that of the sand skeleton.

An upper yield stress (Q_{uy}) was identified from stress-strain curves such as illustrated in Figure 2.3 for a range in testing conditions. The measured volumetric strains up to the upper yield stress were essentially zero. The value of the upper yield stress does not depend on relative density and is only slightly affected by the magnitude of the confining pressure, as illustrated in Figure 3.3. This indicates that the frictional characteristics of the sand skeleton play a minor role, since these two variables have a strong influence on the stress-strain behavior of unfrozen sand.

However, the upper yield stress is very dependent on the strain rate and the temperature, as demonstrated in Figures 3.4 and 3.5, respectively. Although the upper yield stress of frozen sand is larger than the peak strength of polycrystalline ice (Fig. 3.7), both materials have similar power law coefficients, i.e., in the range of 5.5 ± 1.0 . This suggests that the principal physical mechanisms occurring in the upper yield region are probably similar to those controlling the behavior of polycrystalline ice. This is in general consensus with the opinions of other researchers. However, the actual nature of the mechanisms controlling the upper yield response are still poorly understood.

The yield offset stress at 0.01% axial strain (Q_{yo}) is presented in order to bridge the gap between the initial modulus and the upper yield behavior. The relative density has no influence, and there is a modest decrease in Q_{yo} with increasing confining pressure. It is strongly influenced by strain rate and temperature, but to a lesser degree than the upper yield stress (Fig. 3.2). This indicates that the behavior of frozen sand in the small-strain region becomes more strain rate and temperature sensitive as the level of strain increases.

These data present the most comprehensive treatment of the small-strain behavior of a frozen sand available in the literature; we hope they will assist in the development of improved modeling capabilities for describing the small-strain behavior of frozen sands.

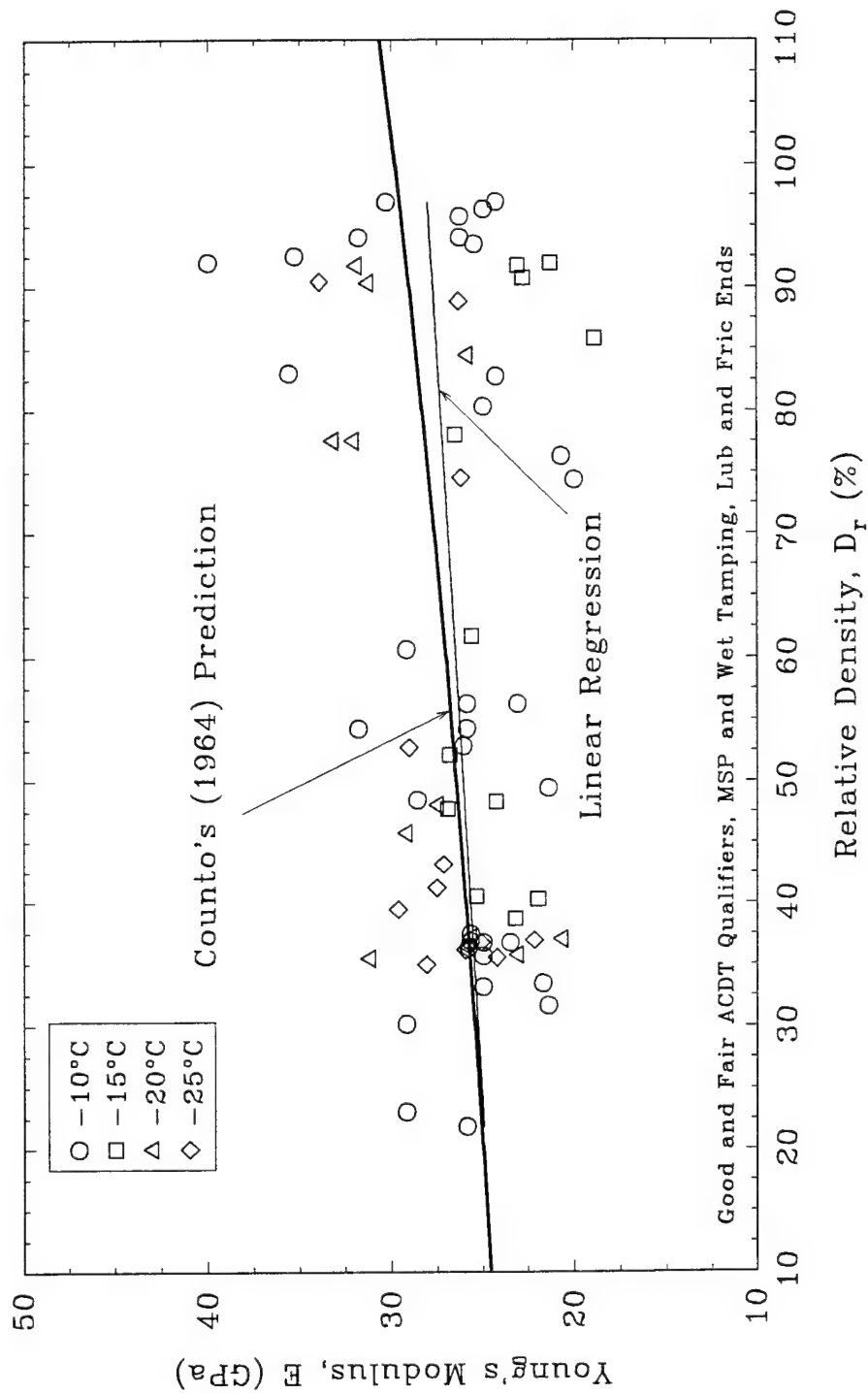


Fig. 3.1 Comparison of Measured and Predicted Young's Modulus vs. Relative Density for Frozen MFS at All Testing Conditions

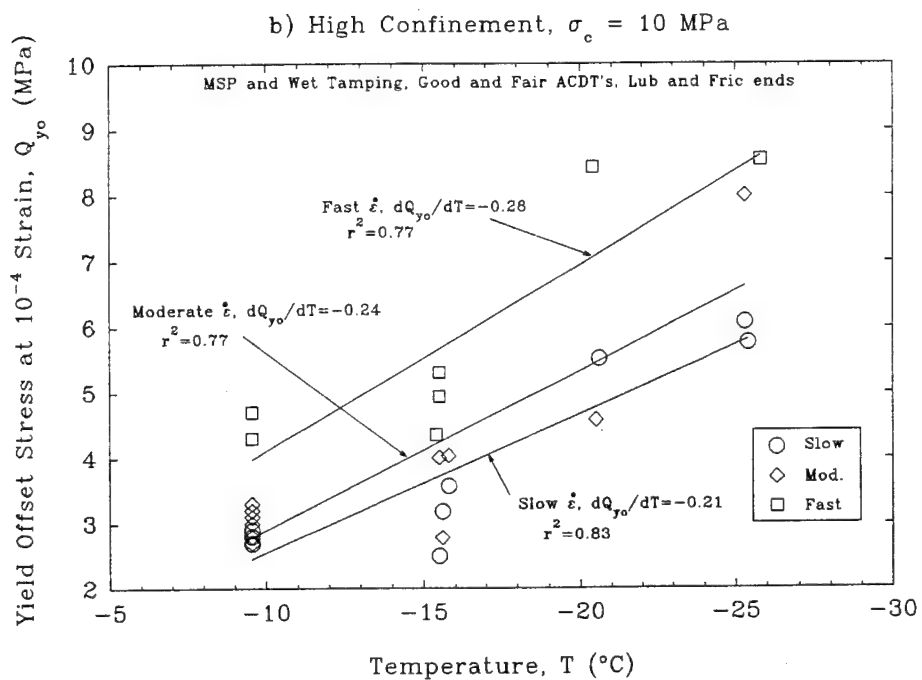
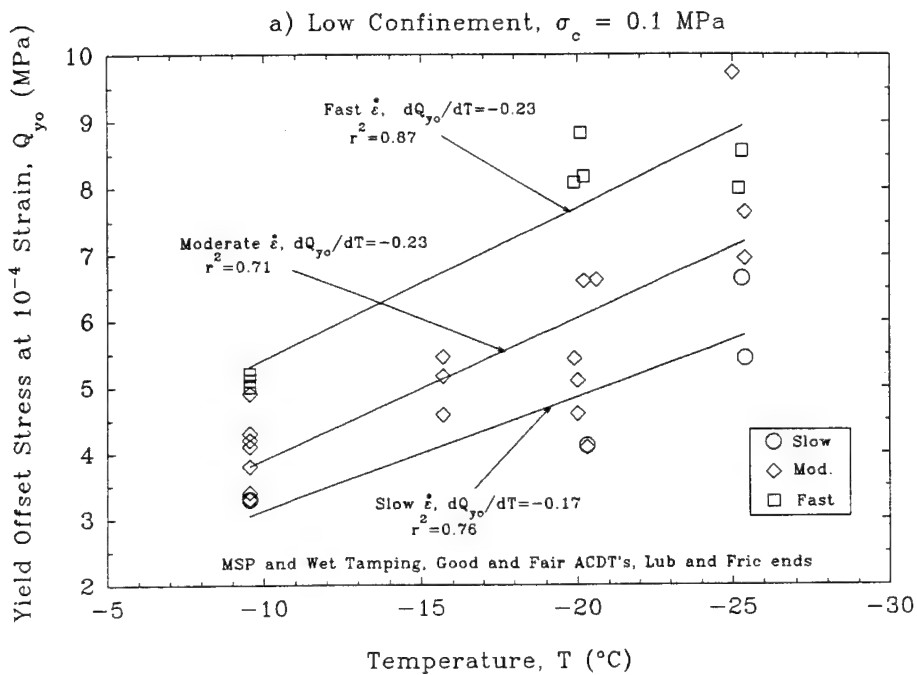


Fig. 3.2

Yield Offset Stress vs. Temperature at Varying Strain Rate and All Relative Densities for Frozen MFS at a) Low Confinement and b) High Confinement

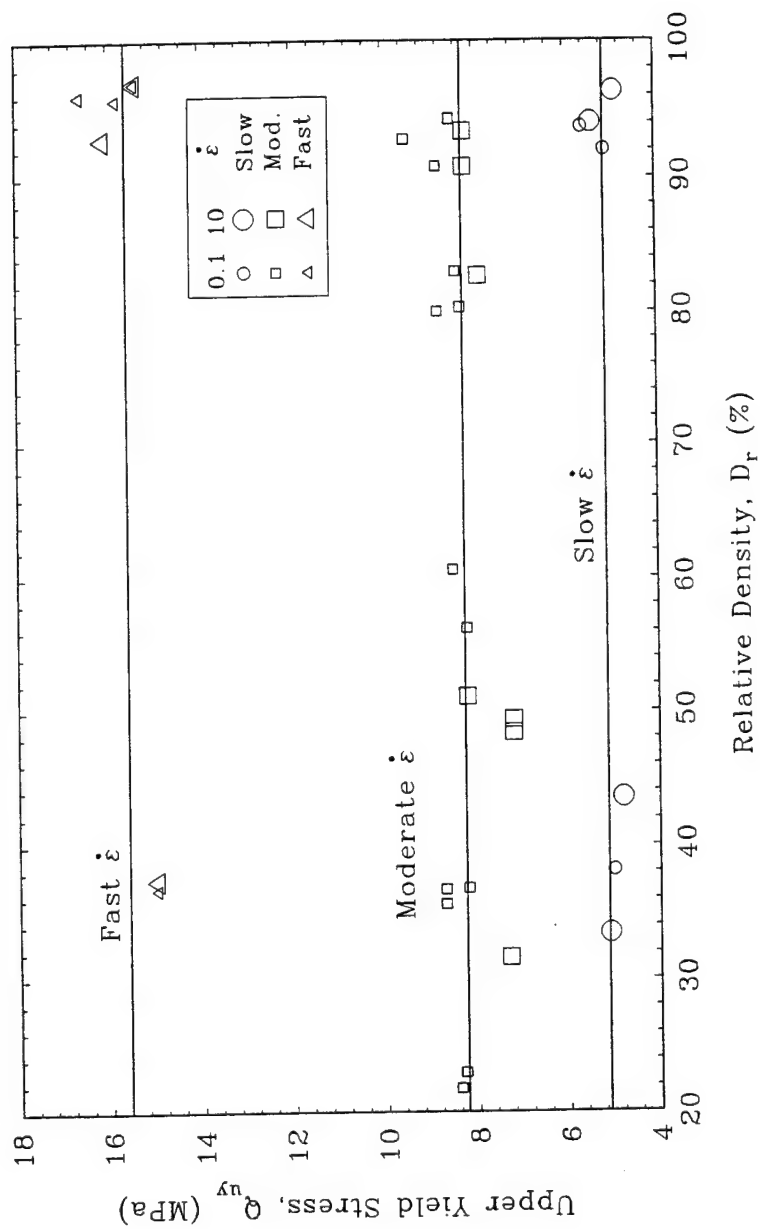


Fig. 3.3 Upper Yield Stress vs. Relative Density for Slow, Moderate and Fast Strain Rates at $T = -10^\circ\text{C}$ for Frozen MFS

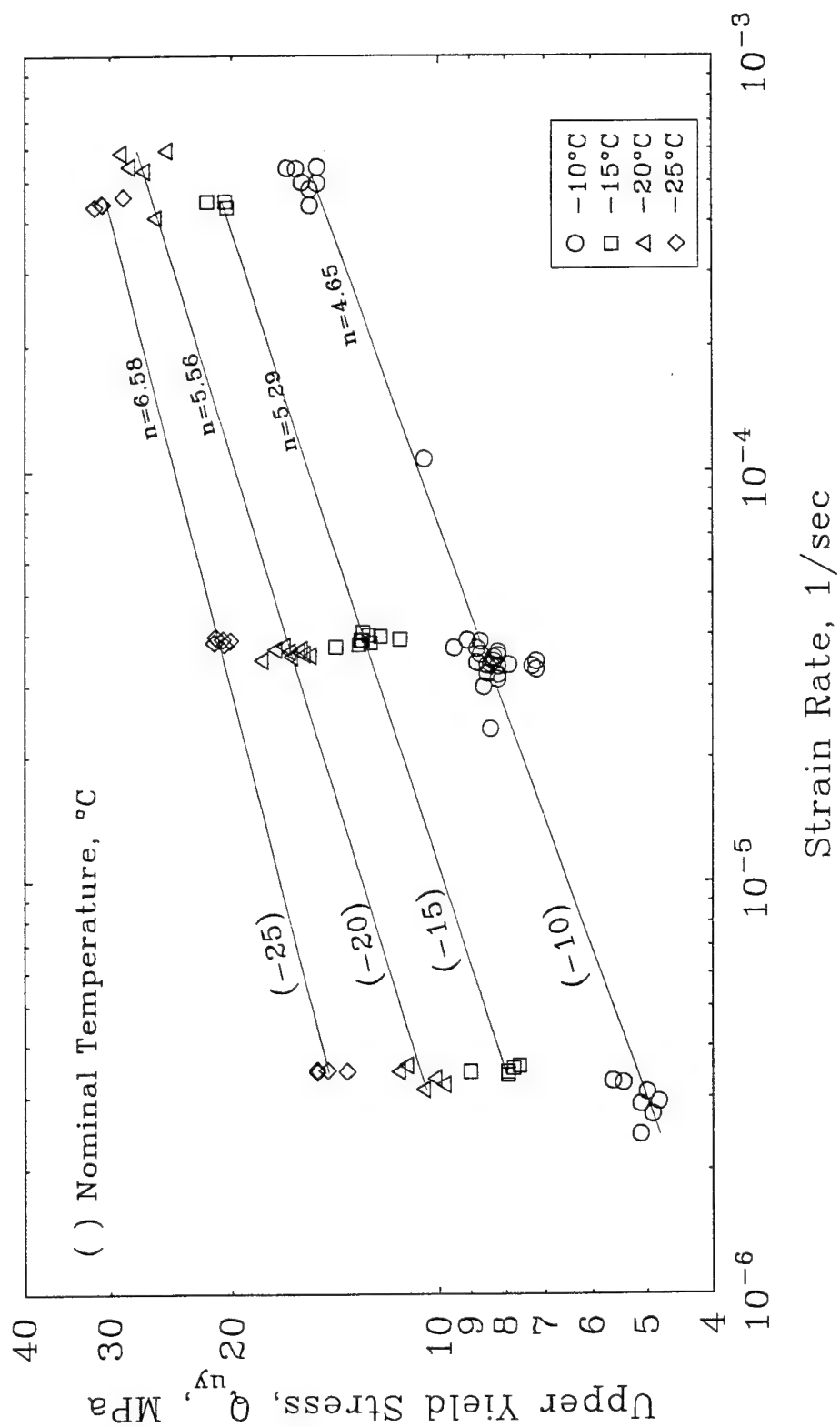


Fig. 3.4 Upper Yield Stress vs. Strain Rate at Varying Temperatures for All Relative Densities and Confining Pressures for Frozen MFS

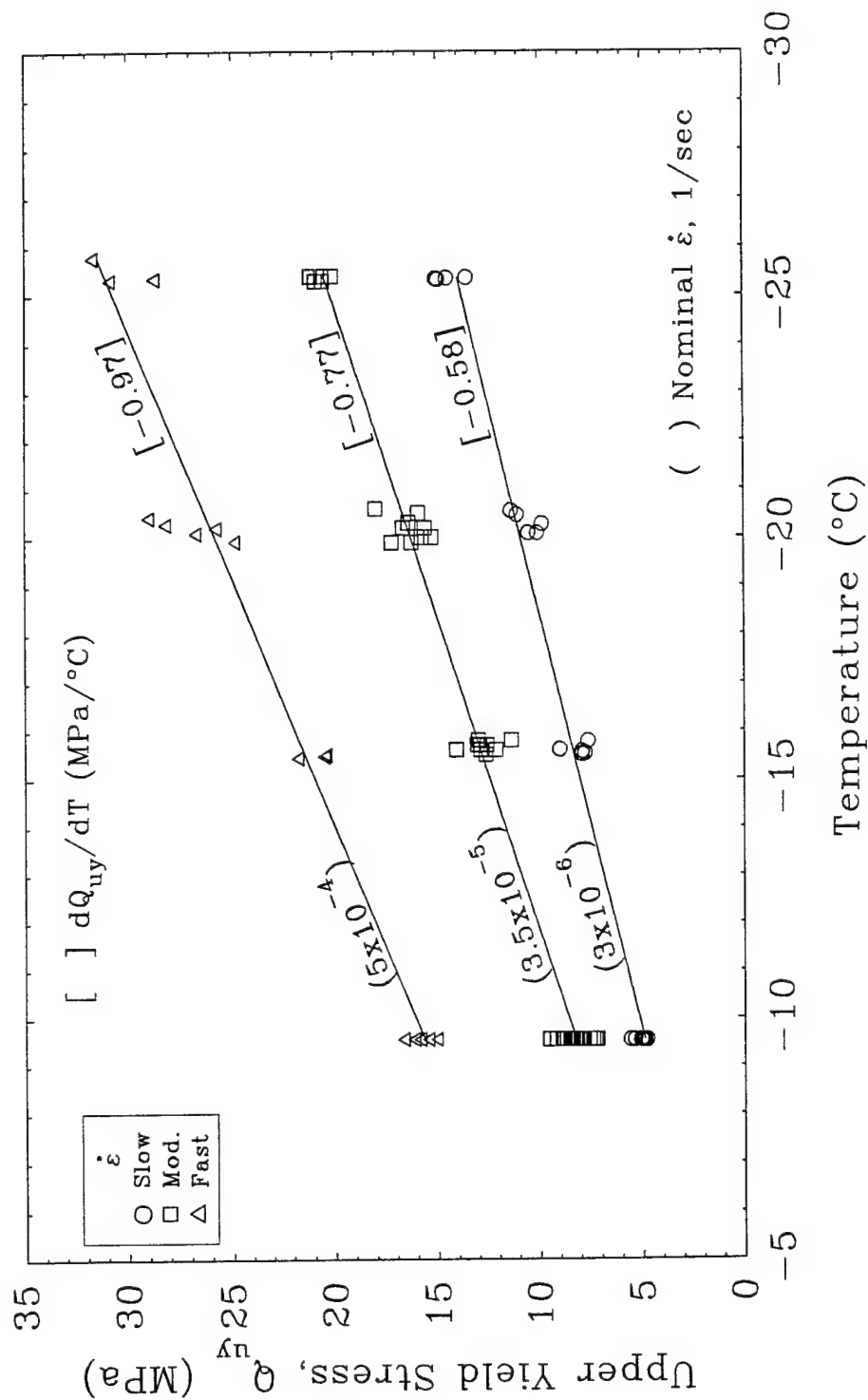


Fig. 3.5 Upper Yield Stress vs. Temperature at Varying Strain Rate for All Relative Densities and Confining Pressures for Frozen MFS

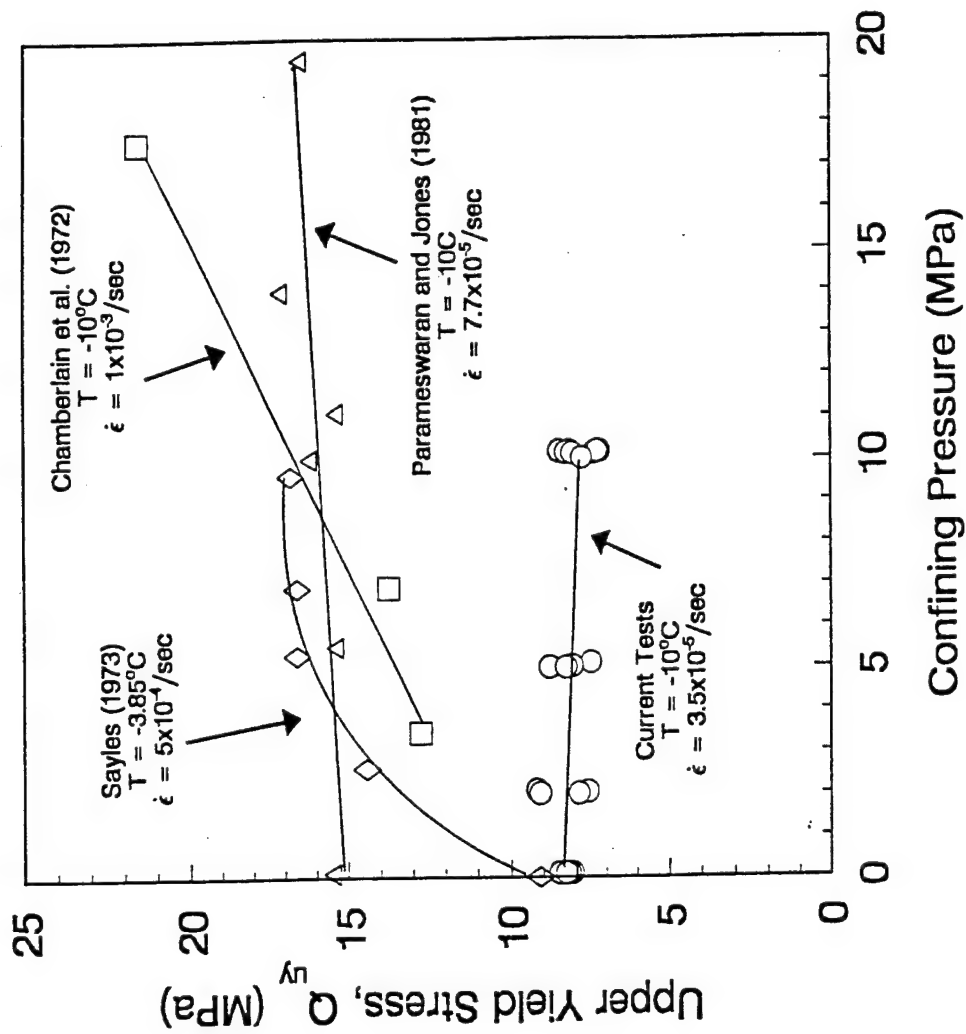


Fig. 3.6 Comparison of Effect of Confining Pressure on Upper Yield Stress with Prior Data on Frozen Ottawa Sands

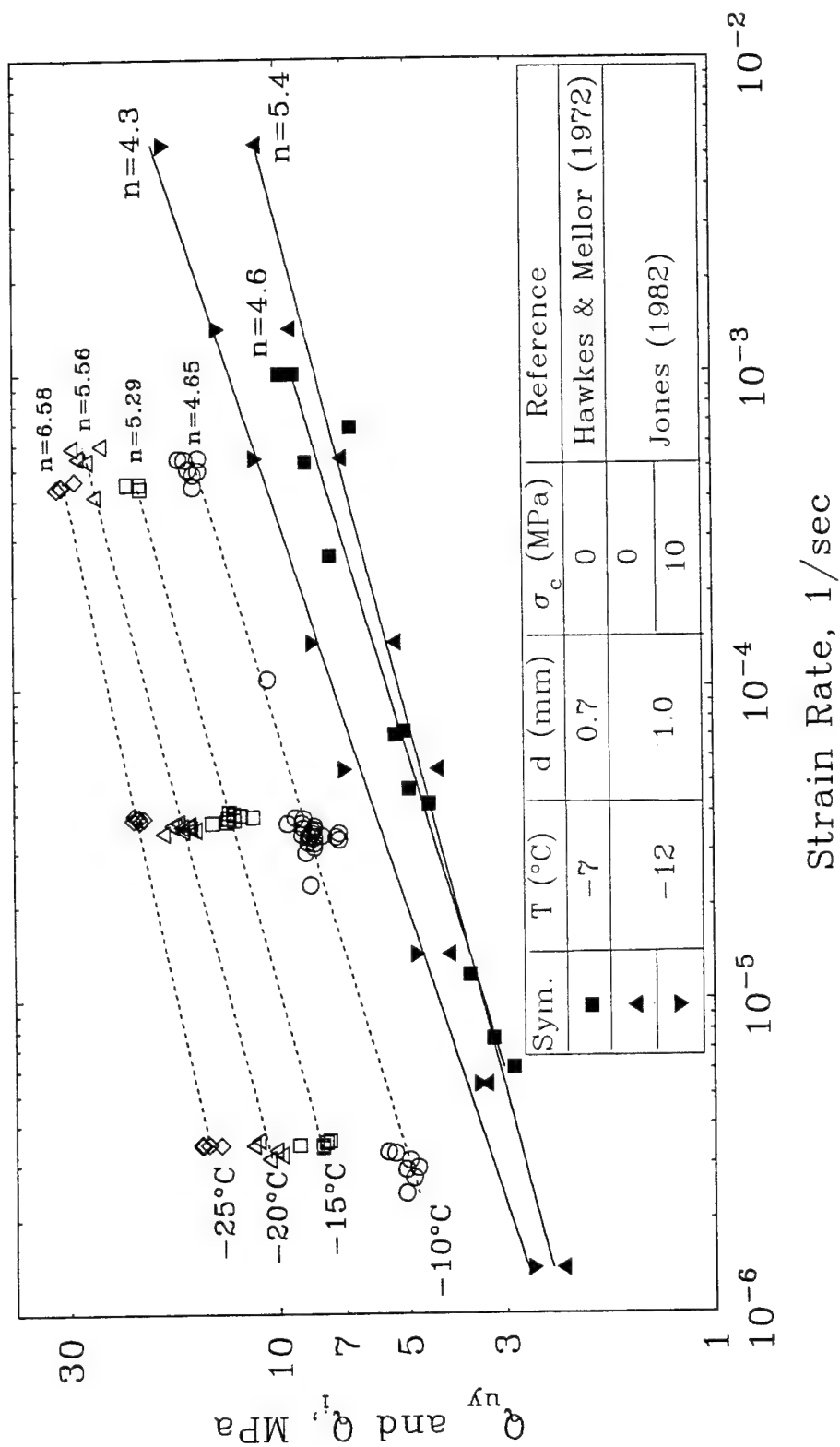


Fig. 3.7 Comparison of Upper Yield Stress of Frozen MFS and Peak Strength of Polycrystalline Ice vs. Strain Rate

4. LARGE-STRAIN BEHAVIOR OF FROZEN SAND

4.1 BACKGROUND

Table B (Sheets B1 to B4 in Appendix B) summarizes experimental programs on saturated (or nearly so) frozen sands that report large-strain behavior. For each program, the table lists the reference and the following information:

- name or type of sand and gradation characteristics, the method of specimen preparation (C = compacted, P = pluviation, V = vibration and MSP = multi-sieve pluviation) and the degree of ice saturation;
- whether or not the program used an on-specimen axial strain device and measured volumetric strains;
- the range of testing variables, i.e., sand density, confining pressure (σ_c), axial strain rate ($\dot{\epsilon}$) and temperature; and
- the principal focus of the programs.

The programs listed in Table B have the following attributes and limitations:

- about three-quarters tested Ottawa sands, the most prevalent being uniform coarse (20-30 sieve) and uniform medium (\approx 20-100 sieve);
- about one-third varied confining pressure and one-third varied strain rate and temperature (with $\sigma_c \approx 0$), while only one program (I) studied these three variables in some detail;
- only two included a detailed study of relative density;

- about half prepared their specimens via compaction (rather than pluviation), which leads to non-uniform densities and scattered results (Baker and Konrad 1985); and
- four made measurements of volumetric strains, and only one measured on-specimen axial strains.

Therefore, the program on frozen Manchester Fine Sand (MFS) is unique by measuring volumetric and on-specimen axial strains on pluviated specimens with lubricated ends; the specimens had a wide range of relative densities (D_r) and were sheared at varying confining pressures (σ_c), strain rates ($\dot{\epsilon}$), and temperatures (T), as summarized in Table 2.1. The only known limitation involves compliance of the loading system that required about 0.5 to 1% axial strain before achieving the nominal (maximum) strain rate. However, the authors believe that the prior slower strain rate should not have a significant effect on the measured large-strain behavior, since Mellor and Cole (1983) show that ice has a direct correspondence between constant strain rate and constant stress creep tests. On the other hand, there is some error in reporting axial stresses normalized by the upper yield stress (i.e., use of the stress ratio = Q/Q_{uy}), since Q_{uy} usually occurred at an instantaneous strain rate about $10 \pm 5\%$ lower than the maximum strain rate. For typical power law coefficients of $n = 10 \pm 5$, this corresponds to an error in Q/Q_{uy} ranging from 0.5 to 3%. Given the inherent scatter in the data, no correction was made for this small error.

Sheets B5 to B11 present tabulated data from the conventional triaxial compression tests run on frozen MFS.

4.2 OVERVIEW OF STRESS-STRAIN BEHAVIOR AT LARGE STRAINS

Section 3.4 concluded that the upper yield stress (Q_{uy}) of frozen MFS varies only with strain rate and temperature, and that this behavior is consistent with the general behavior of polycrystalline ice. But at large strains, changes in sand density and confining pressure have a very significant effect on both the deviator stress ($Q = \sigma_1 - \sigma_3$) and the volumetric strain (ϵ_v). Section 2.5.2 divided the large-strain behavior into four basic types of behavior. These are designated as curve types A, B, C and D, as described in Table 2.2 and Figure 2.4. Note that the stress-strain curves in Figure 2.4 are normalized by using the stress ratio, Q/Q_{uy} .

Figures 4.1 through 4.3 plot actual data in order to support the basis for the four curve types and to illustrate how changes in density and confinement affect the large-strain behavior. These changes can be summarized as follows.

- Figure 4.1 shows that increasing relative density (D_r) at low confinement ($\sigma_c = 0.1$ MPa) initially changes the post-upper yield behavior from strain softening to strain hardening, causes an increase in the peak strength (Q_p) that is followed by more pronounced post-peak strain softening, and causes an increase in the amount of volumetric expansion (dilation). The curve designation changes from Type A or B at low density to Type C at higher densities.

- Figure 4.2 shows that increasing confinement during shear of dense sand ($D_r \approx 90\%$) causes an increase in the degree of post-upper yield strain hardening, which produces higher peak strengths at larger axial strains. This behavior is accompanied by less post-peak strain softening and a large decrease in the amount of dilation. The curve designation changes from Type C to Type D.
- Figure 4.3 shows that increasing relative density at high confinement ($\sigma_c = 10$ MPa) causes more pronounced Type D behavior for shearing at the moderate strain rate and $T = -10^\circ\text{C}$; it causes a change from Type B to Type C behavior for shearing at the fast strain rate and $T = -15^\circ\text{C}$.

Section 2.5.2 described the parameters that will be used to quantify the influence of the four testing variables (D_r , σ_c , $\dot{\epsilon}$ and T) on large-strain behavior. These parameters relate to the amount of post-upper yield strengthening ($\Delta Q = Q_p - Q_{uy}$) and the peak strength (Q_p), the volumetric behavior in terms of the maximum rate of dilation and the amount of dilation at 20% axial strain, and various approaches for relating the amount of post-peak strain softening to the volumetric behavior. These aspects are treated in Sections 4.3, 4.4 and 4.5, respectively. Section 4.6 presents a conceptual hypothesis to explain the large-strain behavior in terms of strengthening mechanisms related to the frictional resistance of the sand skeleton-ice matrix and weakening mechanisms related to damage (fracture) of the ice matrix.

4.3 POST-UPPER YIELD STRENGTHENING AND PEAK STRENGTH

4.3.1 Comparison of Peak Strengths with Prior Data

Figure 4.4 compares the peak strength of frozen MFS with data on other frozen sands as a function of strain rate at temperatures varying from $T = -10^\circ$ to -30°C . All prior programs that investigated the effects of strain rate and temperature we performed on dense to medium-dense sand, and most used unconfined compression tests ($\sigma_c = 0$). Figure 4.4a compares results (from linear regression) at low confinement ($\sigma_c \leq 0.1 \text{ MPa}$) along with the corresponding values of the power law coefficient (n). The location of the MFS and its values of n are representative of frozen sand data with one exception: Bragg and Andersland (1980) show no strength increases beyond $\dot{\epsilon} \approx 10^{-5}/\text{sec}$ (also true for their tests at $T = -6$ and -15°C). Also note the two- to three-fold variation in Q_p at the same strain rate for sands tested at $T = -10^\circ\text{C}$. This variation probably reflects differences in relative density, grain size distribution, degree of ice saturation, and the method of specimen preparation (compaction versus pluviation).

Figure 4.4b compares peak strength versus strain rate for the only other program with similar testing at high confinement ($\sigma_c \approx 10 \text{ MPa}$). The $T = -10^\circ\text{C}$ Shibata *et al.* (1985) data on dense, uniform fine Toyoura sand (that may have been pluviated) lies between the MFS results at $T = -10$ and -15°C . Note: the capacity of MIT's load frame prevented shearing at the fast strain rate at lower temperatures.

Figure 3.4 showed that the upper yield stress of frozen MFS became less rate sensitive (i.e., n increasing from 4.6 to 6.6) at lower temperatures. The collective

results in Figure 4.4 show that the peak strength of dense sands also tends to become less rate sensitive at lower temperatures. However, the rate sensitivity of the strength of dense frozen sands is also much lower than that for the upper yield stress, i.e., higher n values.

4.3.2 Effects of Relative Density and Confining Pressure

Effect of Relative Density

Figure 4.5 plots peak strength (Q_p) versus relative density for tests on frozen MFS at different temperatures at the moderate strain rate and low confinement ($\sigma_c = 0.1$ MPa). All tests at $T = -10$ and -15°C had Type C curves and produce a well-defined, linear increase in Q_p with increasing D_r . However, the looser specimens at lower temperatures had either Type A curves ($Q_p = Q_{uy}$) or Type C curves with Q_p only slightly larger than Q_{uy} . These data sets produce a bilinear Q_p versus D_r relationship where definition of the slope at higher densities can be uncertain. This is illustrated by the results at $T = -20^\circ\text{C}$, where the tests at $D_r \approx 45$ to 50% had lower Q_{uy} values than the test at $D_r = 36\%$. The solid and dashed lines represent two possible interpretations of this data set.

In an attempt to minimize this problem, which basically arises from scatter in the Q_{uy} data (remember that Q_{uy} should not vary with D_r or σ_c as per Section 3.4), the influence of density and confinement on the peak strength is evaluated in terms of the strength increase relative to the upper yield stress. In

other words, the results are also analyzed using $\Delta Q = Q_p - Q_{uy}$, where Q_{uy} is the value measured for each individual test.

Figure 4.6 plots ΔQ versus D_r for tests with low and high confinement at all strain rates and temperatures. Note that results from tests with Type A curves are plotted below the X axis, with the label zero, since they should not be used to define the slope of ΔQ versus D_r relationships. The most extensive data sets (moderate $\dot{\epsilon}$ at $T = -10^\circ\text{C}$ with $\sigma_c = 0.1$ and 10 MPa) show a linear relationship, i.e., a constant value of $d\Delta Q/dD_r$. Hence, linear regression was used to fit data sets having three or more points, leading to the lines shown in Figure 4.6 and having slopes given in parentheses. In general, faster strain rates and lower temperatures cause a downward shift in the ΔQ versus D_r relationships.

Figure 4.7 represents an attempt to quantify the influence of relative density on peak strengths as a function of confining pressure, strain rate and temperature. This analysis applied linear regression to both ΔQ (giving $d\Delta Q/dD_r$) and Q_p data (giving dQ_p/dD_r , but only for tests with curve Types C and D). For simplicity, both ratios will be referred to as dQ/dD_r , even though dQ_p/dD_r usually had slightly higher values than $d\Delta Q/dD_r$ for unexplained reasons. The results in Figure 4.7 show two consistent trends:

- The moderate $\dot{\epsilon}$, -10°C data in Figure 4.7a, produce a linear increase in dQ/dD_r with increasing confinement, with a slope of 0.67 based on the collective ΔQ and Q_p analyses.
- At $\sigma_c = 10 \text{ MPa}$, the slow and moderate strain rate data produce similar values of $dQ/dD_r \approx 11.9 \pm 0.6 \text{ MPa}$ independent of temperature.

In contrast, the values of dQ/dD_r at $\sigma_c = 0.1$ are much more scattered than at high confinement as a function of $\dot{\epsilon}$ and T . The collective results give $dQ/dD_r = 5.6 \pm 1.0 \text{ MPa}$. For slow shearing, the mean data at $\sigma_c = 0.1$ and 10 MPa produce a slope of 0.67, which is the same slope as that for the moderate rate data at $T = -10^{\circ}\text{C}$.

In summary, for test conditions leading to curve Types C and D, dQ/dD_r increases from $5.6 \pm 1.0 \text{ MPa}$ at low confinement to $11.9 \pm 0.6 \text{ MPa}$ at high confinement for shearing at the slow and moderate strain rates (fast shearing produced mostly Type A curves that preclude analysis).

Baker and Konrad (1985) provide the only prior data with detailed measurements of peak strength versus relative density. Their data on pluviated 16-100 Ottawa sand tested in unconfined compression at $\dot{\epsilon} = 1.7 \times 10^{-4}/\text{sec}$ and $T = -10^{\circ}\text{C}$ give $dQ_p/dD_r \approx 12.5 \text{ MPa}$ at $D_r > 65\%$. This value is double that for frozen MFS at low confinement, even though both sands have similar frozen strengths at $D_r = 90\%$ (18 versus 13 MPa for MFS). This suggests the need for further research on the influence of density on the peak strength of frozen sands.

Effect of Confining Pressure

Figure 4.8 plots Q_p and $\Delta Q = Q_p - Q_{uy}$ data versus confining pressure for shearing at the moderate strain rate and $T = -10^\circ\text{C}$. Linear regression was used to obtain values of Q_p and ΔQ at $D_r = 30, 60$ and 90% . As for the analysis of relative density, $dQ/d\sigma_c$ refers to ratios in terms of both Q_p and ΔQ . Figure 4.8 also shows values of the Mohr-Coulomb friction angle (ϕ), that were calculated using the relationship

$$\sin \phi = (dQ/d\sigma_c)/(dQ/d\sigma_c + 2) \quad \dots[4.1]$$

The results in Figure 4.8 show the following trends:

- For dense sand ($D_r = 90\%$), the Q_p data produce a linear increase in strength with confinement ($\phi = 14^\circ$), whereas the ΔQ data produce a slight curvature (ϕ decreases from 18° to 12°).
- A decrease in relative density causes the Q_p and ΔQ versus σ_c relationships to become both more curved and flatter. That is, the pressure sensitivity decreases at lower density and higher confinement, with ϕ decreasing to about 5° or less.

The results in Figure 4.8 represent the only data set having tests sheared at $\sigma_c = 0.1, 2, 5$ and 10 MPa. Consequently, analyses to determine how the pressure sensitivity varies with strain rate and temperature had to rely on values of $dQ/d\sigma_c$ based only on strengths determined at $\sigma_c = 0.1$ and 10 MPa, which can be

somewhat misleading at the lower densities due to the curvature in Q_p and ΔQ versus D_r . Values of Q_p and ΔQ for $D_r = 30, 60$ and 90% were obtained from linear regression and then used to compute $dQ/d\sigma_c$ (but excluded tests having Type A curves). Figure 4.9 presents the results of these analyses, which are based on mean values of $dQ_p/d\sigma_c$ and $d\Delta Q/d\sigma_c$, and shows the following trends:

- $dQ/d\sigma_c$ increases with increasing density, as expected from Figure 4.8;
- at the slow $\dot{\epsilon}$, decreasing temperature causes little or no decrease in pressure sensitivity; and
- at the moderate $\dot{\epsilon}$, decreasing temperature causes a larger decrease in pressure sensitivity, especially for dense sand.

In summary, the pressure sensitivity (i.e., the value of $dQ/d\sigma_c$) of frozen MFS is affected mainly by relative density. Dense sand ($D_r = 90\%$) exhibits a more or less linear increase in Q_p and $\Delta Q = Q_p - Q_{uy}$ with increasing σ_c , leading to friction angles on the order of $\phi = 10^\circ$ to 15° that tend to decrease at faster strain rates and lower temperatures. Lower densities lead to greater curvature in the strength versus confining pressure relationship, with mean friction angles on the order of $\phi = 5^\circ$ or less. At low densities, increases in strain rate and decreases in temperature produce Type A curves ($Q_p = Q_{uy}$) that have zero pressure sensitivity ($dQ/d\sigma_c = 0$).

Several of the programs listed in Table B studied the effect of confining pressure on peak strength, but only for medium-dense to dense sands. Figure 4.10

summarizes data for tests conducted at $T = -10$ or -12°C and having σ_c less than 20 MPa. Four of the five data sets have $dQ_p/d\sigma_c$ ratios ranging from 0.56 to 0.9 (or $\phi = 13^\circ$ to 18°), which are in general agreement with results for dense MFS (Fig. 4.9). In contrast, the tests by Alkire and Andersland (1973) run on 20-30 Ottawa sand produced a much higher pressure sensitivity ($\phi \approx 28^\circ$). Since the reported ice saturation was close to 100%, this behavior appears to be anomalous. Shibata *et al.* also ran tests at $T = -30^\circ\text{C}$ on dense Toyoura sand at three strain rates similar to those used for the current program. These data did not show a consistent change in pressure sensitivity with temperature or with strain rate, whereas Figure 4.9 for dense MFS indicates a decrease in pressure sensitivity at faster strain rates and lower temperatures. Consequently, the pressure sensitivity of frozen sands does not appear to follow the same trends.

Conditions Producing $Q_p = Q_{uy}$

As previously discussed, Figure 4.6 shows a general tendency for a downward shift in $\Delta Q = Q_p - Q_{uy}$ versus relative density with increasing strain rate and decreasing temperature. This trend can be quantified by determining the values of D_r that produce Type A curves for which $Q_p = Q_{uy}$ (and for Type B curves with $Q_p \approx Q_{uy}$). Figure 4.11 does this for low-confinement tests based on mean results of analyses using both ΔQ and Q_p data (i.e., as done for Fig. 4.7). Figure 4.11 suggests a linear increase in the D_r producing $Q_p = Q_{uy}$ with decreasing temperature and that this temperature dependency becomes more pronounced at higher strain rates.

Strain at Peak Strength

Sheets B14 and B15 from Swan (1994) show the following trends in the axial strain at the peak strength (ϵ_p) for Type C and D curves:

- at low confinement ($\sigma_c = 0.1$ MPa), ϵ_p typically equals about $5.5 \pm 2\%$, more or less independent of D_r , $\dot{\epsilon}$ and T (all Type C curves);
- increases in confinement cause a large increase in ϵ_p (e.g., see Sheet B15); and
- at high confinement ($\sigma_c = 10$ MPa), ϵ_p typically ranges between 15 and 25% and tends to decrease with higher densities, higher strain rates and lower temperatures.

4.3.3 Effects of Strain Rate and Temperature

Figure 4.12 plots peak strength and upper yield stress versus strain rate for frozen MFS at two extreme conditions:

- (a) low density and low confinement (hence, minimal effect of frictional resistance of the sand skeleton); and
- (b) high density and high confinement (hence, maximum frictional resistance).

The results in Figure 4.12a show relatively little difference between Q_p and Q_{uy} (except for slow shearing at -10°C), whereas the results in Fig. 4.12b show values of Q_p much larger than Q_{uy} . This comparison illustrates the extreme importance of comparing these two stresses, since Section 3.4 concluded that Q_{uy} is controlled by

the behavior of the ice matrix and therefore, involves very little sand skeleton frictional resistance. It also demonstrates that inspection of Q_p data alone can lead to erroneous conclusions regarding the physical mechanisms controlling frozen sand behavior at large strains.

Figure 4.13 plots $\Delta Q = Q_p - Q_{uy}$ for loose ($D_r = 30\%$) and dense ($D_r = 90\%$) specimens (interpolated from Fig. 4.6) versus strain rate at varying temperatures at low and high confinement. Inspection of the results indicates the following trends (using the slow strain rate of -10°C as the reference):

- For loose sand at low confinement, the minimal strength gain rapidly vanishes at higher strain rates.
- for loose sand at high confinement and for dense sand at low confinement, the moderate strength gain disappears more rapidly with faster shearing at the lower temperatures.
- For dense sand at high confinement, the large strength gain is temperature independent at the slow rate; lower temperatures then cause a progressively smaller strength gain at the higher strain rates.

4.3.4 Summary and Conclusions

Section 4.3 presents a detailed analysis of the amount of strengthening that occurs after reaching the upper yield stress (Q_{uy}). Q_{uy} is taken as the reference stress, since its value does not vary with sand density and confining pressure and is thought to be dominated by the same physical mechanisms that control the behavior of polycrystalline ice. The analysis focuses on combinations of D_r , σ_c , $\dot{\epsilon}$

and T that produce curve Types C and D (see Fig. 2.4 and Table 2.2) for which

$\Delta Q = Q_p - Q_{uy}$ is positive.

1) Relative Density (Figs. 4.5, 4.6 and 4.11)

There is a linear increase in ΔQ with increasing D_r . The rate of increase (dQ/dD_r) is roughly independent of $\dot{\epsilon}$ and T and is highly dependent on confinement; e.g., $dQ/dD_r = 5.6 \pm 1.0$ MPa and 11.9 ± 0.6 MPa at $\sigma_c = 0.1$ and 10 MPa, respectively. Analyses are made to obtain values of D_r producing $Q_p = Q_{uy}$ (i.e., $\Delta Q = 0$ for Type A curves) for tests run at low confinement as a function of $\dot{\epsilon}$ and T . These values of D_r range from about zero to 60% for slow and moderate strain rates.

2) Confining Pressure (Figs. 4.8 and 4.9)

The pressure sensitivity ($dQ/d\sigma_c$) is much higher for dense than for loose sand and tends to decrease at very high confining pressures. Mean values of $dQ/d\sigma_c$ (from data at $\sigma_c = 0.1$ and 10 MPa) for slow and moderate shearing range from about 0.2 to 0.7 (corresponding to friction angles of 5 to 15°) and vary in a complex fashion with D_r , $\dot{\epsilon}$ and T .

3) Strain Rate and Temperature (Figs. 4.12 and 4.13)

Figure 4.13 shows the post-upper yield strength gain, $\Delta Q = Q_p - Q_{uy}$, for loose and dense sand at low and high confinement as a function of strain rate and temperature. The magnitude of ΔQ varies in a complex fashion as a function of D_r , σ_c , $\dot{\epsilon}$ and T . However, one can say that D_r and σ_c dominate at lower strain rates

and higher temperatures, whereas fast shearing and low temperatures produce little strengthening except for dense sand at high confinement.

Sheet B13 evaluates the strength gain normalized by the upper yield stress, $(Q_p - Q_{uy})/Q_{uy}$, and plots this ratio versus temperature for loose ($D_r = 35\%$) and dense ($D_r = 95\%$) sand, as a function of strain rate and confining pressure. One observes that $(Q_p - Q_{uy})/Q_{uy}$ undergoes

- a significant increase with increasing density (note the different scales for loose and dense sand), as expected;
- a significant increase with increasing confining pressure, as expected; and
- a significant increase with decreasing strain rate and increasing temperature. In other words, the relative degree of strengthening is much larger at low values of Q_{uy} than at high values of Q_{uy} .

4) Relative Importance of Testing Variables

Sheet B12 illustrates the relative importance of the testing variables, taking medium-dense sand sheared at low confinement, the moderate strain rate and $T = -15^\circ\text{C}$ as the reference condition (Type C curve). Both an order of magnitude change in strain rate and a 5°C change in temperature have a large effect on the peak strength, due mainly to changes in the upper yield stress (Q_{uy}). Changes in relative density by $\Delta D_r = \pm 30\%$ have a small effect (unless σ_c increases to extremely high values).

4.4 VOLUMETRIC BEHAVIOR

4.4.1 Background

The current program is one of the few to measure volumetric strains (ϵ_v) and only Shibata *et al.* (1985) report ϵ_v data at varying confining pressures, strain rates and temperatures (see Table B). Both programs show essentially zero volumetric strain at low axial strains (up to Q_{uy}) and then varying amounts of volumetric expansion (dilation) that continues to increase with further straining, e.g., see Figures 4.1 through 4.3.

An ice-saturated system having a Poisson's ratio less than 0.5 and sheared by increasing the axial stress at constant cell pressure can undergo only volumetric compression. Consequently, volumetric expansion (dilation) must reflect fracturing (cracking) of the ice matrix and loss of bonding between the ice matrix and the sand particles. In other words, the onset of dilation suggests a decrease in the cohesive strength of the frozen sand system caused by damage of the ice matrix.

The presentation uses two parameters to quantify the dilation behavior at large strains:

- the maximum rate of dilation (MRD) = the maximum slope of the ϵ_v versus ϵ_a curve = $(d\epsilon_v/d\epsilon_a)_{\max}$, and
- the volumetric expansion at 20% axial strain = ϵ_{v20} .

4.4.2 Maximum Rate of Dilation

The maximum rate of dilation (MRD) is affected mainly by the amount of confinement, as illustrated in Figure 4.14a for loose and dense specimens sheared at the moderate strain rate and $T = -10^{\circ}\text{C}$. For this most extensive data set, MRD equals 0.5 ± 0.2 at $\sigma_c = 0.1$ MPa and drops to less than 0.1 at $\sigma_c = 10$ MPa.

Figures 4.14b and 4.14c show the influence of relative density at $\sigma_c = 0.1$ and 10 MPa, respectively, for all strain rates and temperatures. At low confinement, the MRD increases with sand density more or less independent of strain rate and temperature. At high confinement, lower temperatures tend to increase MRD, and sand density plays a very minor role.

4.4.3 Volumetric Expansion at 20% Axial Strains

The ϵ_{v20} parameter follows the same basic trends as MRD, as illustrated in Figure 4.15. At low confinement, ϵ_{v20} increases with D_r from about 3 to 8% and tends to increase at higher strain rates and lower temperatures. At high confinement, $\epsilon_{v20} = 1.05\% \pm 0.85\text{SD}$ independent of D_r , but with a tendency to increase at the fast strain rates.

It is interesting to note that loose specimens at low confinement experience about twice as much dilation at 20% axial strain as unfrozen MFS (Swan 1994). These specimens often expanded to relative densities that approach zero percent. Hence, fracturing of the ice matrix increases the dilation of frozen sand.

4.5 POST-PEAK STRAIN SOFTENING

4.5.1 Objective

The combination of lubricated end platens, which enhances the ability to obtain reliable stress-strain data to very large strains, and measurement of volumetric strains offered a unique opportunity to evaluate the post-peak strain softening behavior of a frozen sand. The analyses looked at a variety of parameters in an attempt to quantify the degree of strength loss as a function of the four testing variables (D_r , σ_c , $\dot{\epsilon}$ and T), with particular emphasis on the role of volumetric expansion (dilation). The stress parameters used in the analyses included various forms of the rate of strain softening, $dQ/d\epsilon_a$, and stress ratios such as Q_{20}/Q_p and Q_{20}/Q_{uy} , where Q_{20} equals $(\sigma_1 - \sigma_3)$ at 20% axial strain. Parameters selected to represent the volumetric behavior included the maximum rate of dilation, $MRD = (d\epsilon_v/d\epsilon_a)_{max}$, and the volumetric strain at 20% axial strain, ϵ_{v20} .

The evaluation focuses on tests conducted at $\sigma_c = 0.1$ MPa, since low confinement produces post-peak strain softening of two types: curve Type A with $Q_p = Q_{uy}$ occurring at small strains ($\epsilon_p = \epsilon_{uy} < 1\%$); and curve Type C with $Q_p > Q_{uy}$ occurring at moderate strains ($\epsilon_p \approx 5.5 \pm 2\%$).

4.5.2 Results of Analyses

Behavior at Low Confinement

Figure 4.16 plots the normalized rate of strain softening,

$NRSS = [(Q_p - Q_{20})/Q_{uy}]/(\epsilon_{20} - \epsilon_p)$, versus relative density from 24 low-confinement

tests having Type C curves. The data produce a well-defined trend, in spite of large changes in both the strain rate and the temperature. The increase in NRSS with relative density comes from the fact that Q_p/Q_{uy} increases with D_r and Q_{20}/Q_{uy} is essentially constant (e.g., see normalized stress-strain curves in Figure 4.1 and subsequent discussion). However, the apparent independence of NRSS on strain rate and temperature at the same D_r was rather surprising. This independence results from two basic trends that cancel each other, as demonstrated below:

- The normalized peak strength ratio, Q_p/Q_{uy} , decreases with increasing strain rate and decreasing temperature, as illustrated in Figure 4.17.
- However, the normalized strength at 20% axial strain, Q_{20}/Q_{uy} , also decreases with increasing strain rate and decreasing temperature, as illustrated in Figure 4.18.

Note that Figure 4.18 also includes data from Type A curves and that both curve types end up with the same normalized stress at 20% axial strain independent of sand density.

Rate of Strain Softening

Figure 4.19 plots the rate of strain softening, $RSS = -dQ/d\epsilon_a$, versus the maximum rate of dilation, $MRD = (d\epsilon_v/d\epsilon_a)_{max}$. The RSS is measured at the axial strain corresponding to the MRD, which typically occurred at $\epsilon_a \approx 15 \pm 5\%$. The figure includes data for all curve types and for all testing conditions. The results show the following trends:

- Most of the specimens having Type D curves are still strain hardening at MRD; hence, they have negative values of RSS. All these data come from tests with high confinement ($\sigma_c = 10$ MPa and a few at 2 and 5 MPa).
- The Type B curves are mostly for loose specimens with high confinement and tested at the higher strain rates and lower temperatures. As for the Type D curves, the RSS is typically less than 10 MPa.
- The Type A and C curves produce significant scatter in the data, but with a clear trend of an increasing rate of strain softening with increasing maximum rate of dilation and no consistent difference between the two curve types. Linear regression on these data suggests somewhat higher values of RSS at the lower temperatures. Note: normalization of RSS to Q_{uy} does not reduce the scatter by a significant amount.

As previously emphasized in Section 4.4.1, the volumetric expansion (dilation) of frozen sand must reflect fracturing of the ice matrix such that the specimen behaves more like a **drained** shear test on a particulate material. However, for drained triaxial compression tests on moderate to dense specimens of **unfrozen** MFS, the peak strength occurs when the sand is experiencing its maximum rate of dilation (Swan 1994). Thus, frozen sand behaves opposite to unfrozen sand, since the maximum rate of dilation for the fractured sand-ice system corresponds to a post-peak decrease in resistance.

Strength Loss

Figure 4.20 plots the stress ratio Q_{20}/Q_p versus the volumetric strain at 20% axial strain, ϵ_{v20} . The trends are similar to those discussed for Figure 4.19. That is, Type A and C curves show larger strength losses (a lower stress ratio) with higher amounts of dilation, again with significant scatter in the data.

Normalized Rate of Strain Softening

Figure 4.16 shows a very consistent relationship between the normalized rate of strain softening, $NRSS = [(Q_p - Q_{20})/Q_{uy}]/(\epsilon_{20} - \epsilon_p)$, and relative density for all tests at $\sigma_c = 0.1$ MPa having Type C curves. Although not plotted, tests having Type A curves did not fit this trend. For example, seven Type A curves from tests having $D_r \approx 35$ to 40% produced NRSS values ranging from 0.9 to 2.65. However, correlating NRSS with the amount of dilation at 20% axial strain (ϵ_{v20}) gives a very consistent relationship for both curve types. This is demonstrated in Figure 4.21, which probably represents the most significant finding from the analysis of strain softening behavior.

4.5.3 Summary and Conclusions

The use of lubricated end platens and measurement of volumetric strains have made possible a unique evaluation of the post-peak strain softening behavior of frozen MFS. For tests at low confinement that produce curve Types A and C (i.e., post-peak strain softening), there appears to be a unique relationship between the rate of strain softening (after normalization to the upper yield stress) and the amount of volumetric expansion (dilation). Figure 4.21 presents this

relationship in terms of the normalized rate of strain softening,

$NRSS = [(Q_p - Q_{20})/Q_{uy}] / (\epsilon_{20} - \epsilon_p)$, versus the amount of dilation at 20% axial strain,

ϵ_{v20} . The collective data, which cover a wide range of relative densities ($D_r = 35$ to 95%), have relatively little scatter about the mean trend and do not show a consistent deviation as a function of strain rate or temperature. However, the individual stress components of the NRSS do vary significantly with the testing variables, as summarized below (for curve Types A and C):

- Q_p/Q_{uy} increases linearly with relative density; these lines move downward and become flatter with increasing strain rate and decreasing temperature. (See Fig. 4.17 for Type C curves.)
- Q_{20}/Q_{uy} is independent of relative density, but also has a smaller magnitude with increasing strain rate and decreasing temperature. (See Fig. 4.18 for both Type A and C curves.)

Analysis of test results at all confining pressures (i.e., up to $\sigma_c = 10$ MPa) produced the results presented in Figures 4.19 and 4.21. For all curve types (i.e., including Type B and D with little or no post-peak strain softening, the rate of strain softening increases with the maximum rate of dilation, and the stress ratio Q_{20}/Q_p decreases with the amount of dilation. Although both plots have significant scatter, they provide additional evidence that the degree of post-peak strain softening or strength loss is strongly related to the rate or amount of dilation.

4.6 CONCEPTUAL MODEL OF THE PHYSICAL MECHANISMS GOVERNING THE LARGE-STRAIN BEHAVIOR OF FROZEN SAND

4.6.1 Introduction

Section 3.4 showed that the upper yield stress (Q_{uy}) of frozen MFS is independent of relative density (D_r) and confining pressure (σ_c) and varies with strain rate ($\dot{\epsilon}$) and temperature (T) in a fashion similar to that of polycrystalline ice. The volumetric strain (ϵ_v) at Q_{uy} is also essentially equal to zero. Section 4.6.2 gives a brief overview of ice behavior and suggests possible mechanisms to help explain why Q_{uy} is greater than the peak strength of ice.

In contrast, the post-upper yield behavior of frozen sand is highly dependent on sand density and confinement, in addition to strain rate and temperature. The four curve Types, A through D, are used to illustrate this dependency on D_r , σ_c , $\dot{\epsilon}$ and T (Table 2.2 and Fig. 2.4). Section 4.6.3 presents a conceptual model to explain the strain hardening/strain softening and volumetric behavior associated with these four curve types in terms of

- weakening mechanisms associated with damage to the ice matrix due to cracking that is reflected by dilation (expansion) of the frozen sand; and
- strengthening mechanisms associated with the frictional resistance of the frozen sand system.

Section 4.6.4 then examines the large-strain behavior of frozen MFS in terms of these weakening and strengthening mechanisms.

4.6.2 Ice Behavior and Upper Yield Strength of Frozen Sand

Figure 4.22 illustrates typical stress-strain curves for polycrystalline ice for the range of testing conditions used for frozen MFS. (The Mellor and Cole 1982 data at $T = -5^{\circ}\text{C}$ should be representative of ice at $T = -10^{\circ}\text{C}$ at the slow and fast strain rates.) According to Mellor and Cole (1982) and Murrell *et al.* (1989), the onset of internal cracking (crack nucleation) begins at the first yield point (at axial strains on the order of 0.05 to 0.5%). The continued formation and growth of cracks result in the peak strength occurring at about 0.5 to 1%, followed by strain softening with $dQ/d\epsilon_a$ becoming less negative with increasing strain. The amount of post-peak strain softening increases at higher strain rates and lower temperatures and is reduced by added confinement. However, in all cases of interest, there is a very significant post-peak loss in the strength of polycrystalline ice having a grain size of about 1 mm.

Figure 3.7 shows that the upper yield stress (Q_{uy}) of frozen MFS is approximately double the peak strength of ice in unconfined compression at $T = -10^{\circ}\text{C}$. If Q_{uy} is primarily controlled by the cohesive strength of the ice matrix, as hypothesized in Section 3.4, then the presence of the sand must cause significant strengthening. The authors agree with Ting *et al.* (1983), who attribute this enhanced strength of the intact ice matrix to

- a difference in ice structure. Although the grain size of ice in frozen sand is probably at least an order of magnitude smaller than typically tested, no data exist to prove that a smaller grain size will necessarily produce a higher strength of intact granular ice.

- an increase in the strain rate due to the presence of the sand grains.
- changes in the state of stress and the added deformational restraints due to the presence of the sand grains.

Since the peak strength of normal granular ice increases with confinement at the higher strain rates and lower temperatures (due to more prevalent cracking activity), one might expect the upper yield stress of frozen sand to increase with confining pressure. However, this was not observed for frozen MFS, although it did occur for the fast strain rate tests of Chamberlain *et al.* (1972) as per Figure 3.6.

Perhaps the Q_{uy} of frozen MFS at high strain rates and low temperatures occurs when the ice matrix is closer to its first yield stress, which may be less pressure sensitive than the peak strength. In any case, the authors have assumed that the ice matrix in frozen sand follows the same general trends as illustrated in Figure 4.22.

4.6.3 Post-Upper Yield Weakening and Strengthening Mechanisms

After frozen sand reaches its yield stress, it is hypothesized that the cohesive strength of the ice matrix decreases because of the continued formation and growth of cracks. This cracking activity will decrease the compressive and tensile strength of the ice and will also decrease the bonding between the ice matrix and the sand particles, thus permitting volumetric expansion (dilation) of the ice-sand composite material. Hence, continued cracking of the ice matrix represents a **weakening mechanism** that, by itself, will cause post-upper yield strain softening of the frozen sand composite such as observed in Type A curves. It is further hypothesized that increasing rates of dilation reflect greater cracking activity and more pronounced weakening.

On the other hand, continued straining of frozen sand beyond Q_{uy} also can produce a **strengthening mechanism** due to the frictional resistance of the ice-sand composite that progressively behaves more like a **particulate** system due to increasing damage of the ice matrix and increasing interaction between the particles of the sand skeleton. Although the ice matrix prevents the sand skeleton from exhibiting the same behavior as observed for unfrozen sand, it still may be valid to use this behavior for general guidance. Based on data summarized in Section 5, (e.g., Figs. 5.2 to 5.6), one observes the following behavioral trends:

- 1) For shear at constant volume (perhaps applicable at low to moderate strains for frozen sand, i.e., before significant dilation):
 - loose sand at low consolidation stresses ($\sigma_c \approx 0.1$ MPa) requires very large strains to reach a very low peak strength (say $Q_p \approx 1$ MPa at $\epsilon_p \approx 25\%$);
 - dense sand at low consolidation stresses requires very large strains to reach a moderate peak strength (say $Q_p \approx 5$ MPa at $\epsilon_a \approx 25\%$); and
 - dense sand at high consolidation stresses ($\sigma'_c = 10$ MPa) requires relatively small strains to reach a moderate peak strength (say $Q_p \approx 5$ MPa at $\epsilon_a \approx 1$ to 2%), followed by continued straining at constant Q .

It needs to be emphasized that initial application of confining pressure to frozen sand does not cause a corresponding increase in the consolidation stress (effective stress) acting on the soil skeleton, since all or most of σ_c is probably carried by the incompressible ice matrix. It also should be noted that Ladanyi's (1985) dilatancy-hardening theory discussed in Section 5 assumes constant volume shear of the sand

skeleton and intact properties for the ice matrix. For example, the tensile strength of ice is assumed to provide significant added confinement and, hence, strength during constant volume shear of dense sand sheared at low confinement.

2) For shear at constant effective confining stress, i.e., so-called drained shear (perhaps applicable at moderate to large strain for frozen sand, i.e., during significant dilation):

- both loose and dense sand at low confinement ($\sigma'_c = 0.1$ MPa) have a negligible peak strength ($Q_p < 0.2$ MPa), which occurs at moderate strains (say $\epsilon_a \approx 5\%$); and
- with increasing confinement, there is a proportional increase in strength and strain at failure (say $Q_p \approx 10-20$ MPa at $\epsilon_a = 10-20\%$ for $\sigma'_c = 5-10$ MPa).

In other words, drained shear at high confinement ($\sigma'_c = 10$ MPa) produces very significant strengths, compared to ice and frozen sand. However, these high strengths also require significant volumetric **compression** during shear.

In addition to the strengthening mechanism caused by the frictional resistance of the sand skeleton (as described above), one can envision strengthening due to interference between the sand particles and the damaged ice matrix, and perhaps some frictional resistance of the fractured ice matrix. In any case, these strengthening mechanisms are attributed to various forms of frictional resistance. It is further hypothesized that these strengthening mechanisms for frozen sand will

- increase with increasing relative density, with this effect being more important for undrained than for drained shear; and
- increase with increasing confining pressure, with this effect being much more important for drained than for undrained shear.

Furthermore, based on the observed volumetric behavior of frozen MFS, one might expect the ice-sand system to behave in an undrained (constant volume) manner at low to moderate strains. For this condition, the effective stresses causing frictional resistance are generated **within** the ice-sand system. At larger strains, as dilatancy becomes more pronounced, the ice-sand system would be expected to approach a drained shear condition wherein the effective stresses causing frictional resistance are generated by the **applied** confining pressure.

4.6.4 Post-Upper Yield Behavior of Frozen MFS

Behavior at Low Confinement ($\sigma_c = 0.1$ MPa)

Type C curves represent the most prevalent type of behavior. After reaching the upper yield stress, the frozen sand exhibits strain hardening, since the strengthening mechanisms are stronger than the weakening mechanisms. The degree of strengthening and the resultant peak strength (Q_p) increase with increasing relative density (D_r), as illustrated in Figures 4.1, 4.6 and 4.17, probably similar to undrained shear. With continued straining, dilatancy reduces the internal frictional resistance, and the weakening mechanisms now predominate to cause strain softening. Moreover, the **normalized** rate of strain softening is uniquely related to the amount of dilation, as per Figure 4.21.

Faster strain strains and lower temperatures produce Type A curves, e.g., test number 36 in Figure 2.2a and test number 97 in Figure 4.1b, especially at the lower sand densities. The weakening mechanisms dominate, due to both a more rapid rate of ice cracking and the relatively low post-yield frictional resistance. It is important to note that the normalized rate of strain softening versus volumetric expansion relationship for Type A curves is the same as for Type B curves (Fig. 4.21). However, Type A curves exhibit a more rapid initial strength loss immediately after yielding at $Q_p = Q_{uy}$ than occurs after the peak strength for Type C curves. But both curve types show an almost linear decrease in strength and increase in dilation at the larger strain levels (e.g., Fig. 4.1).

Behavior at High Confinement ($\sigma_c = 10 \text{ MPa}$)

Type D curves represent the most prevalent type of behavior. After reaching the upper yield stress, the frozen sand exhibits continued strain hardening until reaching the peak strength at large strains. The amount of strength increase with increasing relative density is much larger than for tests at low confinement (Fig. 4.6), since high confinement increases the frictional resistance (more strengthening) and reduces the degree of ice cracking (less weakening).

Faster strain rates and lower temperatures produce Type B curves, e.g., test number 129 in Figure 4.3b, especially at the lower sand densities. The weakening mechanisms dominate immediately after yielding for the same basic reasons as for Type A curves. But thereafter, the increased confinement produces sufficient frictional resistance to offset damage of the ice matrix.

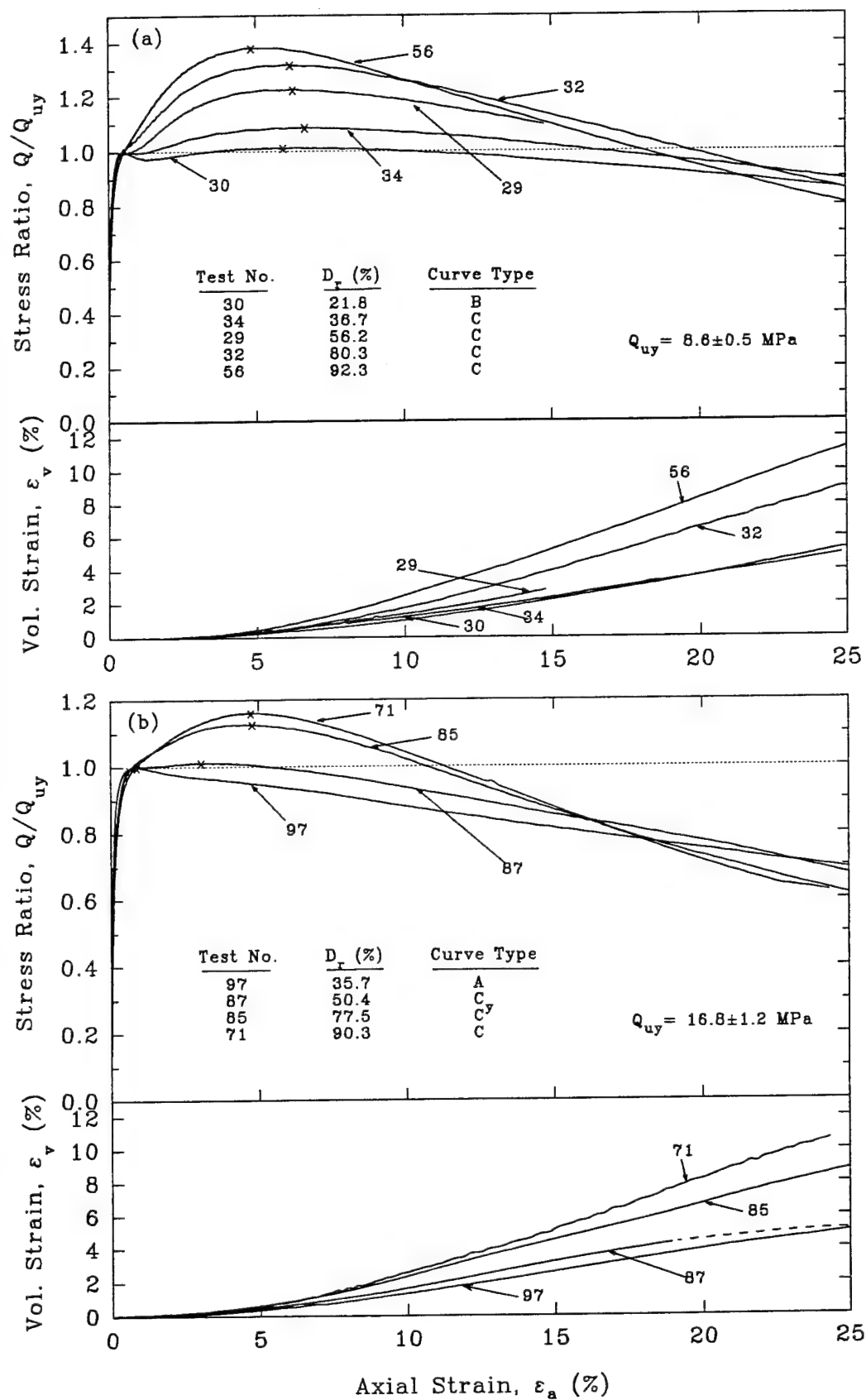


Fig. 4.1 Normalized Stress-Strain Data for Frozen MFS Showing the Effect of Relative Density at Low Confinement ($\sigma_c = 0.1 \text{ MPa}$): (a) Moderate Strain Rate and $T = -10^\circ\text{C}$; (b) Moderate Strain Rate and $T = -20^\circ\text{C}$ [--- questionable data; x=peak stress ratio]

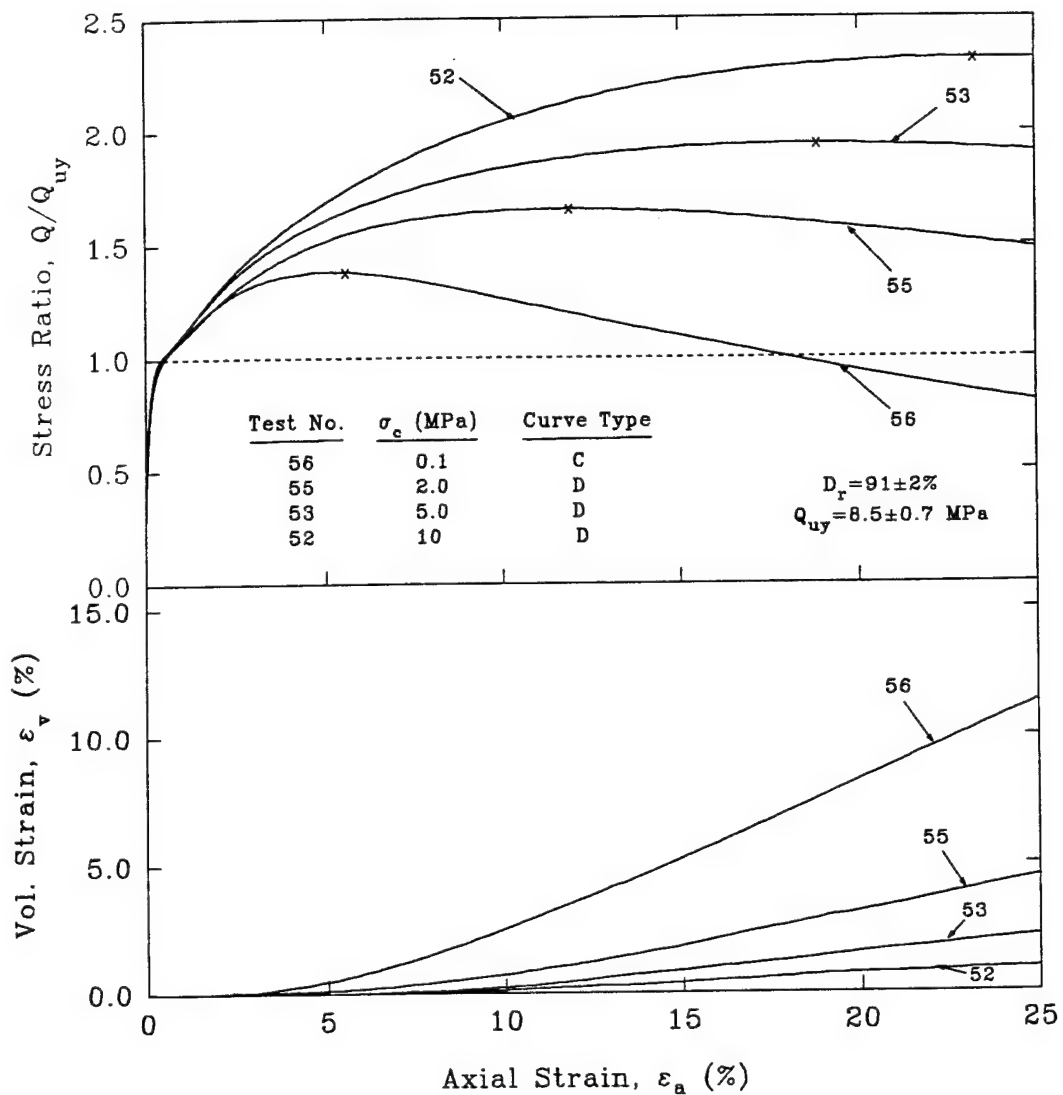


Fig. 4.2 Normalized Stress-Strain Data for Frozen MFS Showing the Effect of Confinement for Dense Specimens at Moderate Strain Rate and $T = -10^\circ\text{C}$ [x=peak stress ratio]

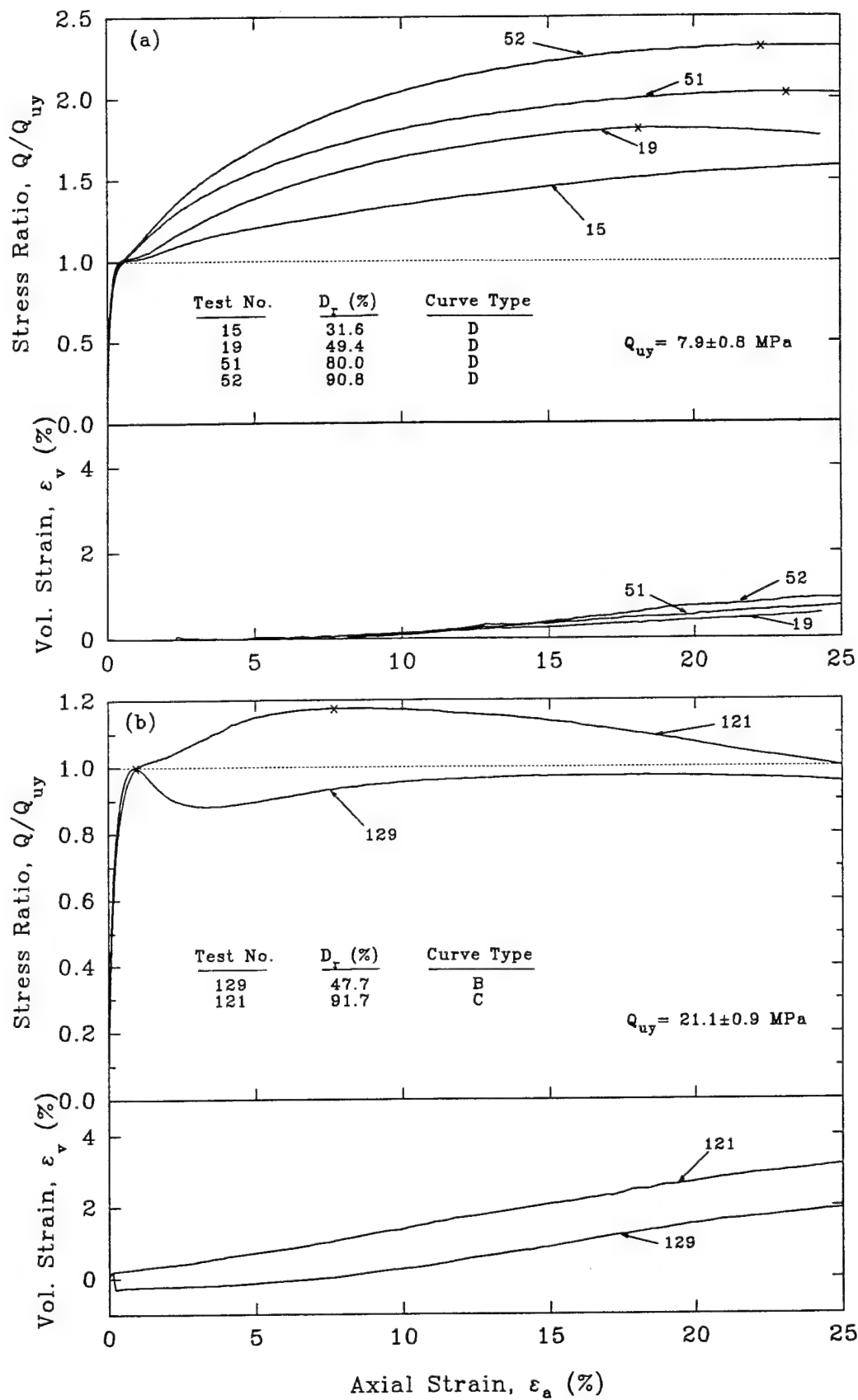


Fig. 4.3 Normalized Stress-Strain Data for Frozen MFS Showing the Effect of Relative Density at High Confinement ($\sigma_c = 10$ MPa): (a) Moderate Strain Rate and $T = -10^\circ\text{C}$; (b) Fast Strain Rate and $T = -15^\circ\text{C}$ [x=peak stress ratio]

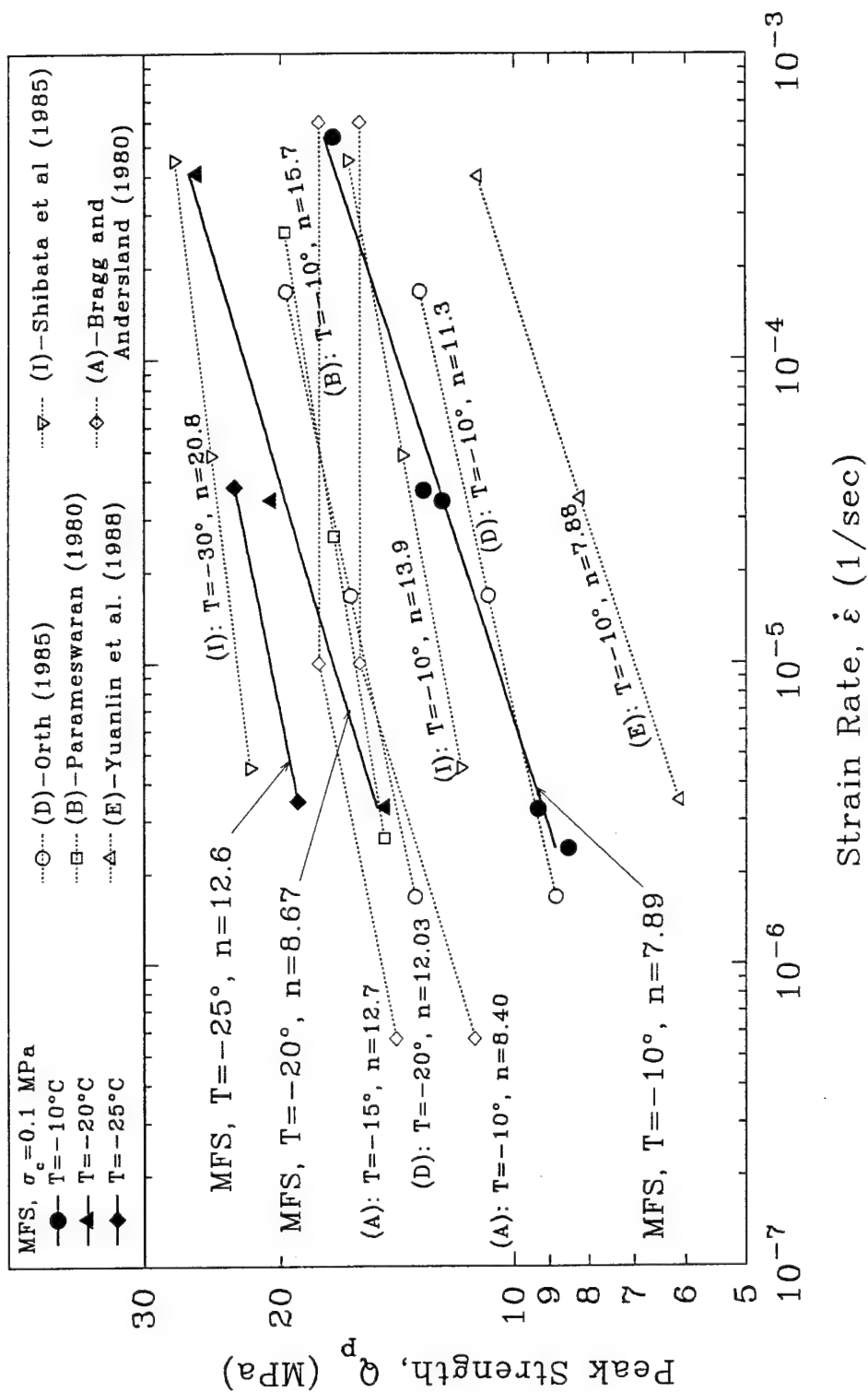


Fig. 4.4a Comparison of Peak Strength vs. Strain Rate of Dense MFS with other Dense Sands at Zero or Low Confinement (letter designations from Table B)

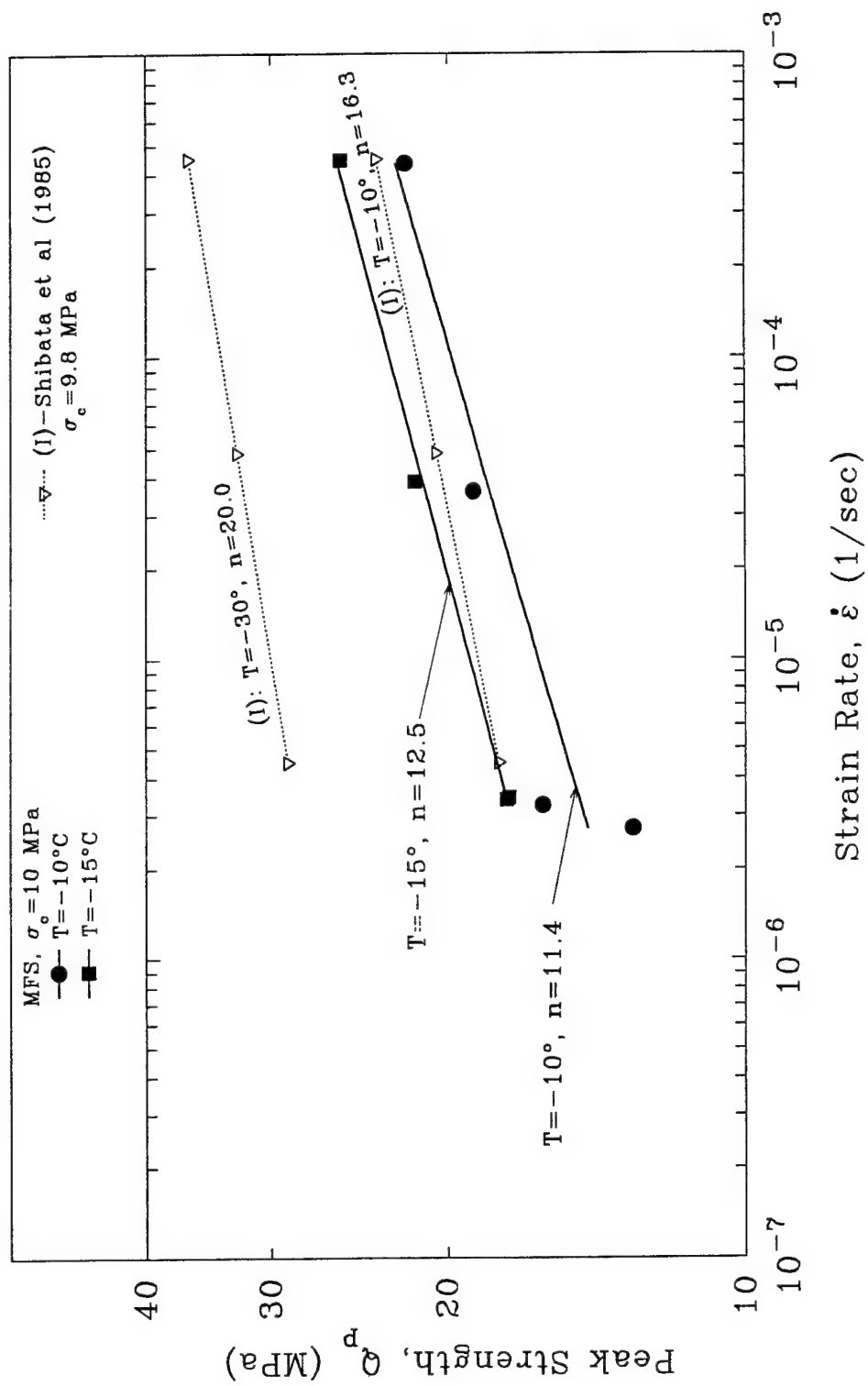


Fig. 4.4b Comparison of Peak Strength vs. Strain Rate of Dense MFS with other Dense Sands at High Confinement (letter designation from Table B)

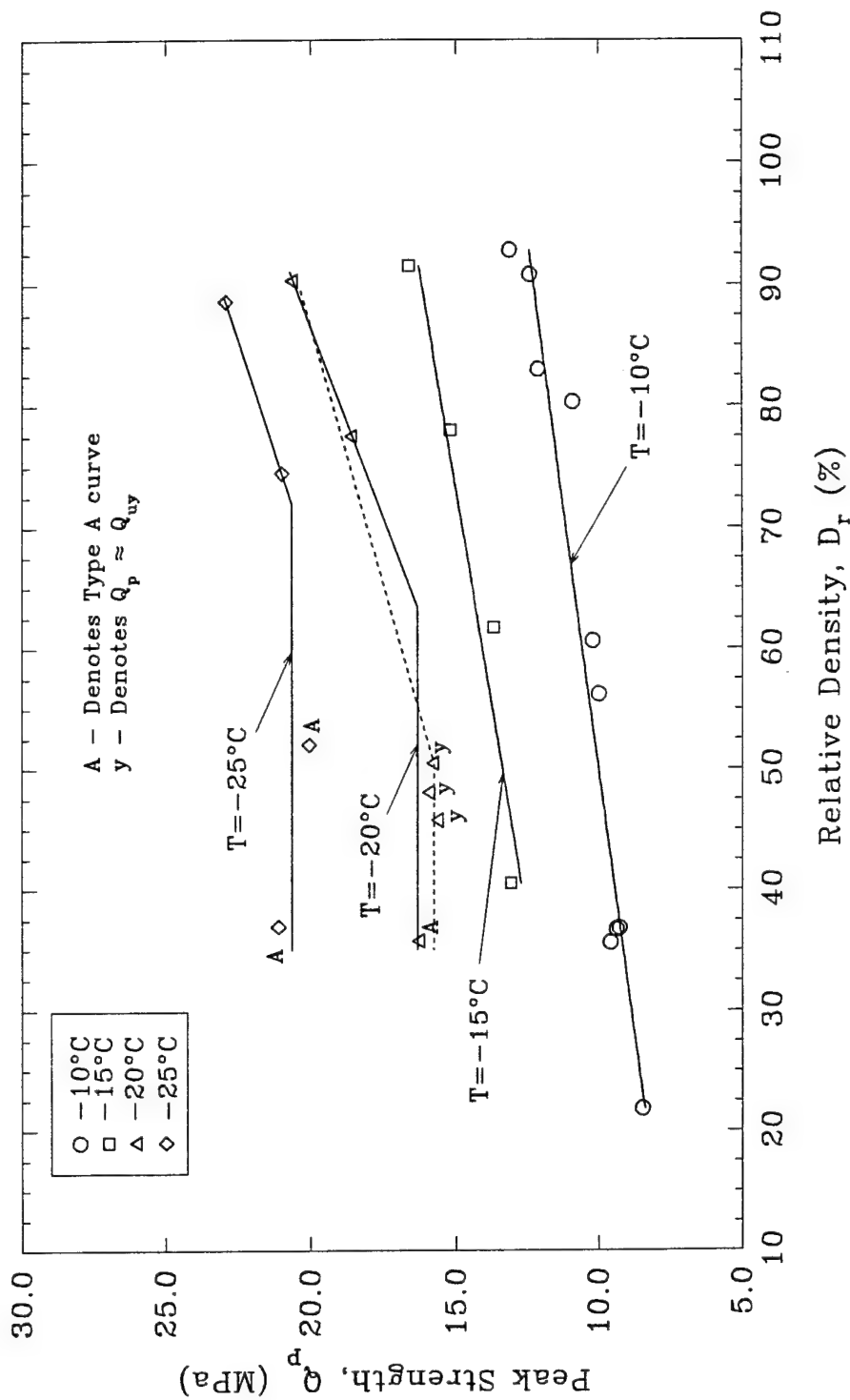


Fig. 4.5 Peak Strength vs. Relative Density for Frozen MFS at Moderate Strain Rate, Low Confinement and Different Temperatures

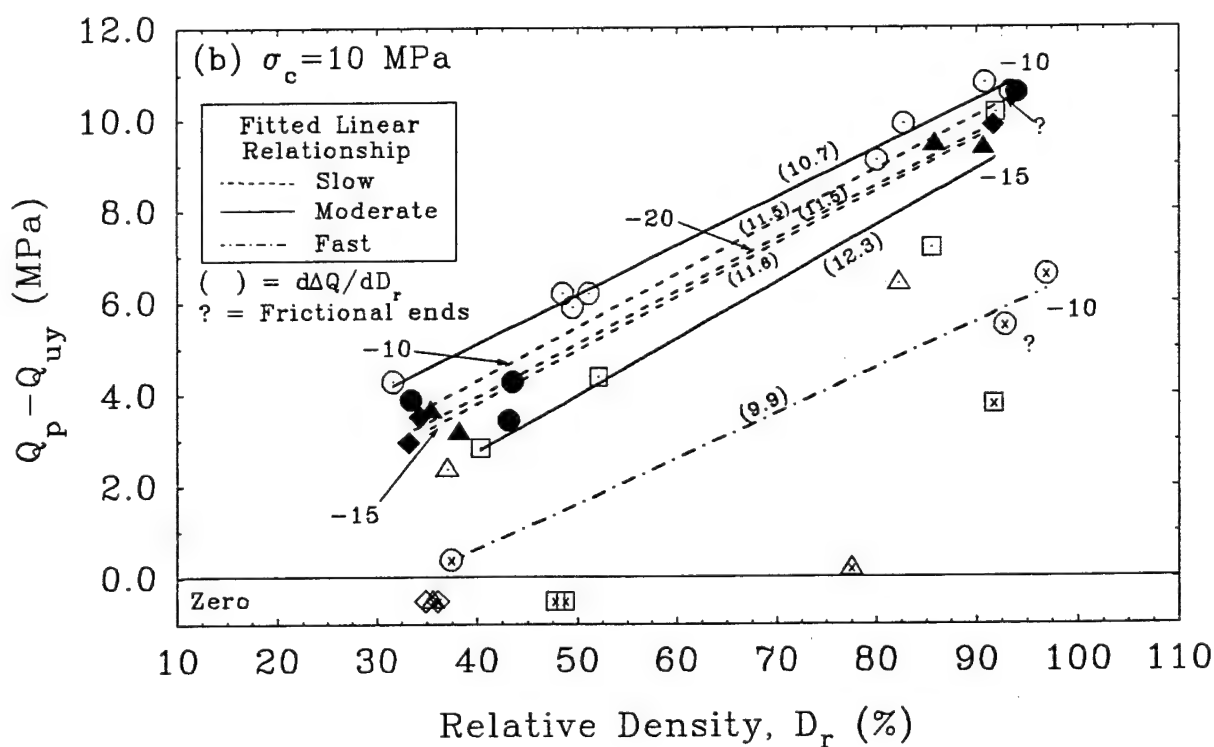
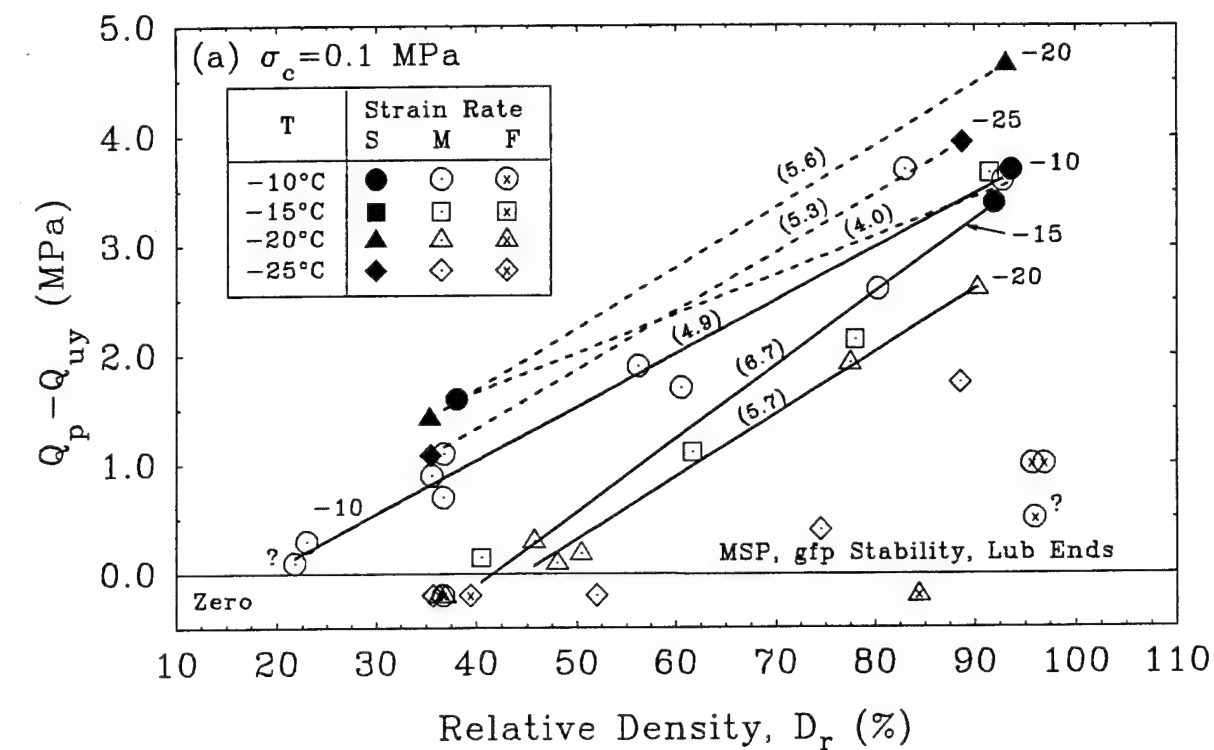


Fig. 4.6 Strength Increase vs. Relative Density of Frozen MFS at Varying Strain Rates and Temperatures: (a) at $\sigma_c = 0.1$ MPa; (b) at $\sigma_c = 10$ MPa

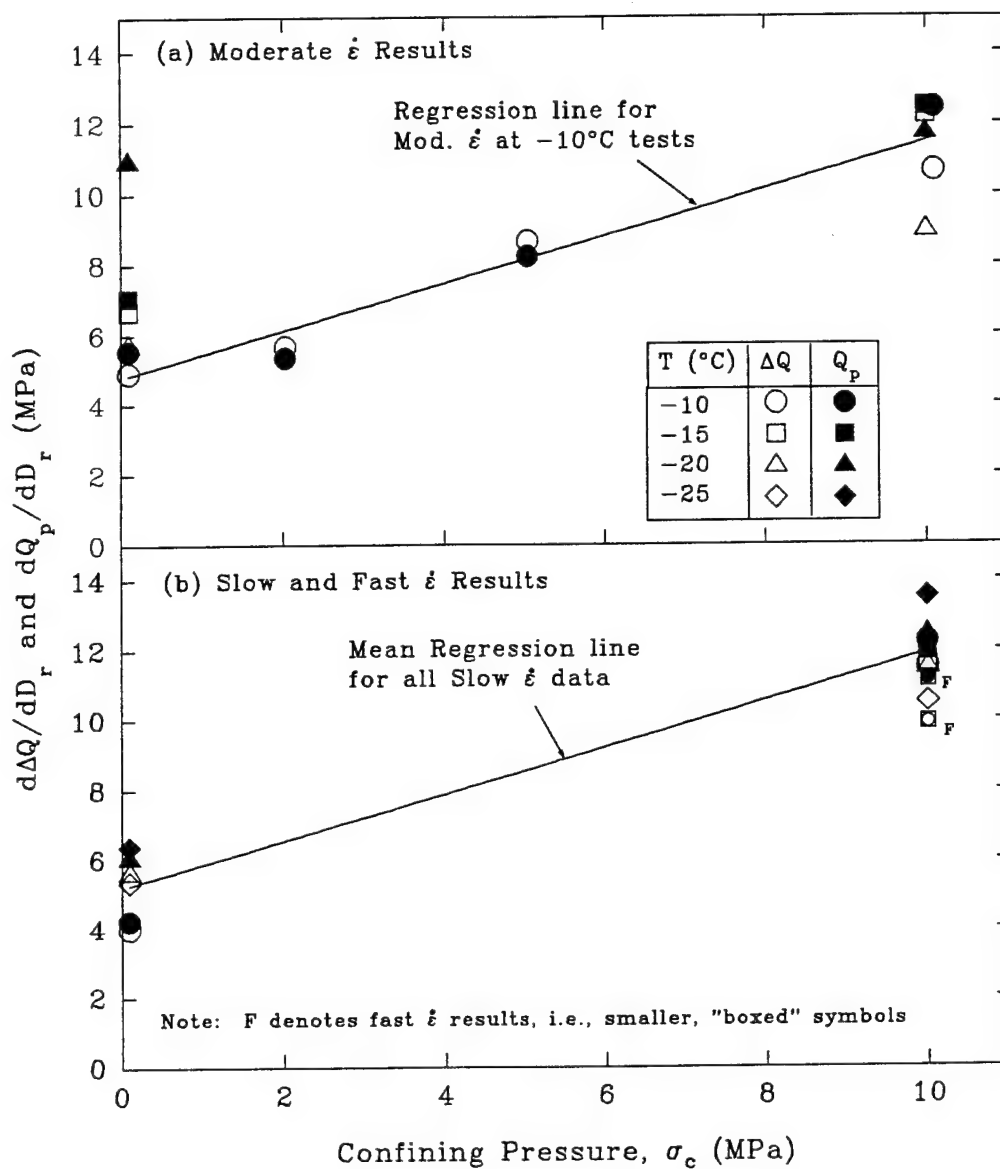


Fig. 4.7 Effect of Confining Pressure on Values of dQ/dD_r at Varying Strain Rates: (a) Moderate Strain Rate; (b) Slow and Fast Strain Rates

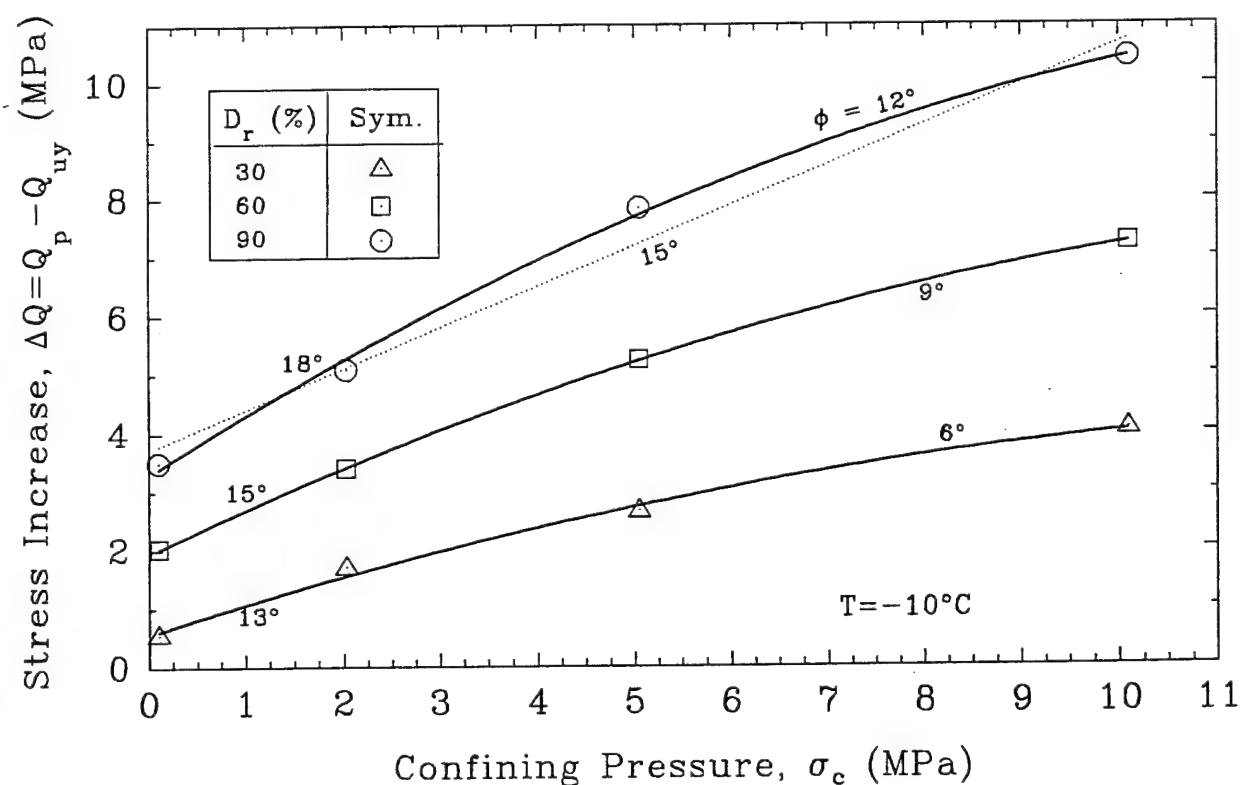
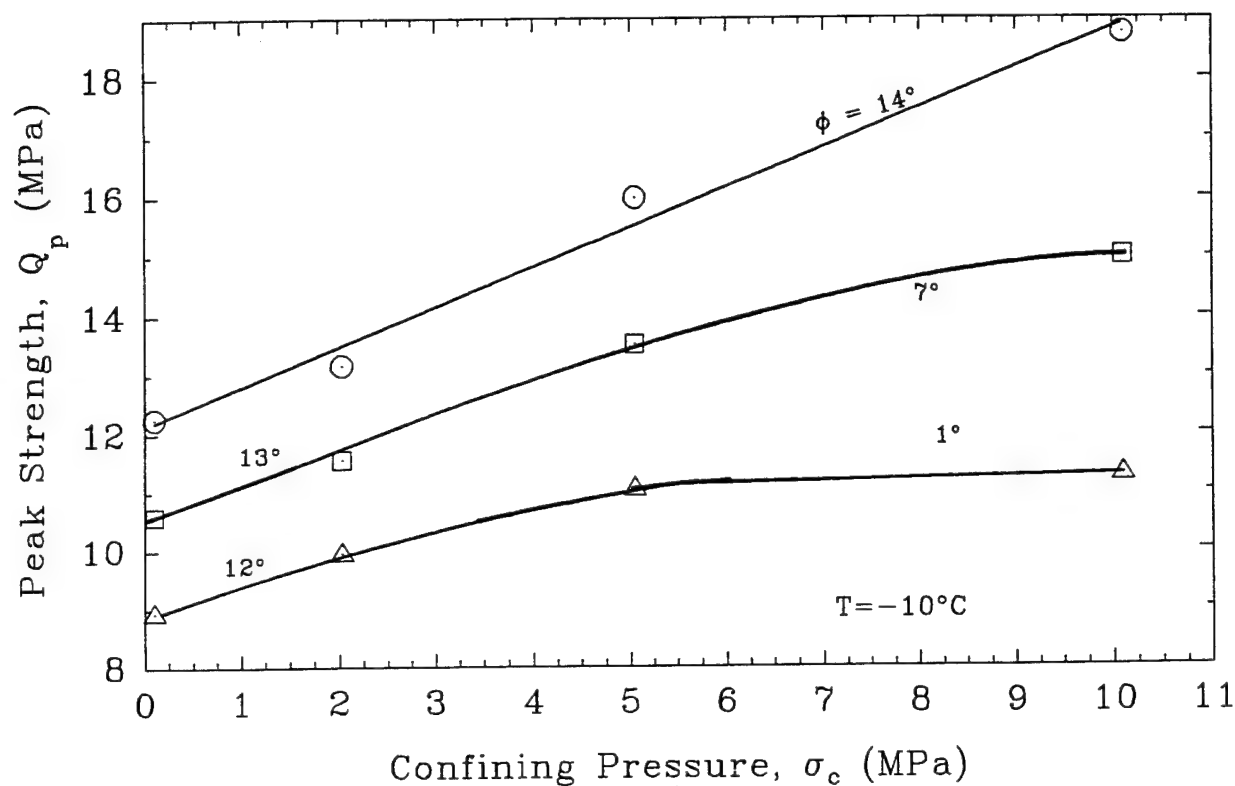


Fig. 4.8 Peak Strength and Stress Increase vs. Confining Pressure for Dense, Moderate and Loose Frozen MFS at Moderate Strain Rate and $T = -10^\circ\text{C}$ (Data points from linear regression)

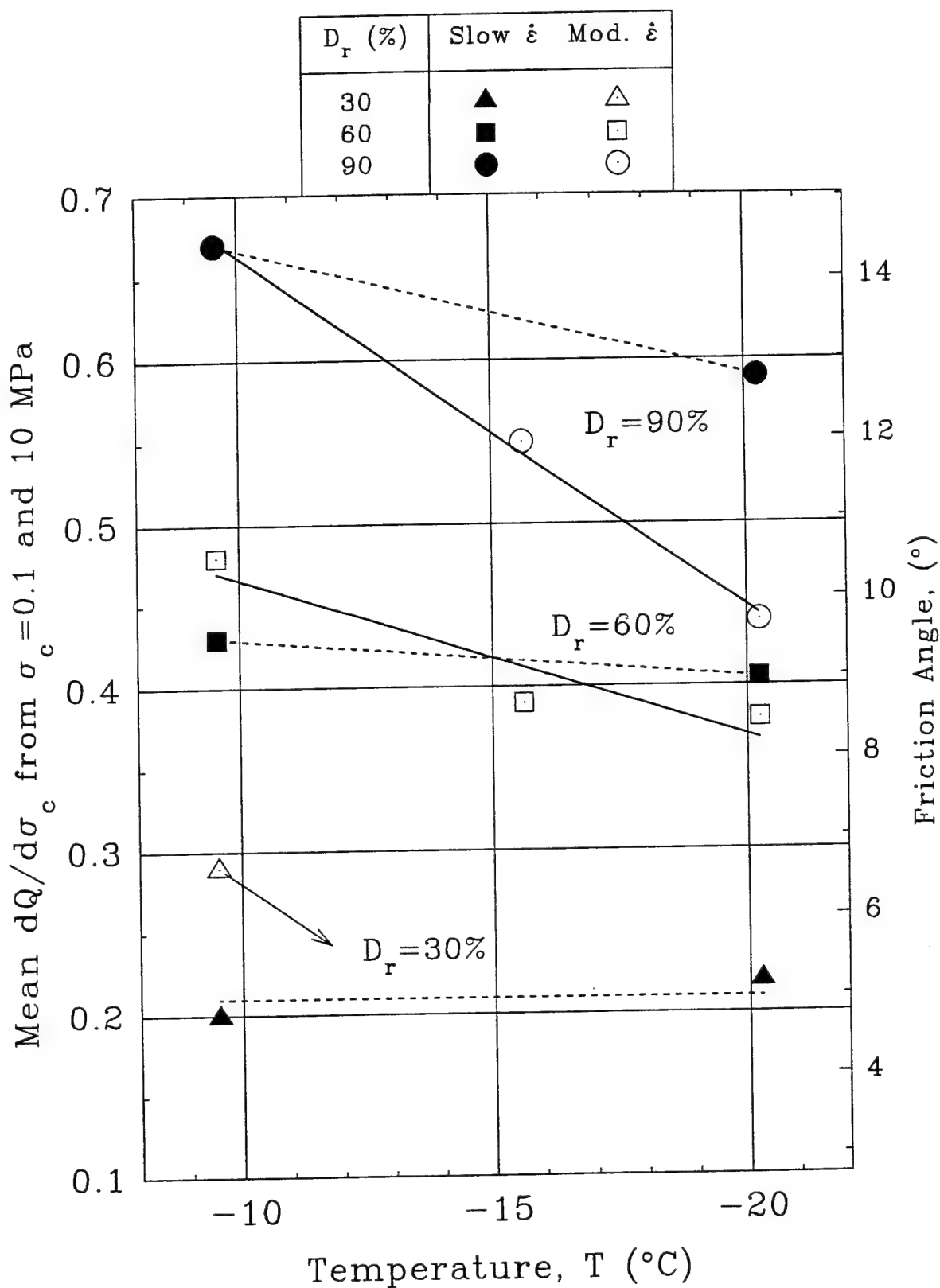


Fig. 4.9 Effect of Relative Density on Strength Gain with Confinement vs. Temperature for Frozen MFS at Slow and Moderate Strain Rates (Mean values from linear regression analyses on Q_p and ΔQ data at $\sigma_c = 0.1$ and 10 MPa)

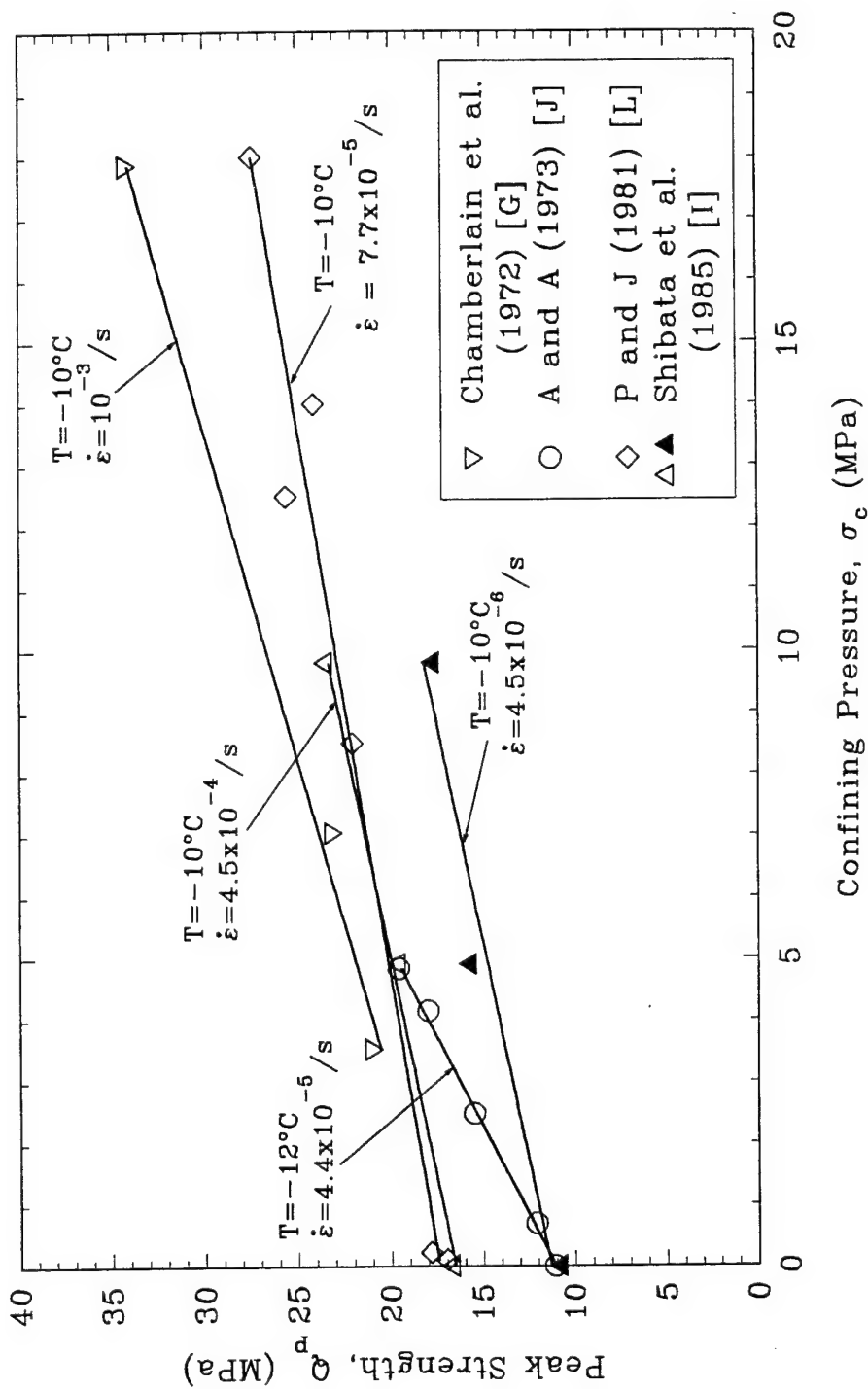


Fig. 4.10 Effect of Confining Pressure on Peak Strength of Dense Sands From Prior Programs at $T \approx -10^\circ\text{C}$

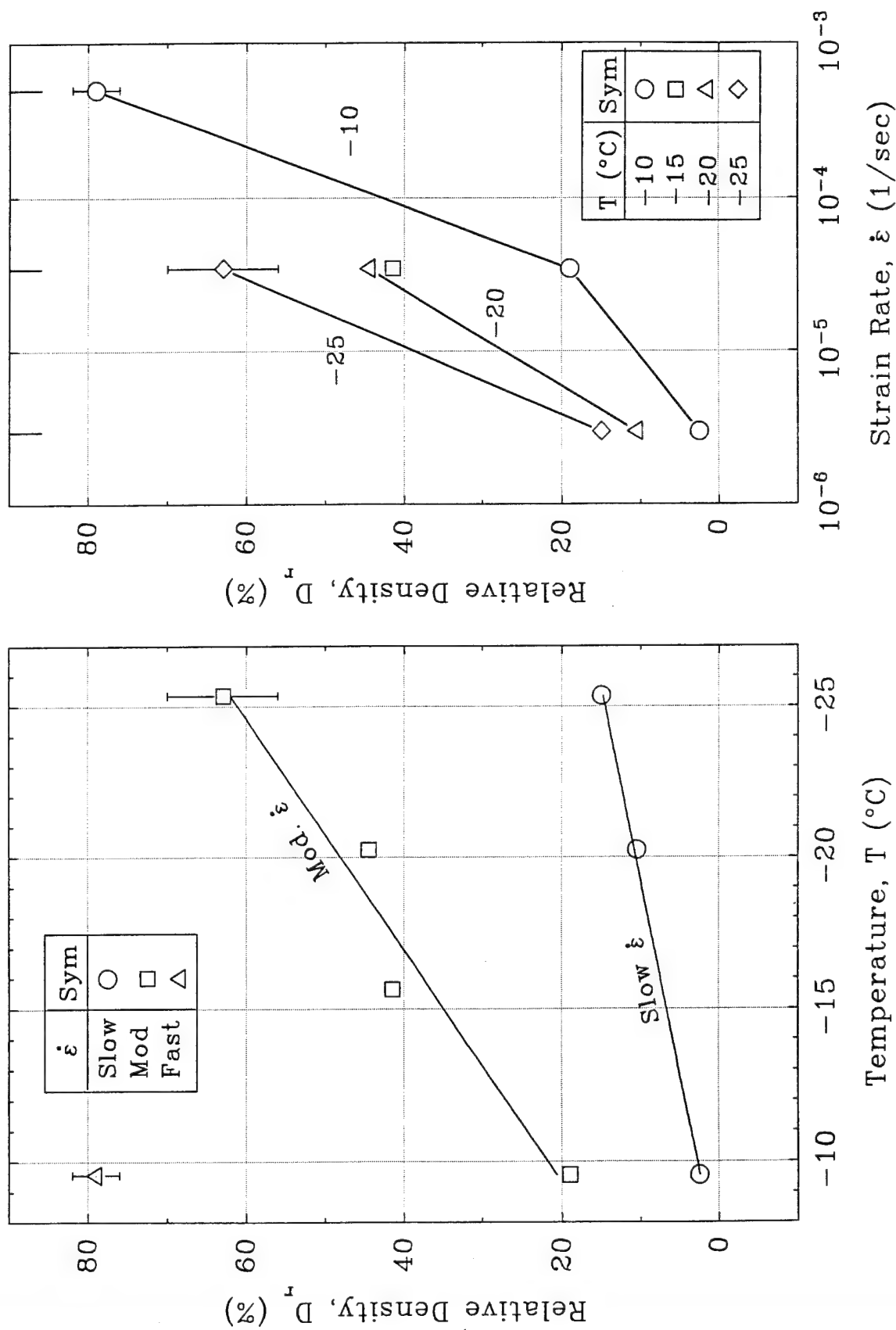


Fig. 4.11 Relative Density Producing $Q_p = Q_{uy}$ at $\sigma_c = 0.1$ MPa: (a) vs. temperature; (b) vs. strain rate

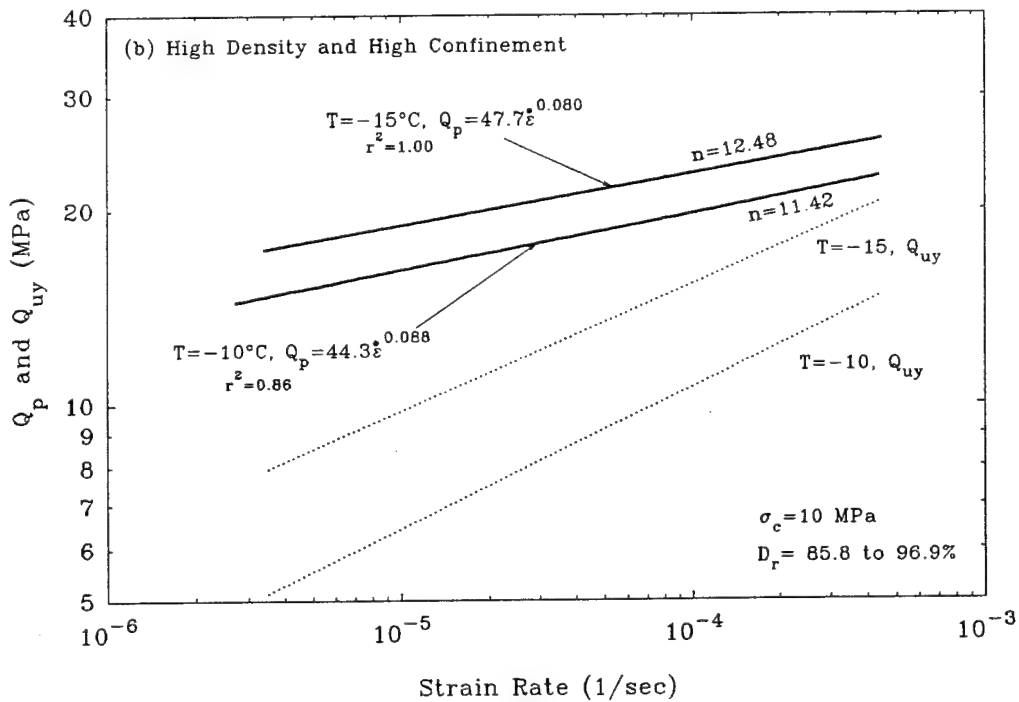
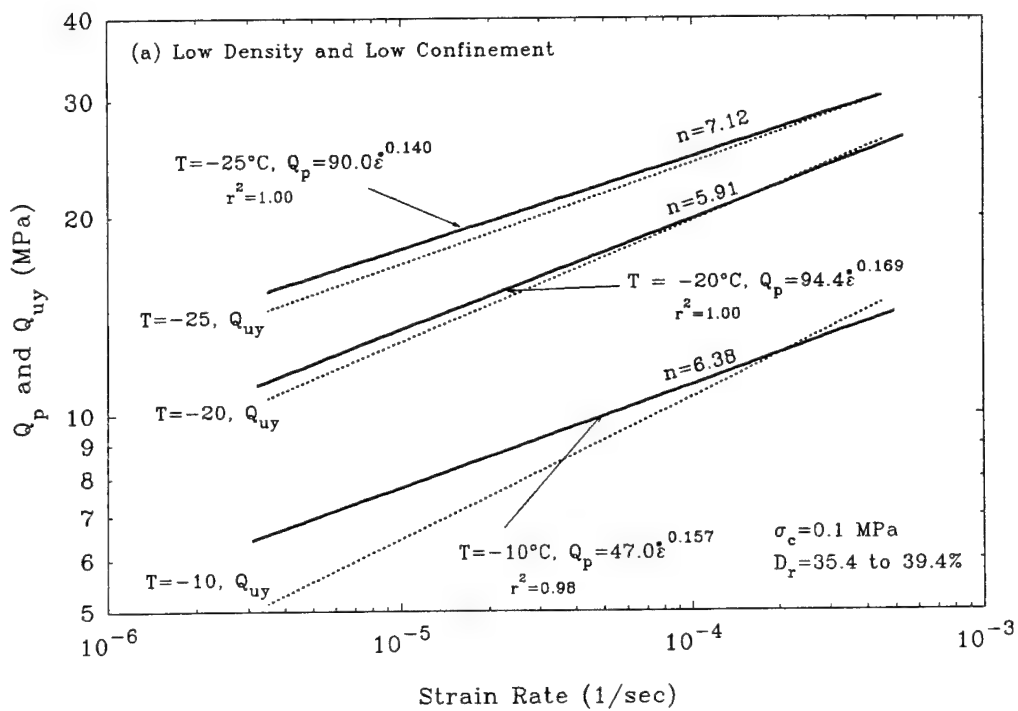


Fig. 4.12 Peak Strength and Upper Yield Stress vs. Strain Rate for Frozen MFS: (a) Low Density and Low Confinement; (b) High Density and High Confinement

T	-10	-15	-20	-25
$D_r = 30\%$	○	□	△	◇
$D_r = 90\%$	●	■	▲	◆

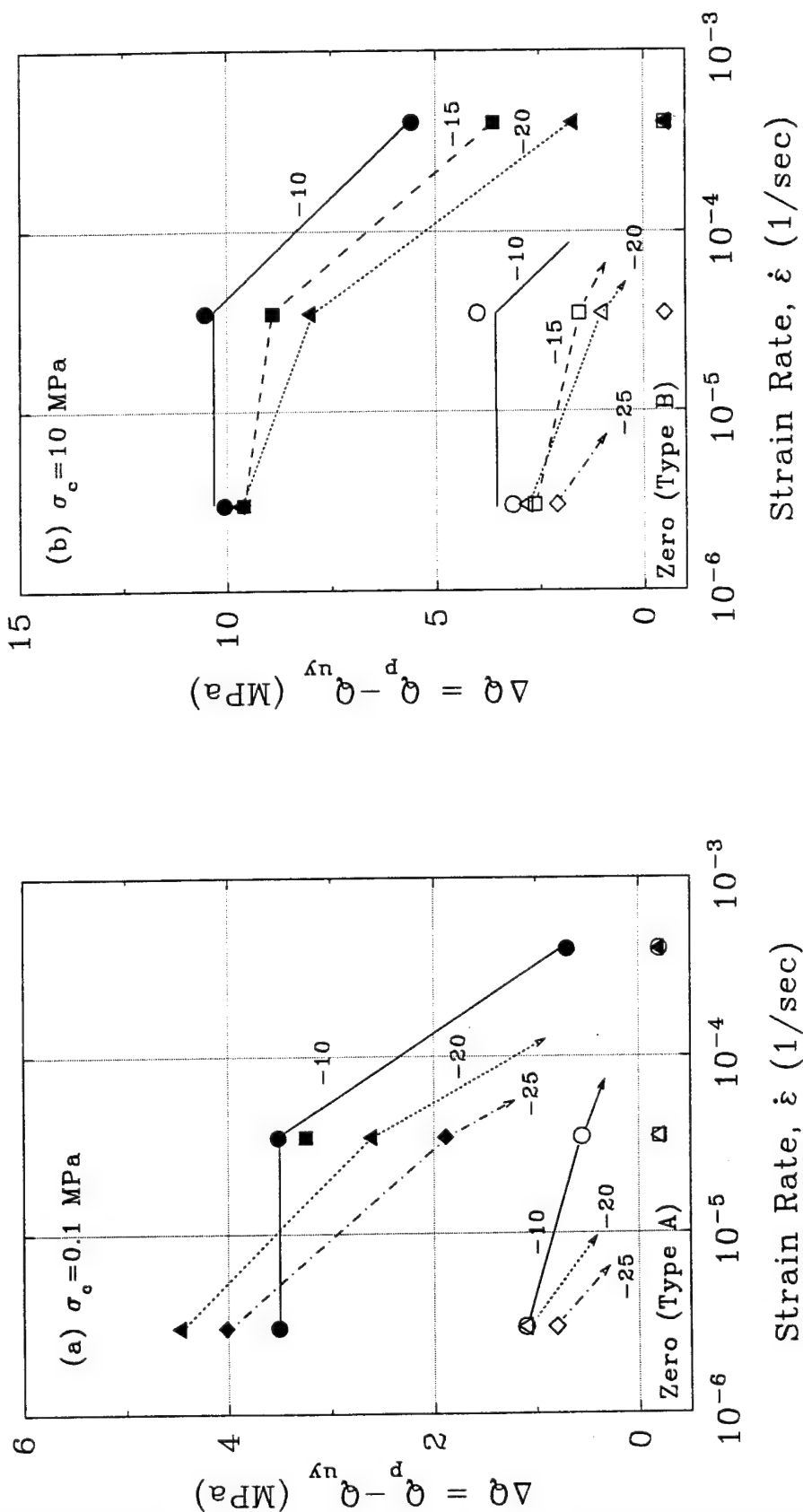


Fig. 4.13 Strength Increase vs Strain Rate for Loose and Dense Specimens of Frozen MFS at Varying Temperatures: (a) $\sigma_c = 0.1$ MPa; (b) $\sigma_c = 10$ MPa (Values from linear regression on data in Fig. 4.6)

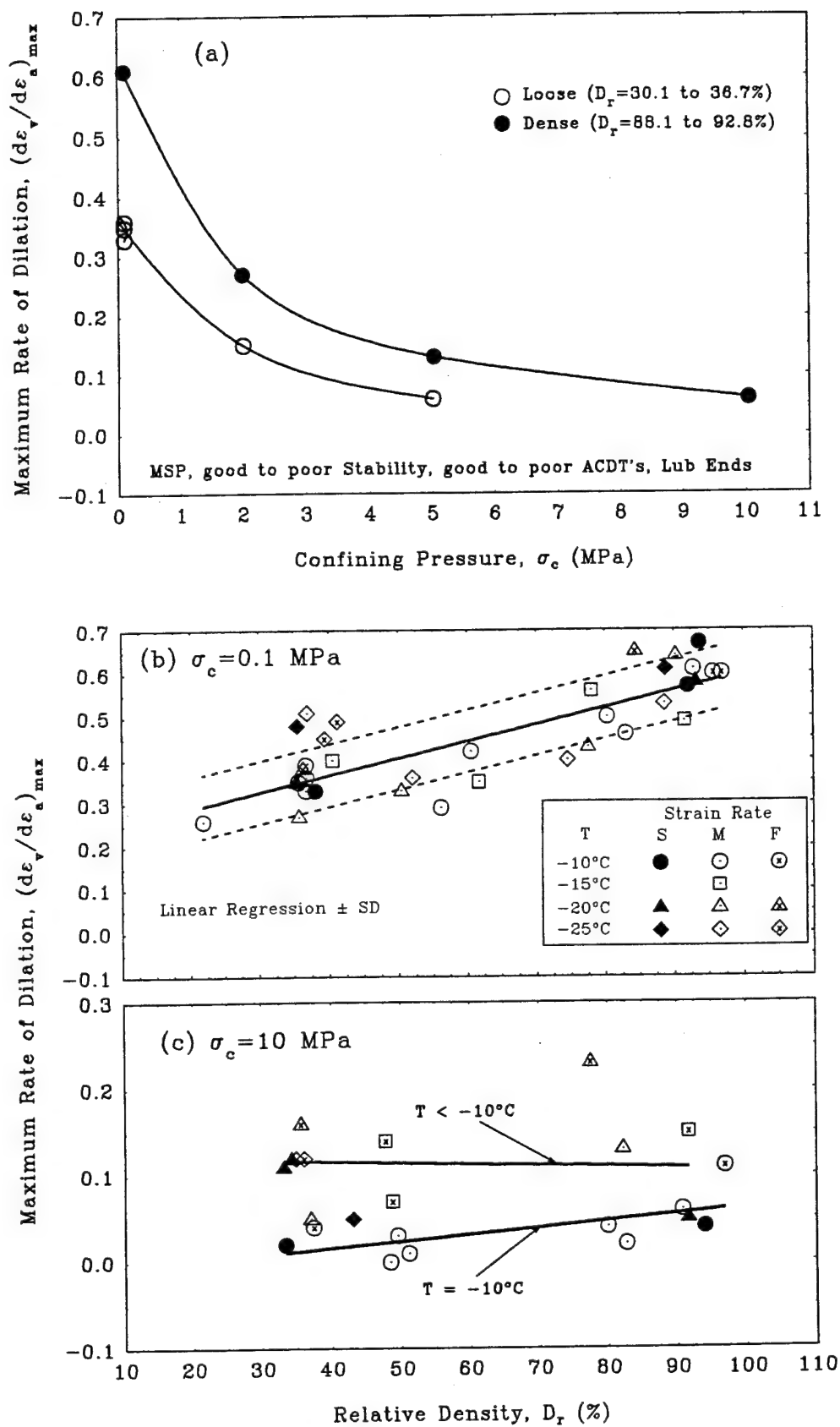


Fig 4.14

Maximum Rate of Dilation of Frozen MFS: (a) vs Confining Pressure at Moderate Strain Rate and $T=-10^\circ\text{C}$; (b) and (c) vs Relative Density at $\sigma_c=0.1$ and 10 MPa, Respectively, at Varying Strain Rates and Temperatures

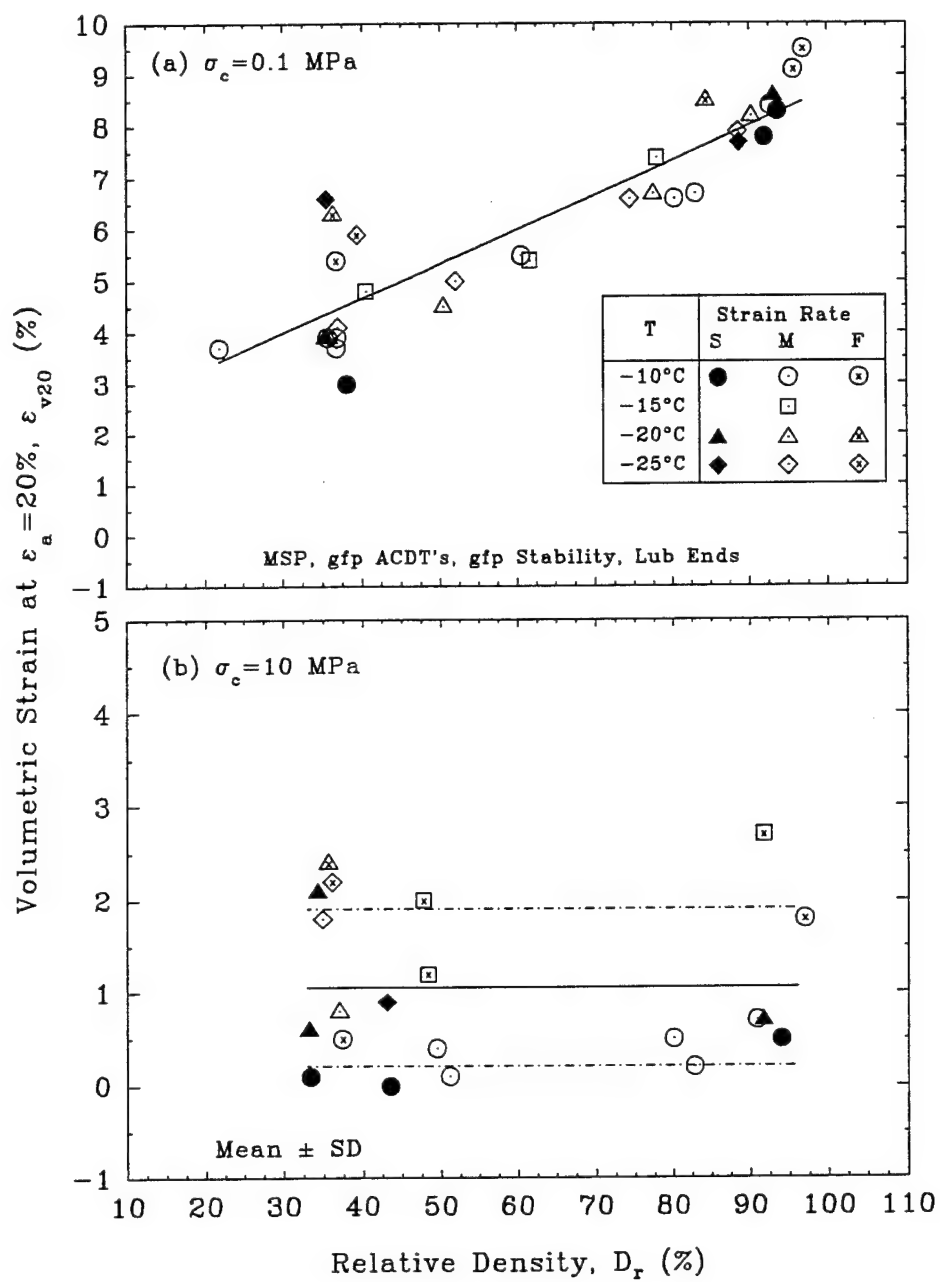


Fig. 4.15 Volumetric Strain at 20% Axial Strain vs Relative Density at Varying Strain Rates and Temperatures for Frozen MFS: (a) at $\sigma_c = 0.1$ MPa; (b) at $\sigma_c = 10$ MPa

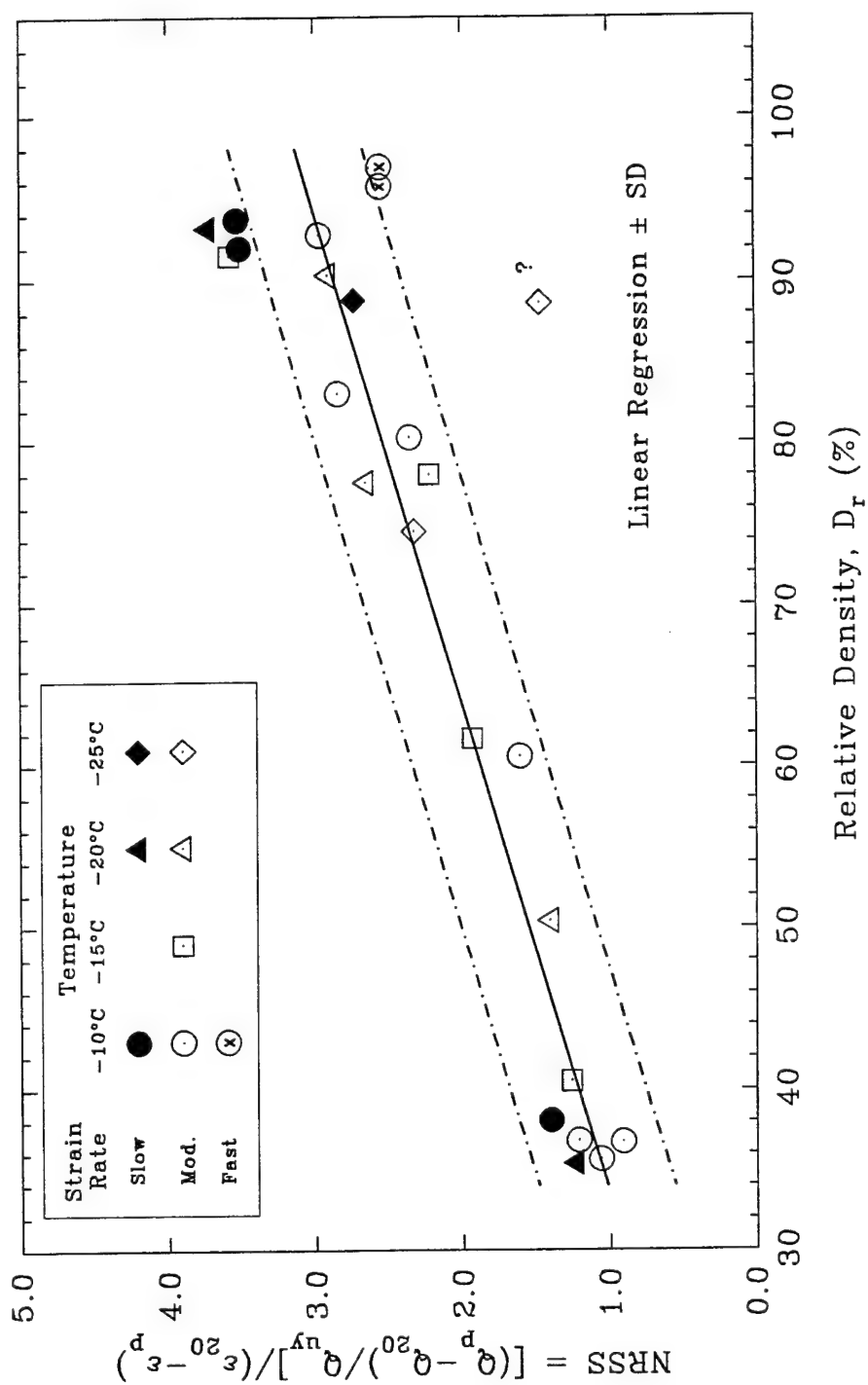


Fig. 4.16 Normalized Rate of Strain Softening vs. Relative Density at Varying Strain Rate and Temperature for Frozen MFS (Type C curves at $\sigma_c = 0.1$ MPa)

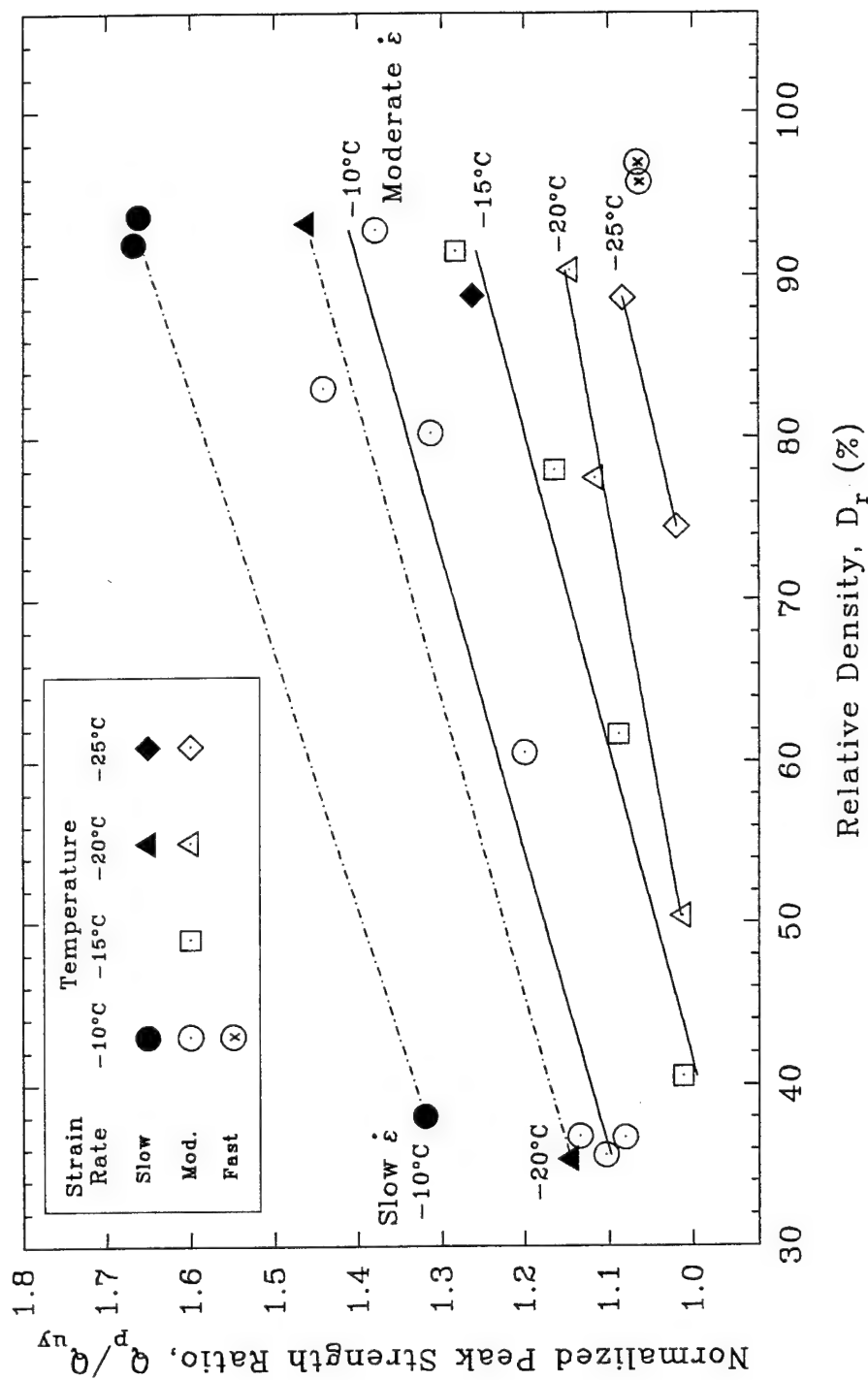


Fig. 4.17 Normalized Peak Strength Ratio vs Relative Density at Varying Strain Rate and Temperature for Frozen MFS (Type C curves at $\sigma_c = 0.1$ MPa)

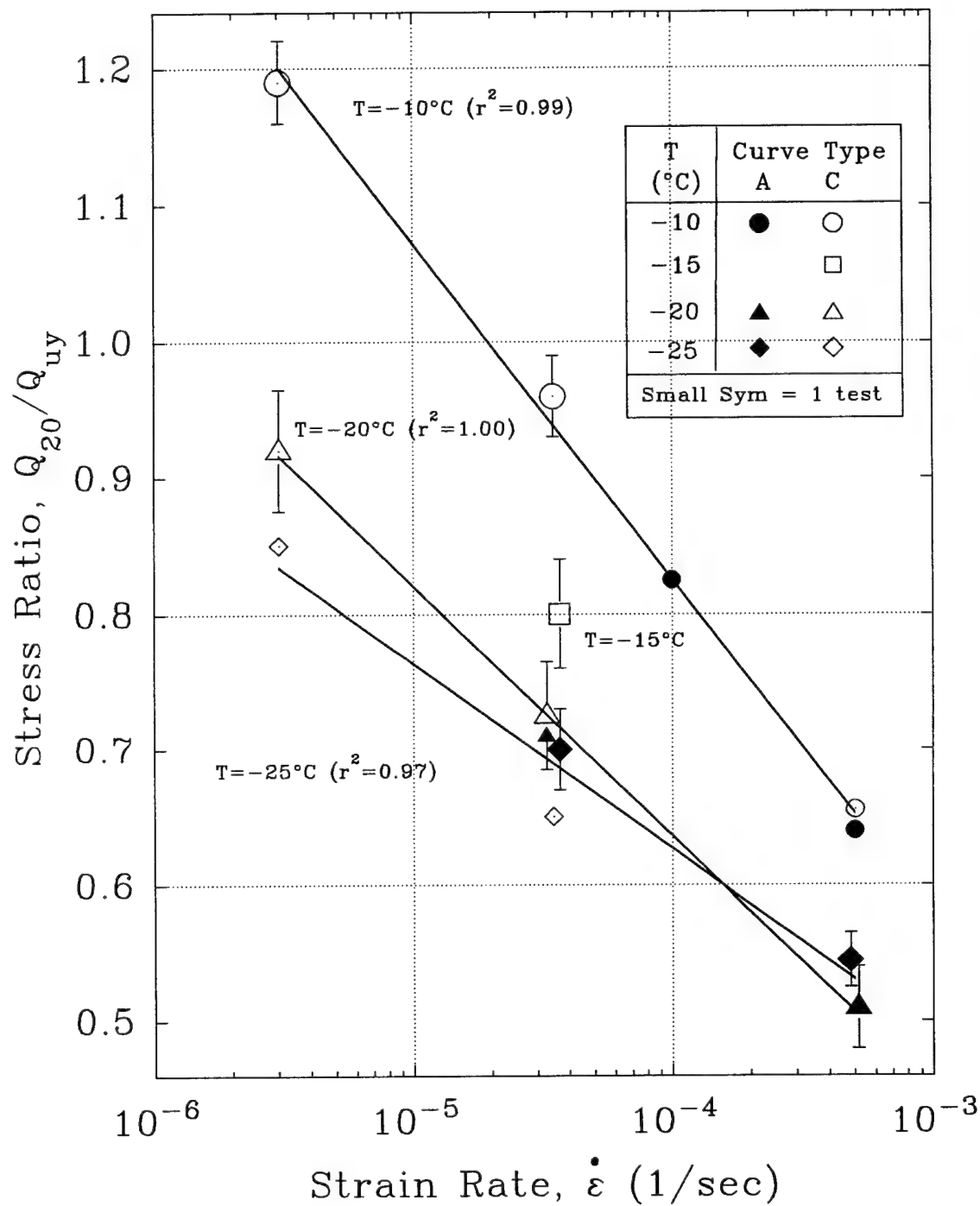


Fig. 4.18 Normalized Strength at 20% Axial Strain vs Strain Rate at Varying Temperatures for Frozen MFS (Type A and C curves at $\sigma_c = 0.1$ MPa)

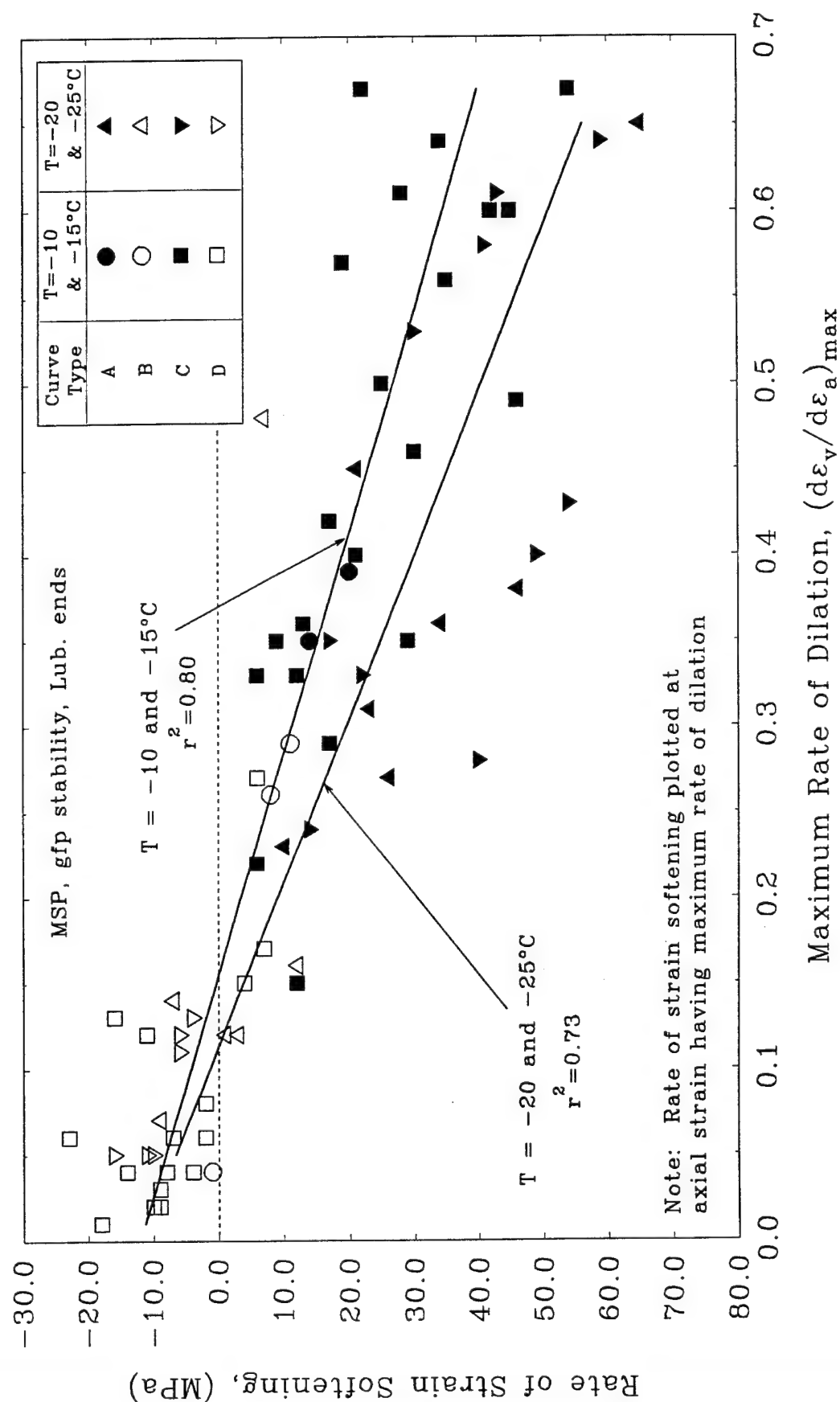


Fig. 4.19 Rate of Strain Softening vs Maximum Rate of Dilation of Frozen MFS as Function of Curve Type for All Testing Conditions

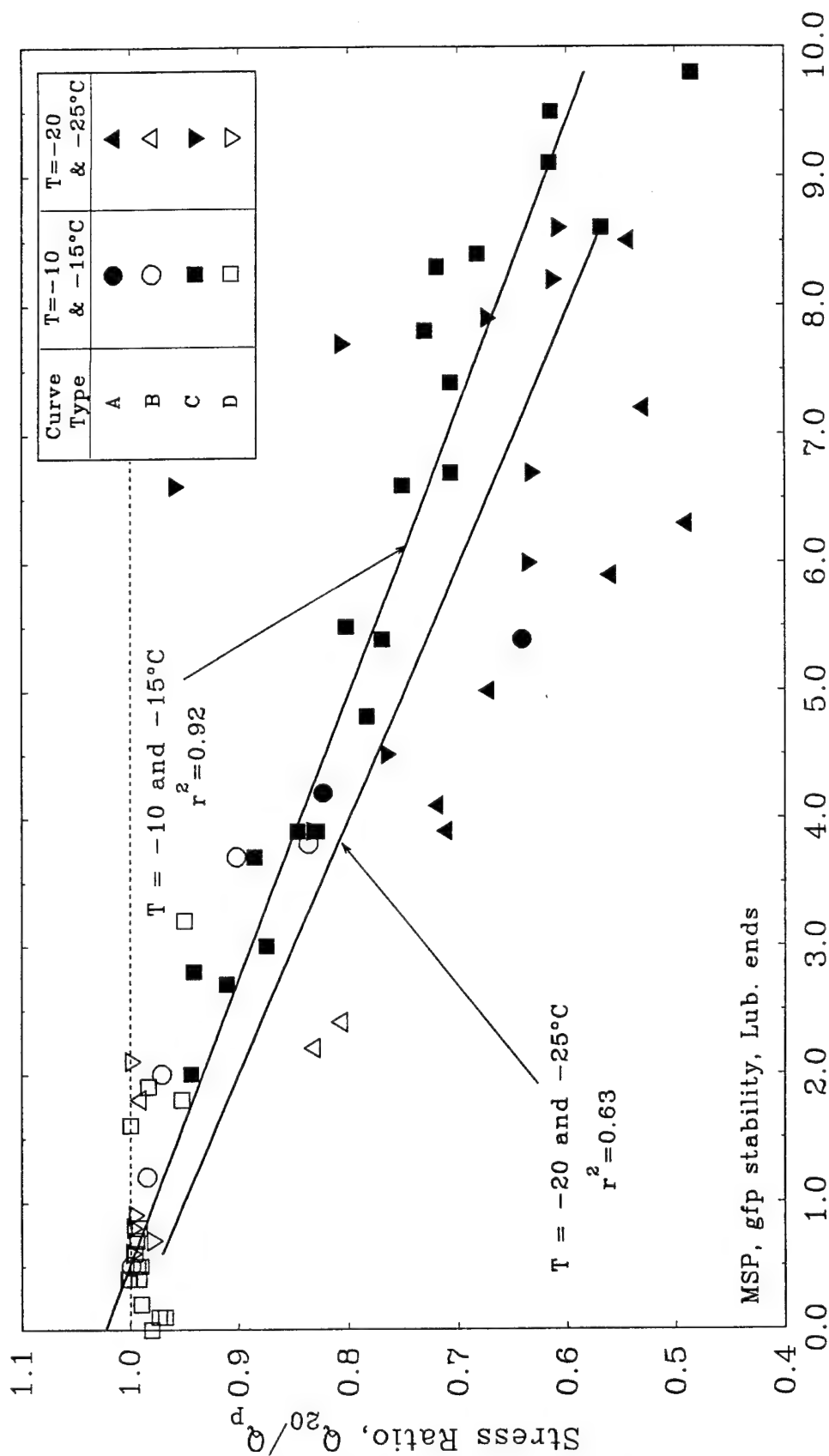


Fig. 4.20 Stress Ratio vs Volumetric Strain of Frozen MFS as a Function of Curve Type for All Testing Conditions

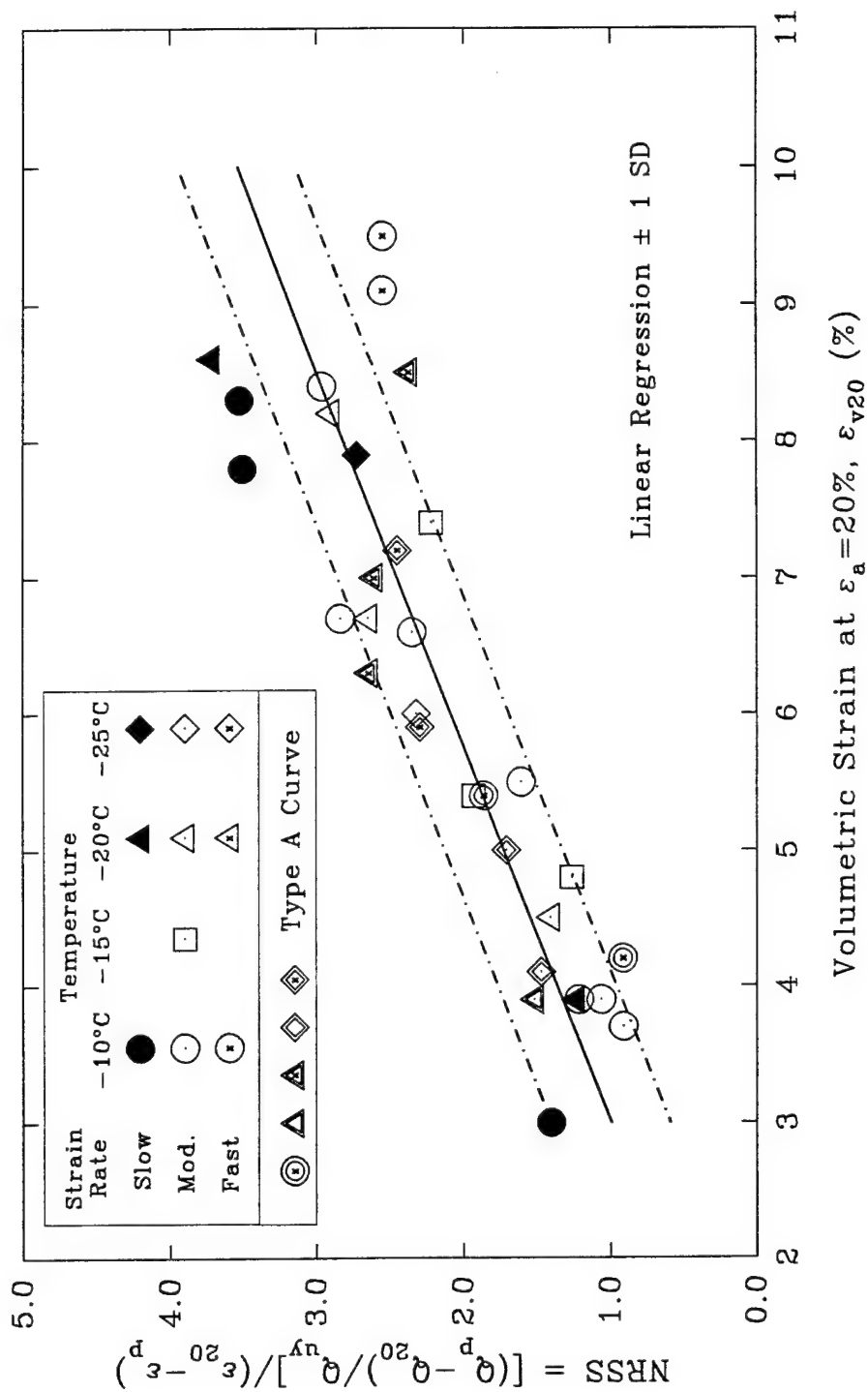


Fig. 4.21 Normalized Rate of Strain Softening vs. Volumetric Strain at Varying Relative Density, Strain Rate and Temperature for Frozen MFS (Type A and C Curves at $\sigma_c = 0.1$ MPa)

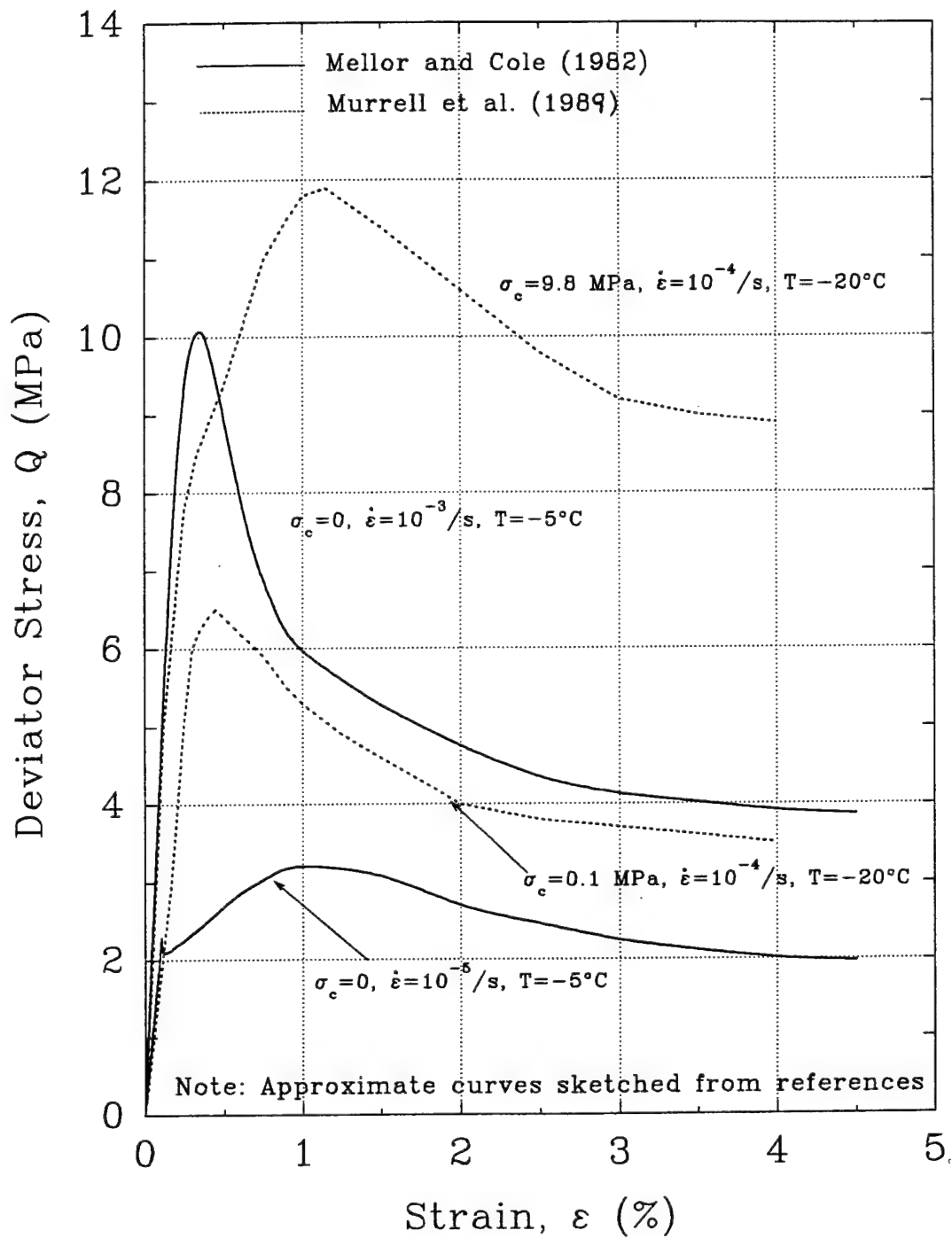


Fig. 4.22 Typical Stress-Strain Curves for Polycrystalline Ice

5. QUANTITATIVE ANALYSIS OF THE STRENGTH OF FROZEN SAND

5.1 INTRODUCTION

Ladanyi *et al.* developed a dilatancy-hardening model to predict the strength of frozen dense sand. Basically, it adds the shear strength of the pore ice, which is assumed equal to that measured in triaxial compression tests on polycrystalline ice, to the **undrained** shear strength of the sand skeleton, which is assumed equal to that measured in triaxial compression tests on unfrozen sand after accounting for the potential development of higher effective stresses provided by the higher tensile strength of the pore ice relative to unfrozen pore water. Section 5.2 describes this model and prior tests to check its validity. Section 5.3 summarizes the triaxial compression behavior of **unfrozen** Manchester Fine Sand (MFS) and presents the unfrozen sand parameters that are required for application of the dilatancy-hardening model. Section 5.4 presents results from *consolidate-freeze* triaxial compression tests on dense frozen MFS, in order to illustrate how the magnitude of the effective stress acting on the sand skeleton prior to freezing affects frozen sand behavior. These data also are relevant to application of Ladanyi's model. Finally, Section 5.5 compares strengths predicted by the dilatancy-hardening model to those measured from both conventional and *consolidate-freeze* triaxial compression tests on frozen MFS.

5.2 DILATANCY-HARDENING MODEL

5.2.1 Assumptions and Development

Ladanyi (1985) developed the dilatancy-hardening model to predict the strength of frozen dense sand, and Ladanyi and Morel (1990) presented experimental

results to check the validity of the model. The basic concept assumes that the *effective* stress path followed by the soil skeleton in a *frozen* sand will be the same as that for unfrozen sand provided that 1) both systems are subjected to the same strain path (axial loading at constant confining pressure and constant volume); and 2) the sand skeleton in both systems starts from the same state (density and effective stress). Unfrozen dense sand sheared undrained at low confinement tends to dilate (expand in volume). This causes development of negative pore pressures that increase the effective stresses acting on the sand which results in increased frictional resistance. The dilatancy-hardening model makes the following assumptions (Ladanyi and Morel 1990):

- 1) All of the pore water in the frozen sand is considered to be frozen.
- 2) The behavior of the sand skeleton is a function of the state parameter Ψ as introduced by Been and Jefferies (1985) and described in Section 5.3.
- 3) No consolidation occurs prior to shear; i.e., the tests are considered as "unconsolidated." The shear starts from a known density and confining pressure.
- 4) So long as the pore ice is continuous and unbroken during shear, the test will behave as "undrained." When the pore ice fails, i.e., breaks up, the test behaves as "drained." This breakup of the ice has been associated with axial strains of 1 to 2% in the literature.
- 5) As long as the test behaves undrained (i.e., before the pore ice becomes broken), the dilatancy-hardening principles established for unfrozen sand

are also applicable to the frozen sand skeleton provided that proper account is made for the tensile strength of the pore ice matrix.

Before further description of the dilatancy-hardening model, the definition of the critical confining pressure, σ'_{cr} , is needed. Seed and Lee (1967) and others have observed that if a dense sand is sheared in an undrained mode with no back pressure in a state where it exhibits a tendency to dilate, i.e., it has a large $-\Psi$ parameter, the pore water pressure decreases, and the effective stresses increase on the sand skeleton until one of two conditions occurs. Either the pore water pressure reaches the tensile strength of water, i.e., it decreases sufficiently to cause cavitation, or the effective stresses increase until the "state point" reaches the Critical Void Ratio Line (CVRL) or alternatively, the Steady State Line (SSL). The transition confining pressure between these two conditions depends on the "critical confining pressure," σ'_{cr} . Seed and Lee (1967) define the "critical confining pressure" as that confining pressure for a given preshear void ratio which results in no net volume change at the peak strength in a drained triaxial compression test on unfrozen sand (or no net change in pore pressure at failure for an undrained test). As used by Ladanyi *et al.*, σ'_{cr} is the initial confining pressure that will result in no further change in *pore pressure at failure* for undrained shear of unfrozen sand at a given initial density (or void ratio). Note: Ladanyi (1989) acknowledges that the Seed and Lee definition "might have been better" and that definition has been adopted by MIT.

Although Ladanyi *et al.* presented stresses in the form $Q = (\sigma_1 - \sigma_3)$ and $\sigma_{oct} = \frac{1}{3}(\sigma_1 + \sigma_2 + \sigma_3)$, application of the model will be illustrated using the MIT format: $q = 0.5(\sigma_1 - \sigma_3)$, $p = 0.5(\sigma_1 + \sigma_3)$ and $p' = 0.5(\sigma'_1 + \sigma'_3)$. This is done in Figure 5.1, which has been drawn to scale, based on specific values for the critical confining pressure (σ'_{cr}) and friction angle (ϕ') of the sand skeleton and the shear strength (q_i) and tensile strength (T_i) of the ice matrix.

The undrained shear strength of the frozen sand skeleton is equal to $q_{fs} = p'_f \tan \alpha' = p'_f \sin \phi'$, where p'_f is the value of p' at failure and ϕ' is the effective stress friction angle (assumed equal to that for unfrozen sand). The total stress (failure) envelope for the frozen sand skeleton, TSE (fs), has the same initial slope as the effective stress envelope, ESE (us and fs), but translated to the left by an amount equal to the tensile strength of the pore ice, T_i . For this initial region, the sand strength is controlled by the magnitude of the negative "pore pressure" that can develop before cavitation of the pore fluid.

The transition point between the cavitating and non-cavitating regimes occurs at a confining pressure (total stress) of

$$\sigma_c = \sigma'_{cr} - T \quad \dots\dots\dots[5.1]$$

where T is the tensile strength of the pore fluid. For pore water, $T = T_w$, which is about 0.1 MPa; for pore ice, $T = T_i$, where $T_i = 2$ MPa for this example. For a confining pressure greater than $\sigma'_{cr} - T$, i.e., for an initial $p (= \sigma_c)$ greater than p_1 in Figure 5.1, the total stress envelope, TSE(fs), assuming an undrained test condition,

becomes horizontal with a value of $q = q_{fs}$. The predicted strength of the soil skeleton in this region is therefore solely controlled by the magnitude of the critical consolidation stress and is calculated as

$$q_{fs} = 0.5 \cdot \sigma'_{cr} \cdot (R_f - 1) \quad \dots\dots\dots[5.2]$$

where R_f is equal to $(\sigma'_1/\sigma'_3)_f = (1 + \sin \phi')/(1 - \sin \phi')$. For a confining pressure less than $\sigma'_{cr} - T_i$, the strength of the sand is governed by the applied confining pressure ($\sigma_3 = \sigma_c$) and the tensile strength of the pore ice, so that

$$q_{fs} = 0.5 \cdot (\sigma_3 + T_i) \cdot (R_f - 1) \quad \dots\dots\dots[5.3]$$

Note: Although the predicted value of q_{fs} in the cavitating regime is controlled by T_i and the total confining stress ($\sigma_3 = \sigma_c$), the undrained shear data presented in Section 5.3 will show that the amount of strain required to reach q_{fs} is very dependent upon the magnitude of the preshear effective stress, $\sigma'_3 = \sigma'_c$.

Since pore ice can support both tensile and shear stresses, Ladanyi and Morel (1990) propose that the shear strength of the ice should be added directly to the shear strength of the sand skeleton, which also has been increased by the tensile strength of the pore ice. Using their methodology, the strength of the frozen sand is represented by a total stress line, TSL ($FS = fs + ice$), where the additional ice strength is added to the sand skeleton strength directly above the effective stress envelope (ESE). For example, for the non-cavitating case starting at p_1 , the sand skeleton ends up at point B on the ESE. The shear strength of the ice, q_i , is then added to obtain point C, which defines the break in the TSL (FS) envelope. In contrast, the MIT

methodology would use the TSE (FS) which represents the actual end points of predicted total stress paths (i.e., points q_1 , q_2 and q_3 in Figure 5.1).

The total shear strength of the frozen system can now be described for both the cavitating and non-cavitating case. In the non-cavitating region, the predicted shear strength of the frozen sand is given by

$$q_{FS} = 0.5 \cdot \sigma'_{cr} \cdot (R_f - 1) + q_i \quad \dots\dots\dots[5.4]$$

where σ'_{cr} is the critical confining pressure for the initial void ratio (density) of the sand skeleton. This equation predicts that the strength of the frozen sand is independent of the actual confining pressure for $\sigma_c = \sigma_3 \geq p_1$.

For the cavitating case, i.e., $\sigma_3 < \sigma'_{cr} - T_i$, the shear strength of the frozen sand (q_{FS}) is predicted to be

$$q_{FS} = q_{fs} + q_i = 0.5 \cdot (\sigma_3 + T_i) \cdot (R_f - 1) + q_i \dots\dots\dots[5.5]$$

where σ_3 is the confining (cell) pressure, T_i is the tensile strength of ice, and q_i is the shear strength of the pore ice. Hence, the shear strength in this region increases linearly with increasing confining pressure with the same slope as the ESE.

5.2.2 Prior Experimental Validation

Ladanyi and Morel (1990) present the results of drained triaxial compression tests on unfrozen sand and conventional triaxial compression tests on frozen specimens of 20-30 Ottawa sand to check the dilatancy-hardening model. The tests were performed on vibrated, dense, saturated specimens ($D_r = 90 \pm 6\%$) at a mean strain rate at failure of 2.7×10^{-4} /sec. Confining pressures (or effective

consolidation stresses) prior to shear ranged from zero to 0.3 MPa. The temperature for frozen tests was -5°C . For the frozen tests, a well-pronounced peak occurred at or a little above 2% axial strain (based on measurement of axial deformation).

Results from 23 frozen tests showed an extremely high pressure sensitivity of $dQ_p/d\sigma_c = 2.75$ ($\phi = 35^{\circ}$), compared to data summarized in Figures 4.8, 4.9, and 4.10; an extremely high rate of dilation at failure of $d\epsilon_v/d\epsilon_a \approx 3.4 \pm 0.15$, compared to the MFS data in Figure 4.14; and a mean peak strength of $Q_p \approx 8.8$ MPa. Two tests on ice with $\sigma_c = 0.2$ MPa and $\dot{\epsilon} = 2.8 \times 10^{-4}$ /sec gave $Q_i = 4.9$ MPa at 2% axial strain. Using $\phi' = 32^{\circ}$ (from drained triaxial compression tests on unfrozen sand), $\sigma_c = 0.15$ MPa and $T_i = 1.75$ MPa in Eq. 5.3 gives $Q_{fs} = 2 q_{fs} = 4.0$ MPa. Hence, the model predicts $Q_{FS} = 4.0 + 4.9 = 8.9$ MPa, which is in excellent agreement with the measured peak strength.

5.3 TRIAXIAL COMPRESSION BEHAVIOR OF UNFROZEN MFS

5.3.1 Scope of Test Program

Sections 2.3 and 2.4 summarize the experimental procedures used by Swan (1994) to conduct a total of 49 useful triaxial compression tests on MFS specimens prepared by multiple sieve pluviation (i.e., same deposition technique as used for the tests on frozen MFS). Note that this is the first program to evaluate the behavior of unfrozen sand for direct comparison with the behavior of frozen soil. After careful backpressure saturation at a consolidation stress of $\sigma'_c = 0.1$ MPa, the following three types of triaxial compression tests were run:

- 1) isotropic consolidation to varying stresses followed by undrained axial loading at constant cell pressure, denoted as CIUC tests;
- 2) anisotropic consolidation ($K_c = \sigma'_{hc} / \sigma'_{vc} = \sigma'_{3c} / \sigma'_{1c}$) to varying stresses followed by undrained axial loading at constant cell pressure, denoted as CAUC tests; and
- 3) isotropic consolidation to varying stresses followed by drained shear at constant $p' = 0.5(\sigma'_1 + \sigma'_3)$, denoted as CIDC tests. These tests were computer controlled to maintain $\Delta\sigma'_3 = -\Delta\sigma'_1$ during shear.

The Series B test program included 24 CIUC tests with D_r ranging from 44 to 104% and $\sigma'_c = 0.1, 2, 5$ and 10 MPa (i.e., same confining pressures as used for frozen MFS sheared at the moderate strain rate and $T = -10^\circ\text{C}$). The Series C test program included 19 CIUC tests, 3 CAUC tests and 13 CIDC tests with D_r varying from 30 to 115% and σ'_c varying from 0.1 to 12.5 MPa. Sheet C6 in Appendix C summarizes typical compression curves for isotropic consolidation up to $\sigma'_c = 10$ MPa. Note that consolidation to this high stress causes secondary compression (drained creep) and often produced relative densities greater than 100% (the minimum void ratio from vibration at low confinement is 0.580).

5.3.2 Stress-Strain-Effective Stress Behavior

Influence of Consolidation Stress

Figures 5.2 and 5.3 illustrate the very significant influence of consolidation stress on the undrained shear behavior of dense MFS (preshear

$D_r \approx 95\%$), as measured in one CAUC and five CIUC tests. For the CIUC tests, one observes that increases in σ'_c cause the following:

- a large increase in the pseudo upper yield stress (first obvious change in the slope of the Q versus ϵ_a curve at roughly 1% axial strain). Sheet C7 shows a linear increase in Q_{uy} with σ'_c .
- a large decrease in the strain required to reach (or nearly reach) the peak undrained strength. However, the magnitude of Q_p remains essentially constant.
- a change from highly dilatant behavior at low stresses (i.e., development of negative excess pore pressures and an effective stress path that climbs up the effective stress failure envelope as in test C-34) to highly contractive behavior at high stresses (i.e., development of positive excess pore pressure and an effective stress path that curves to the left before reaching the effective stress envelope as for tests C-22 and C-25). Note that the CIUC tests used a very high back pressure in order to prevent cavitation in highly dilatant specimens, such as test C-34 which reached $u_e = -2$ MPa.

Figure 5.4 shows that consolidation stress also has a very significant influence on the drained shear behavior of dense MFS. As for undrained shear, increases in σ'_c cause a proportional increase in the initial "stiffness" and a change from dilatant (volumetric expansion) to contractive (volumetric compression) behavior. However, increases in σ'_c also cause a proportional increase in the peak

strength and the strain required to reach Q_p , whereas undrained shear produces the same strength at large strains. Note: although the CIDC tests in Figure 5.4 were run at constant p' , drained shear with increasing axial stress and constant confining pressure (i.e., $\sigma'_3 = \sigma'_c$) will show similar basic trends.

Influence of Relative Density

Figures 5.5 and 5.6 illustrate the influence of relative density on the undrained shear behavior of MFS as measured in CIUC tests having low and moderate consolidation stresses, $\sigma'_c = 0.1$ and 2 MPa, respectively. Sheets C8 and C9 show the corresponding effective stress paths. One observes that increases in D_r have a minor effect on the initial stiffness (i.e., at ϵ_a less than 1%), but produce much higher strengths at large strains. However, the reverse occurs for drained shear as illustrated in Sheet C10, i.e., increasing D_r causes an increase in initial stiffness but has much less effect at large strains.

Implications for Dilatancy-Hardening Model

Section 3.4 showed that changes in sand density (D_r) and confining pressure (σ'_c) did not affect the upper yield stress (Q_{uy}) of frozen MFS, which appears to represent the onset of cracking of the ice matrix and which occurs at less than 1% axial strain. Section 4 showed that sand density and confining pressure have a large effect on the post-upper yield behavior. If the strain-strain behavior of the sand skeleton is similar to that measured for unfrozen MFS, one would expect increases in sand density and confinement to exhibit the following pattern:

Relative Importance of Variable on
Frictional Resistance of Sand Skeleton

Shearing Condition	Variable	Near Q_{uy}	With Increasing Strain
undrained ($\epsilon_v \approx 0$)	increasing D_r	very small	much more significant
	increasing pre-shear σ'_c	extremely large	less significant
drained ($\sigma_c \approx \sigma'_3$)	increasing D_r	small	even less significant
	increasing σ'_c	very large	similar significance

Effective Stress Failure Envelope

Figure 5.7 plots values of q and p' at the maximum obliquity condition (i.e., when $R = \sigma'_1/\sigma'_3$ reaches its maximum value) from the CIUC and CAUC tests run on unfrozen MFS. This condition occurs at about 1% axial strain at low confinement ($\sigma'_c = 0.1$ MPa) and increases to $\epsilon_a \approx 10\%$ at $\sigma'_c = 10$ MPa. Linear regression on these data gives an effective stress friction angle of $\phi' = 34.9^\circ$ that is used in Section 5.5 for application of Ladanyi's dilatancy-hardening model.

5.3.3 Steady State Analysis and Critical Confining Pressure

Application of Ladanyi's model requires determination of the critical confining pressure (σ'_{cr}) in order to define the transition point between cavitating and noncavitating regimes for shearing of frozen sand (e.g., Eq. 5.1). As stated in Section 5.2.1, MIT has defined σ'_{cr} as that consolidation stress for a given preshear density (void ratio) that produces zero excess pore pressure at failure during

undrained triaxial compression. This condition is equivalent to setting Skempton's A parameter equal to zero, i.e., $A_f = (\Delta u - \Delta \sigma_3) / (\Delta \sigma_1 - \Delta \sigma_3) = 0$, where Δu is the measured change in pore pressure at failure. Note: for the MIT CIUC tests, $\Delta \sigma_3 \approx 0$ and $\Delta \sigma_1 \approx \Delta Q$.

Section 5.5 applies Ladanyi's model to frozen MFS for a wide range of densities, which in turn requires determination of the critical confining pressure as a function of void ratio. Since A_f varies with both density and confinement, the analysis used the state parameter ψ proposed by Been and Jefferies (1985), in order to account for the influence of these two variables. As illustrated in Figure 5.8, ψ is defined as the initial (preshear) void ratio of a test specimen minus the void ratio on the steady state line (SSL) at the same effective mean stress. Been and Jefferies (1985) selected the first invariant of the stress tensor to define the effective stress, $I_1 = \sigma'_{oct} = \frac{1}{3}(\sigma'_1 + \sigma'_2 + \sigma'_3)$.

The steady state line (SSL) is defined as the shearing condition representing continued straining at constant void ratio, pore pressure (for undrained shear tests) and shear stress and, hence, at a constant value of I_{ss} . Sheets C1 and C2 tabulate test parameters for CIUC and CAUC tests at or near a steady state condition; Sheet C11 plots the values of e_{ss} and I_{ss} used to define the steady state line for unfrozen MFS. This steady state line is also shown by the dashed line in Figure 5.8. Two points should be emphasized. First, the steady state condition occurs at large strains that often preclude continued straining at exactly constant I_{ss} .

due to limitations of the triaxial test; hence, selection of the steady state condition involved judgment for most of the tests. Second, the tests used to select the steady state points plotted in Sheet C11 had state parameters varying from $\psi = -0.45$ (preshear state far below the SSL and hence highly dilatant behavior) to $\psi = +0.09$ (preshear state above the SSL and hence contractive behavior). Hence, in spite of potential errors in selecting steady state points, the selected SSL should be reasonably accurate. For example, Sheet C12 shows a very consistent relationship between the peak undrained shear strength ratio and ψ for CIUC tests.

Sheets C3 and C4 tabulate various shear parameters (i.e., ϕ' at maximum obliquity, A_f and the peak undrained strength ratio) as a function of the state parameter ψ for 22 CIUC tests, and Figure 5.9 plots A_f versus ψ . This figure shows a well-defined relationship that gives $A_f = 0$ at $\psi = -0.061$. Consequently, the critical confining pressure line for unfrozen MFS is located below the SSL by a difference in void ratio equal to $\Delta e = -0.061$, as shown by the solid line in Figure 5.8. This relationship predicts $\sigma'_{cr} = 0.27$ and 2.52 MPa at $D_r = 20$ and 95% , respectively.

5.4 RESULTS FROM CONSOLIDATE-FREEZE TESTS ON MFS

5.4.1 Objectives and Scope

Figure 5.2 showed that increases in the preshear consolidation stress (σ'_c) cause an enormous increase in the initial stiffness (initial slope of the Q versus ϵ_a curve) of consolidated-undrained triaxial compression tests run on unfrozen dense MFS. Consequently, one could expect that the magnitude of the effective

stress acting on the sand skeleton prior to (and during) freezing could affect the strength-deformation behavior of frozen sand.

A review of the literature in Section 3.6 of Andersen *et al.* (1992) and in Section 2.3.4 of Swan (1994) indicates that no tests have been run to compare the behavior of frozen sand measured in conventional triaxial compression tests with that measured in tests wherein the soil was frozen **after** application of confinement. However, the results in Figure 5.10 suggest that the magnitude of the pre-freezing effective stress can be an important variable. The figure compares stress-strain behavior from two conventional tests run on frozen dense MFS in which one specimen (No. 55) was prepared by **multiple-sieve pluviation**, and the second specimen (No. 26) was prepared by **wet tamping**. The second specimen exhibits a much higher rate of post-upper yield strain hardening, a smaller strain at the peak strength, a higher rate of post-peak strain softening, and a more rapid development of dilation. (Note: similar comparisons at higher confining pressures show similar trends but little change in the peak strength.) One possible explanation for this behavior is that the high compaction effort used to prepare the wet tamped specimen locked in significant effective stresses that were preserved during freezing.

Section 2.4.3 describes the experimental procedures used for the program of ten consolidate-freeze tests run on dense MFS at the moderate strain rate ($\dot{\epsilon} = 3.5 \times 10^{-5}$ /sec) and $T = -10^{\circ}\text{C}$. This preliminary program had three objectives:

- 1) to develop an experimental technique that produces homogeneous frozen specimens (as accomplished for the conventional tests) after consolidation to stresses ranging from $\sigma'_c = 0.1$ to 10 MPa;

- 2) to produce data for comparison with the results from conventional tests in order to obtain a better understanding of the role of sand skeleton frictional resistance on the strength-deformation behavior of frozen sand; and
- 3) to determine if the magnitude of the pre-freezing effective stress is an important variable when applying Ladanyi's dilatancy-hardening model to predict the strength of frozen sands.

5.4.2 Experimental Results and Comparison with Conventional Frozen Tests

Consolidation and Freezing

Sheets D1 and D4 summarize data measured during the consolidation phase of the consolidate-freeze (CF) tests, which resulted in pre-freezing relative densities of $D_r = 93.5 \pm 6.3\%$ SD. Note that volumes changes in three of the tests (CF 06, 07 and 09) were estimated due to leakage of cell fluid into the internal drainage line that provided drainage from the top cap (see sheet D5).

As described in Section 2.4.3, freezing was accomplished by circulating ethylene glycol through a redesigned base pedestal (Sheet D5), while monitoring the temperature in the cell fluid at three locations next to the specimen and the volume of water flow from the internal drainage line connected to the top cap. Sheet D6 plots results during freezing of Test CF02, and Sheet D2 summarizes data for all ten tests. Sheets D2 and D7 show that the measured outflow of water during freezing was always less than the calculated change in volume due to expansion of the pore water as it turns into ice (based on a 9% volume increase), resulting in "efficiencies" (ratio of measured to calculated volumes) ranging from 87% to only 20%. This discrepancy is problematic, since an efficiency of 50% corresponds to an overall

volumetric expansion of the specimen of about 1.7%. Although the assumption of a 9% pore water expansion during freezing may be too high, this aspect of the freezing technique requires further study.

Small Strain Results

Sheet D3 tabulates values of Young's modulus (E) and yield offset stress (Q_{y0}) from six of the ten tests; Sheet D8 compares these values with data from conventional tests. Although the mean E from the CF tests is about 10% lower, the overall agreement is considered acceptable, since Section 3 concluded that E and Q_{y0} should not be affected by the frictional resistance of the sand skeleton.

The upper yield region represents one of the most unexpected aspects of the consolidate-freeze tests, because only two of the ten tests exhibited a distinct yield point, i.e., a plateau in the slope of the Q versus ϵ_a curves. Sheet D3 shows values of Q_{uy} of 8.6 and 7.7 MPa for CF01 and 03 with $\sigma'_c = 0.27$ and 0.17 MPa, respectively, which agrees with the $Q_{uy} = 8.3 \pm 0.6$ MPa for all conventional tests sheared at the same strain rate and temperatures. The lack of a distinguishable upper yield point in the CF tests consolidated to higher stresses is illustrated in Figure 5.11, which compares $Q - \epsilon_a$ curves for the two types of tests at varying confining pressures. The conventional (numbered FRS) tests all show either a slightly increasing or a constant slope after yielding, whereas the CF tests with $\sigma'_c \geq 2$ MPa show a continuous decrease in the slope of the stress-strain curve. The higher stress CF tests also exhibit a much stiffer response beyond a few tenths percent axial strain. This suggests that the frictional resistance of the sand skeleton

becomes significant within the small strain region (i.e., before yielding occurs for conventional tests) for specimens consolidated to very high stresses prior to freezing. The shapes of the stress-strain curves from CIUC tests on unfrozen MFS in Figure 5.2 support this hypothesis.

Large Strain Results

Sheet D9 plots the $Q - \epsilon_v - \epsilon_a$ response of all ten consolidate-freeze tests; Figure 5.12 compares the "best quality" CF test at each confining stress with corresponding data from conventional tests. Comparison of the two data sets, along with that for unfrozen sand, leads to the following observations:

- Increasing confinement in the conventional tests causes a change from curve Type C to curve Type D, whereas all CF tests have Type C curves. CF tests with $\sigma'_c \leq 5$ MPa also have similar rates of post-peak strain softening, whereas $\sigma'_c = 10$ MPa seems to produce somewhat less strain softening (also see Sheet D9). It is interesting to note that the rate of strain hardening ($dQ/d\epsilon_a$) during undrained shear of unfrozen sand is also very similar for values of $\sigma'_c \leq 5$ MPa, as shown in Figure 5.2.
- Increasing confinement causes similar increases in peak strength up to 5 MPa for both types of testing (also see Sheet D10), in spite of very different values of the axial strain at failure. However, further confinement increases Q_p for the conventional tests, but not for the CF tests.

The volumetric strain (ϵ_v) data from the consolidate-freeze tests are disappointing, due to the lack of results at high strains caused, in part, by the poor to

very poor stabilities exhibited by nearly all of the tests (see Sheet D3). However, the available results do show a decrease in the amount of dilation with increasing confinement, as should be expected (Figure 5.12 and Sheet D9). In addition, the CF tests may cause a slight increase in the amount of dilation relative to conventional tests.

5.4.3 Summary and Discussion

The consolidate-freeze (CF) test program presents the first known attempt to measure the influence on frozen sand behavior of the magnitude of the effective stresses acting on the sand skeleton prior to (and during) freezing. On the other hand, the results from the program have definite limitations, due to possible expansion of the sand specimens during freezing (hence, the possibility of non-uniform, ice-rich samples), the lack of data at very large strains and generally poor to very poor large strain specimen stability, and restriction to testing at one strain rate and temperature. With these limitations in mind, increases in the pre-freezing effective stress level from $\sigma'_c \approx 0.2$ to 2, 5 and 10 MPa appear to cause the following behavior trends, compared to conventional tests with similar levels of confinement run on specimens prepared by multiple sieve pluviation (and, hence, having essentially zero effective stress during freezing and also prior to shear independent of the confining pressure):

- no change in stress-strain behavior at very small strains, i.e., constant values of Young's modulus (E) and yield offset stress (Q_{y0}) (Sheet D8), as should be expected;

- perhaps a slight increase in the amount of dilation (Figure 5.12);
- a disappearance of the upper yield point (except for the two CF tests with $\sigma'_c < 0.3$ MPa), which is thought to present the onset of significant cracking of the pore ice matrix from detailed analysis of data from conventional tests on frozen MFS (and from the literature);
- substantial increases in the stiffness within the upper yield region (Figure 5.11), which apparently reflects contributions from the frictional resistance of the sand skeleton based on the measured undrained shear behavior of unfrozen sand (e.g., Figure 5.2); and
- the same increase in peak strength (Q_p) up to 5 MPa, but with very different strains to failure and post-peak rates of strain softening (Figure 5.12 and Sheet D10).

In retrospect, the CF test program should have included more testing at consolidation stresses less than 2 MPa, in order to better define the disappearance of the upper yield point and the presumed influence of sand skeleton frictional resistance within the upper yield region.

The consolidate-freeze test program was expected to affect frozen sand behavior to a much greater extent than observed from comparisons of conventional tests run on specimens prepared by multiple sieve pluviation (MSP) versus wet tamping (WT), wherein the latter preparation technique presumably causes locked-in pre-freezing effective stresses due to compaction (e.g., Figure 5.10). Figure 5.13 compares CF tests run on MSP specimens with conventional tests run on WT specimens of dense MFS having confining stresses of 0.2 ± 0.1 , 2 and 5 MPa. This

comparison suggests that compaction to a dense state produces locked-in stresses of a magnitude equivalent to about 2 MPa. Nevertheless, all compacted specimens exhibited a distinct yield stress with values of Q_{uy} that closely approximated those for conventional tests run on pluviated specimens!

5.5 APPLICATION OF DILATANCY-HARDENING MODEL TO FROZEN MFS

5.5.1 Selection of Model Parameters

From Section 5.2, Ladanyi's dilatancy-hardening model predicts that the peak compressive strength of frozen sand (Q_{FS}) has two components:

$$Q_{FS} = Q_{fs} + Q_i \quad \dots\dots\dots[5.6]$$

where Q_{fs} is the peak compressive strength of the sand skeleton, and Q_i is the peak compressive strength of the ice matrix. In turn, the frictional resistance of the sand skeleton at high confinement leading to the non-cavitation regime is given by

$$Q_{fs} = \sigma'_{cr} (R_f - 1) \dots\dots\dots[5.7a]$$

where σ'_{cr} is the critical confining pressure ($= \sigma'_{3f}$ for zero excess pore pressure at failure for unfrozen sand) and $R_f = (\sigma'_1 / \sigma'_3)_f = (1 + \sin \phi') / (1 - \sin \phi')$. At low confinement leading to cavitation (i.e., for $\sigma_c + T_i < \sigma'_{cr}$ producing tensile failure within the ice matrix), the sand skeleton compressive strength is given by

$$Q_{fs} = (\sigma_c + T_i) (R_f - 1) \dots\dots\dots[5.7b]$$

where $\sigma_c = \sigma_3$ is the applied confining pressure and T_i is the tensile strength of the ice matrix. This relationship assumes that $\sigma'_{3f} = \sigma_c + T_i$ within the sand skeleton at failure of the frozen sand.

Unfrozen Sand Parameters

Figure 5.7 showed the effective stress envelope from consolidated-undrained triaxial compression tests at maximum obliquity for a wide range of sand densities and consolidation stresses, leading to the selection of $\phi' = 34.9^\circ$. This friction angle gives $R_f - 1 = 2.675$. Changing ϕ' by 10% changes the calculated Q_{fs} by about 20%.

Figure 5.8 showed the critical confining pressure line that was obtained by determining the state parameter leading to zero excess pore pressure at failure (i.e., $A_f = 0$ in Figure 5.9). Values of σ'_{cr} were then calculated for each test using

$$\log \sigma'_{cr} \text{ (MPa)} = (0.699 - e)/0.254 \dots \dots \dots [5.8]$$

This relationship and $R_f - 1 = 2.675$ predict the following values of Q_{fs} for the non-cavitating case:

Density	D_r (%)	σ'_{cr} (MPa)	Q_{fs} (MPa)
Loose	35	0.423	1.13
Medium	65	1.035	2.77
Dense	95	2.52	6.74

Note that these values of Q_{fs} apply to all confining pressures, strain rates, and temperatures, as long as σ'_{cr} is less than $\sigma_c + T_i$.

Pore Ice Parameters

Sheets E1 to E3 in Appendix E indicate that the tensile strength of polycrystalline ice exhibits relatively little change with strain rate and temperature over the range of conditions used for the frozen MFS test program, i.e.,

$\dot{\epsilon} = 3 \times 10^{-6}/\text{sec}$ to $5 \times 10^{-4}/\text{sec}$ and $T = -10^\circ\text{C}$ to -25°C . The data in Sheet E3 show

values of T_i typically ranging between about 1.7 and 2.7 MPa. The authors selected $T_i = 2.15$ MPa for analysis of frozen MFS. It is emphasized that variations in T_i of ± 0.5 MPa will not affect the predictions, except for dense sand at low confinement where σ'_{cr} may exceed $\sigma_c + T_i$ (i.e., leading to the cavitation regime).

The literature does not provide data on the peak compressive strength (Q_i) of polycrystalline ice for the range of confining pressures, strain rates and temperatures used for the frozen MFS test program, which also corresponds to the ductile-to-brittle transition regime for granular ice. Consequently, values of Q_i were predicted as follows:

- From the extensive test program by Jones (1982) at an average temperature of $T \approx -11.5 \pm 1^\circ\text{C}$, interpolate values of Q_i at $\sigma_c = 0$ and 10 MPa for strain rates varying from $\dot{\epsilon} = 10^{-6}/\text{sec}$ to $10^{-2}/\text{sec}$. These values are plotted on Sheet E4 and lead to $n = 5.43$ and 4.26 at low and high confinement, respectively. Note: Sheet E5 indicates that Jones' data at $\sigma_c = 0$ agree reasonably well with results from a variety of unconfined creep and constant strain rate test programs on isotropic polycrystalline ice.
- Use the Arrhenius equation combined with Glen's (1955) power law equation (shown at the top of Sheet E4) to fit Jones' data for an assumed activation energy equal to 68 kJ/mole. This leads to the following relationships:

predicted peak strength, Q_{FS} . Note: linear interpolation was used to obtain values of Q_i for confining pressures between 0.1 and 10 MPa.

Effect of Confinement for Dense Sand

Both conventional and consolidate-freeze tests were run at varying levels of confinement on dense MFS at the moderate strain rate and $T = -10^\circ\text{C}$. Figure 5.14 compares these data with predicted peak strengths. Note that the values of Q_p for the conventional tests were obtained from linear regression on Q_p versus D_r data at each confining pressure. At low confinement ($\sigma_c = \sigma'_c < 0.25$ MPa) there is moderate agreement, since Q_{FS} is only about 15% to 20% less than the mean measured strengths. For the assumed tensile strength of ice ($T_i = 2.15$ MPa), $\sigma_c + T_i$ usually is greater than the critical confining pressure; hence, the non-cavitation Eq. 5.7a usually applies. This leads to $Q_{fs} \approx 6 \pm 1$ MPa, compared to $Q_i \approx 4$ MPa. However, the agreement may be fortuitous, due to severe problems with strain compatibility since the ice matrix presumably reaches its peak strength at around 1% axial strain; the sand skeleton requires over 20% strain based on the unfrozen sand data in Figure 5.2; and the frozen specimens failed at about 6% axial strain.

Figure 5.14 shows that increasing confinement produces a much larger increase in measured peak strengths than predicted by the dilatancy-hardening model, e.g., predicted strengths about two thirds of the measured strengths at 5 MPa confinement. The predicted strengthening occurs solely from increases in Q_i due to added confinement, since Q_{fs} remains constant within the non-cavitation regime.

$$Q_i \text{ (MPa)} = 0.0897 e^{(1507/T)} \dot{\epsilon}^{0.184} \text{ for } \sigma_c = 0 \dots \dots \dots [5.9a]$$

$$Q_i \text{ (MPa)} = 0.0415 e^{(1921/T)} \dot{\epsilon}^{0.235} \text{ for } \sigma_c = 10 \text{ MPa} \dots \dots \dots [5.9b]$$

where T is in degrees Kelvin.

- Use Eq. 5.9 to calculate values of Q_i as a function of $\dot{\epsilon}$ and T at low and high confinements. These values are plotted on Sheet E6, which also plots data from Murrell *et al.* (1989). There is reasonable agreement between predicted and measured ice strengths at $T = -20^\circ\text{C}$ at low and high confinement.

5.5.2 Results of Analyses

The analyses proceeded as follows:

- 1) Determine σ'_{cr} for each conventional frozen and consolidate-freeze MFS test, based on the specimen D_r (void ratio).
- 2) Based on the values of σ'_{cr} , $T_i = 2.15 \text{ MPa}$ and the actual confining pressure ($\sigma_c \approx 0.1$ to 10 MPa), determine if the specimen falls within the non-cavitation or cavitation regimes for computation of Q_{fs} using Eq. 5.7. The non-cavitation case applied for all tests except dense sand ($D_r \geq 90\%$) at $\sigma_c = 0.1 \text{ MPa}$.
- 3) Calculate Q_i for each test using Eq. 5.9 based on the nominal σ_c and T and the actual strain rate; add this value to Q_{fs} to obtain the

Strain compatibility also remains problematic, given the following trends in the axial strain at the peak strength (ϵ_p):

- for the conventional tests, ϵ_p increases to more than 20%, whereas ϵ_p for the CF tests decreases slightly (see Figure 5.12); and
- for unfrozen sand, ϵ_p undergoes a large decrease over the range of $\sigma'_c = 0.1$ to 5 MPa during undrained shear (Figure 5.2).

In any case, it would appear that added confinement causes a much greater contribution from the frictional resistance of the sand skeleton than predicted by the model. Confinement may also produce greater strengthening of the ice matrix than assumed by the authors. However, uncertainty in the tensile strength of ice should not be a factor, except possibly within the region of very low confinement.

Note: Sheet E11 plots predicted and measured peak strengths versus relative density from conventional tests having confining pressures of 0.1, 2, 5, and 10 MPa for the moderate strain rate and $T = -10^\circ\text{C}$. In contrast to dense sand, the relative difference between predicted and measured strengths for loose sand does not increase with increasing levels of confinement. The subsequent text discusses loose versus dense sand comparisons in detail.

Effect of Strain Rate and Temperature for Dense and Loose Sand

Figures 5.15 and 5.16 compare measured and predicted peak strengths as a function of strain rate and temperature for dense MFS at $\sigma'_c = 0.1$ and 10 MPa, respectively. The measured strengths are from actual tests (not from linear regression); hence, they reflect scatter due to variations in the testing conditions

(especially relative density). The predictions are for values of D_r , $\dot{\epsilon}$ and T corresponding to each test. At low confinement, Figure 5.15 shows the following trends:

- At $T = -10^\circ\text{C}$, there is excellent agreement (within 10%) between predicted and measured strengths at the slow strain rate. However, the predictions become less satisfactory with increasing strain rate. This results from the fact that the model predicts much higher values of the power law coefficient (n) than measured and, hence, much less rate sensitivity.
- At $T = -20^\circ\text{C}$, the predicted strengths are much less than measured (about one half) and the model again underestimates the rate sensitivity.
- At $T = -25^\circ\text{C}$, the discrepancy in strengths becomes even worse, but with similar rate sensitivities (but based on only two tests).

Collectively, the model predictions become less satisfactory at higher strain rates and at lower temperatures.

For dense MFS at high confinement, the results in Figure 5.16 at $T = -10$ and -15°C show the following trends:

- The predicted strengths are again too low and also become less satisfactory at the lower temperature.
- However, increases in the strain rate now improve the predictions, which is opposite to the results at low confinement.

Figures 5.17 and 5.18 provide similar comparisons for loose MFS at low and high confinement, respectively; they show the following trends:

- At $\sigma_c = 0.1$ MPa, the predicted strengths are much too low and again become less satisfactory at the lower temperatures, but with little influence of strain rate (i.e., similar values of n)
- At $\sigma_c = 10$ MPa, the model greatly overpredicts the rate sensitivity (i.e., values of n that are too low); hence, increases in strain rate lead to better agreement.

It should be emphasized that the predicted contribution of the sand skeleton friction for loose sand ($D_r \approx 35\%$) is only $Q_{fs} \approx 1$ MPa at both levels of confinement (since the sand is well within the non-cavitation regime). Hence, the ice matrix strength (Q_i) dominates the predicted values of Q_{FS} .

5.5.3 Collective Comparison and Revised Model Predictions

Ratio of Predicted to Measured Peak Strengths, Q_{FS}/Q_p

Sheet E8 in Appendix E plots Q_{FS}/Q_p versus temperature for dense ($D_r \approx 95\%$) and loose ($D_r \approx 35\%$) MFS. Q_{FS} equals $Q_{fs} + Q_i$ from Ladanyi's model, and Q_p is the peak strength from conventional frozen tests. The Q_{FS}/Q_p ratios were scaled from Figures 5.15 to 5.18 at the slow, moderate and fast strain rates. For dense frozen MFS, the Q_p values range between about 10 and 25 MPa, compared to a predicted Q_{fs} of about 6 ± 1 MPa, and Q_{FS}/Q_p decreases from roughly 0.7 ± 0.1 at $T = -10^\circ\text{C}$ down to 0.5 at $T = -25^\circ\text{C}$. For loose frozen MFS, the Q_p values range between about 7 and 30 MPa, compared to a predicted Q_{fs} of only about 1.0 to 1.5

MPa, and Q_{fs}/Q_p decreases from roughly 0.6 ± 1 at $T = -10^\circ\text{C}$ down to 0.45 ± 0.1 at $T = -25^\circ\text{C}$. These results will be discussed further after evaluating the Q_i (ice matrix strength) component of the model predictions.

Ratio of Predicted Ice Strength to Measured Upper Yield Stress, Q_i/Q_{uy}

As demonstrated in Section 3.4, the upper yield stress (Q_{uy}) of frozen MFS occurs at low strains ($\epsilon_a \approx 0.3$ to 1.1%) and is not affected by sand density (D_r) and confining pressure (σ_c). If one assumes zero contribution from sand skeleton friction to Q_{uy} , which appears reasonable for conventional frozen tests (i.e., very low effective stresses from pluviation and no increase due to application of the cell pressure), then Q_{uy} may represent the operational or effective strength of the ice matrix prior to the onset of significant cracking. Assuming that the effective Q_i is equal to the measured upper yield stress, $Q_i(\text{eff}) = Q_{uy}$, how do these values compare with the values of Q_i used for the model predictions? Sheet E9 in Appendix E plots the ratio of the predicted Q_i to the measured Q_{uy} versus temperature as a function of strain rate for zero and high (10 MPa) confinement. One observes the following trends:

- At $\sigma_c \approx 0$, Q_i/Q_{uy} decreases from about 0.5 at $T = -10^\circ\text{C}$ to about 0.3 at $T = -25^\circ\text{C}$ with relatively little effect of strain rate.
- At $\sigma_c = 10$ MPa, Q_i/Q_{uy} decreases from about 0.65 to roughly 0.45 ± 0.1 over the same temperature range. In addition, the ratio is

significantly higher in going from the slow to the fast strain rate at the three lower temperatures.

These trends suggest that data in the literature from tests on polycrystalline ice could significantly underestimate the strength of the ice matrix in frozen sand, and that the error becomes progressively worse with decreasing temperature.

Comparison of Trends in Q_{FS}/Q_p and Q_i/Q_{uy}

The comparison is made separately at low and high levels of confining pressure.

Pressure	Trends in Q_{FS}/Q_p (Sheet E8)	Trends in Q_i/Q_{uy} (Sheet E9)
≤ 0.1 MPa	<ul style="list-style-type: none"> • Large decrease with decreasing temperature • Decreases with increasing strain rate for dense sand; much less pronounced for loose sand 	<ul style="list-style-type: none"> • Same general trend • Similar trend at high T, but reverses at low T
10 MPa	<ul style="list-style-type: none"> • Less pronounced decrease with decreasing T (except for loose sand at fast $\dot{\epsilon}$), compared to above • Increases with increasing strain rate for both dense and loose sand 	<ul style="list-style-type: none"> • Same general trend, but more pronounced (except at fast $\dot{\epsilon}$), compared to above • Same general trend, but more pronounced at lower T

If the effective strength of the ice matrix can be approximated by Q_{uy} , then the above comparison offers a reasonable (but still tentative) hypothesis to help explain the following key aspects of the model predictions:

- the fact that Q_{FS}/Q_p decreases with decreasing temperature, as a general rule, independent of sand density and confining pressure; and

- the fact that Q_{FS}/Q_p increases with increasing strain rate at high confinement for both dense and loose sand (as per Q_i/Q_{uy}), whereas the opposite occurs at low confinement. (Q_i/Q_{uy} also shows the opposite, but only at -10°C .)

Revised Model Predictions

In order to further check the hypothesis that the effective strength of the ice matrix can be approximated by $Q_i(\text{eff.}) = Q_{uy}$, revised model predictions were made using the relationship

$$Q_{FS}^* = Q_{fs} + Q_{uy} \dots \dots \dots [5.10]$$

where Q_{FS}^* denotes the new predicted strength, Q_{fs} is calculated as before, and Q_{uy} replaces Q_i . Values of Q_{fs} were calculated for loose and dense sand, giving 1.15 MPa at $D_r = 35\%$ and 6.75 MPa at $D_r = 95\%$. Note: the latter strength becomes 6.0 MPa at $\sigma_c = 0.1$ for the previously assumed $T_i = 2.15$ MPa, but this difference is ignored, given the scatter in T_i as per Sheet E3. Mean values of Q_{uy} were used at each strain rate and temperature, and values of Q_p were obtained for comparison from linear regression on the measured Q_p versus D_r data for tests having Type C and D curves.

Sheet E10 compares the difference in predicted and measured strengths for the revised model. It plots $Q_{FS}^* - Q_p$ versus temperature for dense and loose MFS at $\sigma_c = 0.1$ and 10 MPa. As a general rule, the predicted Q_{FS}^* is either quite accurate or slightly too high at low confinement; whereas at high confinement, the

predicted strength is too low. For added perspective, refer to Figure 4.6 for measured values of $Q_p - Q_{uy}$ plotted versus relative density. In essence, $Q_{FS}^* - Q_p$ is the same as comparing $Q_{fs} - (Q_p - Q_{uy})$. Hence, errors in $Q_{FS}^* - Q_p$ will approach Q_{fs} as Q_p approaches Q_{uy} .

The following comparisons focus on test conditions with Q_p significantly larger than Q_{uy} , i.e., having "solid" Type C and D curves.

Comparison for Dense MFS at $\sigma_c = 0.1 \text{ MPa}$

- $Q_p - Q_{uy} \approx 4 \text{ MPa}$ for slow and moderate $\dot{\epsilon}$ at all temperatures; $\epsilon_p = 6 \pm 1\%$; fast $\dot{\epsilon}$ produces Type A curves at $T \leq -10^\circ\text{C}$.
- Predicted Q_{FS}^* is too high by about 2.5 MPa, which represents about one third of the predicted $Q_{fs} = 6.75 \text{ MPa}$.
- Commentary: the ϵ_p is much too small to expect full mobilization of the sand friction (compared to undrained shear of unfrozen sand; see figure 5.2), which is consistent with the observed overprediction. However, bulk ice would undergo significant strain softening before reaching ϵ_p (e.g., Figure 4.22). Hence, the overall agreement is better than expected, based on separate evaluation of the behavior of unfrozen sand and bulk ice.

Comparison for Dense MFS at $\sigma_c = 10 \text{ MPa}$

- $Q_p - Q_{uy} \approx 10 \pm 1 \text{ MPa}$ for slow and moderate $\dot{\epsilon}$ at $T \geq -20^\circ\text{C}$, $\epsilon_p \approx 22\%$ at slow $\dot{\epsilon}$, -10°C and decreases to $\approx 10\%$ at higher $\dot{\epsilon}$ and lower T .

- Predicted Q_{FS}^* is too low by slightly over 2 MPa, or about double the predicted $Q_{fs} = 1.15$ MPa.
- Commentary: the ϵ_p level should be sufficient to fully mobilize the sand friction (although no direct comparison can be made to unfrozen loose sand at high confinement). One would expect some weakening of the ice matrix at these large strain levels. Hence, the measured strengths are larger than expected from consideration of the separate behaviors.

5.5.4 Summary and Conclusions

Ladanyi's dilatancy hardening model underpredicts the measured peak strength of frozen Manchester Fine Sand (MFS), as measured in conventional tests on loose and dense sand ($D_r \approx 35$ and 95%) at low and high confinement ($\sigma_c = 0.1$ and 10 MPa), as illustrated in Figures 5.15 to 5.18 and Sheet E8 (Q_{FS} is the strength predicted by his model). The magnitude of the error increases with decreasing temperature (a pervasive trend). For dense sand sheared at the moderate strain rate and $T = -10^\circ\text{C}$, the error also increases with confinement for both conventional and consolidate-freeze tests (Figure 5.14).

The above predictions used values of strength for the ice matrix (Q_i) based on data in the literature from testing polycrystalline ice having very large grain sizes (≥ 1 mm), compared to the size of the pores in MFS. It is hypothesized that the operational or effective peak strength of the ice matrix can be approximated by the measured upper yield stress (Q_{uy}) of frozen MFS, since

- Predicted Q_{FS}^* is too low by 3 ± 1 MPa, which represents about one half of the predicted $Q_{fs} = 6.75$ MPa.
- Commentary: for $\epsilon_p = 20 \pm 5\%$, one might expect near-full mobilization of the sand friction (again see Figure 5.2). However, bulk ice would still undergo some strain softening, in spite of the high confinement (e.g., Figure 4.22 plus Sheet E7). Hence, the large strain interaction of the sand-ice composite produces strengths greater than expected from separate behaviors, even after incorporating a much higher peak strength for the ice matrix.

Comparison for Loose MFS at $\sigma_c = 0.1$ MPa

- $Q_p - Q_{uy} \approx 1$ MPa for slow $\dot{\epsilon}$ at all temperatures and moderate $\dot{\epsilon}$ at -10°C ; $\epsilon_p \approx 6 \pm 2\%$.
- Predicted Q_{FS}^* is in excellent agreement (for slow $\dot{\epsilon}$ tests).
- Commentary: the ϵ_p level is too small to expect full mobilization of the sand friction (compared to undrained shear of unfrozen sand; see Figure 5.5). Moreover, bulk ice would again undergo significant weakening at these ϵ_p levels. Hence, there is better agreement than expected from evaluation of the separate behaviors.

Comparison for Loose MFS at $\sigma_c = 10$ MPa

- $Q_p - Q_{uy} \approx 3.5$ for slow $\dot{\epsilon}$ at $T \geq -20^\circ\text{C}$ and moderate $\dot{\epsilon}$ at -10°C ; $\epsilon_p \approx 25\text{-}20\%$.

- Q_{uy} occurs at strain levels ($\epsilon_a \leq 1\%$) consistent with the peak strength of bulk polycrystalline ice; and
- because Q_{uy} is not affected by sand density and confining pressure (i.e., by factors known to affect the frictional resistance of unfrozen sand), it probably involves very little frictional resistance of the sand skeleton.

If the above hypothesis is true, then Sheet E9 shows that Q_i/Q_{uy} , where $Q_{uy} = Q_i$ (effective), has the following trends:

- Q_i/Q_{uy} decreases substantially with decreasing temperature. The same trend is observed for Q_{FS}/Q_p , where Q_{FS} and Q_p are the model predicted and measured strengths, respectively (see Sheet E8).
- Q_i/Q_{uy} increases with increasing strain rate at high confinement; the same trend is observed for Q_{FS}/Q_p . Note: at low confinement, Q_i/Q_{uy} shows little effect of strain rate, whereas Q_{FS}/Q_p decreases with increasing strain rate.

The authors can readily envision a higher effective strength for the ice matrix than measured from tests on bulk ice due to the higher (effective) strain rate, added deformational constraints, etc., as hypothesized by Ting *et al.* (1983). However, they can not offer any explanation for why Q_i/Q_{uy} should undergo such a large decrease with decreasing temperature.

Revised model predictions were made by replacing Q_i with Q_i (effective) = Q_{uy} , leading to $Q_{FS}^* = Q_{fs} + Q_{uy}$, where Q_{fs} is the predicted sand skeleton friction.

Sheet E10 plots the predicted Q_{FS}^* minus the measured peak strength (Q_p) versus temperature for loose ($D_r = 35\%$) and dense ($D_r = 95\%$) MFS at low and high confinement ($\sigma_c = 0.1$ and 10 MPa) for tests having Type C and D curves (i.e., $Q_p > Q_{uy}$). This comparison generally shows that the predicted Q_{FS}^* is either quite accurate or slightly too high at low confinement, whereas the predicted strength is too low at high confinement (for strain rates and temperatures producing maximum values of $Q_p - Q_{uy}$). After considerations of strain compatibility (e.g., insufficient strains to mobilize the full sand friction (Q_{fs}), but excessive strains that produce weakening of the ice matrix), it is tentatively concluded that the measured strengths are larger than would be expected, based on the separate behaviors of an unfrozen sand skeleton and an enhanced ice matrix strength that follows trends observed for bulk ice.

In spite of the above limitations of the revised model predictions (which use Q_{uy} as a base strength), this model does provide reasonable estimates of the peak strength of frozen MFS over a very wide range of sand densities, confining pressures, strain rates and temperatures. However, larger issues still remain, such as

- an explanation for why the ice matrix in frozen sands appears to be much larger than predicted from tests on bulk ice (if, indeed, the effective Q_i equals Q_{uy}),
- a methodology for predicting Q_{uy} ; and

- a methodology for predicting the absence of sand friction, i.e., when the peak strength (Q_p) approaches the upper yield stress (Q_{uy}).

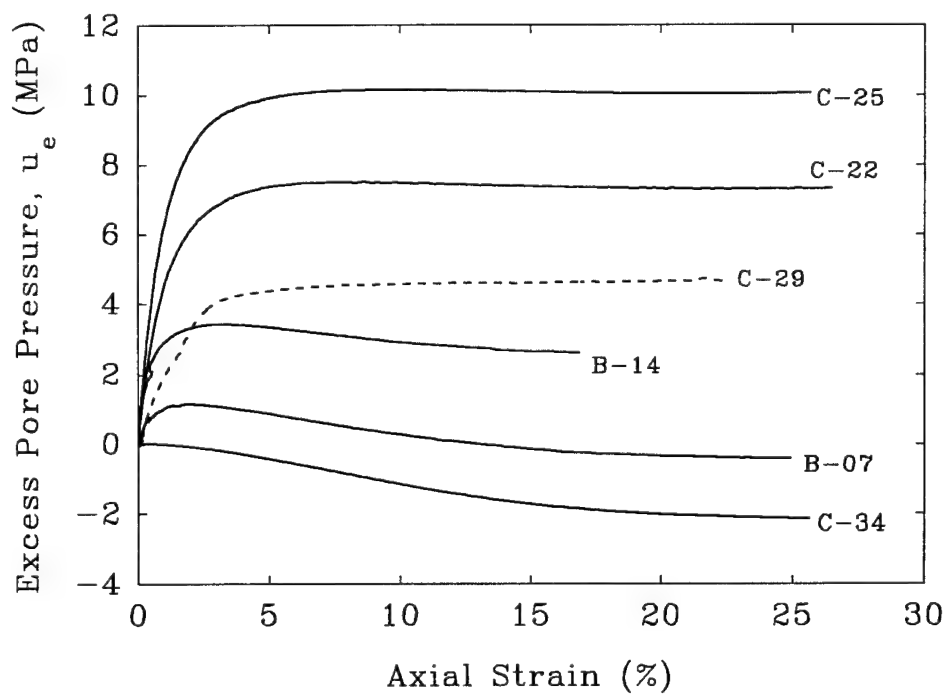
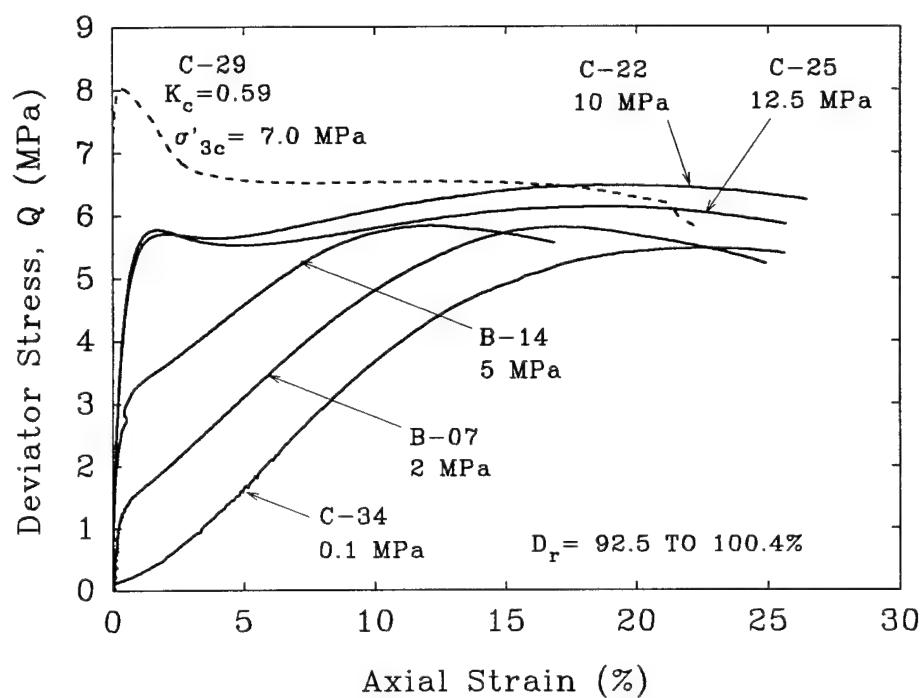


Fig. 5.2 Effect of Consolidation Stress on Undrained Stress-Strain Behavior from CU Triaxial Compression Tests on Unfrozen Dense MFS.

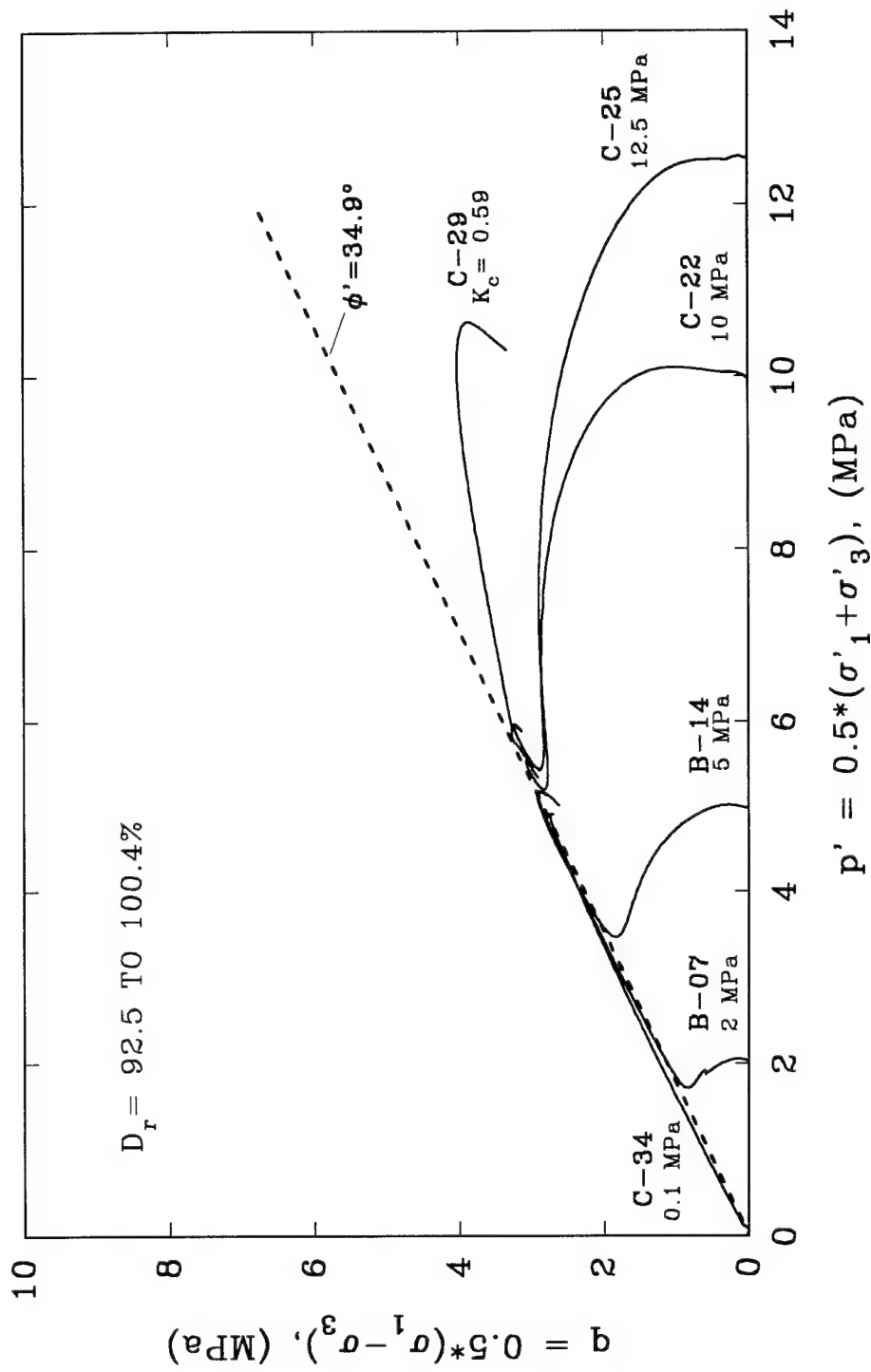


Fig. 5.3 Effect of Consolidation Stress on Effective Stress Paths from CU Triaxial Compression Tests on Unfrozen Dense MFS

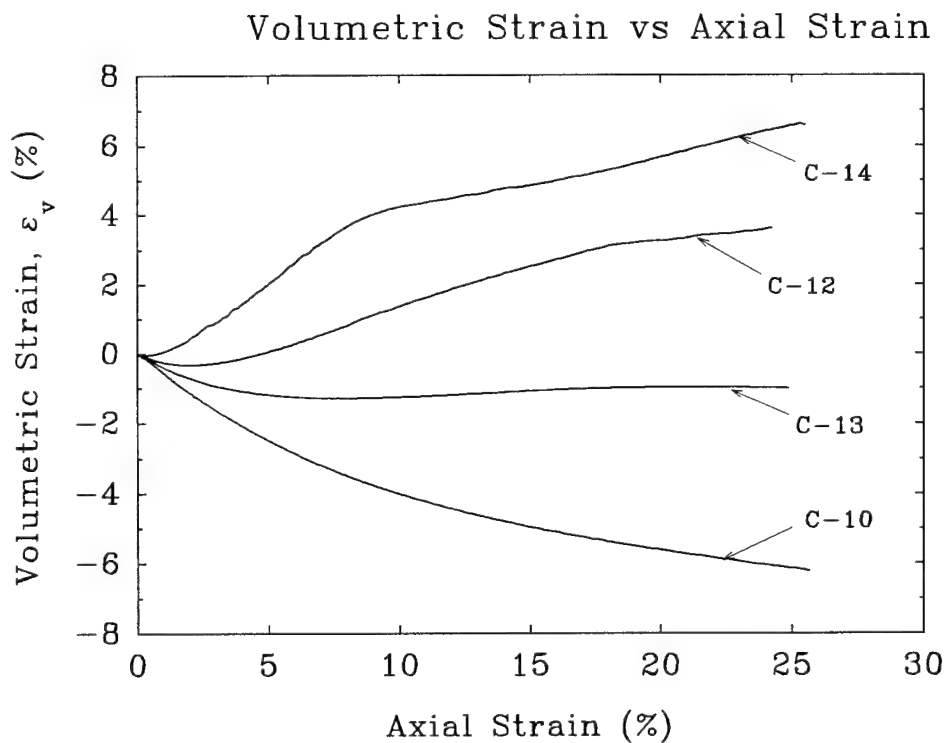
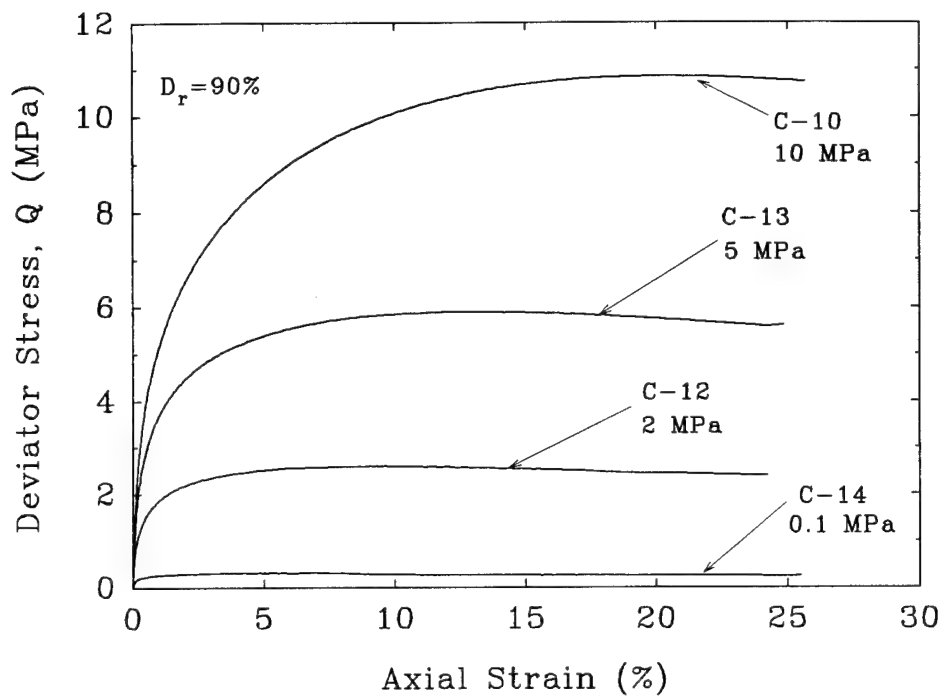


Fig. 5.4 Effect of Consolidation Stress on Drained Stress-Strain and Volumetric Strain Behavior from CD Triaxial Compression Tests on Unfrozen Dense MFS

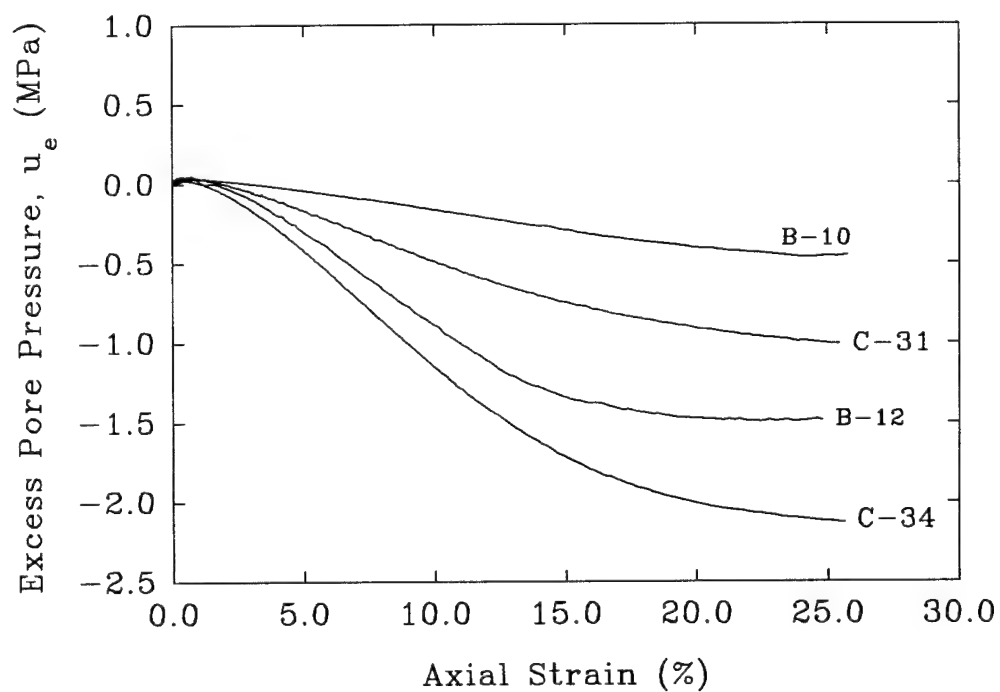
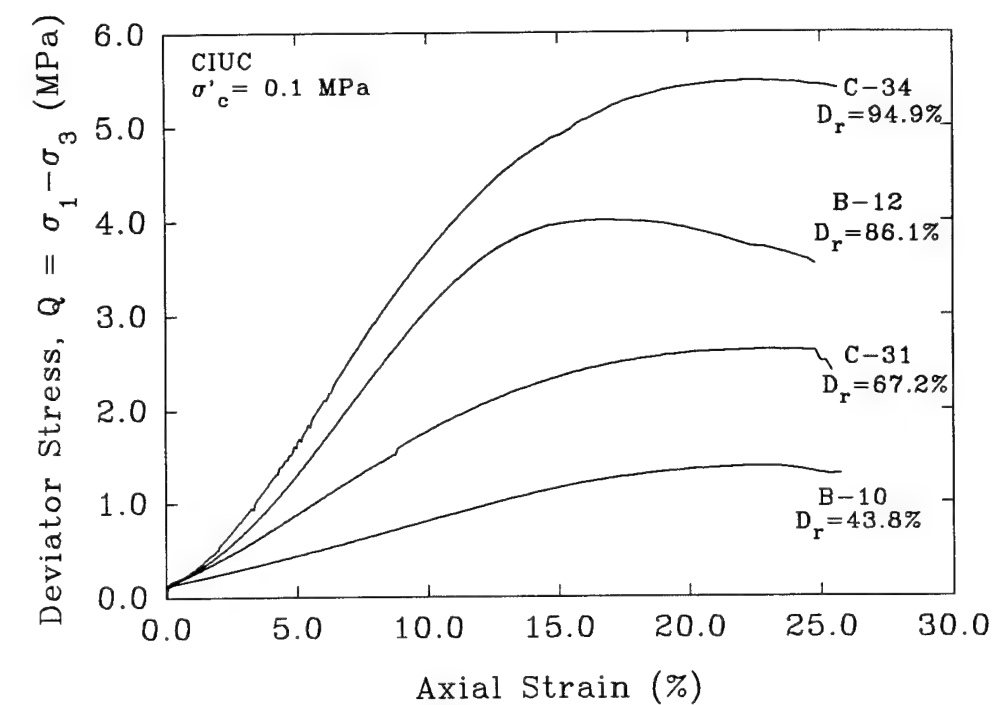


Fig. 5.5 Effect of Relative Density on Undrained Stress-Strain and Pore Pressure Behavior from CU Triaxial Compression Tests at Low Confinement on Unfrozen MFS

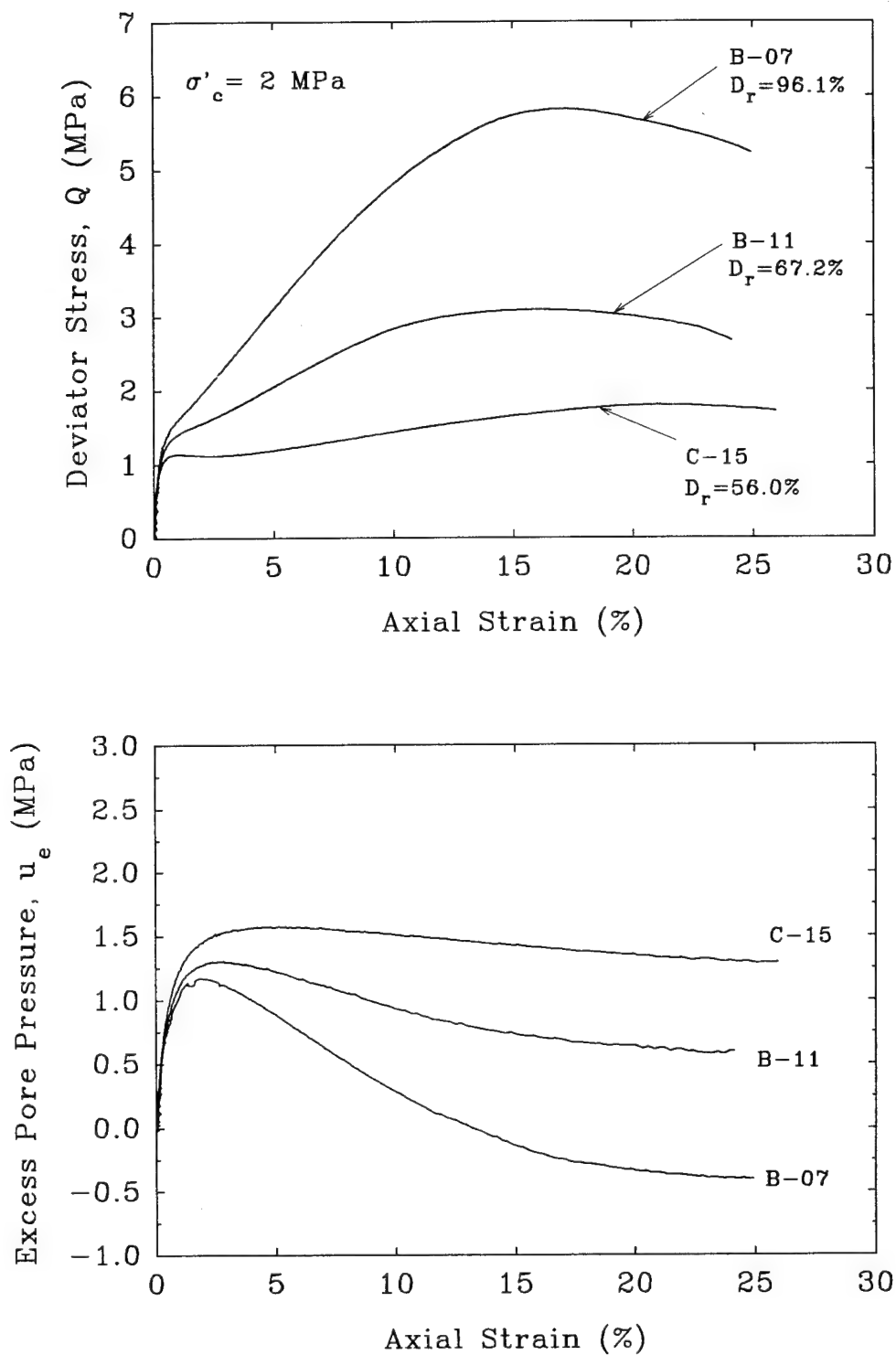


Fig. 5.6 Effect of Relative Density on Undrained Stress-Strain and Pore Pressure Behavior from CU Triaxial Compression Tests at Moderate Confinement on Unfrozen MFS

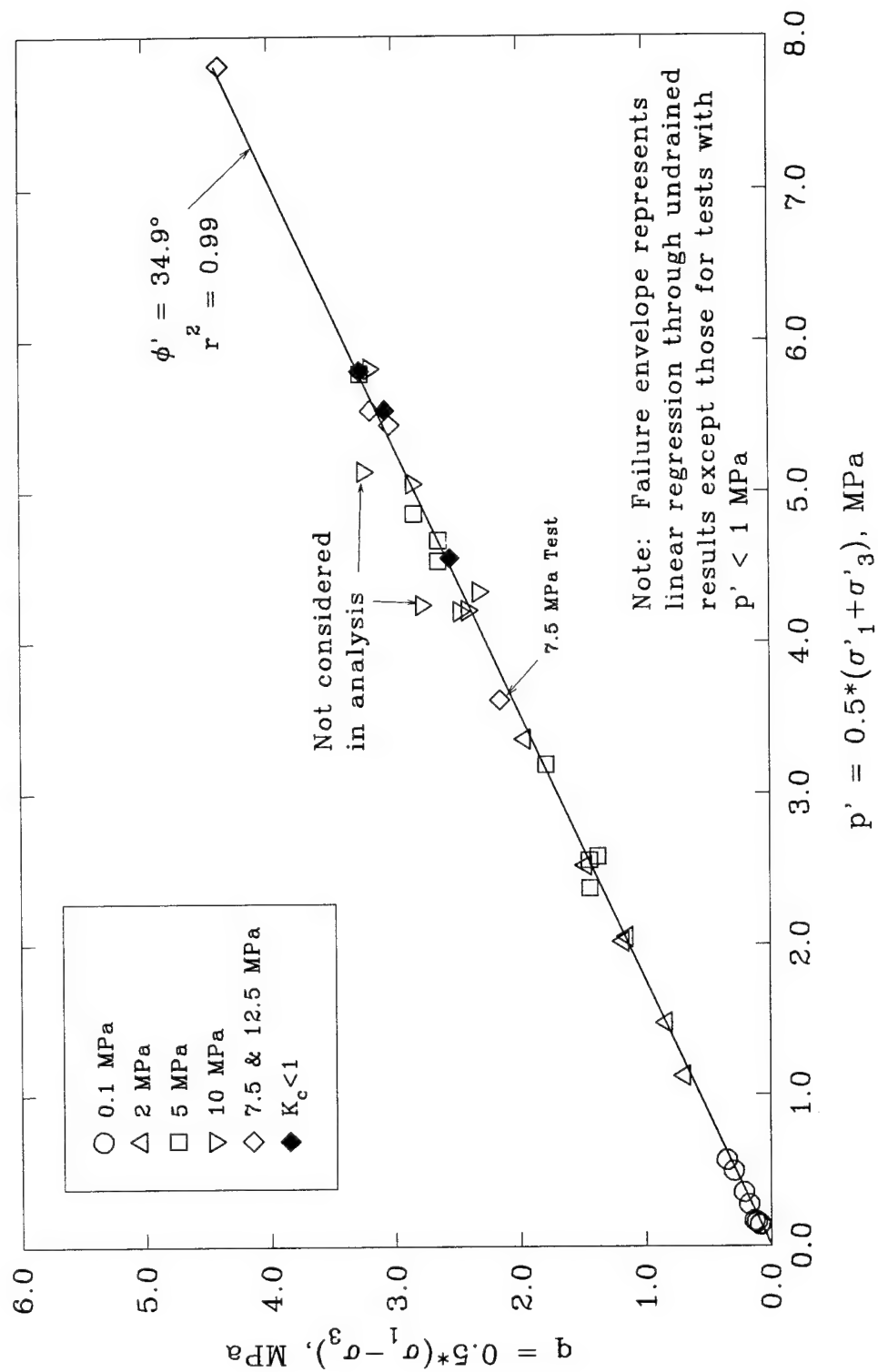
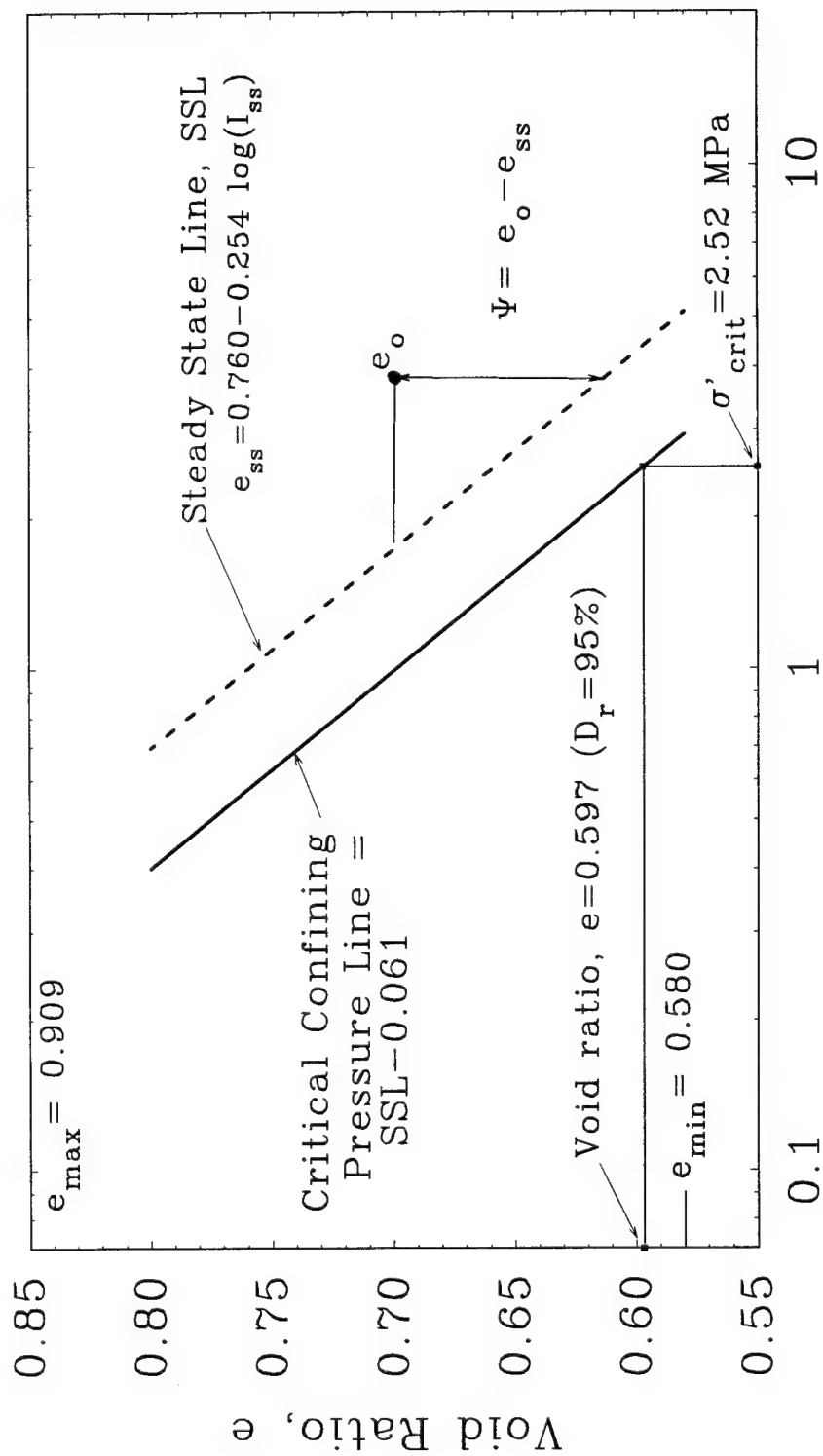


Fig. 5.7 Mobilized Friction Angle at Maximum Obliquity from CU Triaxial Compression Tests on Unfrozen MFS



Mean Effective Stress, I_1 (MPa)

Fig. 5.8 Steady State and Critical Confining Pressure Lines for MFS Based on Steady State Analysis of CIUC Tests

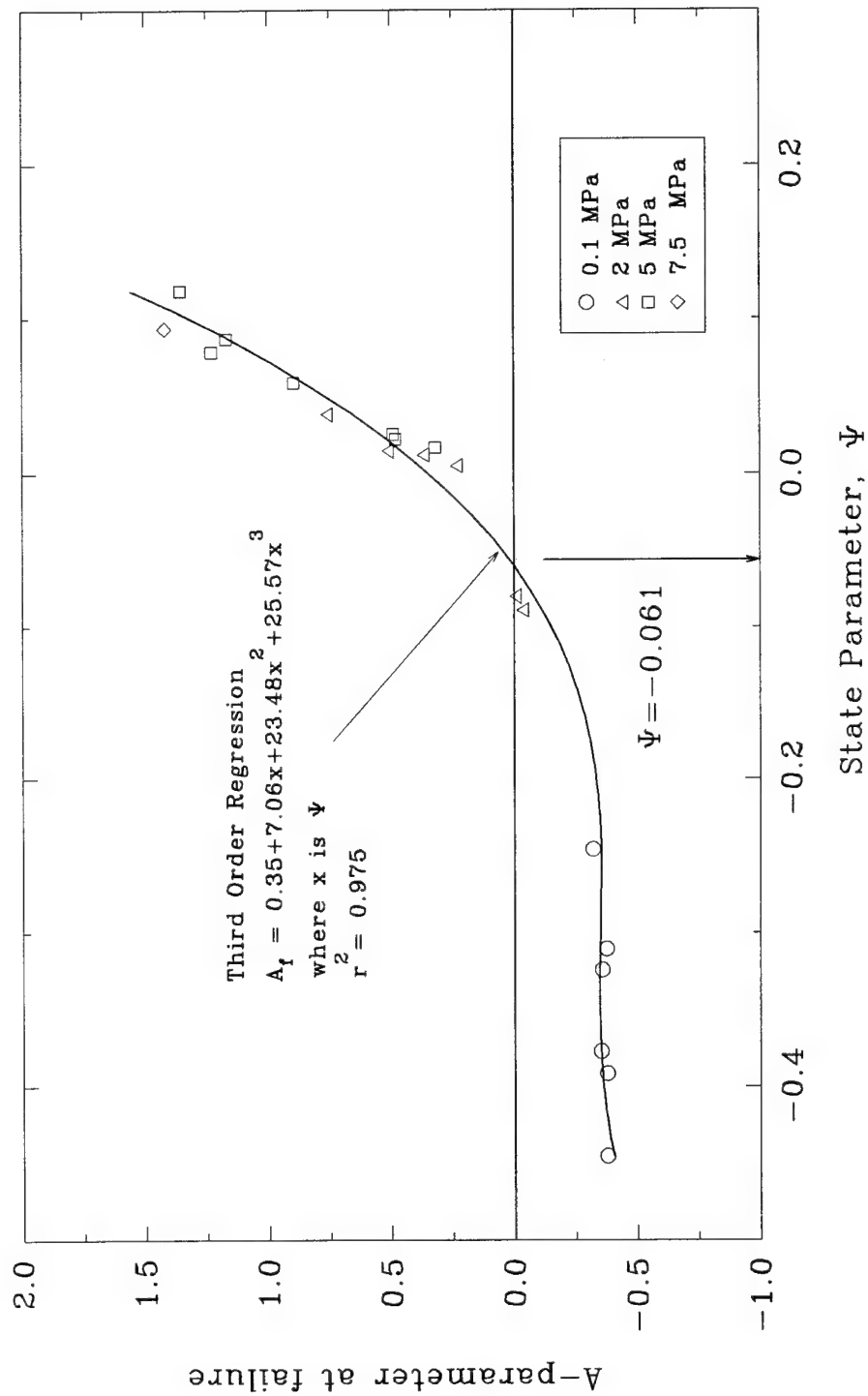


Fig. 5.9 A_f vs State Parameter from CIUC Tests on Unfrozen MFS

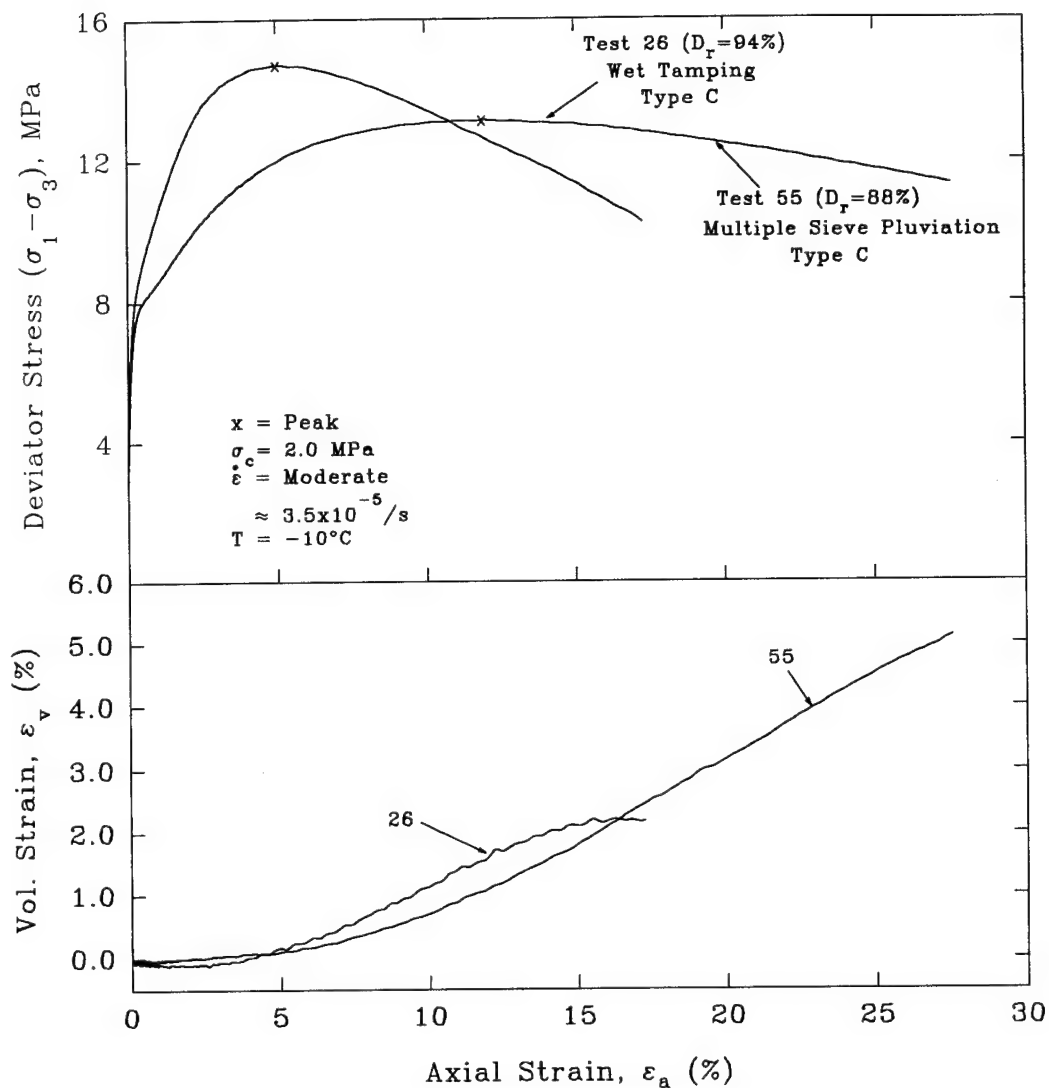


Fig. 5.10 Effect of Specimen Preparation Technique on Stress-Strain Curves from Conventional Tests on Frozen Dense MFS

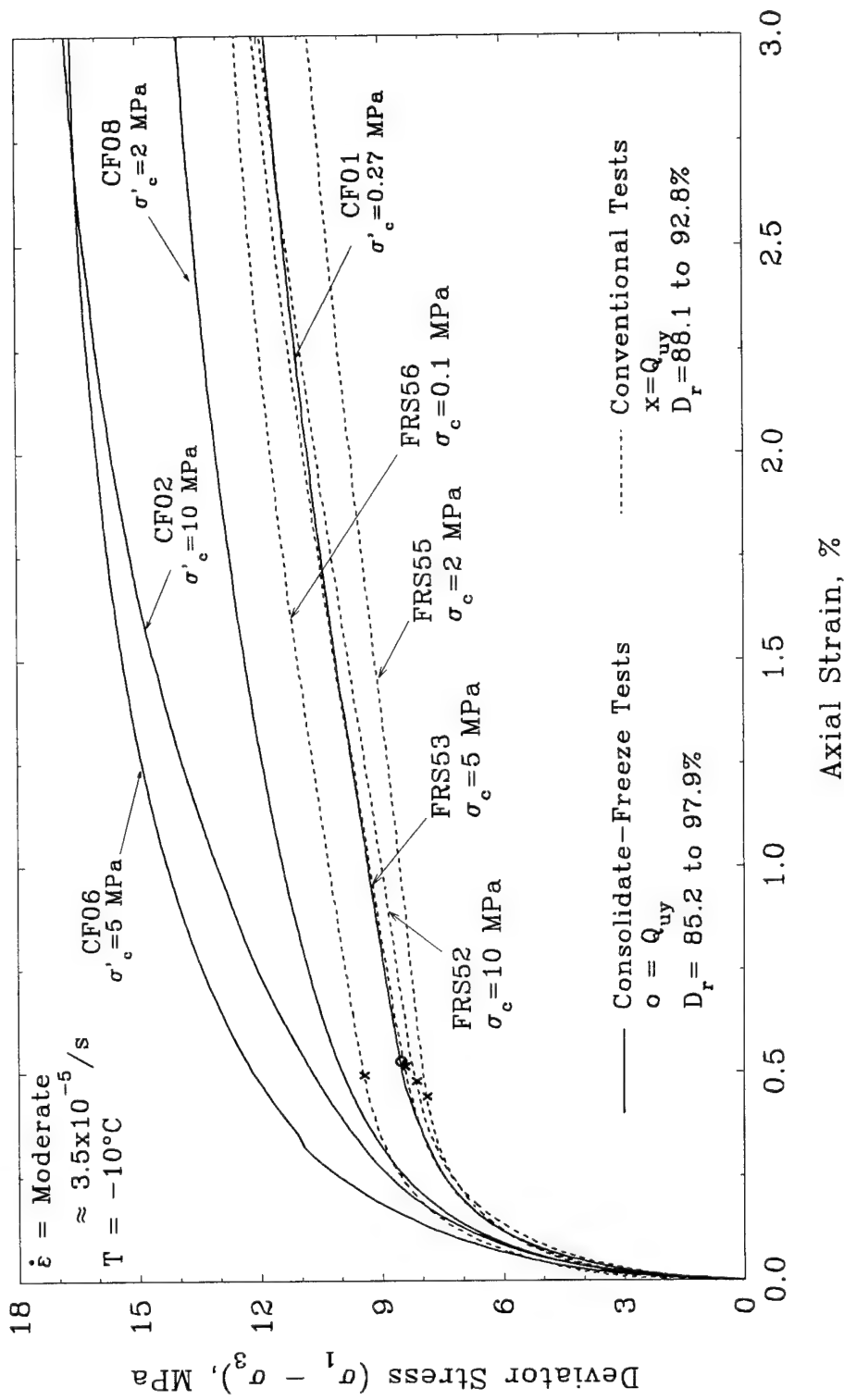


Fig. 5.11 Initial Stress-Strain Curves Showing the Upper Yield Region for Consolidate-Freeze and Conventional Tests on Dense MFS at Moderate Strain Rate and $T = -10^\circ\text{C}$

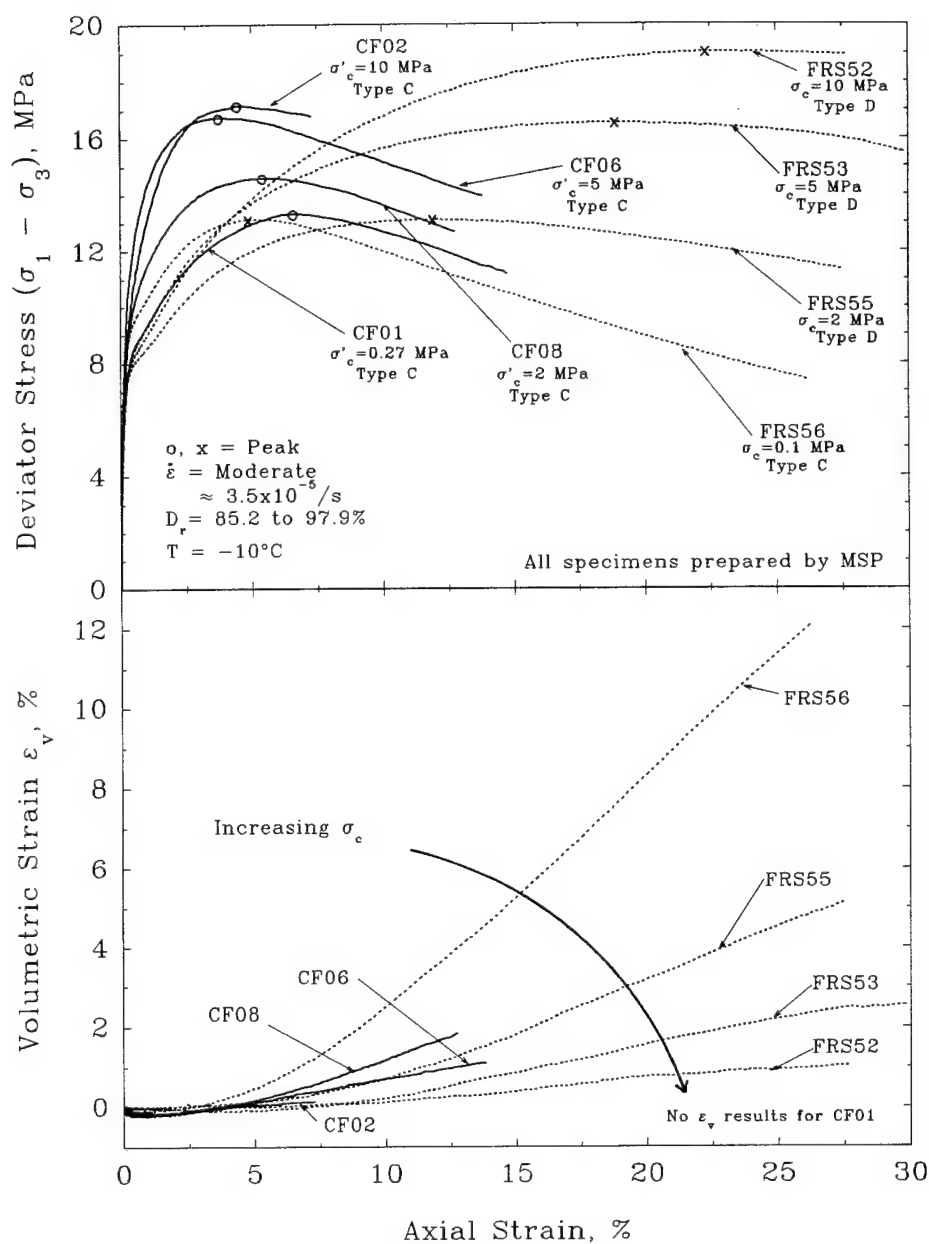


Figure 5.12 Comparison of Stress-Strain Curves for Consolidate-Freeze and Conventional Frozen Tests on Dense MFS at Moderate Strain Rate and $T = -10^\circ\text{C}$

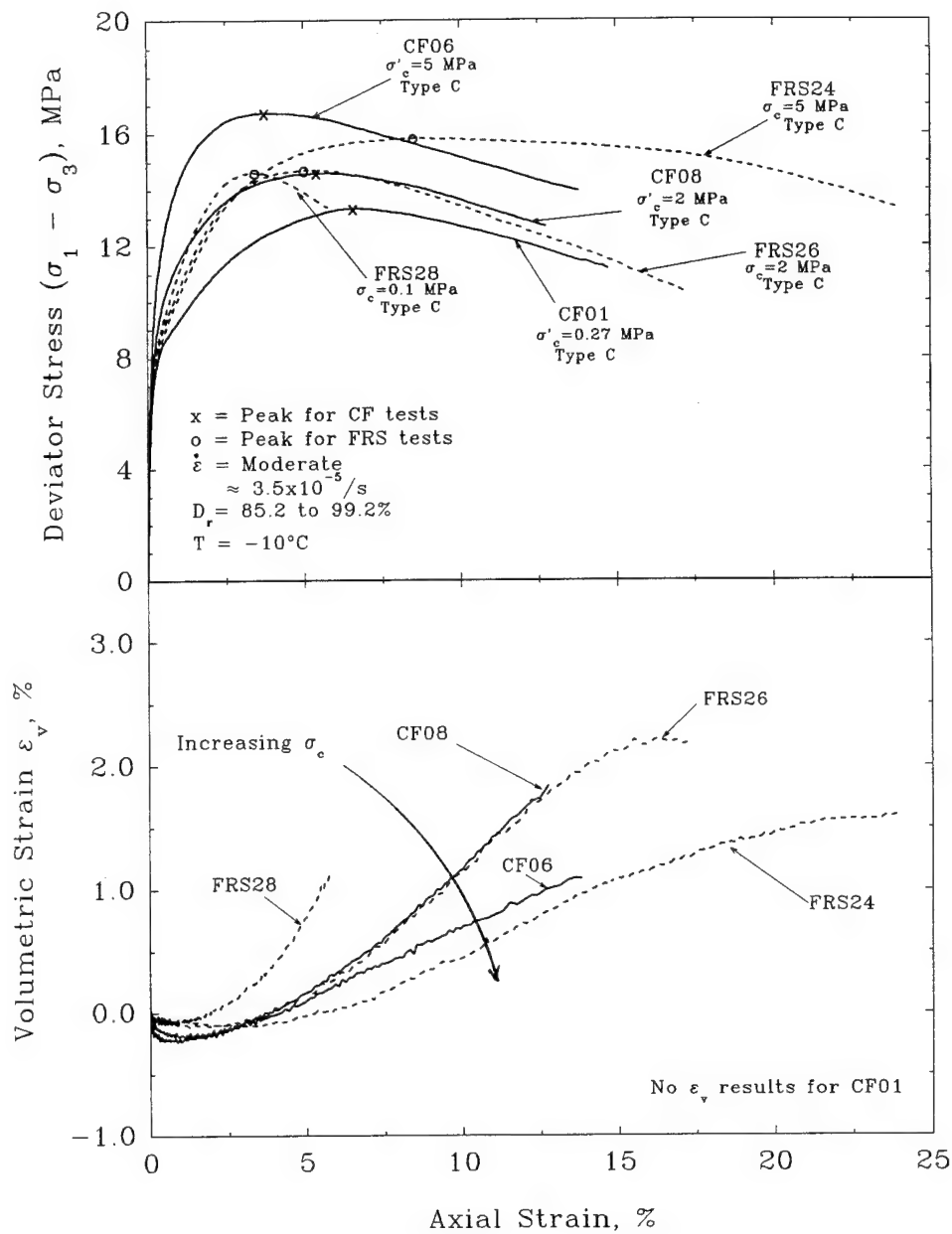


Figure 5.13 Comparison of Stress-Strain Curves for Consolidate-Freeze Tests on MSP Specimens and Conventional Frozen Tests on Wet Tamped Specimens at Moderate Strain Rate and $T = -10^\circ\text{C}$

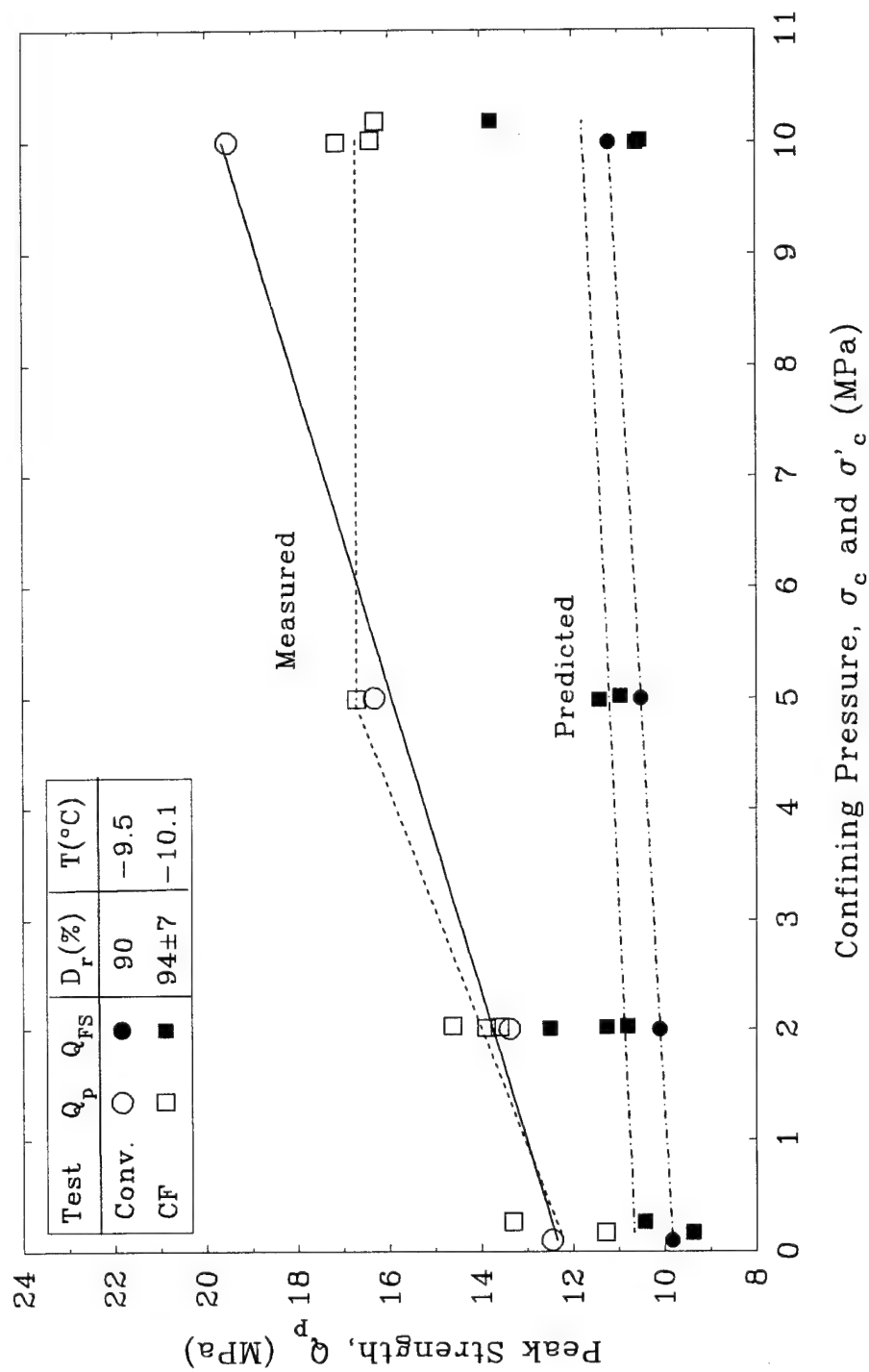


Fig. 5.14 Comparison of Measured vs. Predicted Effect of Confinement on Peak Strength of Conventional and Consolidate-Freeze Tests on Dense MFS at Moderate Strain Rate and $T = -10^\circ\text{C}$

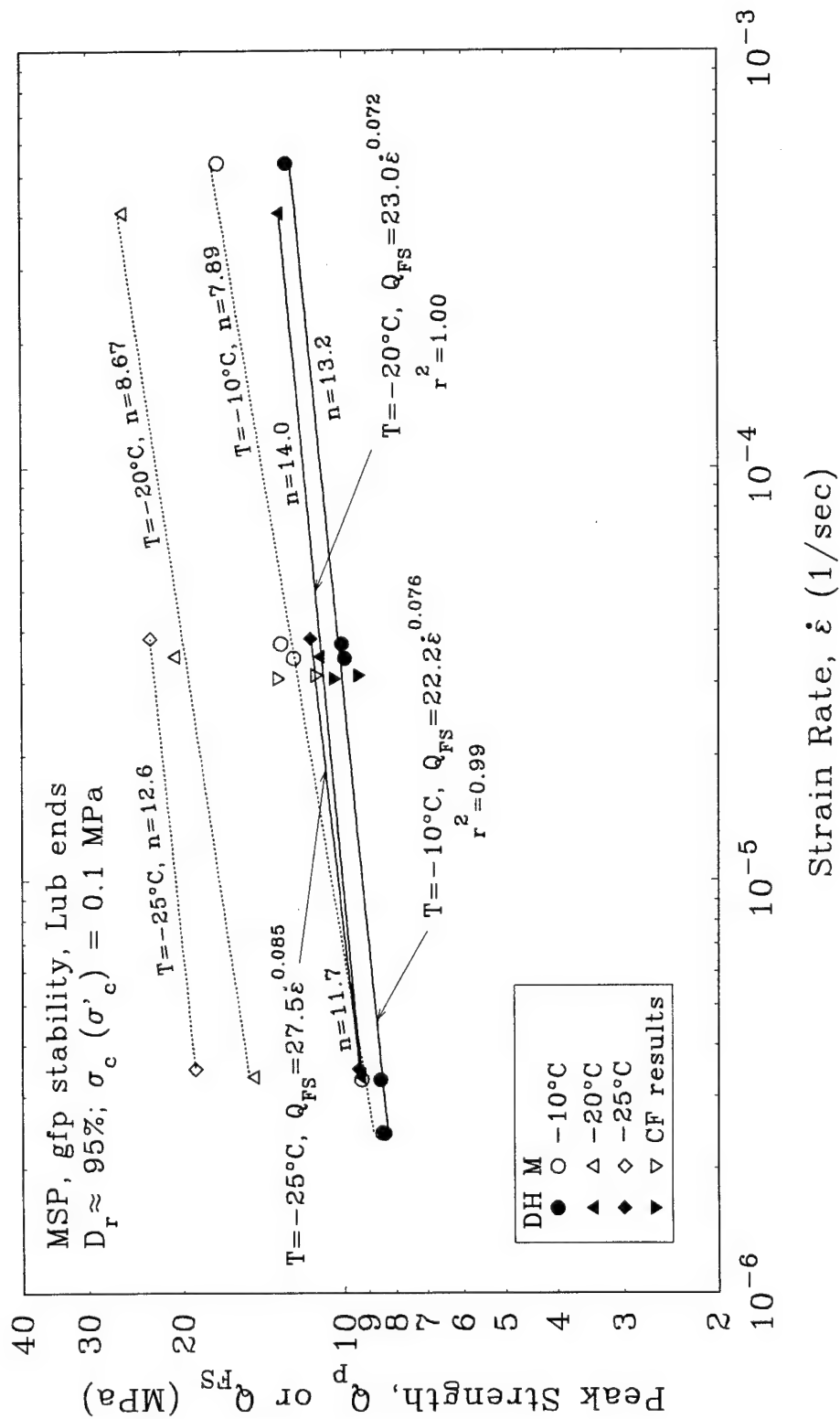


Fig. 5.15 Peak Strength vs Strain Rate Comparing Measured Results from Conventional and Consolidate-Freeze Tests on Dense MFS at Low Confinement with Predicted Results from Dilatancy-Hardening Model

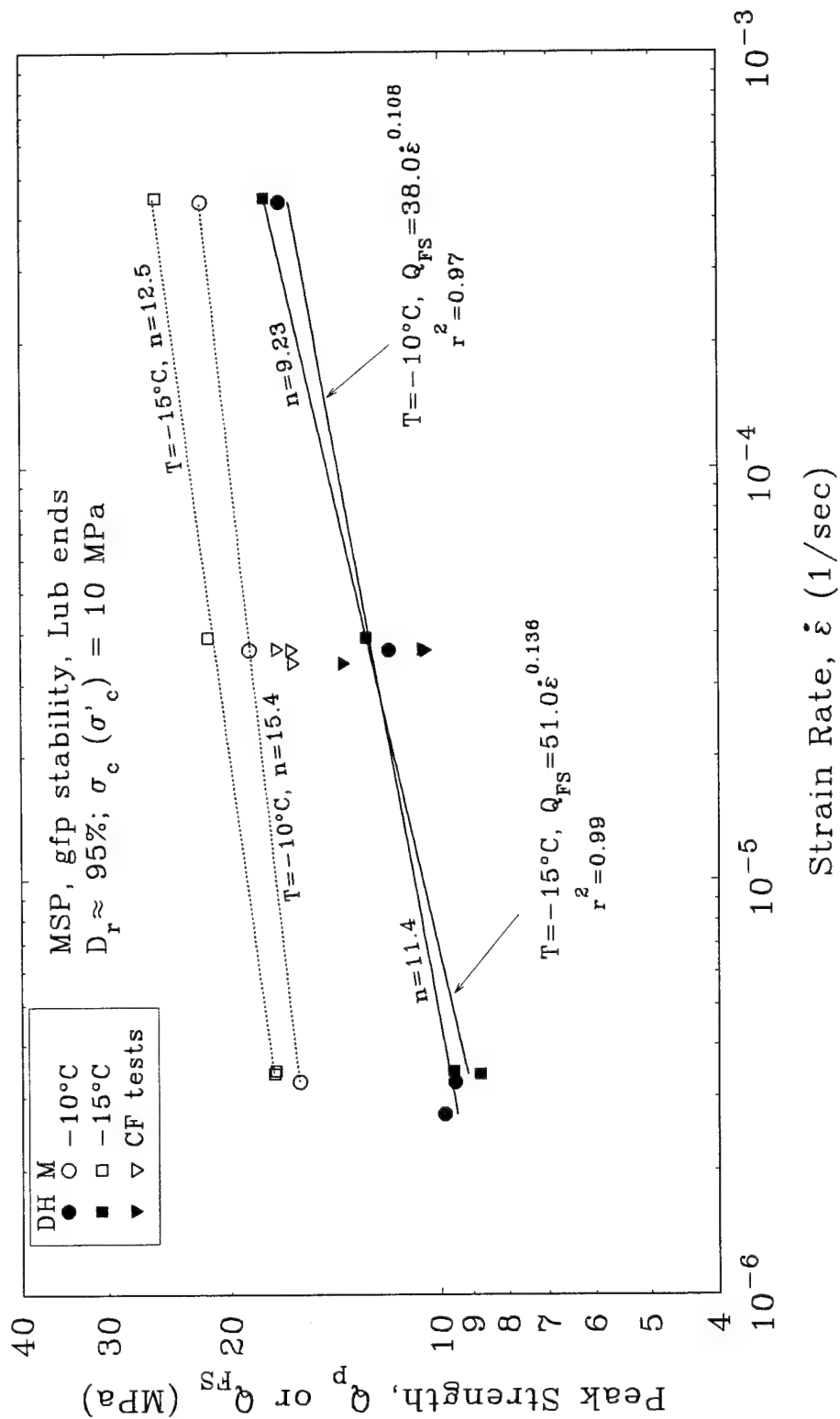


Fig. 5.16 Peak Strength vs Strain Rate Comparing Measured Results from Conventional and Consolidate-Freeze Tests on Dense MFS at High Confinement with Predicted Results from Dilatancy-Hardening Model

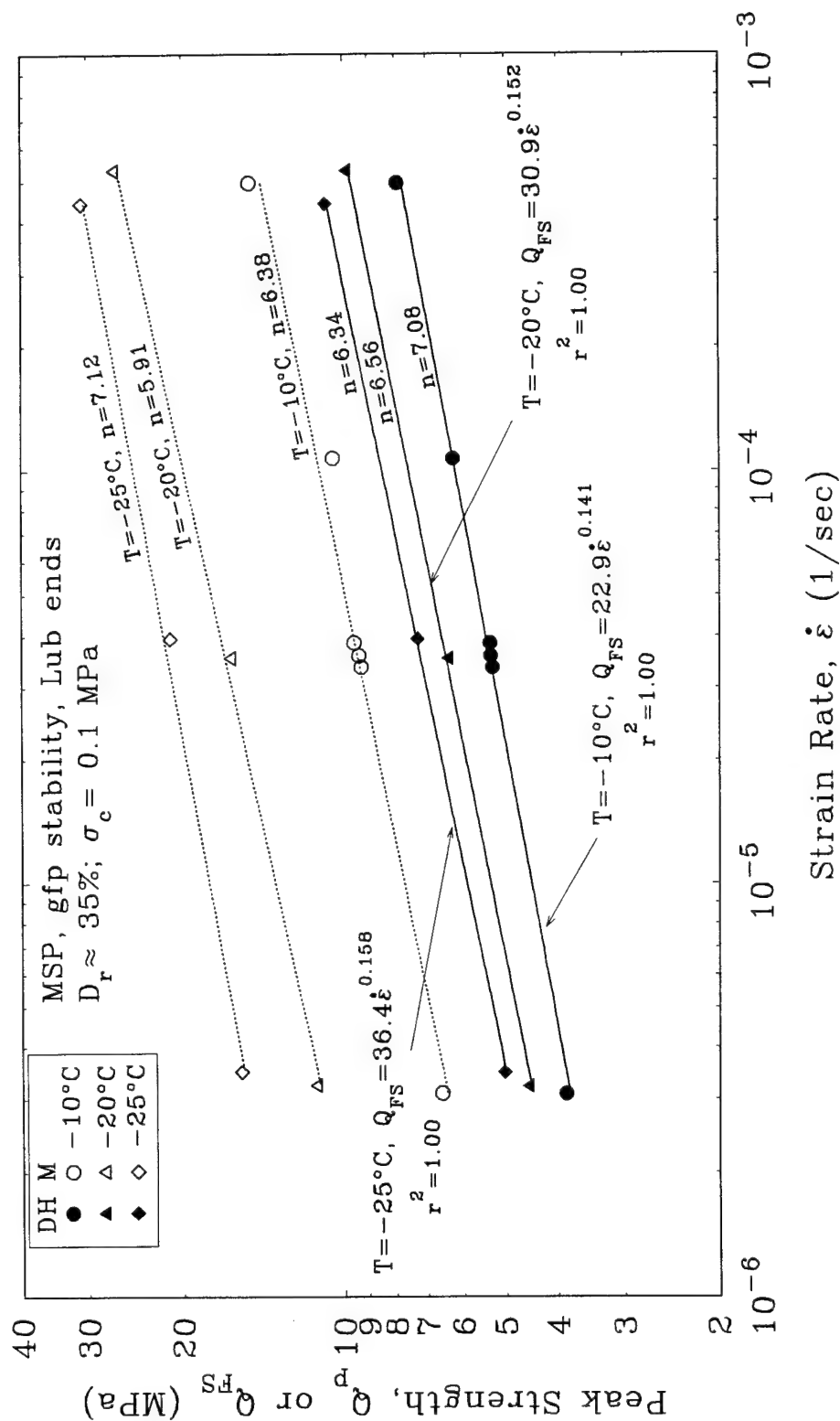


Fig. 5.17 Peak Strength vs Strain Rate Comparing Measured Results from Conventional Frozen Tests on Loose MFS at Low Confinement with Predicted Results from Dilatancy-Hardening Model

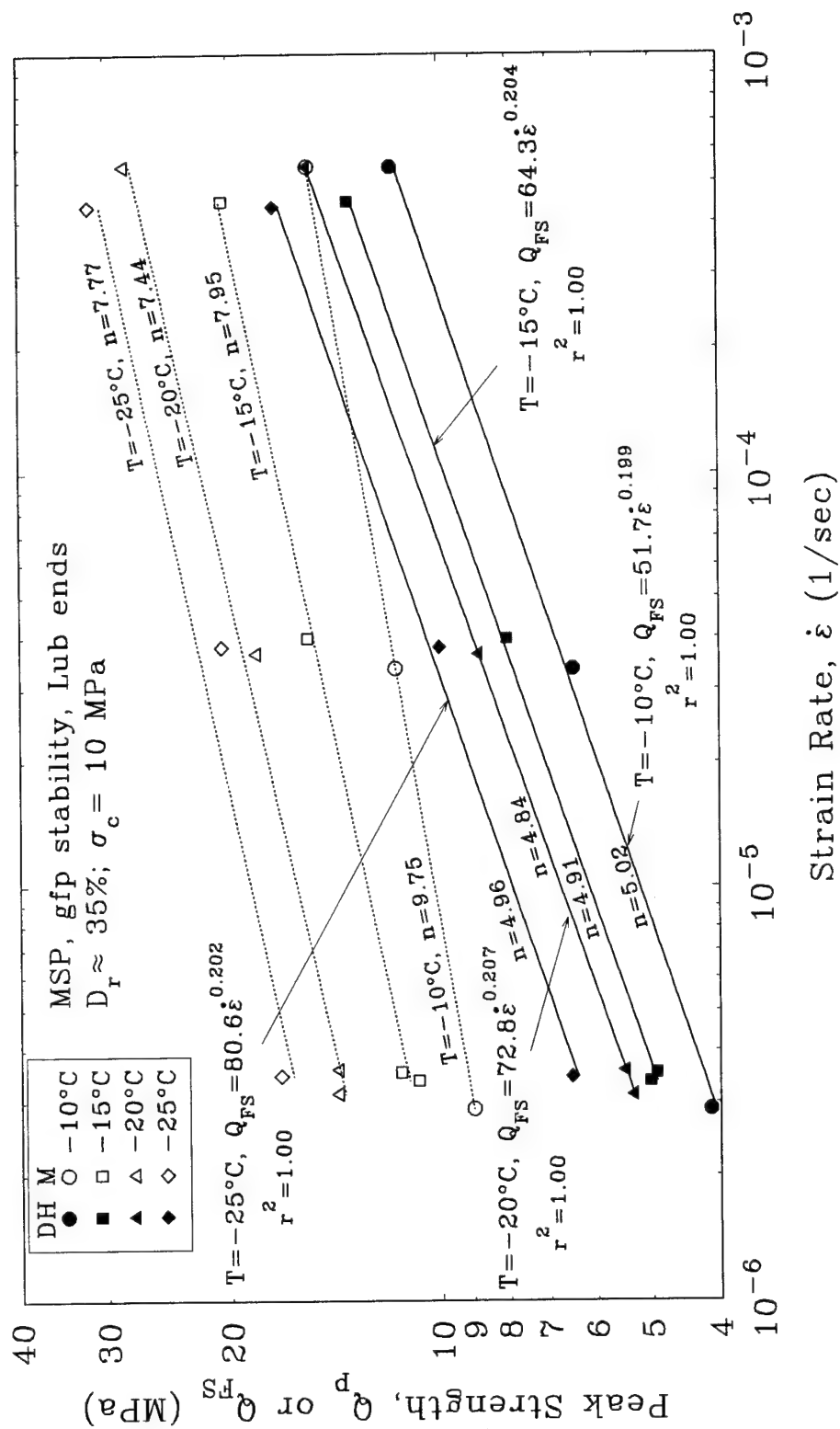


Fig. 5.18 Peak Strength vs Strain Rate Comparing Measured Results from Conventional Frozen Tests on Loose MFS at High Confinement with Predicted Results from Dilatancy-Hardening Model

6. SUMMARY AND CONCLUSIONS

6.1 RESEARCH OBJECTIVES AND SCOPE

Even the simplest form of frozen soil (sand with ice-filled pores) entails a highly complex interaction between the pore matrix (composed of ice and unfrozen water) and the skeleton of sand particles that changes with time as a function of temperature and stress-strain level. Consequently, the development of constitutive relationships to model the stress-strain-time-temperature behavior of frozen sands lags far behind the modeling capabilities of the two principal components, ice and sand. Moreover, progress in modeling first requires a better understanding of the physical mechanisms that control frozen sand behavior. The approach taken by MIT to achieve this latter objective has three components:

- 1) conduct a comprehensive experimental program to precisely measure the behavior of a frozen natural sand over a wide range of testing conditions;
- 2) from a knowledge of the general behavior of polycrystalline ice and of the measured strain-strain behavior of the same sand in an **unfrozen** state, attempt to deduce the relative importance of the
 - ice matrix *per se*
 - frictional resistance of the sand skeleton *per se*, and
 - interaction between the ice matrix and the sand skeleton;
- 3) where possible, employ models for composite materials to quantify the physical mechanisms responsible for the macro-behavior of frozen sands.

Manchester Fine Sand (MFS) was selected for the test material. This river deposit is composed mainly of subangular quartz and feldspar particles having the following characteristics:

- gradation—99% smaller than 0.35 mm, mean diameter = 0.18 mm, and 7% smaller than 0.074 mm (No. 200 sieve).
- density—minimum dry density = 1408 kg/m^3 ($e_{\text{max}} = 0.909$) and maximum dry density = 1701 kg/m^3 ($e_{\text{min}} = 0.580$). The report presents density values in terms of relative density defined as $D_r = (e_{\text{max}} - e) / (e_{\text{max}} - e_{\text{min}})$, where e is the void ratio (volume of voids divided by volume of solids).
- unfrozen water content—less than 0.14% at $T = -9.5^\circ\text{C}$.

All test specimens were prepared by multiple sieve pluviation which gives a very uniform density, in contrast to many prior programs that employed various types of mechanical compaction.

The experimental program consisted of triaxial compression tests performed in a high-pressure triaxial apparatus on three types of specimens: 1) specimens that were frozen in a mold before being placed in the triaxial cell, called conventional frozen tests; 2) specimens that were frozen after being consolidated to varying effective stress levels in the triaxial cell, called consolidate-freeze tests; and 3) specimens that were not frozen, i.e., triaxial tests on unfrozen sand. The experimental procedures used for testing frozen sand had three special features, which collectively make the results unique compared to prior data. These features are

- measurement of on-specimen axial strains (ϵ_a) using special yokes that can resolve ϵ_a to 0.001% and which eliminate the initially S-shaped stress-strain curves commonly reported in the literature;
- measurement of volumetric strains (ϵ_v), although these are subject to an error in ϵ_v of up to $\pm 0.2\%$;
- the use of enlarged, lubricated (via ice caps for the conventional tests) end platens to facilitate lateral straining of the specimen and enable measurement of stress-strain behavior to very large strains ($\epsilon_a = 20\text{-}25\%$).

The experimental procedures also had two less desirable features. First, compliance in the triaxial apparatus required about one percent axial strain before the test specimens experienced a constant strain rate, $d\epsilon_a/dt = \dot{\epsilon}$; however, analysis of the data did use actual values of $\dot{\epsilon}$. Second, there was a temperature gradient of about 0.4°C between the top and bottom of the test specimens during shear that precluded testing at higher temperatures.

Table 2.1 summarizes the testing matrix for the 99 conventional frozen sand tests. The four variables in the parametric study were

- 1) the nominal testing temperature, which varied in 5°C increments from $T = -10^\circ\text{C}$ to -25°C .
- 2) the nominal axial strain rate, which varied from $\dot{\epsilon} = 3 \times 10^{-6}/\text{s}$ (slow) to $\dot{\epsilon} = 3.5 \times 10^{-5}/\text{s}$ (moderate) to $\dot{\epsilon} = 5 \times 10^{-4}/\text{s}$ (fast).

3) the relative density of the sand specimens, which varied from

$D_r = 20$ to 100% . Except at $T = -10^\circ\text{C}$, most specimens were either loose ($D_r \approx 35\%$) or dense ($D_r \approx 95\%$).

4) the confining pressure during shear, which varied from $\sigma_c = 0.1$ to 10 MPa.

Testing at $T = -10^\circ\text{C}$ also included $\sigma_c = 2$ and 5 MPa.

This is the first set of data from conventional frozen tests to fully characterize behavior as a function of sand density (D_r), confining pressure (σ_c), strain rate ($\dot{\epsilon}$) and temperature (T). In fact, only one other program (Baker and Konrad, 1985) has systematically varied sand density over all strain levels, and that was done at only one value of σ_c , $\dot{\epsilon}$ and T .

The program of consolidate-freeze tests consisted of ten tests run on dense sand consolidated to effective consolidation stresses of $\sigma'_c = 0.2, 2, 5$ and 10 MPa, frozen at $T = -10^\circ\text{C}$ and then sheared at the moderate strain rate. This is the first research to perform this type of test on frozen soil, although some aspects of the freezing process still require further verification. The program of triaxial compression tests on unfrozen sand consisted of 49 consolidated-undrained and consolidated-drained tests covering a wide variation in sand density ($D_r \approx 30$ to 100%) and consolidation stresses ($\sigma'_c = 0.1$ to over 10 MPa). This is the first research to perform tests on unfrozen sand for direct comparison with results of tests on frozen sand.

6.2 OVERVIEW AND DEFINITION OF STRESS-STRAIN BEHAVIOR

6.2.1 Overview of Stress-Strain Behavior

Figure 2.2 plots deviator stress ($Q = \sigma_1 - \sigma_3$) versus engineering axial strain (ϵ_a), in order to illustrate the range in types of stress-strain curves measured during the conventional testing program on frozen MFS. Two stress-strain curves are plotted at each strain rate and temperature. One corresponds to specimens having a low relative density ($D_r \approx 35\%$) and low confining pressure ($\sigma_c = 0.1$ MPa) and, hence, presumably reflecting the minimum frictional resistance of the sand skeleton. The other corresponds to specimens having a high relative density ($D_r \approx 95\%$) and high confining pressure ($\sigma_c = 10$ MPa) and presumably reflecting the maximum frictional resistance of the sand skeleton. Figure 2.2a shows the effect of increasing the strain rate ($\dot{\epsilon}$) by two orders of magnitude from slow to fast for specimens sheared at $T = -10^\circ\text{C}$; Figure 2.2b shows the effect of decreasing the temperature by 10°C for specimens sheared at the moderate strain rate.

All of the stress-strain curves in Figure 2.2 exhibit a very distinctive yield point (the knee of the curve) at levels of axial strain ranging from 0.3 to 1.0%, as shown by the circles in the figure. This point represents the onset of highly non-linear behavior and the development of very significant plastic deformations; it is termed the *upper yield* point.

A qualitative assessment of the data in Figure 2.2 shows that the behavior in the small-strain region is largely unaffected by changes in relative density and confining pressure, both of which affect the frictional resistance of the

sand skeleton. The results in Figure 2.2 also clearly demonstrate that strain rate and temperature, which affect ice behavior, have a tremendous influence on the magnitude of the deviator stress at the upper yield point, termed the *upper yield stress* (Q_{uy}).

At larger strains beyond the upper yield region, the data in Figure 2.2 show that changes in relative density and confining pressure obviously have a tremendous influence on stress-strain behavior. These two variables also affect the frictional resistance of the sand skeleton. Moreover, at large strains, all of the test specimens exhibited varying degrees of dilation (volumetric expansion) that depended mainly on sand density and confining pressure, as illustrated by the results presented in Figures 4.1 to 4.3.

6.2.2 Definition of Stress-Strain Parameters

Small-Strain Behavior

Figure 2.3 presents actual stress-strain curves drawn to two different strain scales in terms of the deviator stress ($Q = \sigma_1 - \sigma_3$) and the axial strain (ϵ_a). The parameters that have been selected for the evaluation of the small-strain behavior are the Young's modulus, the yield offset at 0.01% strain, and the upper yield stress. The graphical construction techniques used to obtain these parameters are summarized on the figure and explained as follows:

- the Young's modulus (E). The initial slope of the stress-strain curve is determined visually at levels of axial strain less than 0.01%.

- the yield offset stress at 0.01% strain (Q_{y0}). The intersection point of the stress-strain curve and a line with a slope of the Young's modulus translated by 0.01% strain.
- the upper yield stress (Q_{uy}). The first point on the stress-strain curve where the slope ($dQ/d\epsilon_a$) either becomes zero or reaches its minimum positive value before significant strain hardening.

Large-Strain Behavior

The deviator stress versus axial strain curves in Figure 2.2 have different characteristics regarding the degree of post-upper yield strain softening or strain hardening, i.e., whether Q decreases or increases after reaching Q_{uy} ; and whether or not strain softening occurs after the specimen reaches its peak strength (Q_p). These different characteristics, which depend mainly on sand density and confining pressure, are illustrated in the upper portion of Figure 2.4 for tests conducted at low and high confining pressures ($\sigma_c = 0.1$ and 10 MPa). Note that the deviator stress is normalized by the upper yield stress, since Q_{uy} does not vary with D_r and σ_c . Figure 2.4 also summarizes characteristic volumetric behavior measured at low and high confining pressures.

Figure 2.4 labels four curve types, and Table 2.2 describes their characteristics and the typical testing conditions leading to each type. In way of summary, **Type C curves predominate at low confining pressures ($\sigma_c = 0.1$ MPa) and are characterized by post-yield strain hardening to give a peak strength (Q_p) at**

moderate strains, followed by significant strain softening and significant dilation. For loose sand sheared at higher strain rates and/or lower temperatures, this behavior switches to Type A curves, i.e., $Q_p = Q_{uy}$ followed by significant strain softening and volumetric expansion. In contrast, **Type D curves predominate at high confining pressures** ($\sigma_c = 10$ MPa) and are characterized by significant post-yield strain hardening to give a peak strength at large strains, all with minimal dilation. For loose sand sheared at higher strain rates and/or lower temperatures, this behavior switches to Type B curves, i.e., initial strain softening followed by strain hardening to produce $Q_p \approx Q_{uy}$, again with minimal dilation. *

6.3 Small Strain Behavior of Frozen Sand

6.3.1 Young's Modulus

Figure 3.1 demonstrates that the Young's modulus (E) is nearly independent of all testing variables for conventional tests on frozen MFS. There is a slight (10-15%) decrease in E with σ_c increasing from 0.1 to 10 MPa (considered a second-order effect), and a slight increase (15%) with D_r increasing from 20 to 100%. The measured modulus equals 26.5 ± 4.0 GPa over all the testing variables. This value agrees well with **reliable** measurements (i.e., using on-specimen extensometer or wave propagation) on three other frozen sands and from the consolidate-freeze tests on MFS.

The mineralogy of the sand grains, the sand density, and the ice/silicate bond strength are considered to be the most significant factors that contribute to the initial stiffness properties of frozen MFS in the ranges of temperature and strain rate

investigated in this program. A composite materials model developed by Counto (1964) for concrete has been extended to frozen sands. The excellent agreement between predicted and measured data in Figure 3.1 indicates that composite action between the pore ice and silicate particles is the mechanism responsible for a Young's modulus that is several times greater than that of polycrystalline ice and up to two orders of magnitude greater than that of the unfrozen sand skeleton.

6.3.2 Yield Offset Stress

The yield offset stress (Q_{yo}) is presented in order to bridge the gap between the initial modulus (E) and the upper yield stress (Q_{uy}). The results from conventional tests on frozen MFS in Figure 3.2 show the following trends: relative density has no effect; there is a modest decrease in Q_{yo} with increasing confining pressure; and increases in strain rate and decreases in temperature both cause a significant increase in Q_{yo} , but to a lesser degree than for the upper yield stress (see Figure 3.5 for comparison). This indicates that the behavior of frozen sand in the small strain region becomes more strain rate and temperature sensitive as the level of strain increases. In addition, consolidation to very high stresses prior to freezing did not change Q_{yo} (see Sheet D8).

6.3.3 Upper Yield Stress

The use of on-specimen axial strain measurements enabled reliable determination of the upper yield stress (Q_{uy}) for all stress-strain curves from the program of conventional tests on frozen MFS. The value of Q_{uy} (which occurs between 0.3 to 1.0% axial strain) does not vary with relative density and is affected

only slightly by the magnitude of the confining pressure, as illustrated in Figure 3.3. This indicates that the frictional characteristics of the sand skeleton play a minor role, since density and confining (consolidation) pressure have a major influence on the small strain behavior of unfrozen MFS (e.g., Figures 5.2 and 5.6). However, this important conclusion needs further study because of the following observations:

- The consolidation-freeze tests on MFS show that consolidation to high stresses ($\sigma'_c \geq 2$ MPa) prior to freezing causes a stiffer small-strain response and the disappearance of a distinct upper yield point (Figures 5.11 and 5.12). This suggests that the frictional resistance of the sand skeleton can become significant within the small strain region for dense sand having very high pre-freezing consolidation stresses.
- Some prior data from conventional test programs show a very large pressure sensitivity in Q_{uy} (i.e., Figure 3.6). Whether this reflects a vastly different behavior, compared to frozen MFS, or shortcomings in the experimental procedures (e.g., S-shaped initial stress-strain curves) remains unknown. In addition, preparation of specimens by compaction rather than pluviation alters the measured stress-strain response (e.g., Figure 5.10 and Baker and Konrad, 1985). This fact further complicates direct comparison of Q_{uy} data for different frozen sands.

Figures 3.4 and 3.5 show that the upper yield stress of frozen MFS is very dependent on the strain rate and the temperature. Figure 3.7 compares Q_{uy} of frozen MFS with the peak strength of polycrystalline (granular) ice as a function of

strain rate. The power law coefficients (n) for the ice range from 4.3 to 5.4 and compare well with those for frozen MFS ($n \approx 5.6 \pm 1.0$). This comparison, typical stress-strain behavior for bulk ice (e.g., Figure 4.22), and the independence of Q_{uy} on sand density and confining pressure, suggest that the principal physical mechanisms occurring within the upper yield region are probably similar to those controlling the behavior of granular ice at its peak strength. Chamberlain *et al.* (1972), Bragg and Andersland (1980), Parameswaran and Jones (1981), and Sayles (1989), among others, have also concluded that the upper yield behavior of frozen sand is dominated by the ice matrix.

The authors hypothesize that the upper yield stress of frozen MFS as measured in conventional tests is caused almost entirely by the strength of the ice matrix. However, Figure 3.7 shows that the peak strength of ice (Q_i) is about one-half of Q_{uy} for testing at $T = -10^\circ\text{C}$. Moreover, analyses in Section 5.5 suggest that Q_i/Q_{uy} decreases substantially at lower temperatures (e.g., Sheet E9). Consequently, if Q_{uy} is controlled by the cohesive strength of the ice matrix, then the presence of the sand grains must cause a very significant strengthening of the ice matrix, compared to bulk polycrystalline ice. The authors agree with Ting *et al.* (1983) who attribute this enhanced strength of the intact ice matrix to a difference in the ice structure (e.g., an order of magnitude or more decrease in the grain size of ice in frozen sand), an increase in strain rate, and changes in the state of stress and the added deformational restraints due to the presence of the sand grains. However, these potential strengthening mechanisms are highly speculative and difficult to

quantify. In addition, the validity of the assumed Q_i relationships for bulk ice as a function of confinement, strain rate and temperature requires further verification. More research is also needed to determine possible trends in $Q_{uy} = f(\sigma_c, \dot{\epsilon}$ and $T)$, in terms of sand characteristics such as grain composition, shape, surface roughness and size distribution.

6.4 LARGE STRAIN BEHAVIOR OF FROZEN SAND

6.4.1 Volumetric Behavior

The current program is one of the very few to measure volumetric strains (ϵ_v) and only Shibata *et al.* (1985) report ϵ_v data at varying confining pressures, strain rates and temperatures (but for dense sand only). Both programs show essentially zero volumetric strain below the upper yield stress and then varying amounts of volumetric expansion (dilation) that continues to increase with further straining. Figures 4.1 to 4.3 illustrate typical volumetric behavior for frozen MFS.

Since an ice-saturated frozen sand continuum subjected to increasing axial stress can undergo only volumetric compression (for Poisson's ratio less than 0.5), any volumetric expansion (dilation) must reflect fracturing (cracking) of the ice matrix and loss of bonding between the ice matrix and the sand particles. In other words, the onset of dilation suggests a decrease in the cohesive strength of the frozen sand system caused by damage of the ice matrix.

Two parameters are used to quantify the dilation behavior of frozen MFS at large strains: the maximum rate of dilation ($MRD = (d\epsilon_v/d\epsilon_a)_{\max}$) and the

volumetric expansion at 20% axial strain, ϵ_{v20} . As illustrated in Figures 4.14 and 4.15, both parameters follow similar trends:

- increasing relative density causes an increasing dilation at low confinement ($\sigma_c = 0.1$ MPa), with minimal-to-no influence of strain rate and temperature. It is interesting that frozen loose MFS undergoes about twice as much dilation at 20% axial strain as unfrozen MFS.
- increasing confining pressure causes a very significant decrease in the rate and amount of dilation.
- at high confinement ($\sigma_c = 10$ MPa), sand density plays a very minor role, whereas higher strain rates or lower temperatures may cause a slight increase in dilation.

These trends are used to help explain the post-upper yield stress-strain behavior of frozen sand.

6.4.2 Post-Upper Yield Behavior: Curve Types and Conceptual Model

As previously emphasized, the post-upper yield behavior of frozen sand is highly dependent on sand density and confinement, in addition to strain rate and temperature. The four curve types depicted in Figure 2.4 and further described in Table 2.2 are used to illustrate this dependency on D_r , σ_c , $\dot{\epsilon}$ and T . Section 4.6 presents a conceptual model to explain the post-upper yield strain hardening/strain softening and volumetric behavior associated with these four curve types in terms of **weakening mechanisms** associated with damage to the ice matrix due to cracking that is reflected by dilation of the frozen sand, and

strengthening mechanisms associated with the frictional resistance of the frozen sand system.

Weakening and Strengthening Mechanisms

Figure 4.22 illustrates typical stress-strain curves for polycrystalline ice for the range of testing conditions used for frozen MFS. According to Mellor and Cole (1982) and Murrell *et al.* (1989), the onset of internal cracking begins at the first yield point. The continued formation and growth of cracks result in the peak strength (Q_i) occurring at about 0.5 to 1% axial strain, followed by strain softening that increases at higher strain rates and lower temperatures, but decreases with added confinement. However, assuming that the ice matrix in frozen sand behaves similarly to bulk ice, one would always expect a significant loss in the strength of ice at axial strains greater than about 0.5 to 1% (i.e., after Q_i for ice and Q_{uy} for frozen sand). This represents the weakening mechanism.

On the other hand, continued straining of frozen sand beyond Q_{uy} also will produce a strengthening mechanism due to the frictional resistance of the ice-sand composite that progressively behaves more like a **particulate** system, due to increasing damage of the ice matrix and increasing interaction between the particles of the sand skeleton. Section 4.6.3 contains a detailed discussion of the potential strengthening due to sand skeleton friction if this frictional resistance exhibited the same behavior as observed for unfrozen sand (which is not true, but still may provide general guidance). In addition, one can envision strengthening due to interference between the sand particles and the damaged ice matrix, and perhaps some frictional resistance of the fractured ice matrix. In any case, these

strengthening mechanisms should increase with increasing relative density and increasing confining pressure.

Based on the observed volumetric behavior of frozen MFS, one could expect the ice-sand system to behave in an "undrained" manner at low-to-moderate strains (say up to $\epsilon_a \approx 5\%$), since the amount of dilation is very small, even for tests at low confinement ($\sigma_c = 0.1$ MPa). For a truly constant volume condition, the **effective stresses** producing frictional resistance of the sand skeleton are generated **within** the ice-sand system. On the other hand, as dilatancy becomes more pronounced at larger strains, the ice-sand system could be expected to approach a "drained" condition. For a truly drained shear condition, the effective stresses causing frictional resistance are generated by the **applied stresses**, i.e., by the axial stress and the confining pressure.

Behavior at Low Confinement ($\sigma_c = 0.1$ MPa)

Type C curves represent the most prevalent type of behavior. After reaching the upper yield stress, the frozen sand exhibits strain hardening, since the strengthening mechanisms are stronger than the weakening mechanisms. The degree of strengthening and the resultant peak strength (Q_p) increase with increasing relative density (D_r), as illustrated in Figures 4.6 and 4.17, probably similar to undrained shear. With continued straining, dilatancy reduces the internal frictional resistance, and the weakening mechanisms now predominate to cause strain softening. Moreover, the **normalized** rate of strain softening is uniquely related to the amount of dilation, as per Figure 4.21 and Section 6.4.4.

Faster strain rates and lower temperatures produce Type A curves, e.g., test number 36 in Figure 2.2a and test number 97 in Figure 4.1b, especially at the lower sand densities. The weakening mechanisms dominate, due to both a more rapid rate of ice cracking and the relatively low post-yield frictional resistance. It is important to note that the normalized rate of strain softening versus volumetric expansion relationship for Type A curves is the same as for Type C curves (Fig. 4.21). However, Type A curves exhibit a more rapid initial strength loss immediately after yielding at $Q_p = Q_{uy}$ than occurs after the peak strength for Type C curves. But both curve types show an almost linear decrease in strength and increase in dilation at the larger strain levels (e.g., Fig. 4.1).

Behavior at High Confinement ($\sigma_c = 10$ MPa)

Type D curves represent the most prevalent type of behavior. After reaching the upper yield stress, the frozen sand exhibits continued strain hardening until reaching the peak strength at large strains. The amount of strength increase with increasing relative density is much larger than for tests at low confinement (Fig. 4.6), since high confinement increases the frictional resistance (more strengthening) and reduces the degree of ice cracking (less weakening).

Faster strain rates and lower temperatures produce Type B curves, e.g., test number 129 in Figure 4.3b, especially at the lower sand densities. The weakening mechanisms dominate immediately after yielding for the same basic reasons as for Type A curves. But thereafter, the increased confinement produces sufficient frictional resistance to offset damage of the ice matrix.

6.4.3 Peak Strength: Background

Table B in Appendix B summarizes the scope of 17 prior experimental programs that have investigated the peak strength of saturated (or nearly so) frozen sands. Of these programs, only one measured on-specimen axial strains (and, hence, could identify the upper yield stress), only one included a detailed study of relative density (D_r) (although two included ice-sand mixtures), and only one included variations in confining pressure (σ_c), strain rate ($\dot{\epsilon}$) and temperature (T). In addition, many programs used compacted rather than pluviated specimens, which leads to non-uniform densities and more scattered results. Hence, the scope of the testing program shown in Table 2.1 for frozen MFS is unique.

Figure 4.4 compares the peak strength (Q_p) of frozen MFS with data on other frozen sands as a function of strain rate ($\dot{\epsilon}$) at temperatures ranging from $T = -10^\circ$ to -30°C . The comparison is restricted to dense sands, since all prior studies of $\dot{\epsilon}$ and T used only dense specimens. For testing at low confinement, Figure 4.4a shows that the location of MFS and its values of the power law coefficient (n) are representative of frozen sand data, except for the strain rate insensitivity observed in Program A above $\dot{\epsilon} \approx 10^{-5}/\text{sec}$ for a 30-to-140-mesh silica sand (similar trends also occurred at $T = -6$ and -15°C). But also note the two-to-three-fold variations in Q_p at the same strain rate for sands tested at $T = -10^\circ\text{C}$. This large difference presumably reflects differences in relative density (and maybe method of preparation), degree of ice saturation (all used pure water) and the grain size distribution. For testing at

high confinement, Figure 4.4b shows close agreement between MFS and the uniform fine sand used in Program I.

Figure 4.12 compares the upper yield stress (Q_{uy}) and peak strength (Q_p) of frozen MFS as a function of strain rate and temperature at two extreme conditions: low density and low confinement (hence, minimal effect of sand skeleton frictional resistance); and high density and high confinement (hence, maximum effect of sand skeleton frictional resistance). This comparison illustrates the extreme importance of comparing these two stresses, since Q_{uy} is thought to be dominated by the strength of the ice matrix. Therefore, Q_{uy} is an important baseline strength. The comparison also demonstrates that inspection of Q_p data alone (as done in Figure 4.4) provides little insight regarding the physical mechanisms controlling the peak strength of frozen sands. Consequently, evaluation of the variables that affect the peak strength of frozen MFS is made in terms of the strength increase relative to the upper yield stress. In other words, the results are analyzed by using $\Delta Q = Q_p - Q_{uy}$ or Q_p/Q_{uy} , in order to quantify the net effect of the post-upper yield strengthening and weakening mechanisms. Note that these analyses are restricted to curve Types C and D (Figure 2.4), since $Q_p = Q_{uy}$ for curve Types A and B. The conclusions from these analyses are summarized in Section 6.4.5; but for perspective, that summary will be introduced with a description of a methodology for predicting the maximum strengthening that can occur due to the frictional resistance of the sand skeleton based on Ladanyi's dilatancy-hardening model.

6.4.4 Peak Strength: Dilatancy-Hardening Model

Assumptions

Section 5.2.1 describes the model presented by Ladanyi (1985) and Ladanyi and Morel (1990) for predicting the peak strength of frozen dense sand. Basically, the model assumes that the predicted strength (Q_{FS}) is given by

$$Q_{FS} = Q_i + Q_{fs} \quad \text{.....[6.1]}$$

Q_i is the strength of the ice matrix; it is equated to the peak strength measured in triaxial compression tests run on bulk polycrystalline ice. Q_{fs} is the frictional resistance of the sand skeleton; it is equated to the peak strength computed for undrained shear in triaxial compression. This frictional resistance is basically computed as

$$Q_{fs} = \sigma'_{3f} (R_f - 1) \quad \text{.....[6.2]}$$

where σ'_{3f} is the minor principal stress at failure for undrained shear of the unfrozen sand skeleton, and R_f is the obliquity of the principal stresses at failure, $(\sigma'_1/\sigma'_3) = (1 + \sin \phi')/(1 - \sin \phi')$.

The prediction of σ'_{3f} in the dilatancy-hardening model depends upon whether or not cavitation of the pore ice occurs during constant volume shear of the frozen sand. For combinations of sand density and confining pressure that do not cause cavitation (i.e., tests with low density or high confinement), σ'_{3f} is given by the critical confining pressure (σ'_{cr}), which is uniquely related to the preshear density of the (frozen) sand specimen. For combinations of sand density and

confining pressure that do cause cavitation of the pore ice, (i.e., high density and low confinement), σ'_{3f} equals σ_c plus T_i , where σ_c is the applied confining pressure, and T_i is the tensile strength of the pore ice (equated to the tensile strength of bulk polycrystalline ice). Consequently, the predicted peak strength (Q_{FS}) for the non-cavitation case is give by

$$Q_{FS} = Q_i + [Q_{fs} = \sigma'_{cr} (R_f - 1)] \quad \text{.....[6.3a]}$$

and for the cavitation case, it is given by

$$Q_{FS} = Q_i + [Q_{fs} = (\sigma_c + T_i) (R_f - 1)] \text{.....[6.3b]}$$

Model Parameters for Frozen MFS

Section 5.5.1 describes the approach used to select parameters for the pore ice. Values for the peak strength of ice (Q_i) were obtained by using a combined Arrhenius-Glen (1955) power law equation to fit the Jones (1982) data at $T = -11.5^\circ\text{C}$ for $\sigma_c = 0$ and 10 MPa and then extrapolated to other temperatures, assuming a constant activation energy (Sheets E4 and E6). This approach was adopted due to the lack of experimental data at lower temperatures for the strain rates of interest; it involves significant uncertainty in the Q_i values. The tensile strength of pore ice was taken as $T_i = 2.15$ MPa, based on the data summarized in Sheets E1 to E3.

The extensive program of consolidated-undrained (CU) and consolidated-drained (CD) triaxial compression tests on unfrozen MFS (Section 5.3) provided two types of vital information: 1) how changes in sand density and confining (consolidation) stress cause vastly different stress-strain curves and

effective stress paths (e.g., Figures 5.2 to 5.6); and 2) reliable predictions of the effective stress friction angle (ϕ' , Figure 5.7) and of the variation in critical confining pressure (σ'_{cr}) with sand density. Determination of σ'_{cr} involved the following steps:

- definition of the steady state line (SSL), which represents a state of continued shearing at constant void ratio (density), effective stress and shear stress (Sheet C11). This step required very extensive experimental data.
- use of the state parameter ψ proposed by Been and Jefferies (1985) to predict how changes in density and confinement affect Skempton's pore pressure parameter A at failure [$A_f = \Delta u - \Delta\sigma_3 / (\Delta\sigma_1 - \Delta\sigma_3)$], i.e., the value of $\psi = -0.061$ that produced $A_f = 0$ (Figure 5.9).
- definition of the critical confining pressure line (Figure 5.8).

Sheet E12 shows how relative density (D_r) affects the critical confining pressure (σ'_{cr}) and the predicted frictional resistance of the sand skeleton (Q_{fs}) for frozen MFS having $T_i = 2.15$ MPa and tested at $\sigma_c = 0.1$ MPa confinement. Several important conclusions can be drawn from these model predictions:

- The non-cavitation case applies for all relative densities less than $D_r \approx 90\%$, i.e., for $\sigma'_{cr} \leq \sigma_c + T_i = 2.25$ MPa. Within this region, Q_{fs} varies from 0.7 MPa at $D_r = 20\%$ to $Q_{fs} = 5.8$ MPa at $D_r = 90\%$. Moreover, increases

in confinement do not affect the predicted undrained frictional resistance of the sand skeleton.

- The cavitation case occurs only for relative densities between $D_r \approx 90$ and 100%. Within this region, the predicted frictional resistance remains constant at $Q_{fs} = 6.0$ MPa independent of D_r for $\sigma_c = 0.1$ MPa. However, increases in σ_c will cause a large increase in Q_{fs} (corresponding to $\phi = \phi' = 34.9^\circ$), as long as $\sigma_c + T_i$ remains less than σ'_{cr} .
- Uncertainty in the tensile strength of ice (T_i) will not affect the predicted Q_{fs} of frozen MFS, except for dense sand at low confinement.

Comparison of Predicted and Measured Strengths

Section 5.5.2 presents a detailed comparison of predicted (Q_{FS}) and measured (Q_p) strengths for conventional frozen tests on dense ($D_r \approx 95\%$) and loose ($D_r \approx 35\%$) MFS at low ($\sigma_c = 0.1$ MPa) and high ($\sigma_c = 10$ MPa) confinement, e.g., Figures 5.15 to 5.18. The overall agreement is very poor, except for relatively slow shearing at $T = -10^\circ\text{C}$ of dense sand at low confinement. Perhaps by coincidence, Ladanyi and Morel (1990) obtained excellent agreement for a dense, 20-30 Ottawa sand sheared at $\sigma_c = 0$ to 0.3 MPa, $\dot{\epsilon} = 2.7 \times 10^{-4}/\text{sec}$ and $T = -5^\circ\text{C}$. (Their prediction used the cavitation equations; see Section 5.2.2).

Sheet E8 quantifies the model error by plotting Q_{FS}/Q_p versus temperature for dense and loose frozen MFS at $\sigma_c = 0.1$ and 10 MPa. For dense sand,

the Q_p values range from 10 to 25 MPa (compared to $Q_{fs} \approx 6 \pm 1$ MPa), and Q_{FS}/Q_p decreases from roughly 0.7 ± 0.1 at $T = -10^\circ\text{C}$ down to about 0.5 at $T = -25^\circ\text{C}$. For loose sand, the Q_p values range from 7 to 30 MPa (compared to Q_{fs} of less than 1.5 MPa), and Q_{FS}/Q_p decreases from roughly 0.6 ± 0.1 at $T = -10^\circ\text{C}$, down to 0.45 ± 0.1 at $T = -25^\circ\text{C}$. The fact that the predicted Q_{fs} represents a small fraction of the measured Q_p (at least for loose sand) suggests that the main problem with the model predictions lies with the predicted values for the strength of the ice matrix (Q_i).

Section 6.3.3 hypothesized that the upper yield stress (Q_{uy}) may represent the operational or effective strength of the ice matrix prior to the onset of significant cracking. Sheet E9 plots the predicted Q_i divided by the measured Q_{uy} versus temperature for testing at $\sigma_c = 0$ and 10 MPa. Since the magnitudes and trends in Q_{FS}/Q_p and Q_i/Q_{uy} are amazingly similar, the authors conclude that Q_i should be replaced by Q_{uy} when applying the dilatancy-hardening model to frozen MFS. The revised predictions are denoted by $Q_{FS}^* = Q_{uy} + Q_{fs}$, where Q_{fs} is again given by Eq. 6.3. Note that the predicted Q_{FS}^* minus the measured Q_p should equal Q_{fs} for perfect predictions. The next section includes such comparisons.

6.4.5 Peak Strength: Effect of Testing Variables

As noted earlier, analysis of the influence of testing variables on the peak strength is made primarily in terms of $\Delta Q = Q_p - Q_{uy}$ for the combination of D_r , σ_c , ϵ and T producing curve Types C and D that strain harden after reaching the

upper yield stress (Q_{uy}). Note: dQ will be used to denote changes in both $d\Delta Q$ and dQ_p as a function of changes in D_r , σ_c , etc.

Effect of Relative Density (D_r)

Figure 4.6 shows a linear increase in ΔQ with increasing D_r for frozen MFS. The rate of increase (dQ/dD_r) is roughly independent of $\dot{\epsilon}$ and T , but it is highly dependent on confinement, as further illustrated in Figure 4.7. At $\sigma_c = 0.1$ MPa, $dQ/dD_r = 5.6 \pm 1.0$ MPa and almost doubles to 11.9 ± 0.6 MPa at $\sigma_c = 10$ MPa. The only prior program with a detailed study of relative density (program R in Table B) showed a much higher $dQ_p/dD_r = 13$ MPa from unconfined compression tests on a pluviated 16-100 Ottawa sand at $D_r > 65\%$. Both the original and revised versions of the dilatancy-hardening model predict a non-linear increase in $\Delta Q = Q_{fs}$ with D_r , i.e., Sheet E12 predicts a linear $D_r - \log Q_{fs}$ relationship. In any case, further research is needed to determine how relative density affects post-upper yield behavior for further comparison with the frozen MFS data.

Figure 4.11 shows results of analyses to obtain values of D_r producing $Q_p = Q_{uy}$ (i.e., $\Delta Q = 0$ for Type A curves) for $\sigma_c = 0.1$ MPa tests on frozen MFS as a function of $\dot{\epsilon}$ and T . Although the single data point from program R agrees with the frozen MFS data, added research is needed to predict conditions leading to failure at the upper yield stress.

Effect of Confining Pressure (σ_c)

Figure 4.8 shows the effect of confinement for frozen MFS tested at the moderate strain rate and $T = -10^\circ\text{C}$. The pressure sensitivity (in terms of $dQ/d\sigma_c$ and the corresponding total stress friction angle, ϕ) is much higher for dense than for loose frozen MFS and tends to decrease at very high confining pressures (especially for loose sand). Mean values of $dQ/d\sigma_c$ (from data at $\sigma_c = 0.1$ and 10 MPa) for slow and moderate shearing range from about 0.2 to 0.7 (corresponding $\phi = 5$ to 15°) and vary in a complex fashion with D_r , $\dot{\epsilon}$ and T , as summarized in Figure 4.9.

Several prior programs have studied the effect of confinement on the peak strength of medium-dense to dense frozen sands. Figure 4.10 summarizes data for tests conducted at $T = -11 \pm 1^\circ\text{C}$. The results from the four test series on medium to fine sands (programs G, I and L; also see Table B) give $dQ_p/d\sigma_c \approx 0.56$ to 0.9 ($\phi = 12.5^\circ$ to 18°) and are consistent with data for dense MFS. However, tests on the coarse 20-30 Ottawa sand used for program J produced a much higher pressure sensitivity ($\phi \approx 28^\circ$). In addition, Shibata *et al.* (1985) did not observe a decrease in pressure sensitivity at faster strain rates and lower temperatures, as observed for frozen MFS. Hence, the pressure sensitivity of frozen sands does not appear to follow a consistent trend.

As shown in Figure 5.14, consolidation of dense MFS to $\sigma'_c = 0.1$ to 10 MPa prior to freezing (i.e., results from the consolidate-freeze test program presented in Section 5.4) did not produce peak strengths very different from those

measured in conventional frozen tests. However, consolidation to high stresses ($\sigma_c \geq 2$ MPa) did cause a very significant increase in the deviator stress (Q) at axial strain levels from about $\epsilon_a = 0.5$ to 5%, as illustrated in Figures 5.11 and 5.12. This pronounced stiffening is consistent with the behavior observed in consolidated-undrained triaxial compression tests on unfrozen MFS, as per Figure 5.2. The stress-strain curve in Figure 5.2 for test C-29 also suggests that anisotropic consolidation (i.e., higher vertical than horizontal stresses) will greatly enhance this stiffening at small strains.

Figure 5.14 also compares dilatancy-hardening model predicted strengths (Q_{FS}) with the measured peak strengths (Q_p) for dense MFS at the moderate strain rate and $T = -10^\circ\text{C}$. The model vastly underestimates the measured pressure sensitivity, because it predicts no increase in the frictional resistance (Q_{fs}) of the sand skeleton with added confinement (the modest increase in Q_{FS} occurs only from the predicted increase in Q_i with confinement). The stress-strain data in Figure 5.2 also show little change in the peak undrained strength of unfrozen sand. However, increases in consolidation stress do cause a much stiffer response at smaller strains. Hence, strain compatibility between the cohesive strength of the ice matrix and the frictional resistance of the sand skeleton probably plays an important role in the behavior of the ice-sand composite material.

Effects of Strain Rate and Temperature ($\dot{\epsilon}$ and T)

Figure 4.6 plots the post-upper yield strength gain, $\Delta Q = Q_p - Q_{uy}$, versus relative density for frozen MFS at low and high confinement ($\sigma_c = 0.1$ and 10 MPa).

In general, shearing at the faster strain rates and lower temperatures tends to cause a downward shift in the ΔQ versus D_r relationships. Figure 4.13 provides a more detailed picture of the influence of $\dot{\epsilon}$ and T by plotting ΔQ for loose ($D_r = 30\%$) and dense ($D_r = 90\%$) specimens (interpolated from Figure 4.6) versus $\log \dot{\epsilon}$ for the different temperatures. Inspection of this figure indicates the following complex trends, using the slow strain rate at -10°C as the reference:

- For loose sand at low confinement, the minimal strength gain rapidly vanishes at higher strain rates.
- For loose sand at high confinement and for dense sand at low confinement, the moderate strength gain disappears more rapidly with faster shearing at the lower temperatures.
- For dense sand at high confinement, the large strength gain is temperature independent at the slow rate; for faster shearing, the amount of strengthening reduces at the lower temperatures.

Revised Model Predictions

Sheet E10 plots the predicted $Q_{FS}^* = Q_{uy} + Q_{fs}$ minus the measured peak strength (Q_p) versus temperature for loose ($D_r = 35\%$) and dense ($D_r = 95\%$) MFS at low and high confinement ($\sigma_c = 0.1$ and 10 MPa) for tests having curve Types C and D. This comparison generally shows that the predicted Q_{FS}^* is either quite accurate or slightly too high at low confinement for combinations of $\dot{\epsilon}$ and T producing the maximum values of $\Delta Q = Q_p - Q_{uy}$. However, at high confinement (again for

conditions producing the maximum ΔQ), the predicted Q_{FS}^* is too low. After considerations of strain compatibility, it is tentatively concluded that the measured strengths are larger than would be expected, based on the separate behaviors of an unfrozen sand skeleton and an enhanced ice matrix strength that follows trends observed for bulk ice. That is, the strain levels at the peak strength of frozen MFS are generally too small to mobilize the full frictional resistance of the sand skeleton (Q_{fs}); and the strains are sufficiently large to cause significant weakening of the ice matrix.

6.4.6 Post-Peak Strain Softening Behavior

The use of lubricated end platens and measurement of volumetric strains have made possible a unique evaluation of the post-peak strain softening behavior of frozen MFS. For tests at low confinement that produce curve Types A and C (i.e., post-peak strain softening), there appears to be a unique relationship between the rate of strain softening (after normalization to the upper yield stress) and the amount of volumetric expansion (dilation). Figure 4.21 presents this relationship in terms of the normalized rate of strain softening, $NRSS = [(Q_p - Q_{20})/Q_{uy}]/(\epsilon_{20} - \epsilon_p)$, versus the amount of dilation at 20% axial strain, ϵ_{v20} . The collective data, which cover a wide range of relative densities ($D_r = 35$ to 95%), have relatively little scatter about the mean trend and do not show a consistent deviation as a function of strain rate or temperature. However, the individual stress components of the NRSS do vary significantly with the testing variables, as summarized below (for curve Types A and C):

- Q_p/Q_{uy} increases linearly with relative density; these lines move downward and become flatter with increasing strain rate and decreasing temperature. (See Fig. 4.17 for Type C curves.)
- Q_{20}/Q_{uy} is independent of relative density, but also has a smaller magnitude with increasing strain rate and decreasing temperature. (See Fig. 4.18 for both Type A and C curves.)

Analysis of test results at all confining pressures (i.e., up to $\sigma_c = 10$ MPa) produced the results presented in Figures 4.19 and 4.20. For all curve types (i.e., including Type B and D with little or no post-peak strain softening), the rate of strain softening increases with the maximum rate of dilation, and the stress ratio Q_{20}/Q_p decreases with the amount of dilation. Although both plots have significant scatter, they provide additional evidence that the degree of post-peak strain softening or strength loss is strongly related to the rate or amount of dilation.

7. REFERENCES

CRREL = U.S. Army Cold Regions Research and Engineering Laboratory
IAHR = International Association for Hydraulics Research
JGE = Journal of Geotechnical Engineering*
JGED = Journal of the Geotechnical Engineering Division*
JSMFD = Journal of the Soil Mechanics and Foundations Division*
SPE-AIME = American Institute of Mining, Metallurgical, and Petroleum Engineers

* Published by American Society of Civil Engineers

Alkire, B.D. and O.B. Andersland (1973), "The Effect of Confining Pressure on the Mechanical Properties of Sand-Ice Materials," *Journal of Glaciology*, Vol. 12, No. 66, pp. 469-481

Andersen, G.R. (1991), "Physical Mechanisms Controlling the Strength and Deformation Behavior of Frozen Sand," Sc.D. thesis, Massachusetts Institute of Technology, 560p

Andersen, G.R., J.T. Germaine, C.C. Ladd and C.W. Swan (1992) "Physical Mechanisms Controlling the Strength and Deformation Behavior of Frozen Sand: I," *Final Report to U.S. Army Research Office, Contract Number DAAL03-89-K0023*, April 1992, 166p

Andersen, G.R., C.W. Swan, C.C. Ladd, J.T. Germaine (1995), "Small Strain Behavior of Frozen Sand in Triaxial Compression," *Canadian Geotechnical Journal* (in press)

Baker, T.H.W., S.J. Jones, and V.P. Parameswaran (1982), "Confined and Unconfined Compression Tests on Frozen Sands," *Proceedings of Fourth Canadian Permafrost Conference*, pp. 387-393

Baker, T.H.W. and P.J. Kurfurst (1985), "Acoustic and Mechanical Properties of Frozen Sand," *Fourth International Symposium on Ground Freezing, Sapporo*, pp. 227-234

Baker, T.H.W. and J.M. Konrad (1985), "Effect of Sample Preparation on the Strength of Artificially Frozen Sand," *Fourth International Symposium on Ground Freezing, Sapporo*, pp. 171-176

- Bourbonnais, J. and B. Ladanyi (1985), "The Mechanical Behavior of Frozen Sand Down to Cryogenic Temperatures," *Fourth International Symposium on Ground Freezing*, Sapporo, pp. 235-244
- Bragg, R.A. and O.B. Andersland (1980), "Strain Rate, Temperature, and Sample Size Effects on Compression and Tensile Properties of Frozen Sand," *Second International Symposium on Ground Freezing*, Trondheim, pp. 34-47
- Chamberlain, E, C. Groves and R. Perham (1972), "The Mechanical Behavior of Frozen Earth Materials Under High-Pressure Triaxial Test Conditions," *Géotechnique*, Vol. 22, No. 3, pp. 469-483
- Cole, D.M. (1985), "Grain Size and the Compressive Strength of Ice," *Journal of Energy Resources Technology - ASME*, Vol. 107, Sept. 1985, pp. 369-374
- Cole, D.M. (1986), "Effect of Grain Size on the Internal Fracturing of Polycrystalline Ice," *CRREL Report 86-5*, 79p
- Cole, D.M. (1987), "Strain-Rate and Grain-Size Effects in Ice," *Journal of Glaciology*, Vol. 33, No. 115, pp. 274-280
- Cole, D.M. (1994), "The Effect of Microstructure and Temperature on the Constitutive Behavior of Ice at Low Strains," *IAHR Ice Symposium*, Trondheim, 8 p
- Counto, U.J. (1964), "The Effect of the Elastic Modulus of the Aggregate on the Elastic Modulus, Creep and Creep Recovery of Concrete," *Magazine of Concrete Research*, Vol. 16, No. 48, pp. 129-138
- Glen, J.W. (1955), "The Creep of Polycrystalline Ice," *Proceedings of the Royal Society of London, Series A*, Vol. 228, pp. 519-538
- Goughnour, R.R. and O.B. Andersland (1968), "Mechanical Properties of a Sand-Ice System," *JSMFD*, Vol. 94, No. SM4, pp. 923-950
- Hawkes, I. and M. Mellor (1972), "Deformation and Fracture of Ice Under Uniaxial Stress," *Journal of Glaciology*, Vol. 11, No. 61, pp. 103-131
- Haynes, F.D. (1979), "Temperature Effect On the Uniaxial Strength of Ice," *Fifth International Conference Port and Ocean Engineering Under Arctic Conditions*, Norwegian Institute of Technology, pp. 667-681
- Jones, S.J. (1982), "The Confined Compressive Strength of Polycrystalline Ice," *Journal of Glaciology*, Vol. 28, No. 98, pp. 171-177

- Jones, S.J. and V.R. Parameswaran (1983), "Deformation Behavior of Frozen Sand-Ice Materials Under Triaxial Compression," *Fourth International Conference on Permafrost*, Fairbanks, pp. 560-565
- Jacka, T. H. (1984), "The Time and Strain Required for Development of Minimum Strain Rates in Ice," *Cold Regions Science and Technology*, Vol. 8, pp. 261-268
- Kaplar, C.W. (1963), "Laboratory Determination on the Dynamic Moduli of Frozen Soils and of Ice," *Proceedings Permafrost International Conference*, Lafayette, Indiana, pp. 293-301
- Ladanyi, B. (1985), "Stress Transfer Mechanism in Frozen Soils," *Proceedings of the Tenth Canadian Congress of Applied Mechanics*, University of Western Ontario, London
- Ladanyi, B. and J. Morel (1990), "Effect of Internal Confinement on Compression Strength of Frozen Sand," *Canadian Geotechnical Journal*, Vol. 27, pp. 8-18
- Lambe, T.W. and R.V. Whitman (1969), *Soil Mechanics*, John Wiley and Sons, New York
- Martin, R.T., J.M. Ting and C.C. Ladd (1981), "Creep Behavior of Frozen Sand Final Report Part 1," M.I.T. Department of Civil Engineering, *Research Report No. R81-19*, 237p
- Mellor, M. (1980), "Mechanical Properties of Polycrystalline Ice," *Physics and Mechanics of Ice*, Symposium in Copenhagen 1979 IUTAM, pp. 217-245
- Mellor, M. and D.M. Cole (1982), "Deformation and Failure of Ice Under Constant Stress and Constant Strain-Rate," *Cold Regions Science and Technology*, Vol. 5, pp. 201-219
- Mellor, M. and D.M. Cole (1983), "Stress/Strain/Time Relations for Ice under Uniaxial Compression," *Cold Regions Science and Technology*, Vol. 6, pp. 207-230
- Murrell, S.A.F., P.R. Sammonds and M.A. Rist (1989), "Strength and Failure Modes of Pure Ice and Multi-Year Sea Ice Under Triaxial Loading," *Ice-Structure Interaction*, IUTAM-IAHR Symposium, 1989, St. John's Newfoundland, Canada, pp. 339-361
- Orth, W. (1985), "Deformation Behavior of Frozen Sand and Its Physical Interpretation," *Fourth International Symposium on Ground Freezing*, Sapporo, pp. 245-253

- Parameswaran, V.R. (1980), "Deformation Behavior and Strength of Frozen Sand," *Canadian Geotechnical Journal*, Vol. 17, pp. 74-88
- Parameswaran, V.R., and S.J. Jones (1981), "Triaxial Testing of Frozen Sand," *Journal of Glaciology*, Vol. 27, No. 95, pp. 147-155
- Parameswaran, V.R. and M. Roy (1982), "Strength and Deformation of Frozen Saturated Sand at -30°C ," *Canadian Geotechnical Journal*, Vol. 19, pp. 104-107
- Perkins, T.K. and R.A. Reudrich (1973), "The Mechanical Behavior of Synthetic Permafrost," *Society of Petroleum Engineers Journal*, Transactions SPE-AIME, Vol. 255, pp. 211-220
- Pestana-Nascimento, J.M. (1994), "A Unified Constitutive Model for Clays and Sands," ScD. Thesis, Massachusetts Institute of Technology, 473 p
- Sayles, F.H. (1973), "Triaxial and Creep Tests on Frozen Ottawa Sand," *Second International Permafrost Conference*, North American Contribution, pp. 384-391
- Sayles, F. (1989), "State of the Art: Mechanical Properties of Frozen Soil," *Fifth International Symposium on Ground Freezing*, Jones and Holden, eds., Vol. 1, pp. 143-165
- Sayles, F.H. and N.V. Epanchin (1966), "Rate of Strain Compression Tests on Frozen Ottawa Sand and Ice," Technical Note for Internal Distribution at U.S. Army CRREL
- Shibata, T., T. Adachi, A. Yashima, T. Takahashi and I. Yoshioka, (1985), "Time-Dependence and Volumetric Change Characteristic of Frozen Sand Under Triaxial Stress Condition," *Fourth International Symposium on Ground Freezing*, Sapporo, pp. 173-179
- Shyam Sunder, S. and M.S. Wu (1990), "On the Constitutive Modeling of Transient Creep in Polycrystalline Ice," *Cold Regions Science and Technology*, Vol. 18, pp. 267-294
- Sinha, N.K. (1989), "Elasticity of Natural Types of Polycrystalline Ice," *Cold Regions Science and Technology*, Vol. 17, pp. 127-135
- Swan, C.W. (1994), "Physical Mechanisms Controlling the Deformation and Strength Behavior of Unfrozen and Frozen Manchester Fine Sand," Sc.D. thesis, Massachusetts Institute of Technology, 1044p

- Swan, C.W., C.C. Ladd, J.T. Germaine and G.R. Andersen (1995), "Physical Mechanisms Controlling the Strength and Deformation Behavior of Frozen Sand: Part II," *Final Report to the U.S. Army Research Office, Contract Number DAAL03-92-G0226*, April, 1995
- Ting, J.M., R.T. Martin and C.C. Ladd (1983), "Mechanisms of Strength for Frozen Sand," *Journal of Geotechnical Engineering*, Vol. 109, No. 10, pp. 1286-1302
- Yuanlin, Z., Z. Jiayi and S. Zhongyan (1988), "Uniaxial Compressive Strength of Frozen Medium Sand Under Constant Deformation Rates," *Fifth International Symposium on Ground Freezing*, pp. 225-232

APPENDIX A: Data on Small-Strain Behavior of Frozen MFS

<u>Sheet No.</u>	<u>Description</u>
------------------	--------------------

Tables from Andersen *et al.* (1994) giving specimen properties, testing conditions and measured small strain parameters

A1 & A2	Table 5.	Results at T = -10°C
A3	Table 6.	Results at T = -15°C
A4	Table 7.	Results at T = -20°C
A5	Table 8.	Results at T = -25°C
A6	Results of Linear Regression Analyses on Upper Yield Stress of Frozen MFS	

TABLE 5. Specimen properties, testing conditions and measured small strain parameters:
Results at T = -10°C (Page 1/2)

Test No.	Dry Density (kg/m ³)	Dr (%)	S _i (%)	Method of Prep.	End Cond.	σ _c avg. (MPa)	T (°C)	Strain Rate (10 ⁻⁷ /sec)			Test Parameters				ACDT Qual.
								Q _{yo} ¹	Q _{uy} ²	Maximum	E (GPa)	Q _{yo} (MPa)	Q _{uy} (MPa)	ε _{uy} (%)	
15	1489	31.6	99.2	MSP	Ice	10.15	NA	33	305	336	21.4	2.8	7.3	0.50	good
18	1536	48.4	98.4	MSP	Ice	10.18	NA	34	329	329	28.6	2.7	7.2	0.43	good
19	1539	49.4	99.0	MSP	Ice	10.18	NA	38	344	344	21.4	2.7	7.2	0.43	good
20	1621	76.3	99.4	Tamp	Ice	10.18	NA	44	271	299	20.7	3.2	8.6	0.50	good
21	1615	74.4	98.9	Tamp	Ice	10.18	NA	39	280	311	20.0	3.0	8.2	0.52	good
22	1634	80.3	98.4	Tamp	Ice	10.15	NA	32	300	320	25.0	3.0	8.2	0.51	good
23	1559	56.2	100.2	MSP	Ice	5.12	NA	27	296	330	23.1	3.1	7.4	0.46	good
24	1668	90.5	96.5	Tamp	Ice	5.12	NA	21	295	303	33.3	3.2	8.9	0.54	poor
25	1549	52.8	99.8	MSP	Ice	2.08	NA	29	314	336	26.1	3.4	7.6	0.48	fair
26	1680	94.0	98.0	Tamp	Ice	2.08	NA	21	275	300	31.8	3.7	9.2	0.53	good
27	1668	90.5	99.7	Tamp	Grease	2.07	NA	22	266	348	33.3	3.8	9.0	0.53	poor
28	1698	99.2	100.1	Tamp	Grease	0.103	NA	22	292	386	21.2	3.2	9.1	0.44	poor
29	1559	56.2	99.9	MSP	Ice	0.106	NA	21	334	334	25.9	3.8	8.2	0.47	good
30	1463	21.8	100.0	MSP	Ice	0.106	NA	23	328	339	25.9	4.2	8.4	0.50	good
31	1466	23.0	99.3	MSP	Emery	0.106	NA	17	332	352	29.2	3.8	8.3	0.50	good
32	1634	80.3	98.7	MSP	Ice	0.102	NA	22	314	344	28.0	3.9	8.3	0.42	poor
33	1572	60.6	99.0	MSP	Ice	0.103	NA	30	324	337	29.2	3.4	8.5	0.53	good
34	1503	36.7	99.7	MSP	Ice	0.102	NA	26	358	358	23.5	4.9	8.7	0.47	good
35	1502	36.3	99.6	MSP	Ice	0.101	NA	72	1050	1070	25.8	4.3	10.5	0.65	good
36	1503	36.7	96.4	MSP	Ice	0.101	NA	290	4400	4950	25.0	5.2	15.0	0.74	good
37	1690	96.9	97.8	MSP	Ice	0.101	NA	230	4470	4790	30.3	5.1	15.4	0.83	good
38	1681	94.3	96.6	MSP	Ice	0.101	NA	23	305	322	41.2	4.1	8.5	0.44	poor
39	1676	92.8	97.0	MSP	Grease	10.11	NA	373	5070	5360	29.0	4.4	16.1	1.02	poor
40	1505	37.4	98.3	MSP	Ice	10.13	NA	362	5420	5420	25.7	4.7	15.0	0.83	good
41	1687	96.0	98.4	MSP	Grease	0.102	NA	240	4720	5380	38.5	4.7	16.6	0.89	poor
42	1678	93.4	98.4	MSP	Grease	10.13	NA	24	307	362	25.0	3.1	8.2	0.50	good
43	1669	36.3	99.8	MSP	Grease	0.102	NA	20	322	342	25.9	4.2	8.8	0.50	poor

1 Secant value from start of test

2 Tangent value at upper yield stress

NA - Not Available

Numbers in italics were not used in analysis for Young's modulus or yield offset

TABLE 5. Specimen properties, testing conditions and measured small strain parameters
Results at T = -10°C (Page 2/2)

Test No.	Dry Density (kg/m ³)	Dr (%)	S _i (%)	Method of Prep.	End Cond.	σ _c avg. (MPa)	T (°C)	Strain Rate(10 ⁻⁷ /sec)			Test Parameters			ACDT Qual.	
								Q _{yo} ¹	Q _{uy} ²	Maximum	E (GPa)	Q _{yo} (MPa)	Q _{uy} (MPa)		ε _{uy} (%)
44	1502	36.3	99.8	MSP	Ice	0.102	NA	29	308	336	25.7	4.1	8.2	0.48	good
45	1507	38.1	99.3	MSP	Ice	0.102	NA	2.7	22.3	30.9	28.6	3.0	5.0	0.28	poor
46	1673	92.0	99.0	MSP	Ice	0.101	NA	2.5	24.3	24.3	40.0	3.3	5.1	0.26	good
47	1522	43.5	99.5	MSP	Ice	10.03	NA	2.8	28.9	29.2	20.0	2.7	4.8	0.36	poor
48	1688	96.3	97.0	MSP	Ice	10.04	NA	2.2	27.2	27.2	25.0	2.7	4.9	0.34	good
49	1690	96.9	98.1	MSP	Ice	10.01	NA	393	4380	4380	24.3	4.3	15.4	0.85	good
51	1633	80.0	97.2	MSP	Ice	10.02	NA	26	349	370	31.6	3.3	8.8	0.52	poor
52	1669	90.8	97.5	MSP	Ice	10.04	NA	59	312	355	20.7	2.8	8.2	0.48	poor
53	1675	92.5	99.0	MSP	Ice	5.03	NA	27	310	352	35.3	2.9	8.5	0.51	fair
54	1680	94.0	98.0	MSP	Ice	10.04	NA	2.8	32.2	32.5	26.3	2.8	5.4	0.44	good
55	1660	88.1	98.9	MSP	Ice	2.00	NA	30	355	382	26.1	3.4	7.9	0.44	poor
56	1676	92.8	98.5	MSP	Ice	0.101	NA	21	311	371	46.7	3.8	9.5	0.49	poor
57	1500	35.6	99.9	MSP	Ice	0.101	NA	30	384	384	25.0	3.3	8.7	0.54	good
58	1679	93.7	98.1	MSP	Ice	0.100	NA	0.9	25.9	32.9	14.3	1.8	5.6	0.49	poor
59	1485	30.1	99.1	MSP	Ice	5.01	-9.6	23	313	333	29.2	3.5	8.9	0.44	fair
60	1553	54.2	99.7	MSP	Ice	2.01	-9.5	22	265	339	31.8	3.5	9.2	0.43	fair
61	1494	33.4	98.9	MSP	Ice	10.02	-9.6	3.1	28.9	28.9	21.7	2.9	5.1	0.34	fair
62	1553	54.2	99.7	MSP	Ice	5.00	-9.5	2.8	279	335	25.9	3.4	8.3	0.43	good
63	1544	51.1	98.9	MSP	Ice	10.03	-9.5	32	303	335	24.0	3.0	8.2	0.50	poor
64	1642	82.7	98.9	MSP	Ice	10.02	-9.5	27	295	338	24.3	3.3	7.9	0.48	good
65	1686	95.7	98.0	MSP	Ice	0.102	-9.5	367	4250	4990	26.3	5.0	15.8	0.82	good
66	1643	83.0	96.1	MSP	Ice	0.102	-9.6	20	220	235	35.6	4.3	8.4	0.27	good
67	1483	33.1	96.1	MSP	Ice	2.01	-9.6	31	268	339	25.0	3.6	8.0	0.42	good

1 Secant value from start of test

2 Tangent value at upper yield stress

NA - Not Available

Numbers in italics were not used in analysis for Young's modulus or yield offset

TABLE 6. Specimen properties, testing conditions and measured small strain parameters:
Results at T = -15°C

Test No.	Dry Density (kg/m ³)	Dr (%)	S _i (%)	Method of Prep.	End Cond.	σ_c avg. (MPa)	T (°C)	Strain Rate (10 ⁻⁷ /sec)			Test Parameters			ACDT Qual.	
								Q _{yo} ¹	Q _{uy} ²	Maximum	E (GPa)	Q _{yo} (MPa)	Q _{uy} (MPa)		ϵ_{uy} (%)
121	1672	91.7	99.6	MSP	Ice	9.99	-15.4	299	4030	4476	23.1	4.4	21.7	1.04	fair
123	1669	90.7	98.8	MSP	Ice	9.94	-15.6	0.5	30.7	34.6	22.8	3.2	7.9	0.55	fair
126	1536	48.3	100.2	MSP	Ice	9.99	-15.5	233	4336	4336	24.3	4.9	20.3	0.94	good
127	1499	35.4	100.4	MSP	Ice	9.96	-15.5		29.4	35.3	NA	NA	7.8	1.09	poor
128	1547	52.1	99.6	MSP	Ice	9.97	-15.6	17.3	383	394	26.9	2.8	12.2	0.76	good
129	1534	47.7	99.2	MSP	Ice	9.91	-15.5	202	4400	4480	26.9	5.3	20.4	0.94	good
130	1507	38.7	99.1	MSP	Ice	9.86	-15.8		33.7	33.7	22.9	NA	7.6	0.68	good
131	1656	86.9	94.4	MSP	Ice	9.94	-15.6	2.6	25.6	34.6	14.2	1.9	9.0	0.54	poor
133	1632	79.8	101.9	MSP	Ice	10.02	-15.6	18	337	403	28.9	3.1	12.9	0.70	poor
134	1652	85.8	100.3	MSP	Ice	9.96	-15.5	2.1	29	34.0	18.9	2.5	7.9	0.46	good
135	1651	85.5	98.7	MSP	Ice	10.02	-15.6	46	351	372	21.6	4.8	14.1	0.82	poor
136	1575	61.7	98.8	MSP	Ice	0.099	-15.7	15	381	381	25.6	5.2	12.6	0.78	good
138	1627	78.0	99.8	MSP	Ice	0.099	-15.7	17	351	377	26.5	5.5	13.1	0.60	good
141	1513	40.3	99.6	MSP	Ice	9.94	-15.5	23	363	397	22.0	4.0	12.6	0.70	fair
142	1514	40.5	99.9	MSP	Ice	0.100	-15.7	16	385	386	25.4	4.6	12.9	0.75	fair
146	1673	91.9	100.1	MSP	Ice	9.99	-15.8	25	313	389	21.3	4.0	11.4	0.55	fair
148	1671	91.5	99.5	MSP	Ice	0.099	-15.8	12	334	387	33.0	5.0	13.0	0.50	poor

1 Secant value from start of test

2 Tangent value at upper yield stress

NA - Not Available

Numbers in italics were not used in analysis for Young's modulus or yield offset

TABLE 7. Specimen properties, testing conditions and measured small strain parameters:
Results at T = -20°C

Test No.	Dry Density (kg/m ³)	Dr (%)	S _i (%)	Method of Prep.	End Cond.	σ_c avg. (MPa)	T (°C)	Strain Rate (10 ⁻⁷ /sec)			Test Parameters			ACDT Qual.
								Q _{yo} ¹	Q _{uy} ²	Maximum	E (GPa)	Q _{yo} (MPa)	Q _{uy} (MPa)	ϵ_{uy} (%)
70	1647	84.4	101.6	MSP	Ice	0.100	-20.2	142	3900	4089	25.9	8.2	25.7	0.76 good
71	1667	90.3	98.7	MSP	Ice	0.100	-20.6	16	336	346	31.3	6.6	18.0	1.00 good
72	1672	91.7	97.0	MSP	Ice	10.06	-20.6	1.5	29.1	34.6	31.9	5.5	11.4	0.43 good
74	1493	33.2	98.7	MSP	Ice	9.99	-20.5	2.7	30.3	35.8	27.7	0.8	11.1	0.65 poor
75	1535	48.0	99.2	MSP	Ice	0.101	-20.4	9.9	333	368	27.5	4.6	15.8	0.89 fair
76	1513	40.3	99.9	MSP	Ice	0.101	-20.3	17	313	355	29.2	5.1	15.3	0.89 fair
85	1625	77.5	99.9	MSP	Ice	0.102	-20.2	14	326	375	32.1	6.7	16.7	0.76 good
86	1504	37.0	100.0	MSP	Ice	10.06	-20.5	25	303	364	20.7	4.6	15.9	0.91 good
87	1542	50.4	98.7	MSP	Ice	0.102	-20.2		293	358	22.9	NA	15.6	0.68 poor
88	1499	35.4	98.6	MSP	Ice	0.101	-20.3	1.9	20.4	32.2	31.2	4.1	9.8	0.37 fair
89	1504	37.1	96.5	MSP	Ice	0.102	-19.9	177	4800	5939	25.7	8.1	24.8	0.68 good
92	1500	35.6	99.2	MSP	Ice	10.05	-20.3		4200	5436	NA	NA	28.1	0.70 poor
93	1625	77.4	98.6	MSP	Ice	10.02	-20.4	254	4950	5858	33.2	8.4	28.9	0.99 good
94	1677	93.2	99.8	MSP	Ice	0.101	-20.1		22.7	33.4	NA	NA	10.1	0.35 NA
95	1645	86.3	100.2	MSP	Ice	0.100	-20.3	14	261	363	18.8	4.1	16.4	0.90 NA
97	1500	35.7	99.5	MSP	Ice	0.101	-19.9	15	314	353	23.1	5.4	16.3	0.87 good
98	1496	34.3	99.4	MSP	Ice	10.03	-20.1		23	31.3	NA	NA	10.5	0.34 fair
99	1502	36.3	99.7	MSP	Ice	0.102	-20.1	256	4460	5308	25.8	8.8	26.7	0.74 fair
100	1640	82.2	100.8	MSP	Ice	10.03	-19.9	10	298	367	30.5	3.3	17.2	0.73 poor

1 Secant value from start of test

2 Tangent value at upper yield stress

NA - Not Available

Numbers in italics were not used in analysis for Young's modulus or yield offset

CC 3/5/95

TABLE 8. Specimen properties, testing conditions and measured small strain parameters:
Results at T = -25°C

Test No.	Dry Density (kg/m ³)	Dr (%)	S _i (%)	Method of Prep.	End Cond.	σ _c avg. (MPa)	T (°C)	Strain Rate(10 ⁻⁷ /sec)			Test Parameters			ACDT Qual.	
								Q _{yo} ¹	Q _{uy} ²	Maximum	E (GPa)	Q _{yo} (MPa)	Q _{uy} (MPa)		ε _{uy} (%)
102	1549	52.7	100.3	MSP	Ice	0.101	-25.0	171	4020	4433	29.0	9.7	30.9	0.82	fair
103	1500	35.5	101.3	MSP	Ice	0.148	-25.4	1.6	32.4	34.8	24.2	5.4	14.5	0.59	good
104	1504	36.9	101.6	MSP	Ice	0.100	-25.4	13	366	394	22.2	7.7	21.1	0.83	fair
106	1662	88.7	102.6	MSP	Ice	0.100	-25.3	1.2	34.9	34.9	26.4	6.6	15.0	0.87	fair
107	1668	90.4	100.7	MSP	Ice	9.96	-25.3	1.7	30.2	34.5	33.9	6.1	15.0	0.94	good
109	1615	74.5	99.4	MSP	Ice	0.100	-25.4	17	353	389	26.2	7.0	20.5	0.99	good
110	1662	88.6	101.3	MSP	Ice	0.099	-25.3	16	381	382	25.0	5.9	20.9	1.00	poor
111	1498	34.9	100.8	MSP	Ice	9.95	-25.3	25	347	378	28.1	8.0	20.5	0.84	good
113	1547	52.0	100.8	MSP	Ice	0.101	-25.4	15	361	386	26.0	7.4	20.1	0.79	poor
114	1516	41.2	101.5	MSP	Ice	0.098	-25.2	146	4400	4599	27.5	8.0	28.7	0.77	fair
115	1521	43.1	100.3	MSP	Ice	10.00	-25.4	2.1	31.8	34.6	27.2	5.8	13.6	0.55	fair
116	1511	39.4	101.3	MSP	Ice	0.094	-25.3	166	4400	4417	29.6	8.6	30.8	0.86	fair
117	1501	36.1	101.0	MSP	Ice	10.02	-25.8	293	4240	4346	26.0	8.5	31.6	0.97	good

1 Secant value from start of test

2 Tangent value from upper yield stress

NA - Not Available

Numbers in italics were not used in analysis for Young's modulus or yield offset

Results of Linear Regression Analyses on the Upper Yield Stress of Frozen MFS

(a) Strain Rate Dependency: $Q_{uy} = A (\dot{\epsilon})^{1/n}$

Mean T (°C)	A (MPa)	n	r^2	No. of Tests
-9.55	78.4	4.65	0.95	43
-15.6	88.8	5.29	0.97	17
-20.25	106.6	5.56	0.98	19
-25.35	98.6	6.58	0.99	13

(b) Temperature Dependency: $Q_{uy} = C + DT$

Ave. Strain [*] Rate (1/sec)	C (MPa)	D (MPa/°C)	r^2	No. of Tests
2.9×10^{-6}	-0.61	-0.58	0.97	21
3.35×10^{-5}	0.82	-0.77	0.98	51
4.35×10^{-4}	6.37	-0.97	0.96	19

* Average of mean values of tangent $\dot{\epsilon}$ at Q_{uy}
for each temperature

Sheet A6

APPENDIX B: Programs Reporting Large-Strain Behavior of Saturated Frozen Sands and Data on Large-Strain Behavior

<u>Sheet No.</u>	<u>Description</u>
B1 to B4	Table B Summary of Programs Reporting Large-Strain Behavior of Saturated Frozen Sands (Modified from Andersen 1991) Tables from Andersen (1991) and Swan (1994) Giving Specimen Properties, Testing Conditions and Measured Parameters
B5 & B6	Results at $T = -10^{\circ}\text{C}$
B7	Results at $T = -15^{\circ}\text{C}$
B8	Results at $T = -20^{\circ}\text{C}$
B9	Results at $T = -25^{\circ}\text{C}$
B10 & B11	Additional Large Strain Parameters to Supplement Sheets B5 to B9
B12	Parametric Analysis Illustrating the Relative Importance of Testing Variables on the Peak Strength of Frozen MFS
B13	Normalized Strength Increase vs. Temperature at Varying Strain Rates for Loose and Dense Frozen MFS
B14 & B15	Axial Strain at Peak Strength vs. Relative Density and Confining Pressure

3/12/95 4/95

Table B Programs Reporting Large Strain Behavior of Saturated Frozen Sands (p 1 of 4)

Reference (Program Letter)	Material Tested			Strain Meas.		Testing Variables				Focus Remarks
	Name (d_{50} , mm)	* Prep.	S_i (%)	On- Specimen ϵ_a	Volum.	Density	σ_c (MPa)	$\dot{\epsilon}$ ($10^{-6}/\text{sec}$)	T ($^{\circ}\text{C}$)	
Bragg and Andersland (1980) (A)	Wedron Silica 30-140 $d = 0.1-0.6, C_u = 1.5$	P V	98 ± 2	No	No	Dense $Q \approx 0.56$	0	0.6 to 1800	-2 -6 -10 -15	Focus on $\dot{\epsilon}$ & T
Parameswaran (1980) (B)	Ottawa 30-100 $C_u = 1.9$ (0.37)	C	Not reported ≈ 95 ?	No	No	Dense $Q = 0.53$	0	0.2 to 5000	-2 -6 -10 -15	Focus on $\dot{\epsilon}$ & T
Parameswaran and Roy (1982) (C)	"	C	Same	No	No	"	0	0.5 to 6000	-30	To complete Program B
Orth (1985) (D)	Karlsruhe $C_u = 2.4$ (0.6)	MSP	91	No	No	V. dense $Q = 0.54$	0	0.2 to 330	-2 -10 -15 -20	Focus on $\dot{\epsilon}$ & T
Yuanlin et al. (1988) (E)	Lanzhou Medium $C_u = 2.5$ (0.3)	C	≈ 90 ± 3	No	No	Dense $Q = 0.47$	0	0.5 to 7000	-2 -5 -10 -15	Focus on $\dot{\epsilon}$ & T

* C = Compaction; P = Pluviation; V = vibration; MSP = multiple sieve pluviation

Table B Programs Reporting Large Strain Behavior of Saturated Frozen Sands (p2 of 4)

Reference (Program Letter)	Material Tested			Strain Meas.		Testing Variables				Focus † Remarks
	Name (d_{50} , mm)	* Prep.	S_i (%)	On- Specimen ϵ_a	Volum.	Density	σ_c (MPa)	$\dot{\epsilon}$ (10^{-6} /sec)	T (°C)	
Bourbonnais † Ladanyi (1985) (F)	Le Sueur 16-30 rounded silica $C_u < 1.5$ (≈ 0.7)	P † V	92	No		Medium dense $q \approx 0.65$	0	30 to 3000	-7 -20 -44 -110	Focus on $\dot{\epsilon}$ † T
Chamberlain et al. (1972) (G)	Ottawa 100-200 $C_u < 1.5$ (0.13)	C ? "molded"	100	No	Yes	Medium dense $q \approx 0.6$	3.5 to 275	1000	-10	Focus on σ_c
Sayles (1973) (H)	Ottawa 20-30 $C_u < 1.5$ (0.7)	C ? "packed"	100	No	No	Medium dense $q = 0.59$	0.34 to 8.2	0.5 to 30,000	-3.85	Focus on σ_c † $\dot{\epsilon}$
Shibata et al. (1985) (I)	Toyoura $C_u = 1.5$ (0.18)	P † V ?	100 ?	No	Yes	V. dense $q = 0.65$ ($D_r \approx 95\%$)	0 4.9 9.8	4.5 48 450	-2 -10 -30 -50	All variables except D_r ϵ_v from ϵ_a † $\dot{\epsilon}$
Aikire † Andersland (1973) (J)	Ottawa 20-30 $C_u < 1.5$ (0.7)	V	97	No		Medium dense $q \approx 0.58$	0 to 6.9	44	-12	Focus on σ_c Also data for $S_i = 55\%$

* C = Compaction; P = Pluviation; V = vibration; MSP = multiple sieve pluviation

Table B Programs Reporting Large Strain Behavior of Saturated Frozen Sands (p3 of 4)

Reference (Program Letter)	Material Tested			Strain Meas.		Testing Variables				Focus Remarks
	Name (d_{50} , mm)	* Prep.	Si (%)	On- Specimen ϵ_a	Volum.	Density	σ_c (MPa)	$\dot{\epsilon}$ (10^{-6} /sec)	T (°C)	
Perkins & Raudrich (1973) (K)	Penn 40-200 quartz	V	Not reported 100?	No	No	Dense	0 to 11.5	11	-7.8	Focus on σ_c
Parameswaran & Jones (1981) (L)	Ottawa 30-100 $C_u = 1.9$ (0.37)	C	" "	No	No	Med. dense $\rho = 0.59$ $w = 20\%$	0 to 76	77	-10	Focus on σ_c
Goughnour & Andersland (1968) - (M)	Ottawa 20-30 $C_u < 1.5$ (0.7)	C?	97	No	Yes	Varied	0 0.7	2.2 & 4.4	-3.9 & -12	Mostly ice- sand mixtures
Jones & Parameswaran (1983) (N)	Ottawa 30-100 $C_u = 1.9$ (0.37)	C	Not reported 95?	No	No	Varied	0.1 to 82	77	-11	Ice-sand mixtures
Sayles & Epanehin (1966) (P)	Ottawa 16-100 (ASTM C-109) $C_u = 2$ (0.4)	V	100	No	No	Dense $\rho = 0.55$ ± 0.05	0	30 to 20,000	-3 -6.5 -10 -30	Focus on ϵ & T

* C = Compaction; P = Pluviation; V = vibration; MSP = multiple sieve pluviation

Table B Programs Reporting Large Strain Behavior of Saturated Frozen Sands (p 4 of 4)

[illegible]

* C = Compaction; P = Pluviation; V = vibration; MSP = multiple sieve pluviation

TABLE 5.3 (page 1 of 5)
MEASURED CONVENTIONAL FROZEN TESTS RESULTS
Test Results at $T = -10^{\circ}\text{C}$ (from Andersen 1991)

FRS Test #	D_r %	σ_c MPa	TEMP ($^{\circ}\text{C}$)	STRAIN RATE /sec $@\dot{\epsilon}_{yo} \times 10^7$	SMALL STRAIN RESPONSE E GPa	UPPER YIELD REGION Q_{uy} MPa	PEAK STRENGTH Q_p MPa	$Q - \epsilon_a$ Curve Type	VOLUMETRIC BEHAVIOR Max. $d\epsilon_v/d\epsilon_a \times 10^2$	ϵ_{v20} %	$S^* A^*$ f f p vp
15	31.6	10.15		31	21.4	7.3	11.6	D	NA	NA	f
18	48.4	10.18		27	28.6	7.2	13.4	D	NA	NA	f
19	49.4	10.18		24	21.4	7.2	13.1	D	3	0.4	f
120	76.3	10.18		31	20.7	8.6	16.7	D	5	0.4	f
121	74.4	10.18		27	311	20.0	16.0	D	4	0.3	p
122	80.3	10.15		22	320	25.0	16.3	D	5	0.4	p
23	56.2	5.12		19	330	23.1	12.7	D	4	0.6	p
124	90.5	5.12		19	303	33.3	15.8	D	12	1.5	f
25	52.8	2.05		21	336	26.1	10.9	D	17	2.0	p
126	94.0	2.08		18	300	31.8	14.7	C	23	NA	p
127	90.5	2.07		15	348	33.3	15.1	C	31	NA	p
128	99.2	0.103		15	386	21.2	14.6	C	42	NA	p
29	56.2	0.106		15	334	25.9	10.1	C	29	NA	f
30	21.8	0.106		17	339	25.9	8.5	By	26	3.7	f
31	23.0	0.106		12	352	29.2	8.6	By	29	3.8	f
32	80.3	0.102		16	344	28.0	10.9	C	50	6.6	f
33	60.6	0.103		22	337	29.2	10.2	C	42	5.5	f
34	36.7	0.102		24	358	23.5	9.4	C	33	3.7	f
35	36.3	0.101		53	1070	25.8	10.6	A	35	4.2	f
36	36.7	0.101		230	4950	25.0	15.0	A	39	5.4	f
37	96.9	0.101		180	4790	30.3	16.4	C	60	9.5	p
38	94.3	0.101		14	322	41.2	11.7	C	47	7.4	vp
39	92.8	10.11		260	5360	29.0	21.6	D	12	1.8	p

Numbers in *italics* not used in presentations (see Table 5.2 for summary of conditions)

- 1 = Specimens formed by Wet Tamping
2 = Specimens with non-lubricated ends
 S^* = Stability Qualifiers
 A^* = ACDT Qualifiers
NA = Not Available
See Fig. 5.21 for Curve Types

TABLE 5.3 (page 2 of 5)
MEASURED CONVENTIONAL FROZEN TESTS RESULTS
Test Results at T = -10 °C (from Andersen 1991)

FRS Test #	D _r %	σ _c MPa	TEMP (°C)	STRAIN RATE /sec @Q _{y0} x10 ⁷	SMALL STRAIN RESPONSE		UPPER YIELD REGION		PEAK STRENGTH REGION		Q - ε _a Curve Type	VOLUMETRIC BEHAVIOR Max. dε _v /dε _a x10 ²	S* ε _f p vp	A* ε _f p p	
					E GPa	Q _{y0} MPa	Q _{uy} MPa	ε _y %	Q _p MPa	ε _p %					
40	37.4	10.13		400	25.7	4.7	15.0	0.83	15.4	16.5	B	4	0.5	g	p
41 ²	96.0	0.102		180	5380	38.5	4.7	16.6	0.89	17.1	C	67	9.8	g	p
42 ²	93.4	10.13		19	362	25.0	3.1	8.2	0.50	17.8	C	8	0.8	g	p
43 ²	90.8	0.102		16	342	25.9	4.2	8.8	0.50	12.4	C	64	8.6	g	p
44	36.3	0.102		17	366	25.7	4.1	8.2	0.48	9.3	C	36	3.9	g	p
45	38.1	0.102		1.6	30.9	28.6	3.0	5.0	0.28	6.6	C	33	3.0	g	p
46	92.0	0.101		1.3	24.3	40.0	3.3	5.1	0.26	8.5	C	57	7.8	g	p
47	43.5	10.03		1.9	29.2	20.0	2.7	4.8	0.36	9.1	D	NA	0	g	p
48	96.3	10.04		2.0	27.2	25.0	2.7	4.9	0.34	13.1	D	NA	NA	vp	g
49	96.9	10.01		370	4380	24.3	4.3	15.4	0.85	22.0	D	11	1.8	p	g
51	80.0	10.02		20	370	31.6	3.3	8.8	0.52	17.9	D	4	0.5	f	p
52	90.8	10.04		27	355	20.7	2.8	8.2	0.48	19.0	D	6	0.7	f	p
53	92.5	5.03		15	352	35.3	2.9	8.5	0.51	16.5	D	13	1.6	p	f
54	94.0	10.04		3.1	32.5	26.3	2.8	5.4	0.44	16.0	D	4	0.5	g	p
55	88.1	2.00		24	382	26.1	3.4	7.9	0.44	13.1	D	27	3.2	g	p
56	92.8	0.101		12	371	46.7	3.8	9.5	0.49	13.1	C	61	8.4	f	p
57	35.6	0.101		18	384	25.0	3.3	8.7	0.54	9.6	C	35	3.9	g	p
58	93.7	0.100		0.7	32.9	14.3	1.8	5.6	0.49	9.3	C	67	8.3	g	p
59	30.1	5.01	-9.60	23	333	29.2	3.5	8.9	0.44	11.5	D	6	0.4	f	f
60	54.2	2.01	-9.50	20	339	31.8	3.5	9.2	0.43	11.4	C	22	2.8	f	f
61	33.4	10.02	-9.57	2.8	28.9	21.7	2.9	5.1	0.34	9.0	D	2	0.1	g	p
62	54.2	5.00	-9.47	19	335	25.9	3.4	8.3	0.43	12.8	D	6	0.4	g	p
63	51.1	10.03	-9.53	28	335	24.0	3.0	8.2	0.50	14.4	D	1	0.1	g	p
64	82.7	10.02	-9.50	23	338	24.3	3.3	7.9	0.48	17.8	D	2	0.2	f	g
65	95.7	0.102	-9.54	290	4990	26.3	5.0	15.8	0.82	16.8	C	60	9.1	p	f
66	83.0	0.102	-9.57	18	235	35.6	4.3	8.4	0.27	12.1	C	46	6.7	f	g
67	33.1	2.01	-9.62	26	339	25.0	3.6	8.0	0.42	10.2	D	15	1.9	g	g

See page 1 for notes

TABLE 5.3 (page 3 of 5)
MEASURED CONVENTIONAL FROZEN TESTS RESULTS
Tests Results at T = -15 °C

FRS Test #	Dr %	σ_c MPa	TEMP (°C)	STRAIN RATE /sec @Q _{y0} x10 ⁷	STRAIN RATE /sec Nom. x10 ⁷	SMALL STRAIN RESPONSE E GPa	SMALL STRAIN RESPONSE Q _{y0} MPa	UPPER YIELD REGION Q _{uy} MPa	UPPER YIELD REGION ϵ_y %	PEAK STRENGTH REGION Q _p MPa	PEAK STRENGTH REGION ϵ_p %	Q - ϵ_a Curve Type	VOLUMETRIC BEHAVIOR Max. d ϵ_v /d ϵ_a x10 ²	VOLUMETRIC BEHAVIOR ϵ_{v20} %	S* g f p vp	A* g f p
121	91.7	9.99	-15.4	286	4480	23.1	4.4	21.7	1.04	25.5	7.69	C	15	2.7	f	f
123	90.7	9.94	-15.6	1.9	34.6	22.8	3.2	7.9	0.55	17.3	15.0	D	NA	NA	f	f
126	48.7	9.99	-15.5	230	4340	24.3	4.9	20.3	0.94	20.3	0.94	B	7	1.2	g	p
127	35.4	9.96	-15.5		35.3	NA	NA	7.8	1.09	11.4	22.1	D	NA	NA	g	p
128	52.1	9.97	-15.6	19	394	26.9	2.8	12.2	0.76	16.5	21.1	D	NA	NA	g	p
129	47.7	9.91	-15.5	201	4480	26.9	5.3	20.4	0.94	20.4	0.94	B	14	2.0	g	p
130	38.2	9.86	-15.8		35.7	22.9	NA	7.6	0.68	10.8	21.3	D	NA	NA	g	p
131	86.9	9.94	-15.6	2.5	34.6	14.2	1.9	9.0	0.54	17.0	8.61	D	NA	NA	vp	vp
133	79.8	10.02	-15.6	18	403	28.9	3.1	12.9	0.70	19.6	10.7	D	NA	NA	vp	vp
134	85.8	9.96	-15.5	1.9	34.0	18.9	2.5	7.9	0.46	17.4	14.2	D	NA	NA	p	p
135	85.5	10.02	-15.6	20	372	21.6	4.8	14.1	0.82	21.3	13.0	D	NA	NA	g	p
136	61.7	0.099	-15.7	15	381	25.6	5.2	12.6	0.78	13.7	7.02	C	35	5.4	f	f
138	78.0	0.099	-15.7	15	377	26.5	5.5	13.1	0.60	15.2	4.60	C	56	7.4	f	f
141	40.3	9.94	-15.5	23	397	22.0	4.0	12.3	0.70	15.5	22.3	D	NA	NA	g	f
142	40.5	0.100	-15.7	14	384	25.4	4.6	12.9	0.75	13.1	2.59	C _y	40	4.8	f	f
146	91.9	9.99	-15.8	20	388	21.3	4.0	11.4	0.55	21.5	12.6	D	NA	NA	f	f
148	91.5	0.099	-15.8	11	387	33.0	5.0	13.0	0.50	16.6	4.91	C	49	NA	p	p

See page 1 for notes

TABLE 5.3 (page 4 of 5)
MEASURED CONVENTIONAL FROZEN TESTS RESULTS
Tests Results at T = -20 °C

FRS Test #	D _r %	σ _c MPa	TEMP (°C)	STRAIN RATE /sec		SMALL STRAIN RESPONSE		UPPER YIELD REGION		PEAK STRENGTH REGION		Q - ε _a Curve Type	VOLUMETRIC BEHAVIOR		S*	A*
				@Q _{y0} x10 ⁷	Nom. x10 ⁷	E GPa	Q _{y0} MPa	Q _{uy} MPa	ε _y %	Q _p MPa	ε _p %		Max. dε _v /dε _a x10 ²	ε _{v20} %		
70	84.4	0.100	-20.2	118	4090	25.9	8.2	25.7	0.76	25.7	0.76	A	65	8.5	g	g
71	90.3	0.100	-20.6	18	346	31.3	6.6	18.0	1.00	20.6	4.74	C	64	8.2	g	g
72	91.7	10.06	-20.6	18	34.6	31.9	5.5	11.4	0.43	21.2	15.9	D	5	0.7	g	p
74	33.2	9.99	-20.5	1.5	35.8	21.7	0.8	11.1	0.65	14.0	19.6	D	11	0.6	g	p
75	48.0	0.101	-20.4	9.4	368	27.5	4.6	15.8	0.89	15.9	3.44	C _y	24	4.0	g	p
76	45.7	0.101	-20.3	14	355	29.2	5.1	15.3	0.89	15.6	4.13	C _y	28	4.1	g	p
85	77.5	0.102	-20.2	11	375	32.1	6.7	16.7	0.76	18.6	4.52	C	43	6.7	g	p
86	37.0	10.06	-20.5	25	364	20.7	4.6	15.9	0.91	18.3	16.8	D	5	0.8	g	p
87	50.4	0.102	-20.2		358	22.9	NA	15.6	0.68	15.8	3.06	C _y	33	4.5	g	p
88	35.4	0.101	-20.3	1.3	32.2	31.2	4.1	9.8	0.37	11.3	4.44	C	35	3.9	g	p
89	37.1	0.102	-19.9	180	5940	25.7	8.1	24.8	0.68	24.8	0.68	A	50	7.0	g	p
92	35.6	10.05	-20.3	27	5440	NA	NA	28.1	0.70	28.1	0.70	B _y	16	2.4	g	p
93	77.5	10.02	-20.4		5860	33.2	8.4	28.9	0.99	28.9	0.99	A	23	NA	g	g
94	93.2	0.101	-20.1	14	33.3	NA	NA	10.1	0.35	14.7	4.62	C	58	8.6	g	NA
95	86.3	0.100	-20.3	14	363	18.8	4.1	16.4	0.90	18.9	4.27	C	38	6.3	g	NA
97	35.7	0.101	-19.9	14	353	23.1	5.4	16.3	0.87	16.3	0.87	A	27	3.9	g	g
98	34.3	10.03	-20.1		31.3	NA	NA	10.5	0.34	14.1	19.6	D	12	2.1	g	f
99	36.3	0.102	-20.1	253	5310	25.8	8.8	26.7	0.74	26.7	0.74	A	47	6.3	g	f
100	82.2	10.03	-19.9	231	367	30.5	3.3	17.2	0.73	23.6	12.3	D	13	NA	g	p

See page 1 for notes

TABLE 5.3 (page 5 of 5)
MEASURED CONVENTIONAL FROZEN TESTS RESULTS
Tests Results at T = -25 °C

FRS Test #	D _r %	σ_c MPa	TEMP (°C)	STRAIN RATE /sec		SMALL STRAIN RESPONSE		UPPER YIELD REGION		PEAK STRENGTH REGION		Q - ϵ_a Curve Type	VOLUMETRIC BEHAVIOR		S*	A*
				@Q _{yo} x10 ⁷	Nom. x10 ⁷	E GPa	Q _{yo} MPa	Q _{uy} MPa	ϵ_y %	Q _p MPa	ϵ_p %		Max. d ϵ_v /d ϵ_a x10 ²	ϵ_{v20} %		
102	52.7	0.101	-25.0	171	4430	29.0	9.7	30.9	0.82	30.9	0.82	A	45	NA	vp	f
103	35.5	0.148	-25.4	1.5	34.8	24.2	5.4	14.5	0.59	15.6	6.34	B	48	6.6	g	g
104	36.9	0.100	-25.4	13	394	22.2	7.7	21.1	0.83	21.1	0.83	A	51	4.3	f	f
106	88.8	0.100	-25.3	1.1	34.9	26.4	6.6	15.0	0.87	19.0	4.85	C	61	7.9	g	f
107	90.4	9.96	-25.3	1.7	34.5	33.9	6.1	15.0	0.94	23.4	12.6	D	11	2.0	vp	g
109	74.5	0.100	-25.4	17	389	26.2	7.0	20.6	0.99	21.0	3.99	C _y	40	6.0	p	g
110	88.6	0.099	-25.3	16	382	25.0	5.9	21.2	1.00	23.0	5.63	C	53	7.7	g	p
111	34.9	9.95	-25.3	26	378	28.1	8.0	20.5	0.84	20.5	0.84	B _y	12	1.8	g	p
113	52.0	0.101	-25.4	15	386	26.0	7.4	20.1	0.79	20.1	0.79	A	62	5.0	f	g
114	41.2	0.098	-25.2	206	4600	27.5	8.0	28.7	0.77	28.7	0.77	A	49	7.2	vp	f
115	43.1	10.00	-25.4	2.2	34.6	27.2	5.8	13.6	0.55	17.0	24.0	D	5	0.9	g	f
116	39.4	0.094	-25.3	175	4420	29.6	8.6	30.8	0.86	30.8	0.86	A	45	5.9	p	f
117	36.1	10.02	-25.8	303	4350	26.0	8.5	31.6	0.97	31.6	0.97	B _y	12	2.2	f	g

See page 1 for notes

CCL 3/11/95

SUNATLSA.WK3 page 1

12-Feb-95/CWS

FRS Test Results

LOW CONFINEMENT

Temperature = -10°C

Test #	Sig c	Dr	SR	T	Quy	euY	Op	ep	evp	SHmax	dV max	edvmax	SHEROD	ev20	Q20	CT	Qp-Quy	Qp/Quy	Q20-Qp	Q20/Qp	ev20-evp	ev20-edvmax
29	0.106	56.2	3.34B-05	-9.55	8.2	0.47	10.1	6.2	0.531	73	29	13.2	-17	7.67	By	1.9	1.2317	-0.83	0.9024	3.229	-9.9	-7
30	0.106	21.8	3.39B-05	-9.55	8.4	0.5	8.5	6.1	0.471	26	26	13.2	-14	7.19	By	0.1	1.0119	-1.41	0.836	3.709	-10.9	-9.9
31	0.106	23	3.52B-05	-9.55	8.3	0.5	8.6	4.8	0.491	15	15	15.7	-11	8.13	By	0.3	1.0361	-1.71	0.7514	6.045	-12.4	-12.4
32	0.102	80.3	3.44B-05	-9.55	8.3	0.42	10.9	5.2	0.555	96	50	18.5	-21	8.19	By	2.6	1.3133	-2.02	0.802	4.98	-12.3	-12.3
33	0.102	36.6	3.37B-05	-9.55	8.5	0.53	10.2	5.2	0.52	100	42	17.4	-17	8.22	By	1.7	1.12	-1.08	0.8851	3.252	-12.3	-12.3
34	0.102	36.7	3.58B-05	-9.55	8.7	0.47	9.4	6.4	0.448	31	33	19.2	-14	8.22	By	0.7	1.0805	-1.86	0.8229	4.243	-18.93	-18.93
35	0.101	36.3	3.07B-04	-9.55	10.5	0.67	10.5	0.67	0.403	33	35	19.6	-20	8.22	By	0	1	-1.58	0.6413	5.431	-15.86	-15.86
36	0.101	36.7	4.95B-04	-9.55	15	0.74	15	0.74	0.031	25	39	16.6	-45	8.22	By	0	1	-6.32	0.6146	8.713	-7.5	-7.5
37	0.101	96.9	4.79B-04	-9.55	15.4	0.83	15.4	3.9	0.787	54	60	11.4	-54	8.22	By	0.5	1.0649	-8.32	0.4848	9.291	-11.4	-11.4
41	0.102	90.8	3.38B-05	-9.55	8.8	0.5	12.4	3.9	0.855	158	64	19.5	-34	8.22	By	3.6	1.4031	-5.36	0.5677	7.745	-14.6	-14.6
43	0.102	36.8	3.36B-05	-9.55	8.2	0.48	9.3	3.9	0.161	46	33	16.4	-13	8.22	By	2.4	1.5667	-2.29	0.7306	6.593	-14.6	-14.6
44	0.102	38.1	3.09B-06	-9.55	5.1	0.26	8.5	8.1	0.297	154	57	12.2	-19	8.22	By	3.4	1.5667	-2.29	0.7306	6.593	-14.6	-14.6
45	0.101	92.8	3.71B-05	-9.55	9.5	0.49	13.1	5.2	0.807	100	61	19.6	-28	8.22	By	0.9	1.1034	-1.48	0.8458	3.789	-17.3	-17.3
46	0.101	35.6	3.84B-05	-9.55	8.7	0.54	9.3	6.4	0.111	38	35	21.3	-9	8.22	By	3.7	1.6807	-2.61	0.7134	8.525	-11.3	-11.3
58	0.1	93.7	3.29B-06	-9.55	15.8	0.49	9.3	6.8	0.164	128	67	18.1	-22	8.22	By	3.7	1.6807	-2.61	0.7134	8.525	-11.3	-11.3
65	0.102	95.7	4.99B-04	-9.55	15.8	0.82	16.8	5.1	0.575	46	60	15.7	-42	8.22	By	3.7	1.6807	-2.61	0.7134	8.525	-11.3	-11.3
66	0.102	83	2.35B-05	-9.55	8.4	0.27	12.1	5.1	0.475	185	46	12.6	-30	8.22	By	3.7	1.4405	-3.55	0.7066	6.225	-7.5	-7.5

Temperature = -15°C

Test #	Sig c	Dr	SR	T	Quy	euy	Qp	ep	evp	SH	dv	max	edvmax	SHEROD	ev20	Q20	CT	Qp-Quy	Qp/Quy	Q20-Qp	Q20/Qp	ev20-evp	ev20-edvmax	
136	0.099	61.7	3.81B-05	-15.74	12.57	0.78	13.68	7.02	1.124	37.2	35	19.8	-29	10.53	C	5.4	10.53	C	1.11	1.083	-3.15	0.7697	4.276	-12.78
138	0.099	78	3.77B-05	-15.73	13.06	0.6	15.2	4.6	0.58	91.1	56	17.2	-35	10.74	C	7.4	10.74	C	2.14	1.1639	-4.46	0.7066	6.82	-12.6
142	0.1	40.5	3.86B-05	-15.74	12.91	0.75	13.06	2.59	0.106	6.6	40	18.4	-21	10.23	Cy	4.8	10.23	Cy	0.15	1.0116	-2.83	0.7833	4.694	-15.81
148	0.099	91.5	3.87B-05	-15.81	12.97	0.5	16.64	4.91	0.869	137	49	11.3	-46	9.63	C	9.63	9.63	C	3.67	1.283	-7.01	0.5787	-0.869	-6.39

Temperature = -20°C

Set #	sig c	Dr	SR	T	Quy	euY	Qp	ep	evp	SH	dV max	edvmax	SHEROD	ev20	Q20	CT	Qp-Quy	Qp/Quy	Q20-Qp	Q20/Qp	ev20-evp	ev20-edvmax
70	0.1	84.4	4.09E-04	-20.2	25.72	0.76	25.72	0.76	0.371	-163	65	12.3	-65	8.5	13.97	A	0	1.145	-11.75	0.5432	8.129	-11.54
71	0.1	90.3	3.46E-05	-20.41	15.8	0.89	15.8	4.74	0.493	127	64	17.7	-59	8.2	12.63	C	2.61	1.45	-7.98	0.512	7.707	-11.94
75	0.101	45.7	3.55E-05	-20.29	15.3	0.89	15.6	4.13	0.433	28	28	5.2	-40	4	12.63	Cy	0.1	1.056	-7.98	0.6128	7.707	-11.94
85	0.102	77.5	3.75E-05	-20.15	16.65	0.76	16.65	4.52	0.501	79.9	43	10.5	-54	4.1	11.75	Cy	0.3	1.056	-6.83	0.6324	6.199	-3.87
87	0.102	50.4	3.58E-05	-20.16	15.57	0.68	15.57	3.06	0.26	8.4	33	12.1	-22	4.5	11.75	Cy	1.93	1.159	-6.83	0.6324	6.199	-3.87
88	0.101	35.4	3.22E-06	-20.28	9.84	0.37	9.84	4.44	0.382	60.4	35	21.5	-17	3.9	11.75	C	1.93	1.022	-6.83	0.7552	4.24	-9.04
94	0.101	98.2	3.34E-05	-20.09	10.09	0.35	10.09	4.62	0.61	182	58	14.2	-41	8.6	9.38	C	1.43	1.153	-1.89	0.823	3.518	-17.06
97	0.101	35.7	3.53E-05	-19.93	16.26	0.87	16.26	0.87	0.068	-35	27	11.3	-26	6.3	8.96	A	4.65	1.409	-5.78	0.679	7.99	-9.58
99	0.102	36.3	5.31E-04	-20.09	26.68	0.74	26.68	0.74	0.737	-700	47	12	-46	3.9	13.08	A	0	1	-13.6	0.7109	3.968	-10.43
														6.3	11.06	A	0	1	-13.6	0.4903	5.563	-11.26

Temperature = -25°C

test #	Sig c	Dr	SR	T	Quy	euy	Qp	ep	evp	SH	dV max	edvmax	SHEROD	ev20	Q20	CT	Qp-Quy	Qp/Quy	Q20-Qp	Q20/Qp	ev20-evp	ev20-edvmax
103	0.148	35.5	3.48B-06	-25.35	14.51	0.59	15.6	6.34	1.503	33.4	48	16.8	-7	6.6	14.95	B	1.09	1.0751	-0.65	0.9583	5.097	-10.46
104	0.1	36.9	3.94B-05	-25.38	21.11	0.83	21.11	0.83	0.169	-134	31	14.6	-23	4.1	15.18	A	0	1	-5.93	0.7191	7.931	-13.77
106	0.1	88.8	3.49B-06	-25.34	15.04	0.87	18.99	4.85	0.887	175	61	18.5	-43	7.9	12.78	C	3.95	1.2626	-7.62	0.6373	7.931	-13.77
109	0.1	74.5	3.89B-05	-25.36	20.6	0.99	21	3.95	0.86	25.8	40	18.2	-49	7.6	13.35	Cy	0.4	1.0194	-7.65	0.6357	5.4	-14.31
110	0.099	88.6	3.82B-05	-25.3	21.2	1	22.95	5.63	1.351	70.5	53	20.6	-30	7.7	18.5	Cy	1.75	1.0825	-4.45	0.8061	6.349	-14.31
113	0.101	52	3.86B-05	-25.35	20.05	0.79	20.05	0.79	0.07	-129	36	19.5	-34	5.9	13.48	A	0	1	-6.57	0.6223	4.93	-18.17
116	0.094	39.4	4.42B-04	-25.32	30.79	0.86	30.79	0.86	0.338	-342	45	19.8	-21	5.9	17.25	A	0	1	-13.54	0.5602	5.562	-18.94

Sheet B10

SUMATISA.WK3 page 2 See p1 for notation

FRS Test Results

HIGH CONFINEMENT
Temperature = -10°C

Test #	Sig C	Dr	SR	T	Quy	euy	Qp	ep	evp	SHmax	dV max	edvmax	SHEROD	ev20	Q20	CT	Qp-Quy	Qp/Quy	Q20-Qp	Q20/Qp	ev20-evp	ev20-edvmax
15	10.15	31.6	3.368-05	-9.55	7.3	0.5	11.6	27.7	0.37	46	3	16.5	9	0.4	11.25	D	4.3	1.589	-0.35	0.9698		
18	10.18	48.4	3.338-05	-9.55	7.2	0.33	13.4	24.9	0.84	73	12	11	11	0.4	13.2	D	6.2	1.8611	-0.2	0.9851		
19	10.18	49.4	3.448-05	-9.55	7.2	0.33	13.4	18.4	0.37	81	12	11	11	0.4	13.2	D	5.9	1.8194	-0.1	0.9924	0.03	1.9
39	10.11	32.8	3.368-04	-9.55	16.1	1.02	13.1	18.4	0.84	104	4	16.4	2	0.5	20.58	D	5.5	1.3416	-0.02	0.9528	0.946	2.1
40	10.13	37.4	3.428-04	-9.55	15	0.93	15.4	16.9	0.281	14	4	9.4	2	0.8	15.39	B	0.4	1.0267	-0.01	0.9994	0.219	7.5
42	10.13	33.4	3.328-05	-9.55	8.2	0.5	18.8	17.8	0.608	185	8	16.4	0	0	18.55	D	10.6	2.2927	-0.15	0.992	0.192	1.4
47	10.03	43.5	2.228-06	-9.55	4.8	0.36	19.1	24.4	-0.304	54	11	15.5	0	0	8.2	D	4.3	1.8958	-0.18	0.9802	0.304	24.4
48	10.04	36.3	2.228-06	-9.55	4.9	0.34	13	13	0.37	119	11	15.5	0	0	9.07	D	8.1	2.6531	-0.33	0.9377		
49	10.01	36.9	4.368-04	-9.55	15.4	0.85	22	14.9	11	117	4	21.1	0	1.8	21.12	C	6.6	1.4286	-0.88	0.96	-9.2	-0.6
51	10.02	80	3.708-05	-9.55	8.8	0.42	17.9	23.4	0.655	152	6	14.1	23	0.5	17.78	D	9.1	2.0341	-0.12	0.9933	-0.155	2.3
52	10.04	90.8	3.558-05	-9.55	8.2	0.48	19	22.9	0.886	158	6	14.1	14	0.7	18.09	D	10.6	2.3171	-0.11	0.9942	-0.186	8.8
54	10.04	34	3.358-06	-9.55	5.4	0.44	16	22.9	0.555	142	2	18.3	14	0.5	15.95	D	10.6	2.3171	-0.11	0.9942	-0.186	8.8
63	10.02	33.4	2.358-06	-9.55	5.1	0.34	14.4	26.6	0.236	46	2	13.1	10	0.1	8.71	D	6.2	1.7647	-0.29	0.9678	-0.055	3.6
63	10.03	51.1	3.358-05	-9.55	8.2	0.5	14.4	26.6	0.236	81	1	13.1	18	0.1	14.02	D	6.2	1.7647	-0.29	0.9678	-0.055	3.6
64	10.02	82.7	3.388-05	-9.55	7.9	0.48	17.8	24	0.236	127	2	19.6	9	0.2	17.62	D	9.3	2.2532	-0.38	0.9736	-0.008	13.3
																			-0.18	0.9899	-0.096	4.4

Temperature = -15°C

Test #	Sig C	Dr	SR	T	Quy	euy	Qp	ep	evp	SH	dV max	edvmax	SHEROD	ev20	Q20	CT	Qp-Quy	Qp/Quy	Q20-Qp	Q20/Qp	ev20-evp	ev20-edvmax
121	9.986	91.7	4.488-04	-15.44	21.71	1.04	25.51	7.69	1.052	78.6	15	10.4	-12	2.7	23.24	C	3.8	1.175	-2.27	0.911	1.648	-2.71
123	9.944	90.7	4.348-06	-15.57	7.92	0.53	17.3	15	0.195	162	7	13	9	1.2	20.01	By	9.38	2.1843	-0.32	0.9843	1.005	-12.06
126	9.986	48.7	4.348-04	-15.54	20.33	0.94	20.33	0.34	0.195	51.2	7	13	9	1.2	20.01	By	3.65	1.4704	-0.59	0.9711	2.249	-11.56
127	9.959	35.4	3.538-06	-15.54	7.78	1.09	11.4	22.14	0.195	44.9	14	12.5	7	2	19.85	B	4.39	1.3613	-0.59	0.9711	2.249	-11.56
128	9.972	52.1	3.348-05	-15.54	12.15	0.74	16.4	21.06	-0.249	49.2	14	12.5	7	2	19.85	B	3.18	1.4168	-0.59	0.9711	2.249	-11.56
129	9.906	47.7	4.488-04	-15.47	20.44	0.94	20.44	0.34	-0.249	49.2	14	12.5	7	2	19.85	B	3.18	1.4168	-0.59	0.9711	2.249	-11.56
130	9.86	38.2	3.378-06	-15.38	7.63	0.38	10.1	21.35	0.38	189	14	12.5	7	2	19.85	B	3.18	1.4168	-0.59	0.9711	2.249	-11.56
134	9.961	85.8	3.408-06	-15.51	7.92	0.46	17.38	14.33	0.38	189	14	12.5	7	2	19.85	B	3.18	1.4168	-0.59	0.9711	2.249	-11.56
135	10.02	85.5	3.378-05	-15.57	14.1	0.82	21.38	12.38	0.38	189	14	12.5	7	2	19.85	B	3.18	1.4168	-0.59	0.9711	2.249	-11.56
141	9.938	40.3	3.378-05	-15.55	12.63	0.7	15.47	12.38	0.38	189	14	12.5	7	2	19.85	B	3.18	1.4168	-0.59	0.9711	2.249	-11.56
146	9.992	91.9	3.898-05	-15.64	11.38	0.55	21.53	12.36	0.38	189	14	12.5	7	2	19.85	B	3.18	1.4168	-0.59	0.9711	2.249	-11.56

Temperature = -20°C

Test #	Sig C	Dr	SR	T	Quy	euy	Qp	ep	evp	SH	dV max	edvmax	SHEROD	ev20	Q20	CT	Qp-Quy	Qp/Quy	Q20-Qp	Q20/Qp	ev20-evp	ev20-edvmax
72	10.06	91.7	3.468-06	-20.55	11.36	0.33	21.4	15.94	0.446	165	5	12.2	16	0.7	20.8	D	9.88	1.8697	-0.44	0.9793	0.254	3.74
74	9.99	33.2	3.368-06	-20.46	11.07	0.55	14.04	19.6	0.603	59.3	11	14	10	0.6	14.02	D	2.97	1.2683	-0.02	0.9986	-0.003	5.6
86	10.06	37	3.448-05	-20.5	15.94	0.91	18.12	16.8	0.603	28.5	5	10.8	10	0.8	18.28	D	2.38	1.1493	-0.04	0.9978	0.139	6
92	10.05	35.6	5.448-04	-20.38	28.12	0.7	28.12	0.7	0.112	-356	16	13	-12	2.4	22.68	By	0	0	-5.44	0.8065	2.288	-12.3
93	10.02	77.5	5.468-04	-20.42	28.12	0.99	28.12	0.99	1.839	-193	23	14	-10	2.1	14.05	D	3.53	1.3352	-0.01	0.9993	-0.01	8.3
98	10.03	34.3	3.328-06	-20.93	10.53	0.34	14.06	19.6	2.11	72.5	13	11.3	4	2.1	14.05	D	6.41	1.3722	-0.01	0.9993	-0.01	8.3
100	10.03	82.2	3.678-05	-19.93	17.22	0.73	23.63	12.33	2.11	169	13	11.3	4	2.1	14.05	D	6.41	1.3722	-0.01	0.9993	-0.01	8.3

Temperature = -25°C

Test #	Sig C	Dr	SR	T	Quy	euy	Qp	ep	evp	SH	dV max	edvmax	SHEROD	ev20	Q20	CT	Qp-Quy	Qp/Quy	Q20-Qp	Q20/Qp	ev20-evp	ev20-edvmax
111	9.95	34.9	3.768-05	-25.26	20.54	0.84	20.54	0.84	0.206	-87.8	12	19.8	-1	1.8	20.36	By	3.45	1.2546	-0.18	0.9912	1.594	-18.96
115	10	43.1	3.468-06	-25.36	13.55	0.55	17	23.39	0.939	36.9	5	14.4	11	0.9	16.93	D	0	0	-0.07	0.9959	-0.029	9.59
117	10.016	36.1	4.358-04	-25.78	31.64	0.97	31.64	0.97	0.283	-361	12	13.7	-3	2.2	26.31	B	0	0	-5.33	0.8315	1.917	-12.73

Sheet B11

3/11/95

Parametric Analysis Illustrating the Relative Importance of Testing Variables on the Peak Strength of Frozen MFS

A. Reference Condition (Type C curve)







$$\bullet D_r = 60\% \quad \bullet \sigma_c = 0.1 \text{ MPa} \quad \bullet \dot{\epsilon} = 3.5 \times 10^{-5} / \text{s (Moderate)} \quad \bullet T = -15.6^\circ \text{C}$$

$$\therefore Q_p = Q_{uy} + \Delta Q = 12.8 + 1.45 = 14.25 \text{ MPa}$$

B. Results of Parametric Analysis

Variable	$\frac{\Delta Q_p}{\text{Reference } Q_p}$	Remarks
1) Strain Rate ($\dot{\epsilon}$)		
• Decrease by $\times 1/11.7$ (Slow)	- 23%	Large effect that increases with increasing strain rate
• Increase by $\times 14.3$ (Fast \rightarrow Type A curve)	+ 48%	
2) Temperature (T)		
• Increase by $\Delta T = 5^\circ \text{C}$	- 22%	Large effect that is proportional to ΔT
• Decrease by $\Delta T = 5^\circ \text{C}$	+ 21%	
3) Relative Density (D_r)		
• Decrease to $D_r = 30\%$ (Type A)	- 10%	Moderate effect that is proportional to ΔD_r for Type C curves
• Increase to $D_r = 90\%$	+ 12%	
4) Confining Pressure (σ_c)		
• Increase σ_c to 1 MPa	+ 3%	Small effect unless have very large increase in $\Delta \sigma_c$
• Increase σ_c to 10 MPa	+ 29%	

Sheet B12

$\sigma_c(\text{MPa})$	Slow	Mod.	Fast
0.1			
10			

Note: Q_p from linear regression on Q_p vs. Dr data

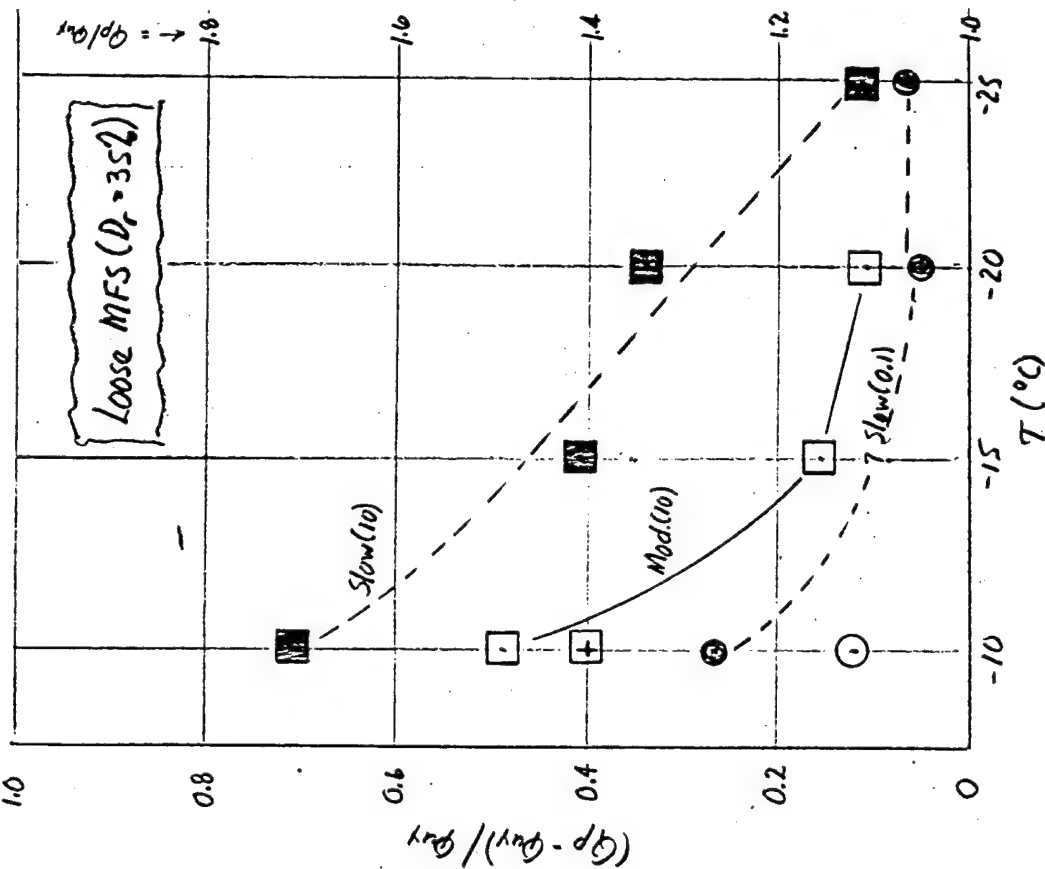
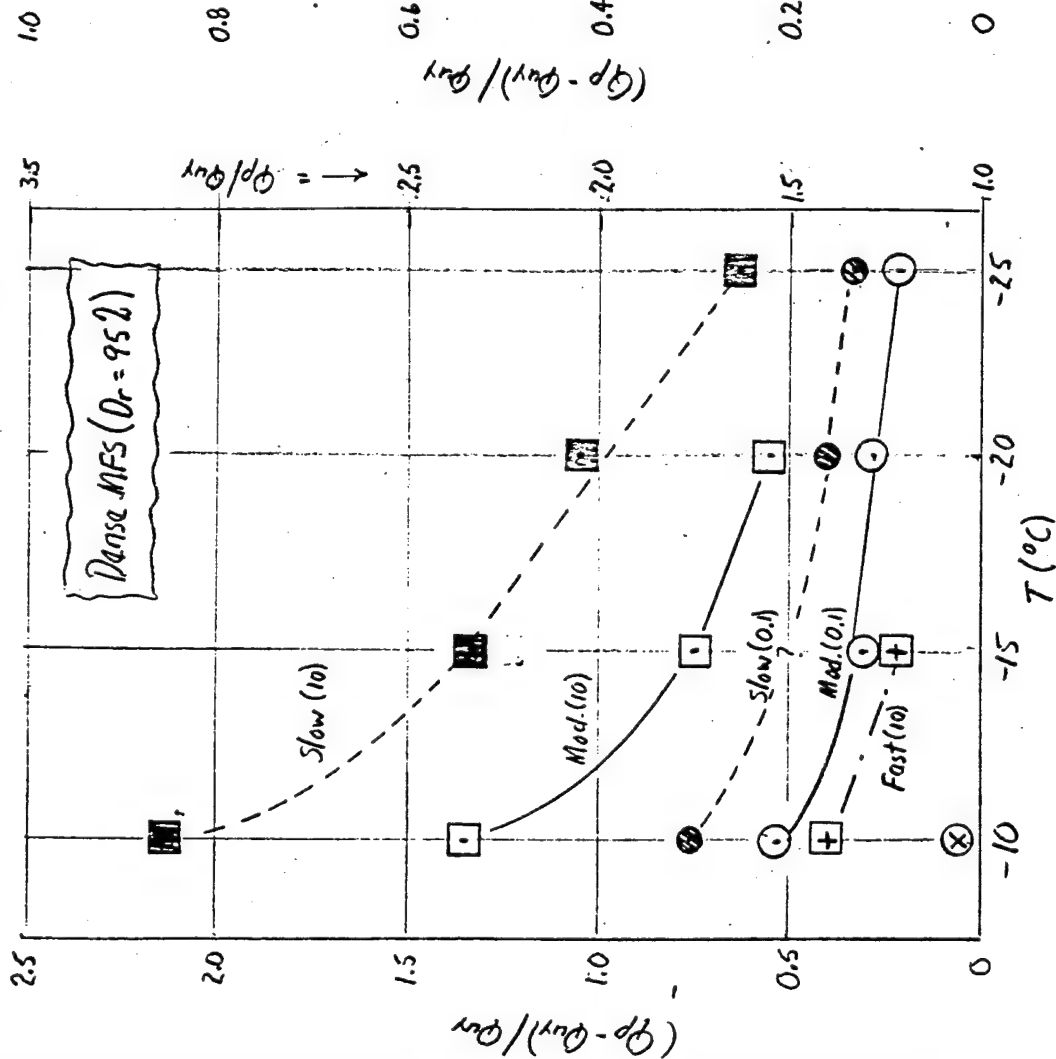


Fig. B4 $(Q_p - Q_{uv})/Q_{uv}$ vs. Temperature at Varying Strain Rates for Loose and Dense MFS

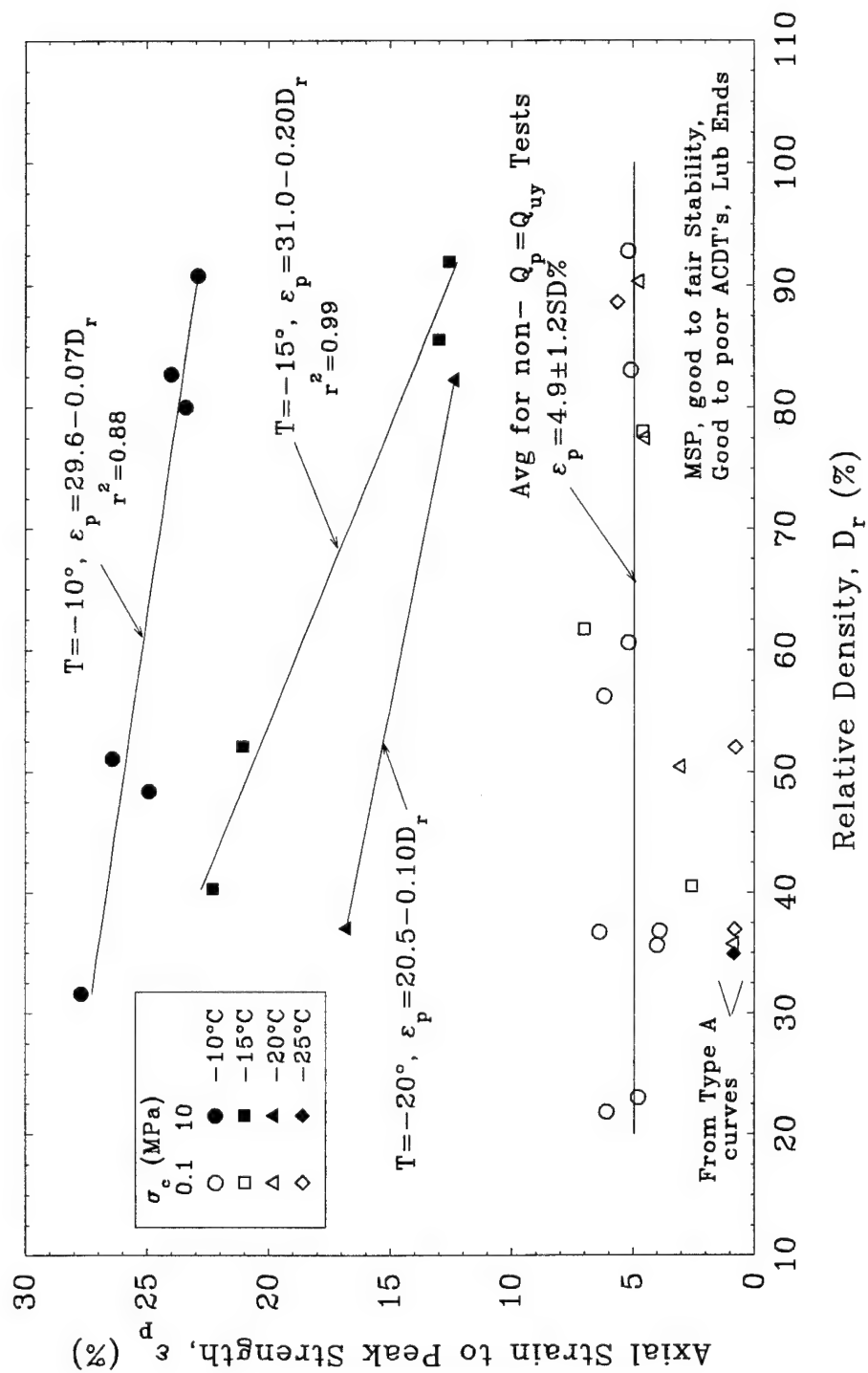


Figure 5.44a Axial Strain to Peak Strength versus Relative Density for Conventional Frozen MFS Tests at Moderate Strain Rate and Different Temperatures

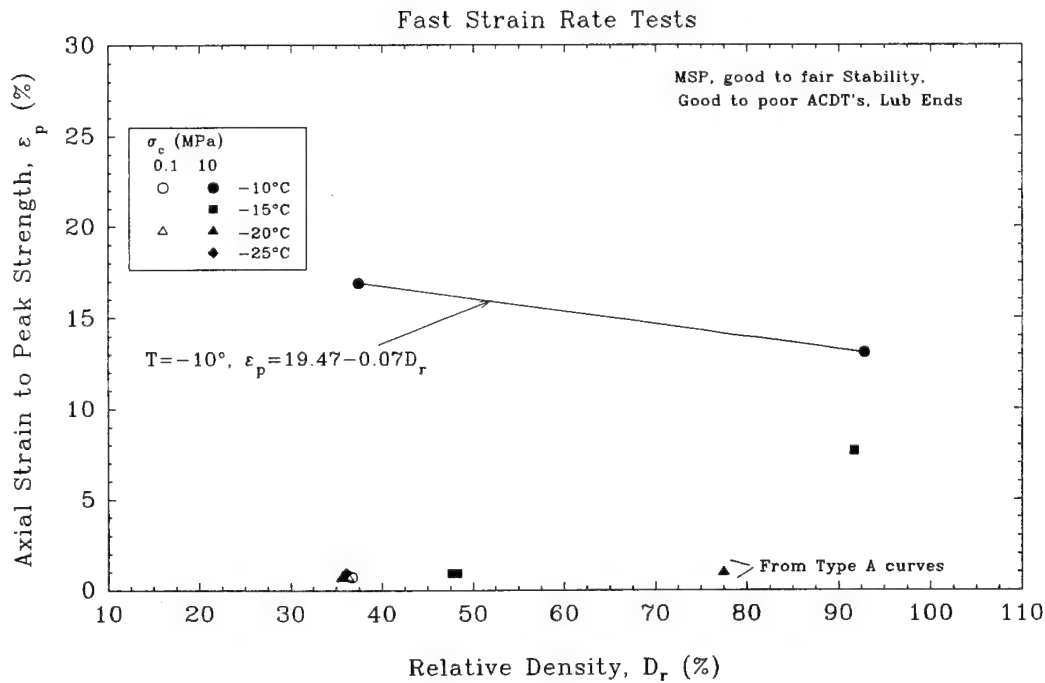
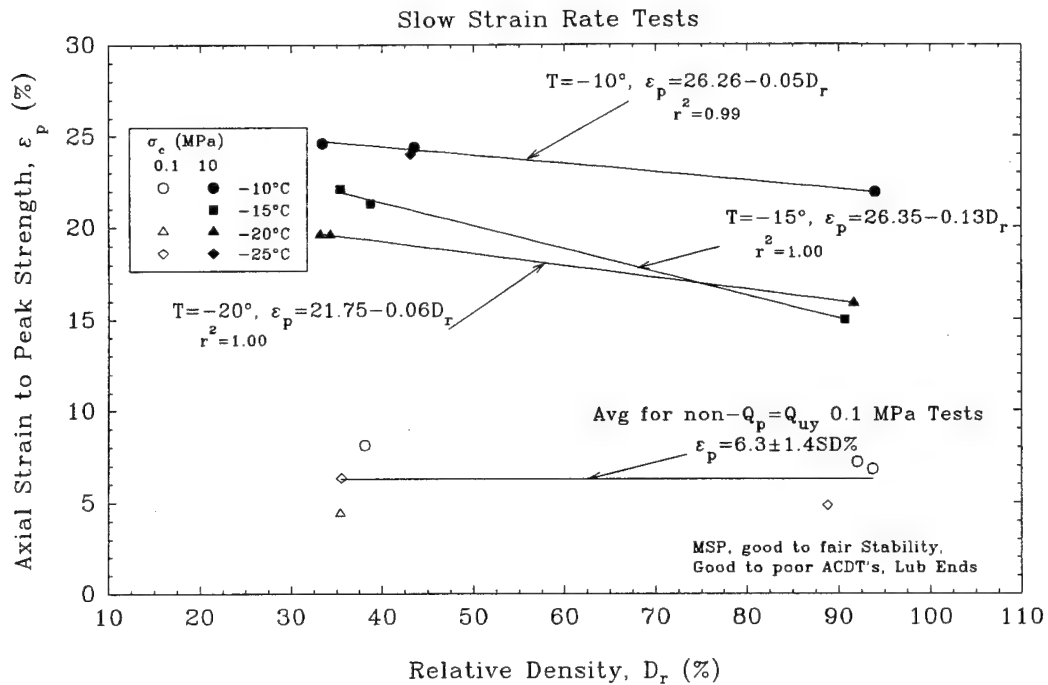


Figure 5.44b Axial Strain to Peak Strength versus Relative Density for Conventional Frozen MFS Tests at Slow and Fast Strain Rates and Different Temperatures

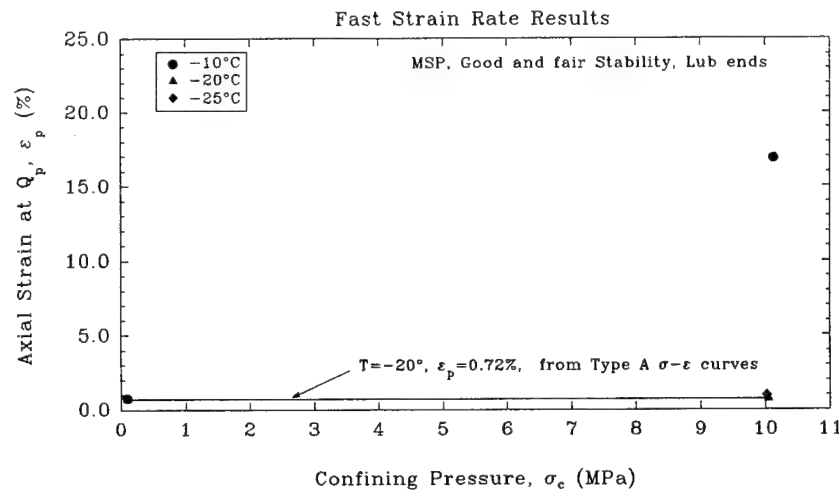
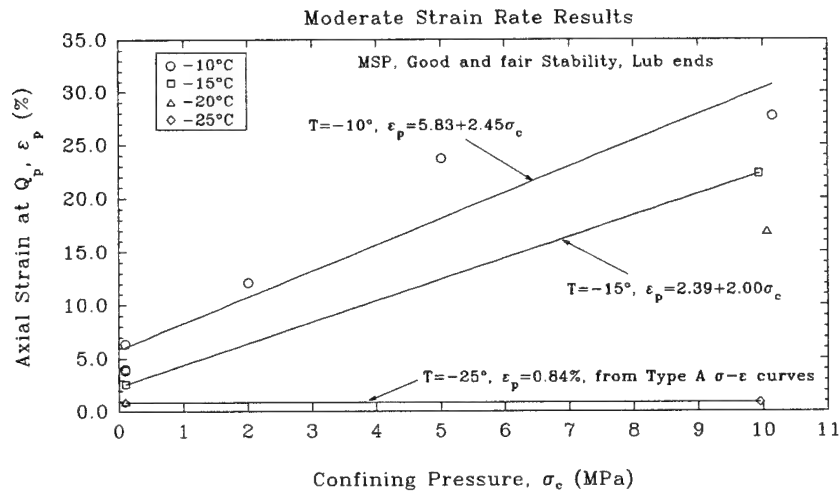
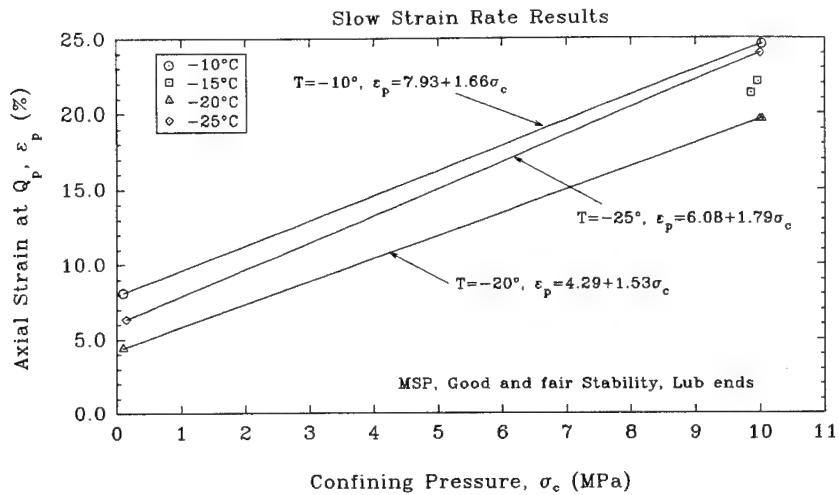


Figure 5.45a

Axial Strain at Q_p versus Confining Pressure for Conventional Frozen MFS Tests on Loose Specimens at Different Temperatures

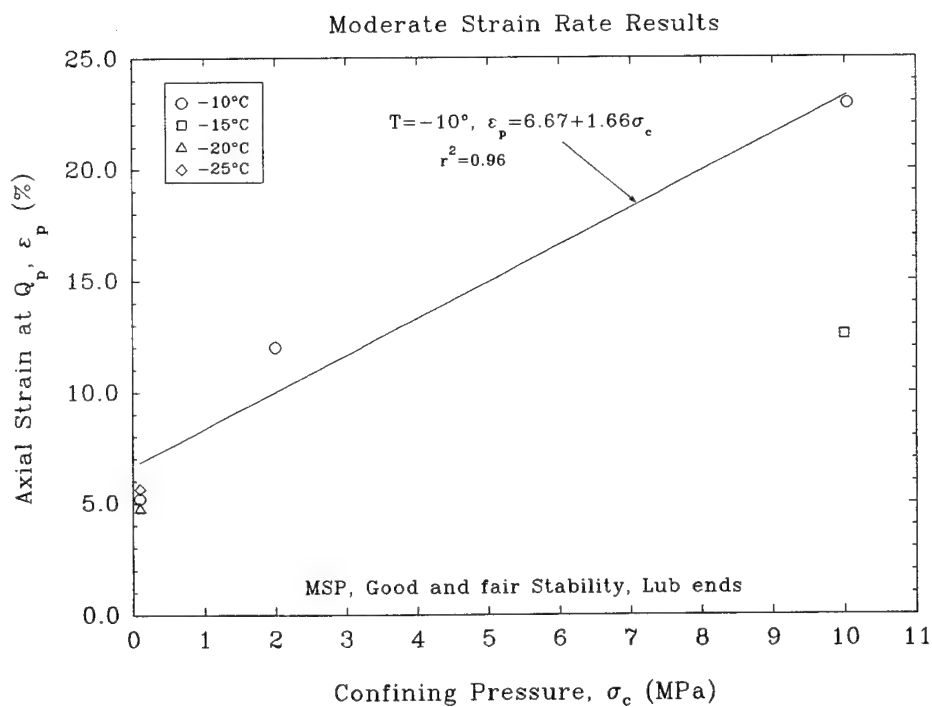
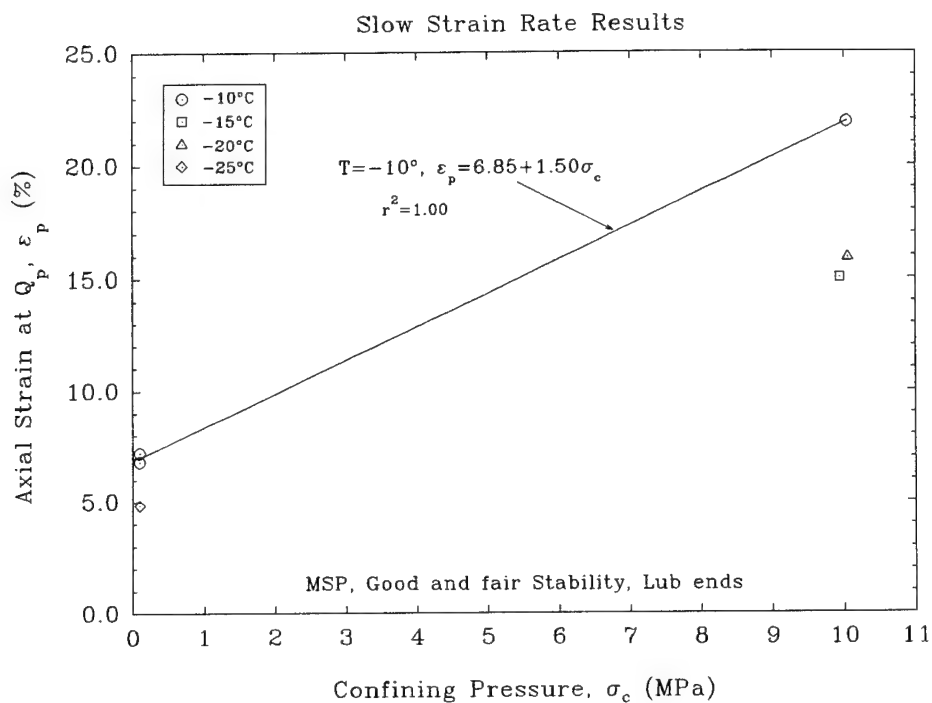


Figure 5.45b

Axial Strain at Q_p versus Confining Pressure for
Conventional Frozen MFS Tests on Dense Specimens
at Different Temperatures

APPENDIX C: Data from Triaxial Compression Tests on Unfrozen MFS

<u>Sheet No.</u>	<u>Description</u>
C1 & C2	Shear Characteristics at or near Steady State from CIUC and CAUC Tests
C3 & C4	Steady State Parameters from CIUC Tests
C5	Steady State Parameters from CIDC Tests
C6	Void Ratio vs. Consolidation Stress
C7	Effect of Consolidation Stress on Upper Yield Stress
C8 & C9	Effect of Relative Density on Effective Stress Paths from CIUC tests with $\sigma'_c = 0.1$ and 2 MPa
C10	Effect of Relative Density on Drained Behavior from CIDC Tests with $\sigma'_c = 0.1$ MPa
C11	Steady State Line from CIUC and CAUC Tests
C12	Undrained Strength Ratio vs. State Parameter from CIUC Tests

TABLE 4.8 (page 1 of 2)
SHEAR CHARACTERISTICS - SERIES B
Conditions At or Near Steady State
(Swan 1994)

CUC Tests

Test Group	Test No.	D_r (%)	e	I_c (MPa)	Strain (%)	p' (MPa)	q (MPa)	I_{ss} (MPa)	Δu (MPa)	A	ϕ'	q/ I_c
0.1 MPa Tests	10	43.8	0.765	0.102	25.27	1.209	0.648	0.993	-0.460	-0.355	32.4	6.33
	12	86.1	0.626	0.110	22.53	3.353	1.859	2.788	-1.494	-0.402	33.6	16.93
2 MPa Tests	06	65.4	0.694	2.035	25.28	2.291	1.210	1.960	0.837	0.346	30.9	0.59
	07	96.1	0.593	2.030	24.92	4.979	2.616	4.147	-0.406	-0.078	31.4	1.29
	11	67.2	0.688	2.013	22.58	2.619	1.429	2.308	0.585	0.205	30.9	0.71
5 MPa Tests	01	72.7	0.670	4.982	22.40	2.888	1.595	2.371	3.714	1.164	33.4	0.32
	02	104.9	0.564	5.017	22.82	6.356	3.403	5.221	2.038	0.299	32.4	0.68
	05	91.5	0.608	5.009	17.58	5.039	2.618	4.174	2.584	0.493	31.3	0.52
	13	64.5	0.697	5.184	23.09	2.399	1.241	1.986	3.986	1.605	31.2	0.24
	14	92.5	0.605	5.003	16.18	5.154	2.812	4.216	2.652	0.472	33.1	0.56
	15	94.3	0.599	5.033	23.74	6.086	3.027	5.077	1.978	0.327	29.8	0.60
10 MPa Tests	23	89.1	0.616	10.174	8.44	5.050	2.851	4.100	8.030	1.408	34.4	0.28
	24	85.8	0.627	10.027	18.79	4.316	2.673	3.425	8.484	1.587	38.3	0.27

Conditions "at" steady state are highlighted by boldface type

TABLE 4.8 (page 2 of 2)
SHEAR CHARACTERISTICS - SERIES C
(Swan 1994)
Conditions at or near Steady State

CIUC Tests

Test Group	Test No.	D_r (%)	e	I_c (MPa)	Strain (%)	p' (MPa)	q (MPa)	I_{ss} (MPa)	Δu (MPa)	λ	ϕ'	q/I_c
0.1 MPa Tests	C-26	68.7	0.683	0.106	22.83	2.511	1.395	2.046	-0.996	-0.357	33.7	13.16
	C-31	67.2	0.688	0.115	24.79	2.423	1.306	1.988	-0.999	-0.388	32.6	11.36
	C-34	94.9	0.597	0.077	25.63	4.911	2.700	4.011	-2.131	-0.395	33.4	35.06
2 MPa Tests	C-15	56.0	0.725	1.948	26.14	1.517	0.853	1.233	1.289	0.770	34.2	0.44
	C-27	63.5	0.700	1.972	27.04	1.980	1.073	1.622	1.064	0.505	32.8	0.55
	C-33	93.4	0.602	2.031	22.43	4.863	2.678	3.970	-0.147	-0.028	33.4	1.32
5 MPa Tests	C-23	75.5	0.661	5.010	18.08	2.868	1.490	2.371	3.614	1.226	32.4	0.30
	C-24	81.2	0.642	4.979	25.04	3.494	1.908	2.859	3.361	0.894	33.1	0.38
7.5 MPa Test	C-04	84.6	0.631	7.529	23.08	3.554	1.889	2.924	5.834	1.602	32.1	0.25
10 MPa Tests	C-01	82.7	0.637	9.375	10.04	4.331	2.316	3.559	7.481	1.630	32.3	0.25
	C-02	82.7	0.637	9.921	8.50	4.208	2.411	3.404	8.101	1.691	35.0	0.24
	C-03	77.3	0.655	10.108	19.08	4.392	2.505	3.557	8.147	1.635	34.8	0.25
	C-16	104.3	0.566	9.968	19.71	5.232	3.299	4.133	8.046	1.223	39.1	0.33
	C-22	95.3	0.596	9.991	24.10	5.943	3.187	4.881	7.321	1.157	32.4	0.32
12.5 MPa Test	C-25	100.4	0.579	12.534	25.67	5.384	2.934	4.406	10.073	1.733	33.0	0.23
	C-35	113.2	0.540	12.527	20.64	5.535	3.182	4.474	10.152	1.617	35.1	0.25

CAUC Tests

Test No.	D_r (%)	e	I_c (MPa)	K_c	Strain (%)	p' (MPa)	q (MPa)	I_{ss} (MPa)	Δu (MPa)	ϕ'	q/I_c
C-28	92.1	0.606	9.480	1.76	14.95	5.573	3.072	4.549	5.503	33.5	0.41
C-29	98.5	0.585	9.204	1.95	15.10	5.803	3.259	4.716	4.607	34.2	0.47
C-32	83.9	0.633	7.529	1.70	23.08	4.764	2.604	3.896	3.412	33.1	0.47

Conditions "at" steady state are highlighted by boldface type

CUC Tests TABLE 4.9 (page 1 of 2) (Swan 1994)
SHEAR CHARACTERISTICS - SERIES B
Steady State Parameters

Test Group	Test No.	D _r (%)	e	I' _c (MPa)	Measured I' _{ss} (MPa)	Calculated I' _{ss} (MPa)	Cal. Ψ	Shear Parameters		
								ϕ'_{max}	A _f	q _{max} /I' _c
0.1 MPa Tests	B-08	83.0	0.636	0.104	NA	3.081	-0.373	40.1	NA	NA
	B-09	82.7	0.637	0.114	NA	3.054	-0.362	38.5	NA	NA
	B-10	43.8	0.765	0.102	0.993	0.956	-0.246	37.5	-0.318	6.77
	B-12	86.1	0.626	0.110	2.788	3.574	-0.377	49.4	-0.352	18.24
	B-22	94.0	0.600	0.122	NA	4.272	-0.392	56.4	-0.419	19.68
2 MPa Tests	B-06	65.4	0.694	2.035	1.960	1.820	0.020	34.2	0.361	0.63
	B-07	96.1	0.593	2.030	4.147	4.553	-0.089	35.8	-0.045	1.43
	B-11	67.2	0.688	2.013	2.308	1.920	0.005	36.0	0.226	0.77
	B-01	72.7	0.670	4.982	2.371	2.263	0.087	34.3	1.167	0.32
5 MPa Tests	B-05	91.5	0.608	5.009	4.174	3.973	0.026	34.5	0.491	0.56
	B-13	64.5	0.697	5.184	1.986	1.771	0.118	37.5	1.354	0.29
	B-14	92.5	0.605	5.003	4.216	4.083	0.022	35.7	0.481	0.58
	B-15	94.3	0.599	5.033	5.077	4.311	0.017	34.5	0.320	0.69

TABLE 4.9 (page 2 of 2)
SHEAR CHARACTERISTICS - SERIES C
Steady State Parameters
(Swin 1994)

CIUC Tests

Test Group	Test No.	D_r (%)	e	I'_c (MPa)	Measured I'_{ss} (MPa)	Calculated I'_{ss} (MPa)	Cal. ψ	Shear Parameters		
								ϕ'_{max}	A_f	q_{max}/I'_c
0.1 MPa Tests	C-26	68.7	0.683	0.106	2.046	2.011	-0.324	44.1	-0.357	13.16
	C-31	67.2	0.688	0.115	1.988	1.922	-0.310	38.6	-0.374	11.43
	C-34	94.9	0.597	0.077	4.011	4.390	-0.445	42.5	-0.377	35.59
2 MPa Tests	C-15	56.0	0.725	1.948	1.233	1.374	0.038	38.2	0.754	0.46
	C-27	63.5	0.700	1.972	1.622	1.724	0.015	34.8	0.505	0.55
	C-33	93.4	0.602	2.031	3.970	4.195	-0.080	35.6	-0.012	1.36
5 MPa Tests	C-23	75.5	0.661	5.010	2.371	2.456	0.079	32.3	1.228	0.30
	C-24	81.2	0.642	4.979	2.859	2.918	0.059	34.1	0.894	0.39
7.5 MPa Test	C-04	84.6	0.631	7.529	2.924	3.225	0.093	36.6	1.417	0.29

(Swan 1994)

TABLE 4.10
SHEAR CHARACTERISTICS - SERIES C: CIDC TESTS
Steady State Parameters

Test Group	Test No.	D_r (%)	e	I'_c (MPa)	Measured I'_{ss} (MPa)	Calculated I'_{ss} (MPa)	Cal. ψ	Shear Parameters ϕ'_{max}	Shear Parameters $(\Delta\epsilon_v/\Delta\epsilon_a)_{max}$ (%)
0.1 MPa Tests	C-14	86.1	0.626	0.163	NA	3.374	-0.334	56.0	0.649
	C-17	31.0	0.807	0.125	NA	0.653	-0.182	35.0	0.140
	C-18	29.8	0.811	0.106	NA	0.629	-0.196	42.0	0.142
	C-19	31.7	0.805	0.099	NA	0.665	-0.211	37.5	0.166
	C-20	78.2	0.652	0.096	NA	2.665	-0.366	47.0	0.755
	C-21	84.3	0.632	0.098	NA	3.195	-0.383	48.0	0.789
2 MPa Tests	C-11	71.2	0.675	1.936	NA	2.163	-0.012	37.1	0.151

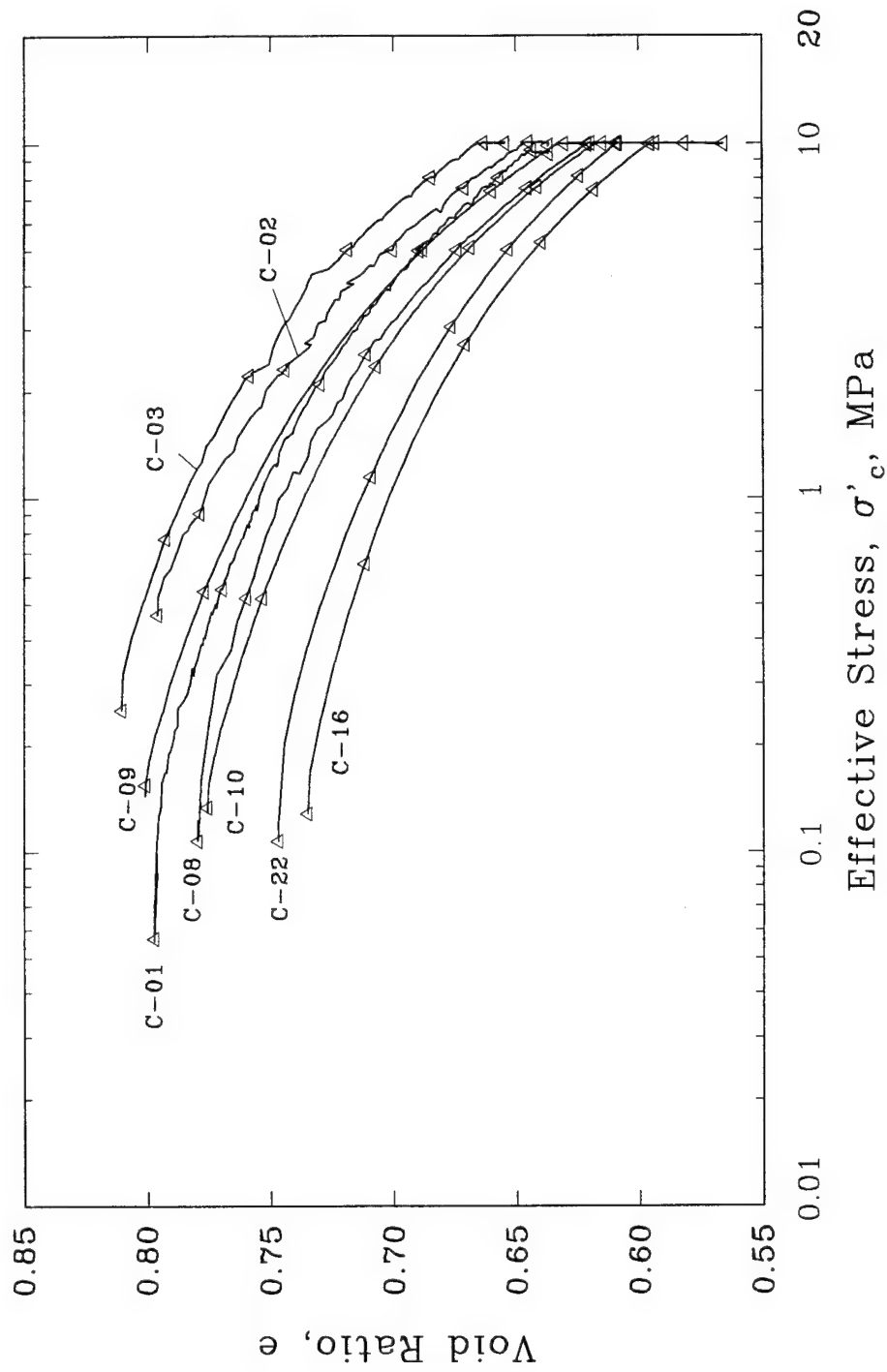
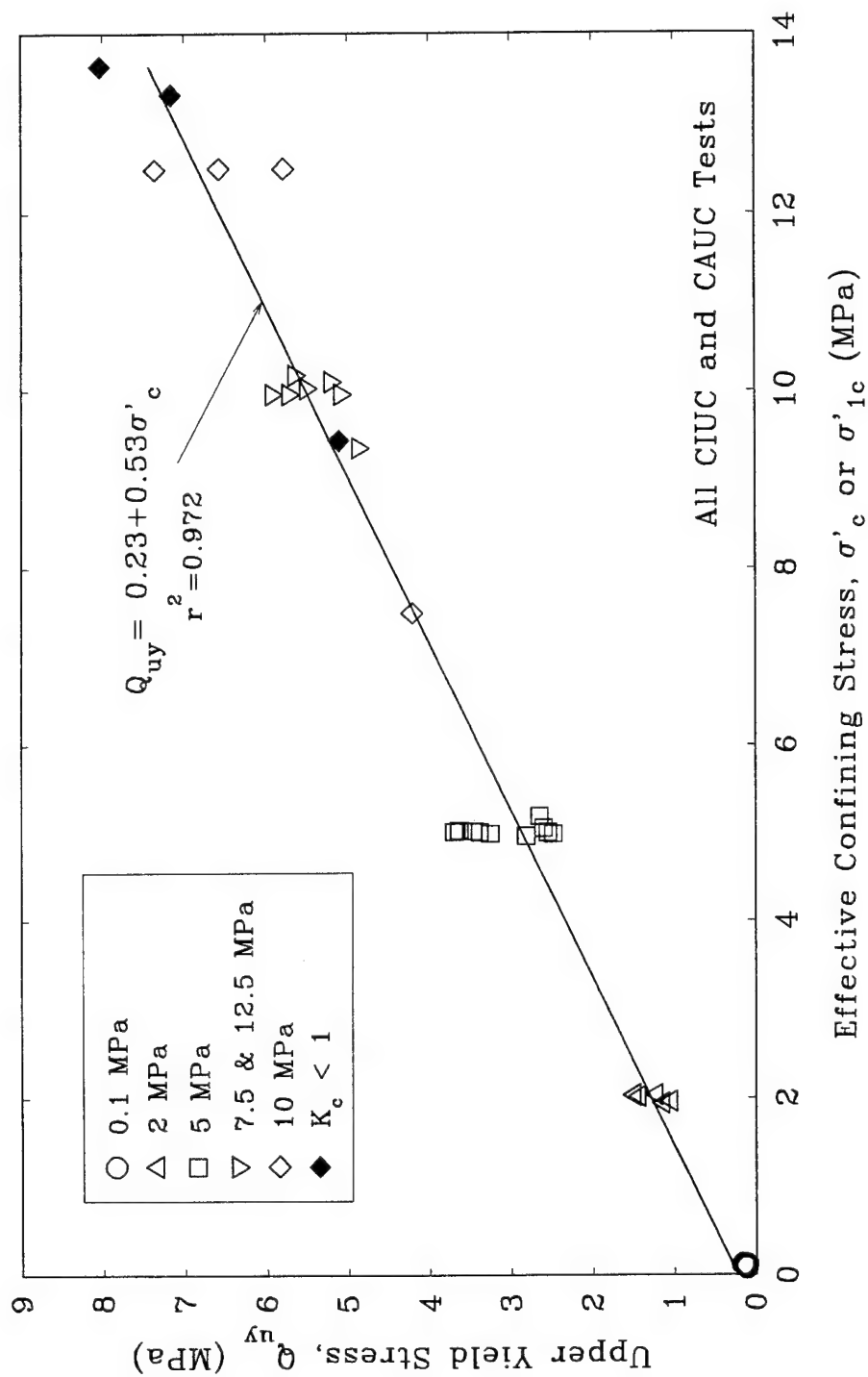


Figure 4.3b Void Ratio versus Effective Stress for Isotropic Consolidation of MFS: $\sigma'_c = 10$ MPa, Series C Tests (Swan 1994)



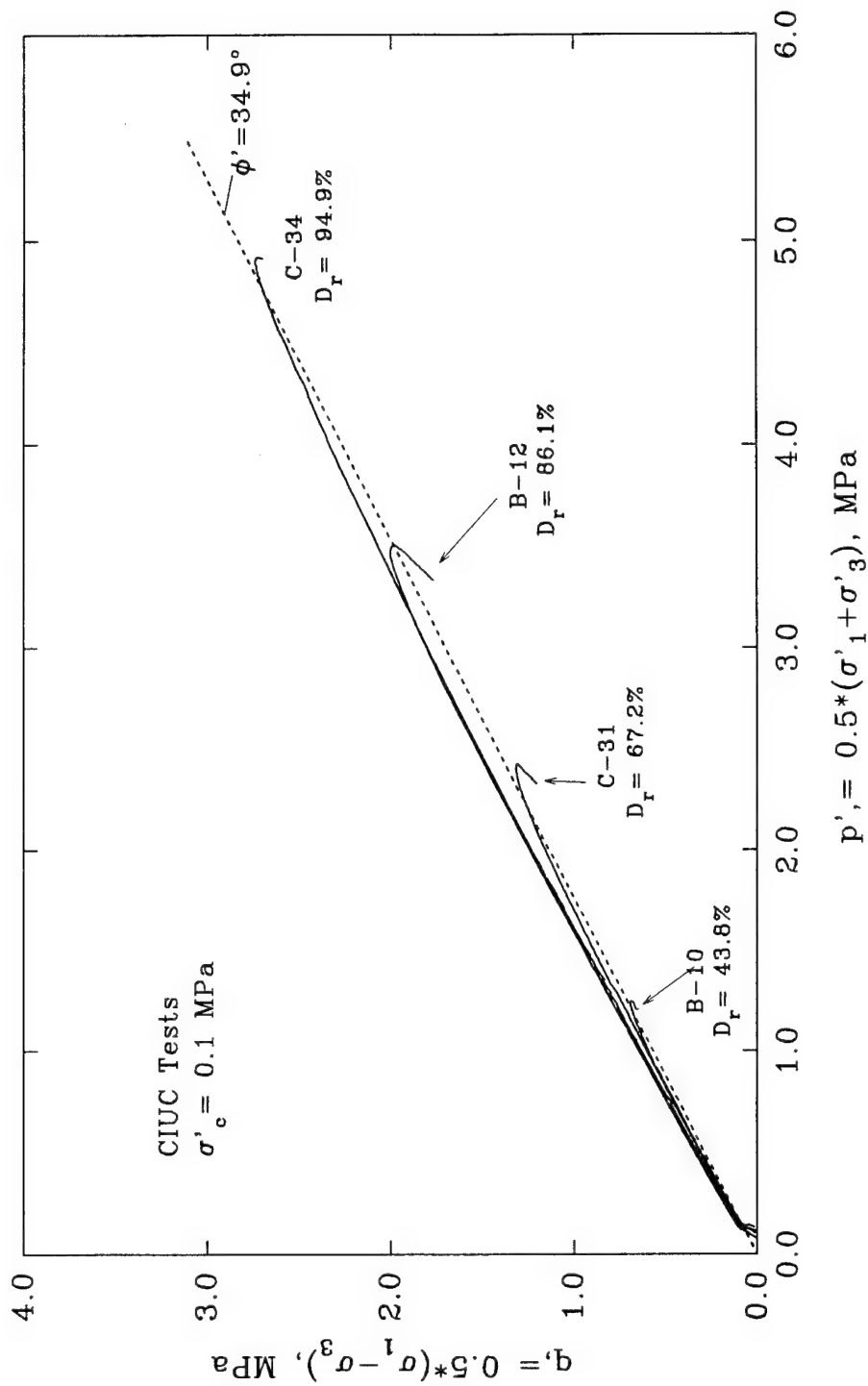


Figure 4.44 Effective Stress Paths for Unfrozen CIUC Tests
 with Similar Confinement: 0.1 MPa (Swan 1994)

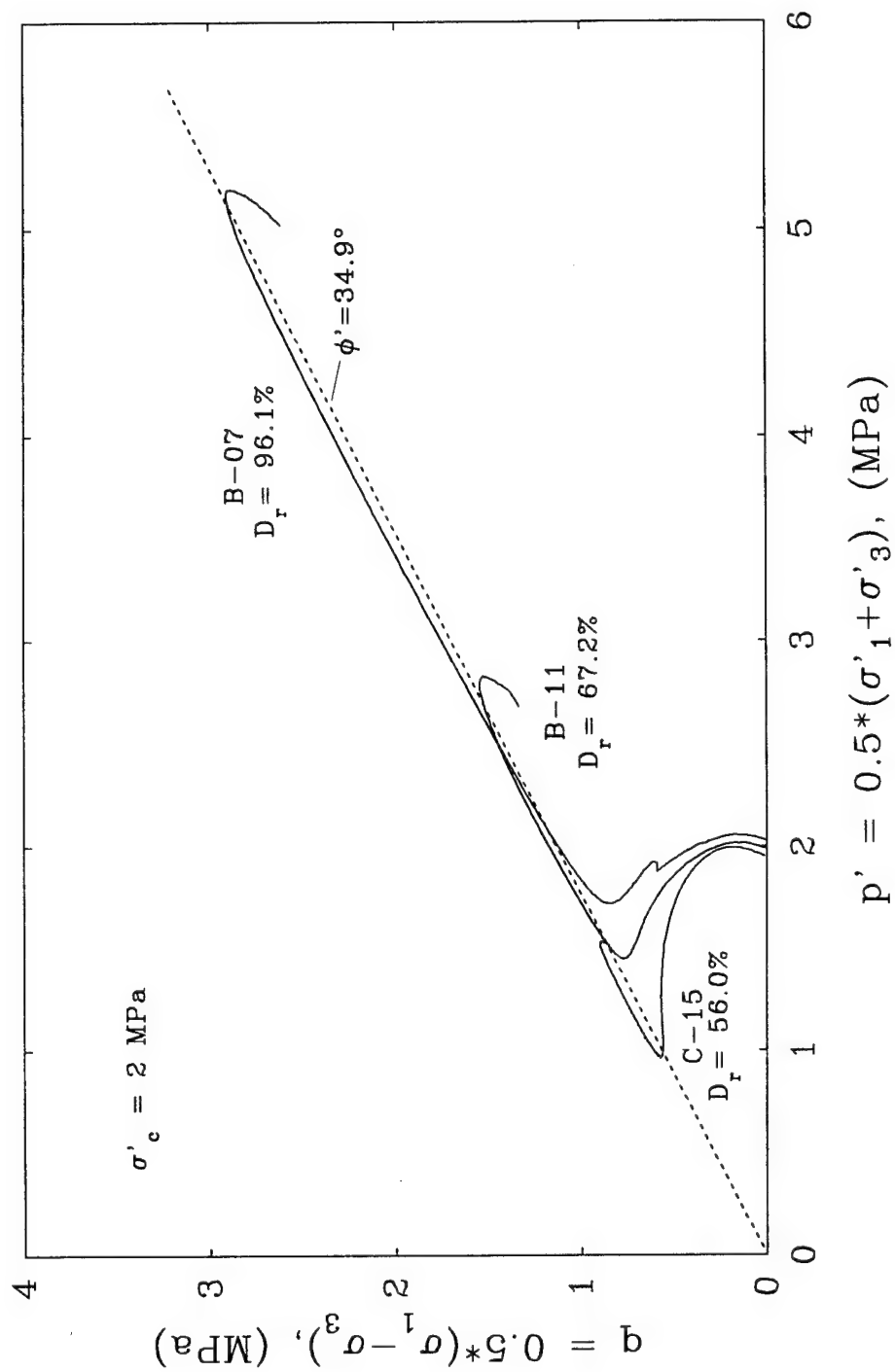


Figure 4.46 Effective Stress Paths for Unfrozen CIUC Tests with Similar Confinement: 2 MPa (Swan 1994)

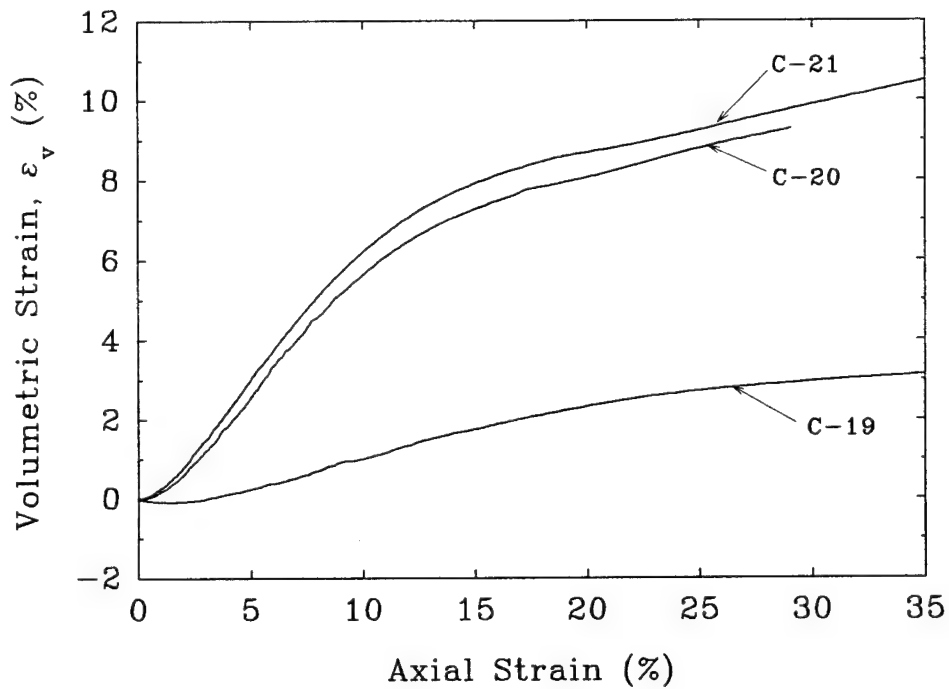
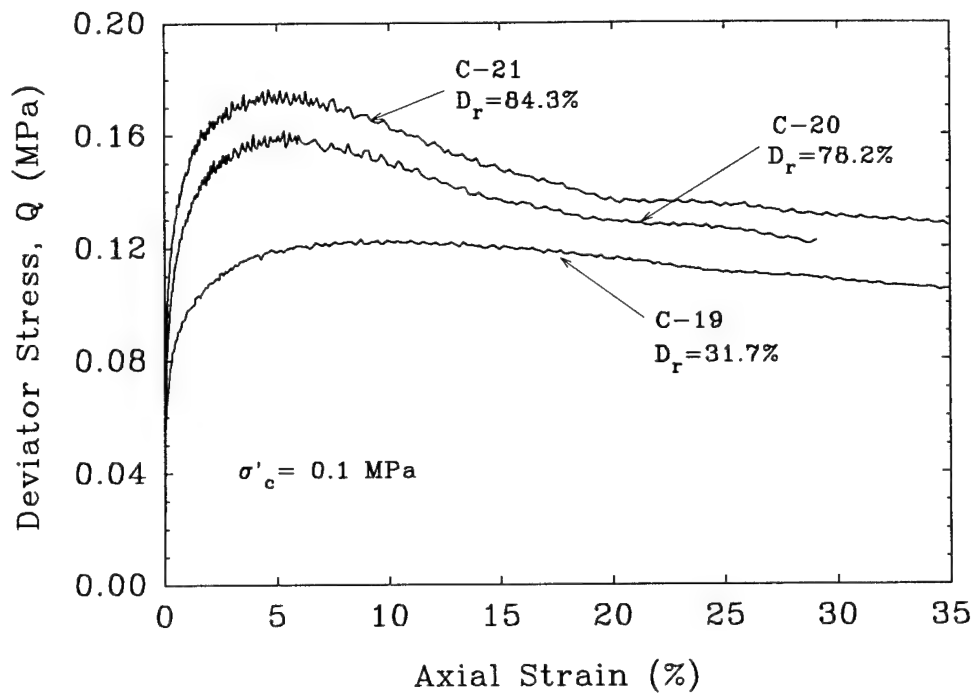


Figure 4.49 Stress-Strain and Volumetric Strain Responses for Unfrozen CIDC Tests at Similar Confinement: 0.1 MPa

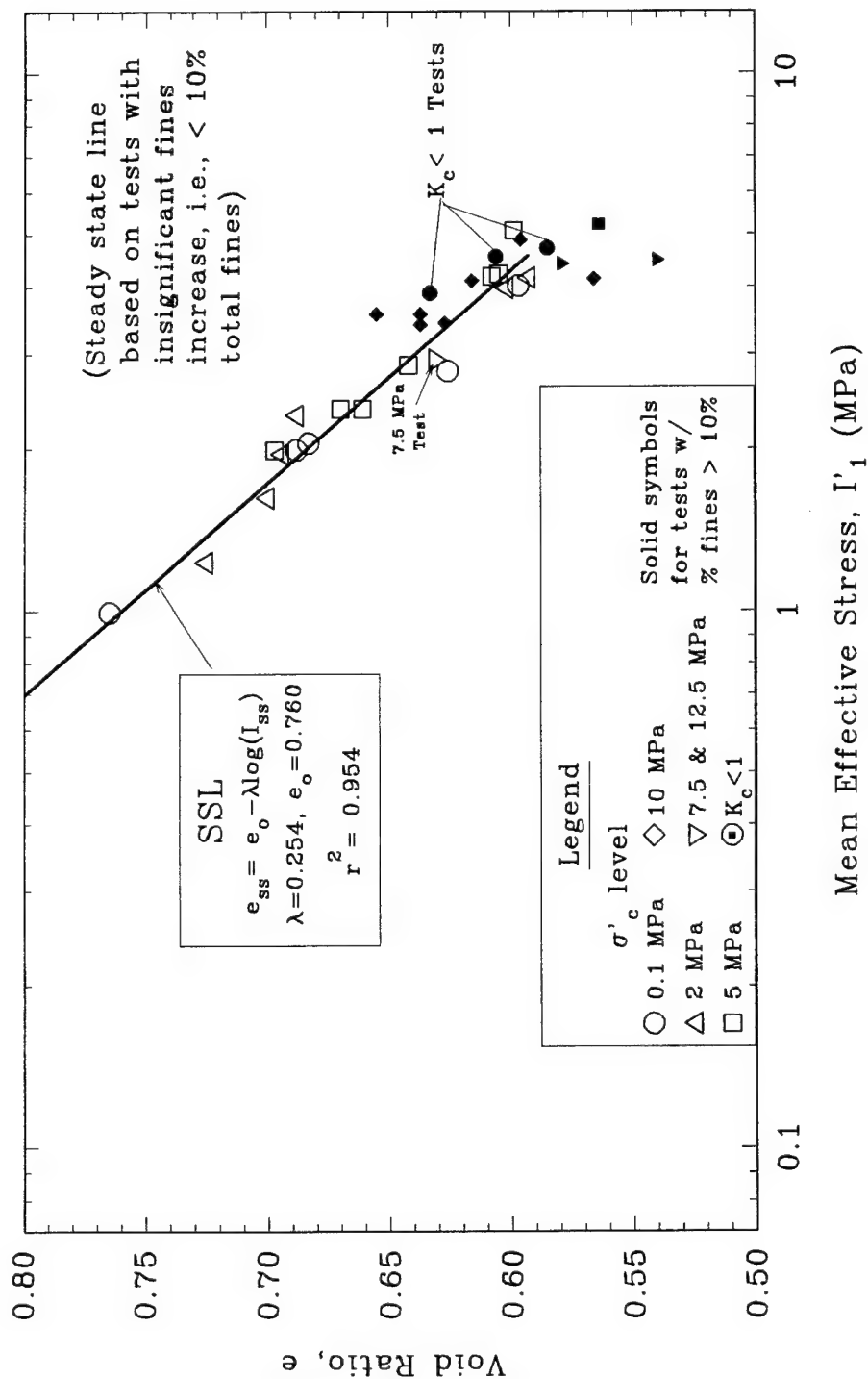


Figure 4.53 Steady State Line and Parameters as Determined by Undrained Tests from Series B and Series C Tests (Swan 1994)

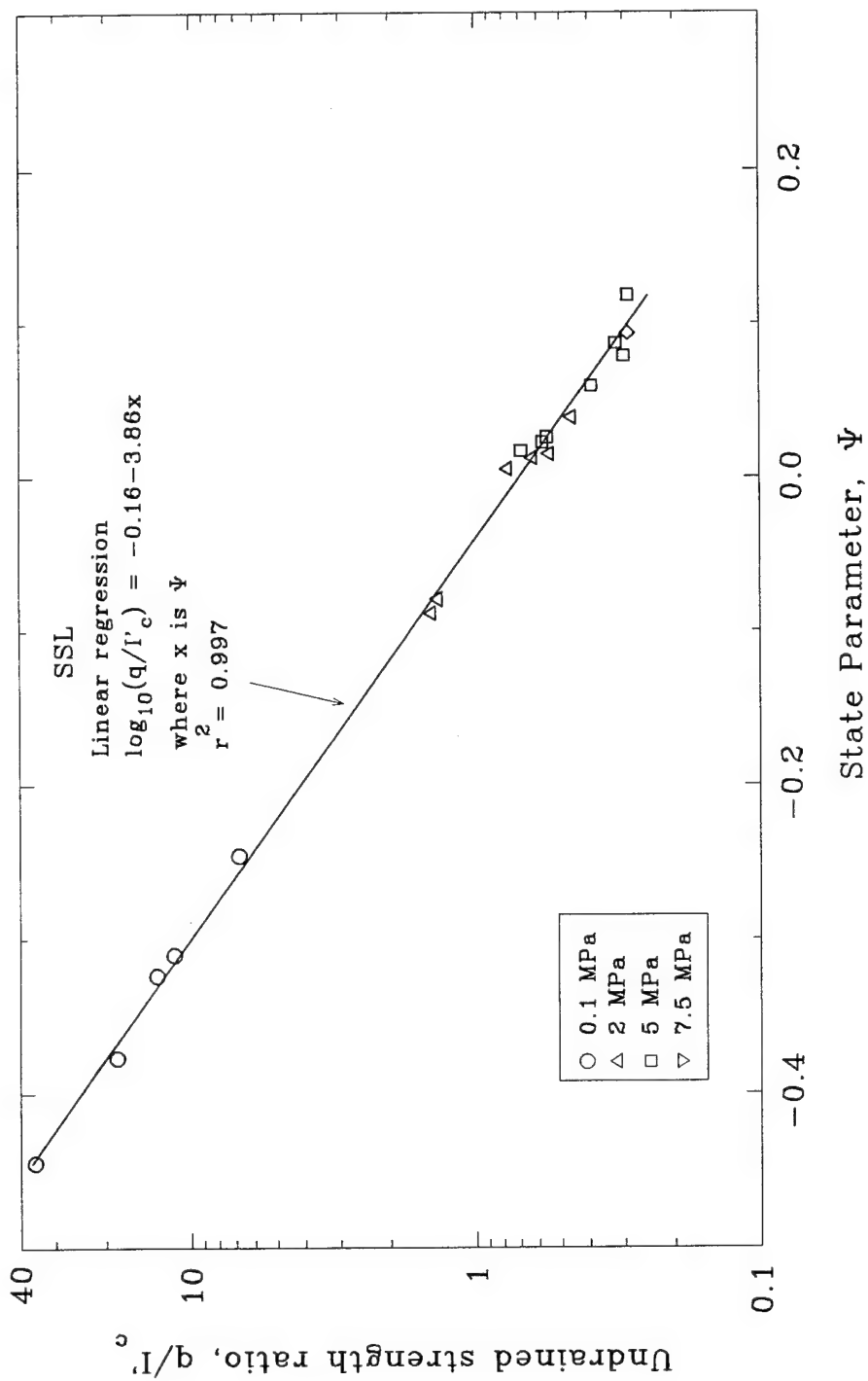


Figure 4.55 Undrained Strength Ratio, q/I'_c , versus State Parameter for CIUC Tests on Unfrozen MFS (Swan 1994)

APPENDIX D: Data from Consolidate-Freeze Triaxial Compression Tests on MFS

<u>Sheet No.</u>	<u>Description</u>
D1 to D3	Tabulated Data from Consolidate-Freeze Tests: Consolidation, Freezing and Shearing Results
D4	Compression Curves during Consolidation
D5	Cell Modifications for Consolidate-Freeze Tests
D6	Pore Water Volume and Temperature Changes during Freezing of CF02
D7	Efficiency during Freezing
D8	Comparison of E and Q_{y0} from Conventional and Consolidate-Freeze Tests
D9	Stress-Axial Strain-Volumetric Strain Curves from Ten Consolidate-Freeze Tests
D10	Q_p vs. Confining Stress from Conventional and Consolidate-Freeze Tests

TABLE 5.7
CONSOLIDATION CHARACTERISTICS
CONSOLIDATE-FREEZE TESTS
(Swun 1994)

Test No.	Eff. Stress		Volume		Void Ratio, e		Axial Strain		Vol. Strain (%)	Consol. Time		Final D_r (%)
	Init. (MPa)	Final (MPa)	Init. (cc)	Final (cc)	ΔV (cc)	Init. Final	DCDT (%)	ACDT (%)		Prim. (min)	Sec. (min)	
CF02	0.084	9.938	69.48	63.09	6.39	0.794	0.629	2.73	3.50	49	239	85.2
CF04	0.088	10.09	69.65	62.49	7.16	0.752	0.572	2.01	2.71	59	309	102.5
CF05	0.083	9.946	69.31	62.51	6.80	0.803	0.626	3.03	3.24	39	182	84.9
CF06	0.098	4.992	70.78	67.14 ¹	3.64	0.686	0.600 ¹	1.02	1.12	23	190	94.1 ¹
CF07	0.090	2.010	70.98	67.73 ¹	3.25	0.669	0.592 ¹	0.58	0.83	13	131	96.4 ¹
CF08	0.089	1.993	71.09	69.17	1.92	0.648	0.603	0.52	0.71	17	174	93.0
CF09	0.100	1.980	69.15	66.80 ¹	2.35	0.630	0.575 ¹	0.45	0.93	18	70	101.7 ¹
CF10	0.059	4.980	70.81	67.28	3.53	0.686	0.601	1.49	1.34	30	244	91.7

Notes:

NA - Not available

¹ Value represents best estimate due to leakage of oil into internal drainage line

TABLE 5.8
SPECIMEN FREEZING CHARACTERISTICS
CONSOLIDATE-FREEZE TESTS
(Swan 1994)

Test No.	Nominal σ'_c (MPa)	Freezing Temperature $^{\circ}\text{C}$	Initial Volumes			Volume Change		Elapsed Time (min)	Comments
			V_1 (cc)	V_s^2 (cc)	V_w (cc)	Meas. (cc)	Calc. Eff. (%)		
CF01	0.1	-8	70.80	44.60	26.20	0.46	2.35	100	Excess ice noted around top
CF02	10	-8	63.08	38.74	24.35	1.42	2.19	230	
CF03	0.1	-15	72.44	44.68	27.76	0.60	2.50	105	Manual Δ volume measurement
CF04	10	-15	62.49	39.75	22.74	1.11	2.05	120	Manual Δ volume measurement
CF05	10	-15	62.51	38.35	24.16	1.03	2.17	90	Manual Δ volume measurement
CF06	5	-15	67.14	41.97	25.27	0.48 ³	2.27	120	Oil leak into drainage line
CF07	2	-8	67.73	42.54	25.19	1.91 ³	2.27	180	Oil leak, stopped prematurely
CF08	2	-8	69.17	43.14	26.03	1.74	2.34	240	
CF09	2	-8	66.80	42.43	24.37	1.91 ³	2.19	200	Oil leak into drainage line
CF10	5	-8	67.28	41.85	25.43	1.90	2.29	500	

Notes:

- ¹ V = Total volume after consolidation
- ² V_s = Volume of solids based on after test weight
- ³ Measured volume change represents best estimate due to leakage of oil into internal drainage line

TABLE 5.9
CONSOLIDATE-FREEZE TESTS RESULTS
(Swin 1994)

CF Test No.	D_r (%)	σ_c (MPa)	TEMP (°C)	NOMINAL STRAIN RATE (/sec) $\times 10^6$	SMALL STRAIN RESPONSE		UPPER YIELD REGION		PEAK STRENGTH REGION		Q - ϵ_a Curve Type	VOLUMETRIC BEHAVIOR		S ⁴	A ⁵
					E (GPa)	Q_{y0} (MPa)	Q_{uy} MPa	ϵ_y (%)	Q_p (MPa)	ϵ_p (%)		Max. $d\epsilon_v/d\epsilon_a$ $\times 10^2$	ϵ_{v10} (%)	ϵ f p vp	ϵ f p p
01	97.4	0.265	-10.3	30.6	26.5	2.7	8.6	0.50	13.3	6.6	C	NA	NA	f	f
02	85.2	10.00	-10.3	36.4	23.6	3.2	NA	NA	17.2	4.4	C	38	NA	p	p
03	87.6	0.170	-9.84	31.1	NA	NA	7.7	0.80	11.3	6.5	C	443	1.5	vp	f
04	102.5	10.19	-9.99	33.7	NA	NA	NA	NA	16.3	5.2	C	63	0.6	vp	p
05	84.9	10.02	-10.0	36.2	22.2	3.5	NA	NA	16.4	5.8	C	48	0.4	p	p
06	94.1 ¹	4.99	-10.2	38.1	20.8	4.0	NA	NA	16.7	3.7	C	57	0.7	p	p
07	96.4 ¹	2.02	-10.5 ²	29.5	NA	NA	NA	NA	13.6	3.3	C	236	1.5	vp	p
08	93.0	2.03	-10.1	39.4	22.5	3.5	NA	NA	14.6	5.4	C	233	1.2	vp	f
09	101.7 ¹	2.01	-10.2	33.0	26.9	3.3	NA	NA	13.9	4.0	C	205	0.7	p	g
10	91.7	5.02	-10.1	38.1	NA	NA	NA	NA	15.8 ³	4.2	C	NA	NA	f	g

Notes:

NA - Not Available

¹ Relative density is best estimate

² Temperature based on bottom thermistor

³ Maximum reliable deviator stress, but higher stresses may have been possible (see Fig. 5.58).

⁴ S = Stability Qualifiers

⁵ A = ACDT Qualifiers

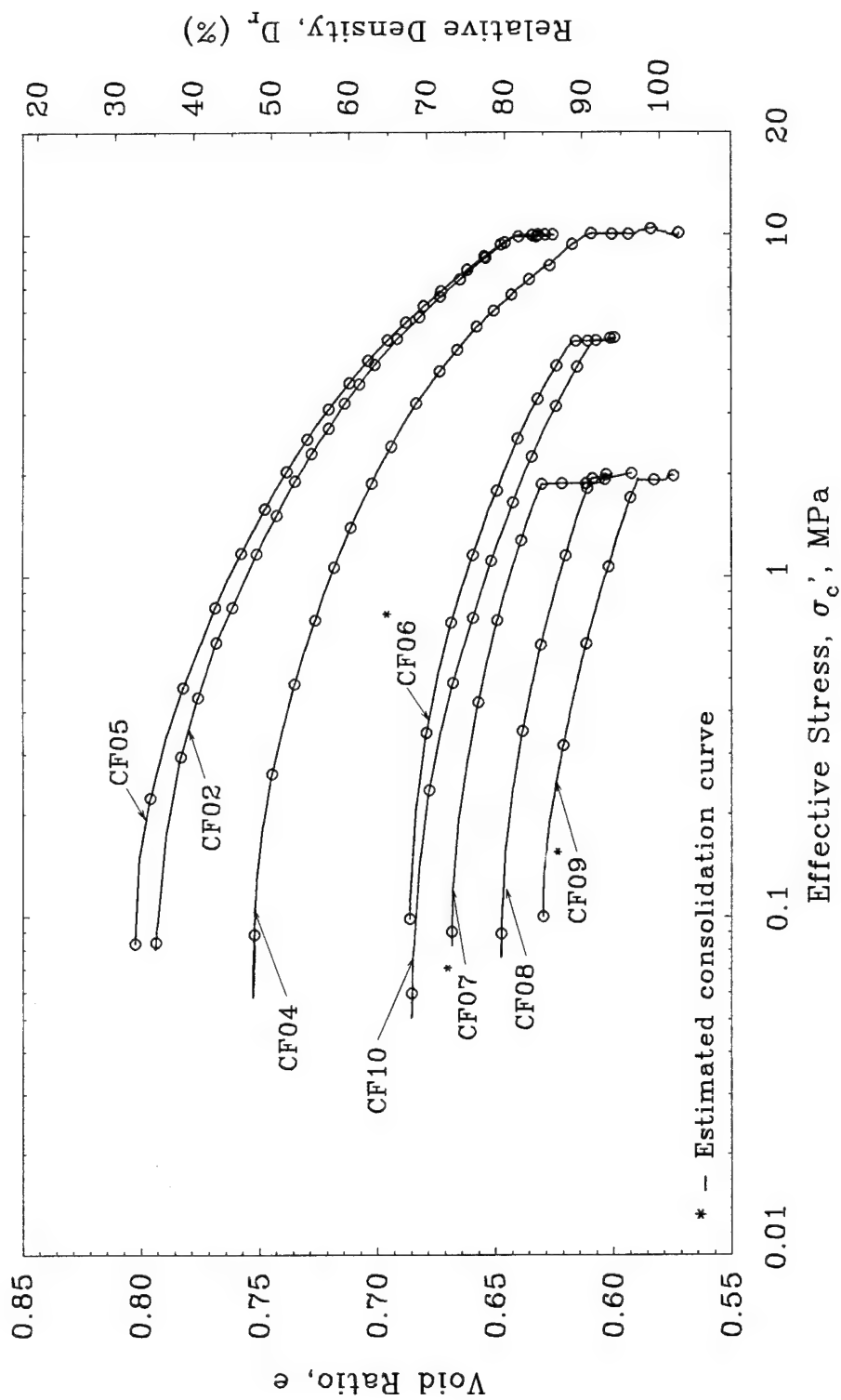


Figure 5.54 Void Ratio and Relative Density versus Effective Stress for Isotropically Consolidated Consolidate-Freeze Tests (Swan 1994)

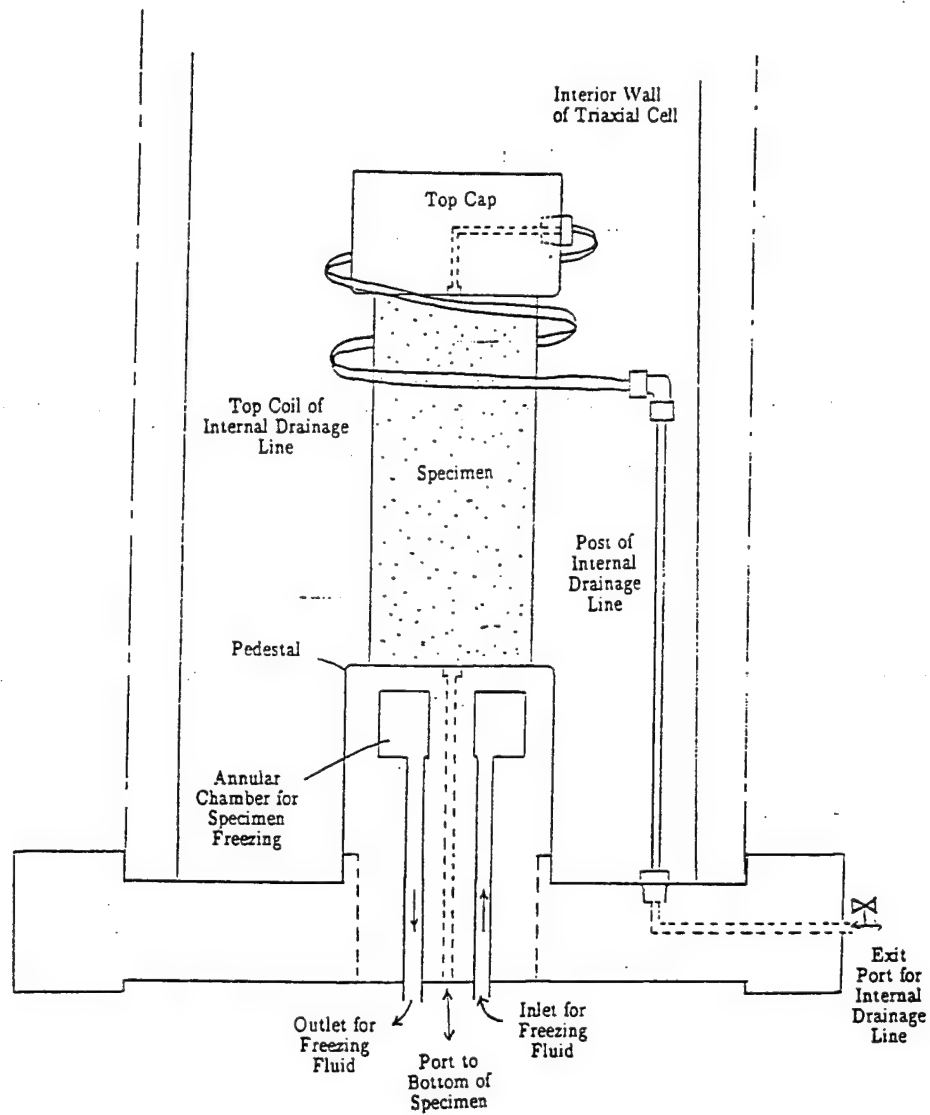


Figure 3.4 Details of Internal Modifications for Consolidate-Freeze Testing Program
(Swan 1994)

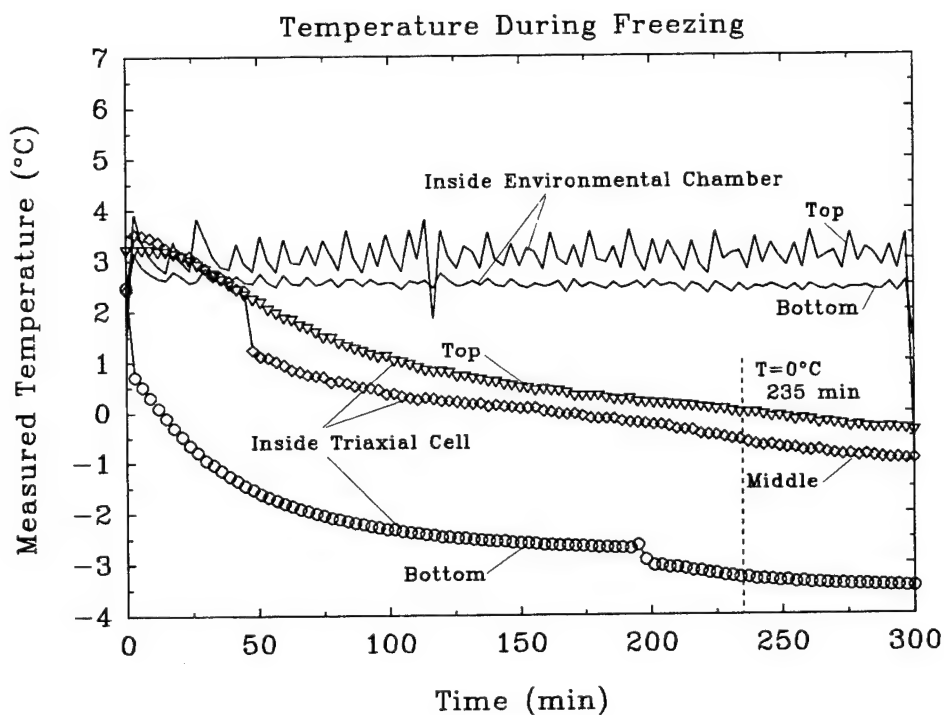
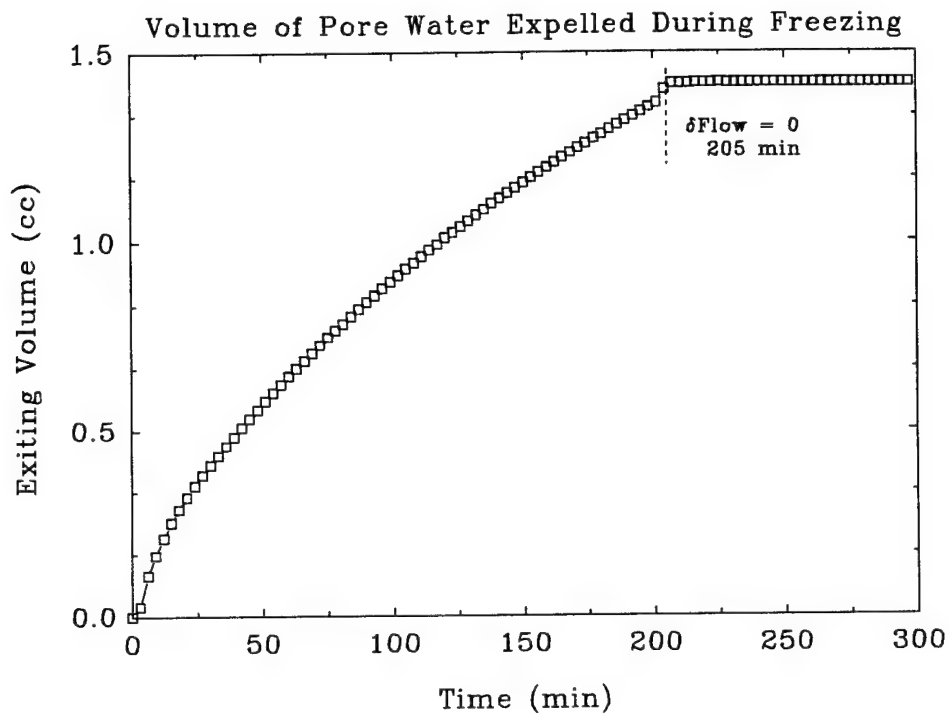


Figure 3.13 Pore Volume Expelled and Temperature Changes During Specimen Freezing Phase of CF02 (Swan 1994)

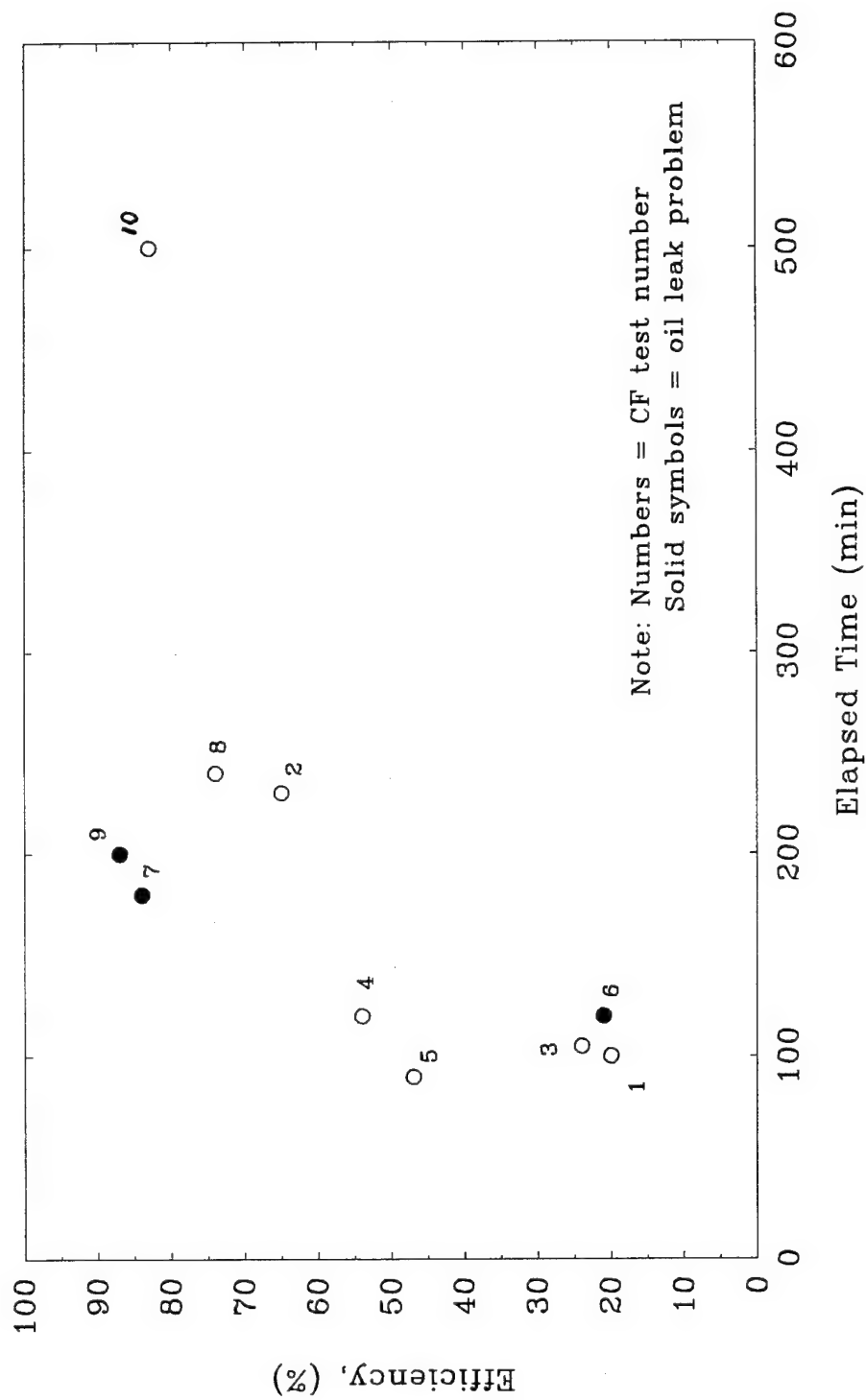


Figure 5.55 Efficiency of Specimen Freezing versus Elapsed Freezing Time for Consolidate--Freeze Tests on Dense Specimens (Swan 1994)

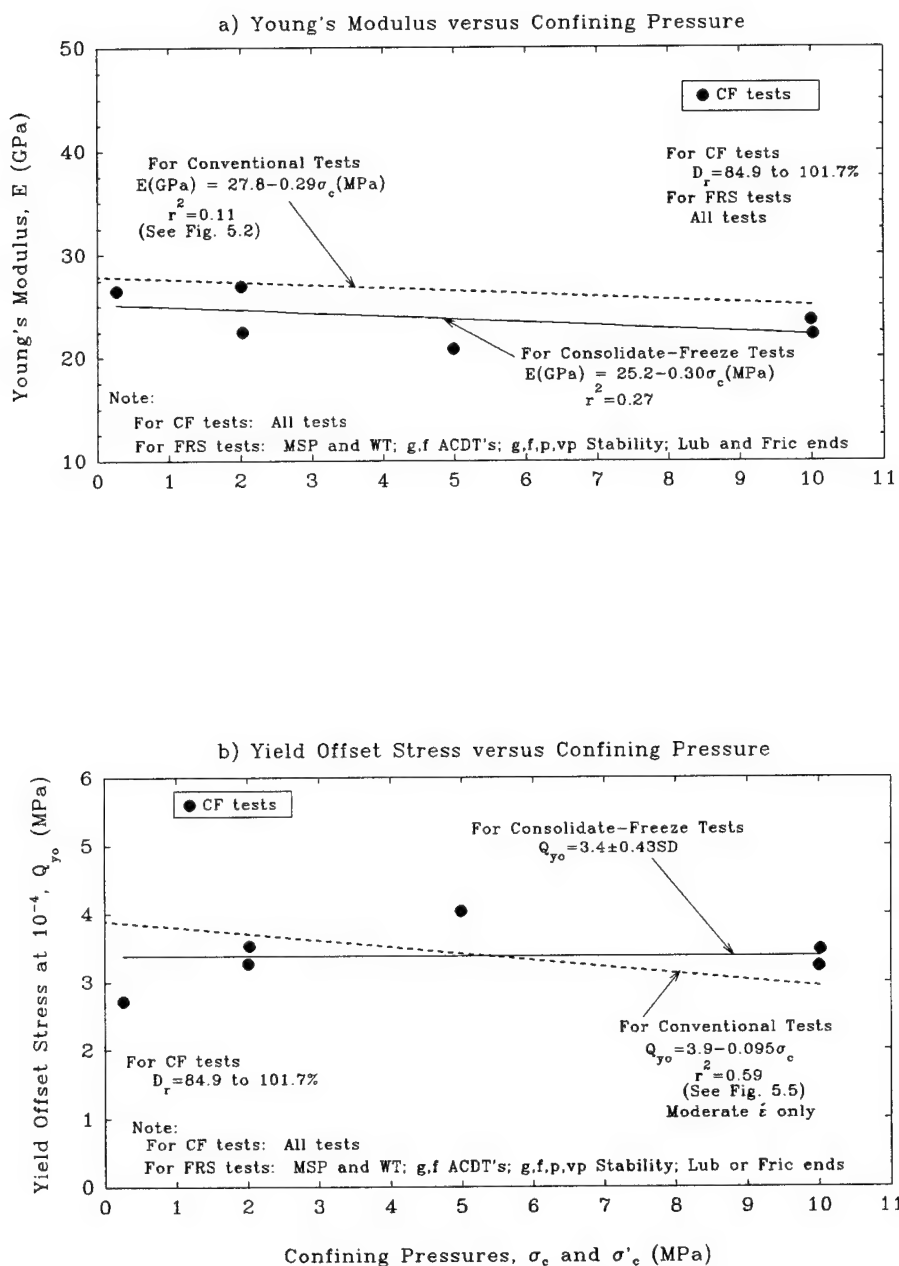


Figure 5.56 Small Strain Parameters versus Confining Pressure for Consolidate-Freeze and Conventional Frozen Tests on Dense Specimens at $T = -10^\circ\text{C}$ (Swan 1994)

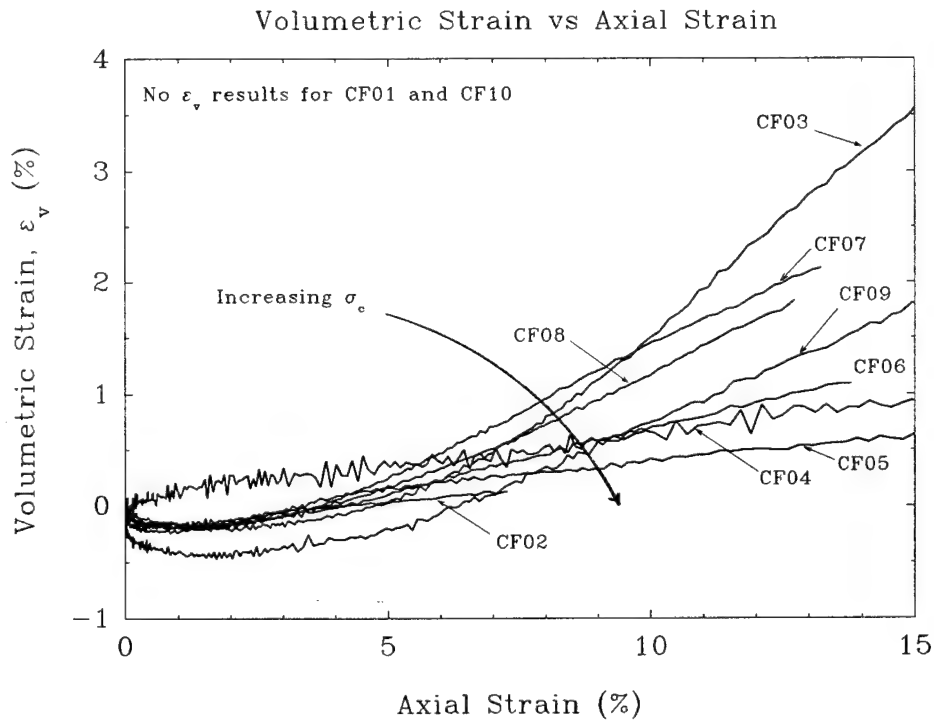
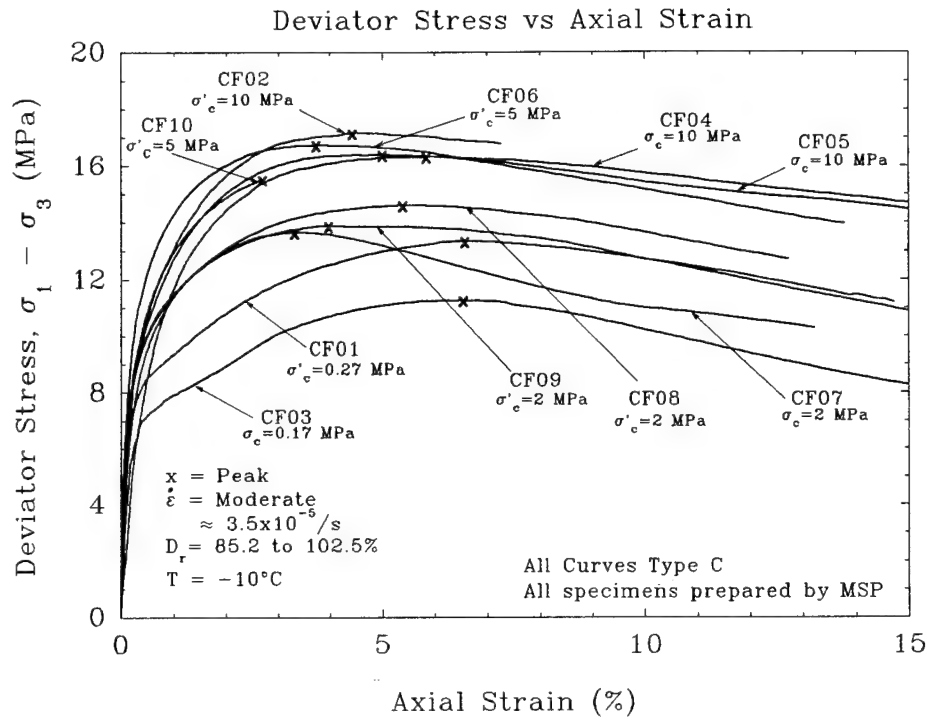


Figure 5.58 Comparison of Stress-Strain Curves for Consolidate-Freeze Tests on Dense Specimens at Moderate Strain Rate and $T = -10^\circ\text{C}$ (Swan 1994)

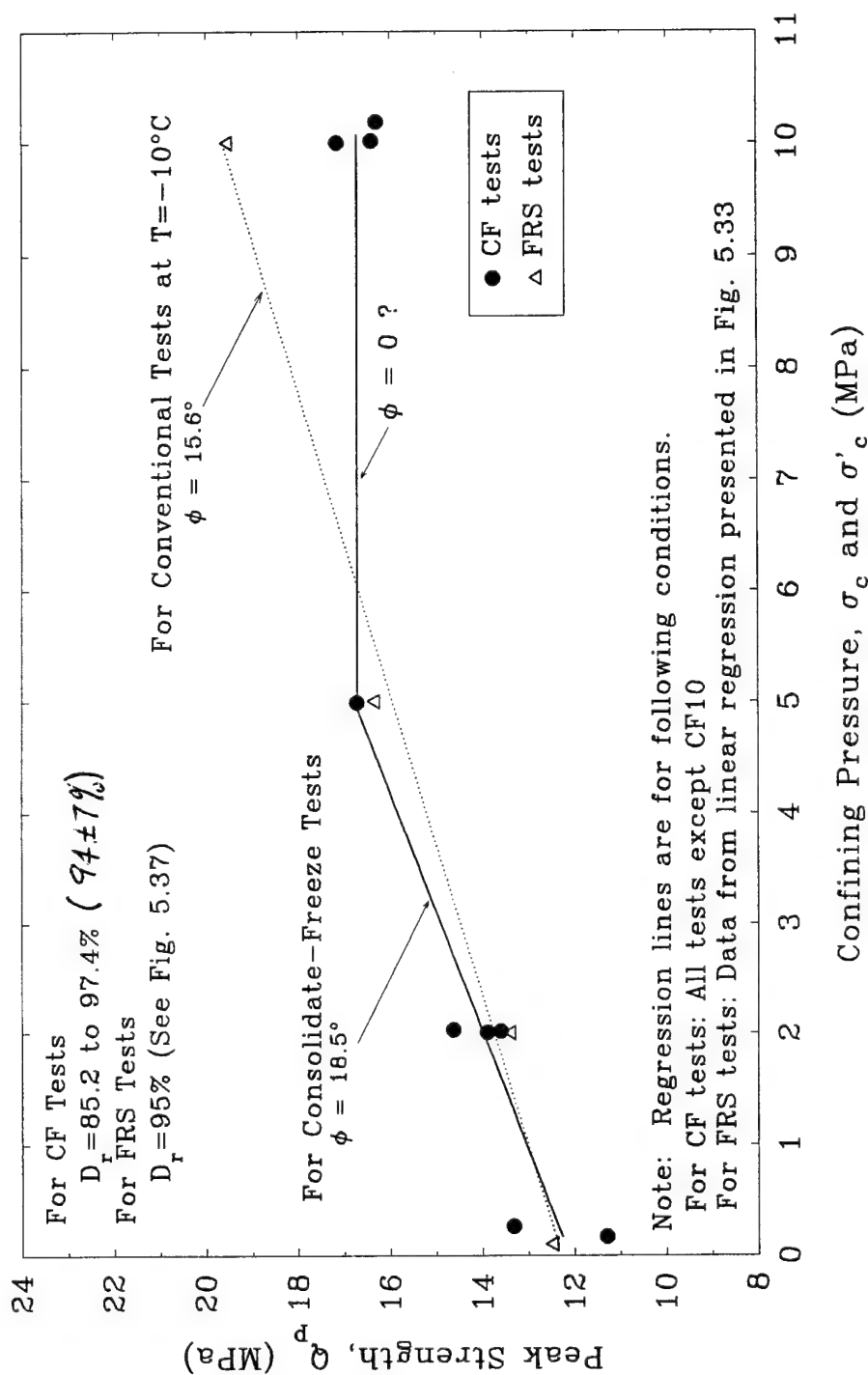


Figure 5.60 Peak Strength versus Confining Pressure for Consolidate-Freeze and Conventional Tests on Dense Specimens at Moderate Strain Rate and $T = -10^\circ\text{C}$ (Swan 1994)

APPENDIX E: Application of Dilatancy-Hardening Model to Frozen MFS

<u>Sheet No.</u>	<u>Description</u>
E1 to E3	Data on the Tensile Strength of Polycrystalline Ice
E4	Compressive Strength of Polycrystalline Ice at $\sigma_c = 0$ and 10 MPa from Jones (1982)
E5	Unconfined Compressive Strength of Isotropic Polycrystalline Ice from Constant Stress and Constant Strain Rate Test Programs
E6	Compressive Strength of Polycrystalline Ice Used in Dilatancy Hardening Model Compared to Results of Murrell <i>et al.</i> (1989)
E7	Effect of Confinement on Stress-Strain Behavior of Ice
E8	Ratio of Dilatancy-Hardening Model Predicted to Measured Peak Strength for Frozen MFS
E9	Ratio of Predicted Ice Strength to Measured Upper Yield Stress of Frozen MFS
E10	Modified D-H Model Predicted Strength minus Measured Peak Strength for Frozen MFS
E11	Comparison of D-H Model Predicted and Measured Peak Strength vs. Relative Density at Varying Confining Pressures
E12	Relative Density vs. Critical Confining Pressure and Undrained Strength for MFS

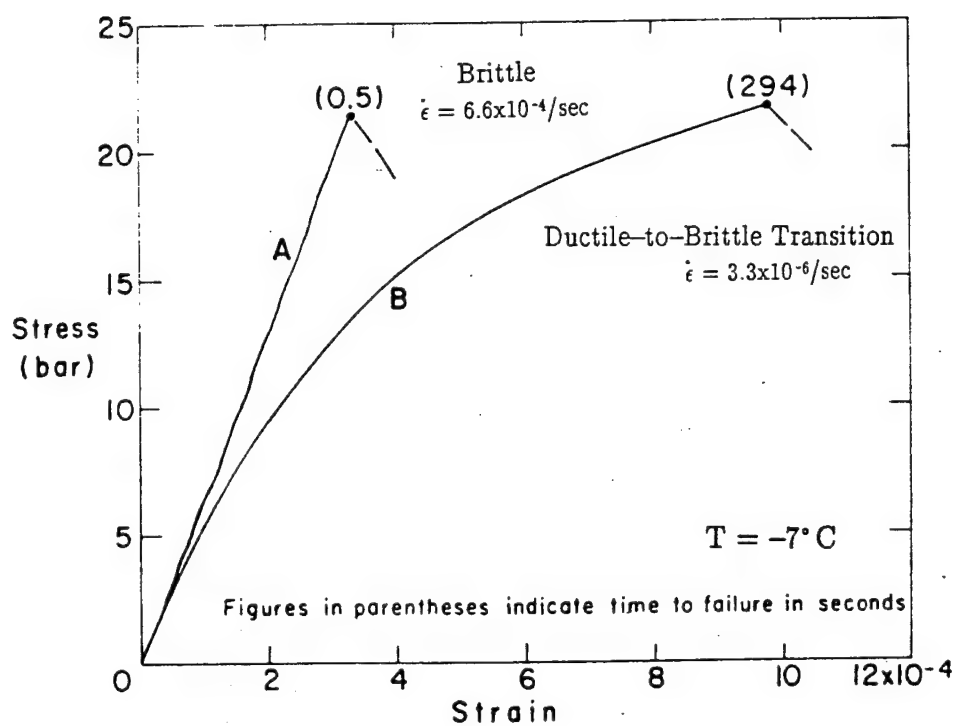


Figure 2.46

Stress-strain Curves From Uniaxial Tension Tests on Polycrystalline Ice (from Hawkes and Mellor 1972)

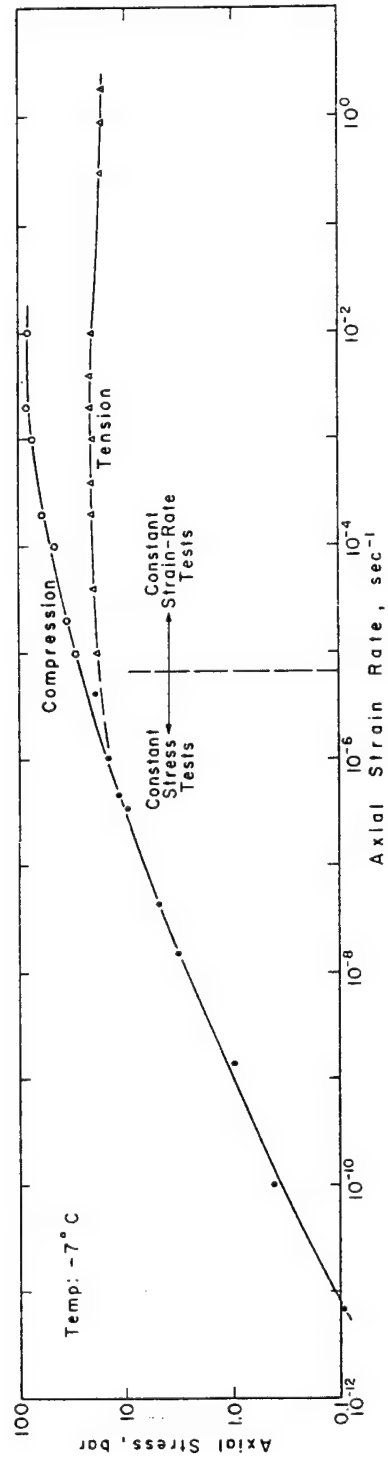


Figure 2.49 Stress/Strain-Rate Relationship for Uniaxial Tests on Granular Ice at -7°C (from Mellor 1980)

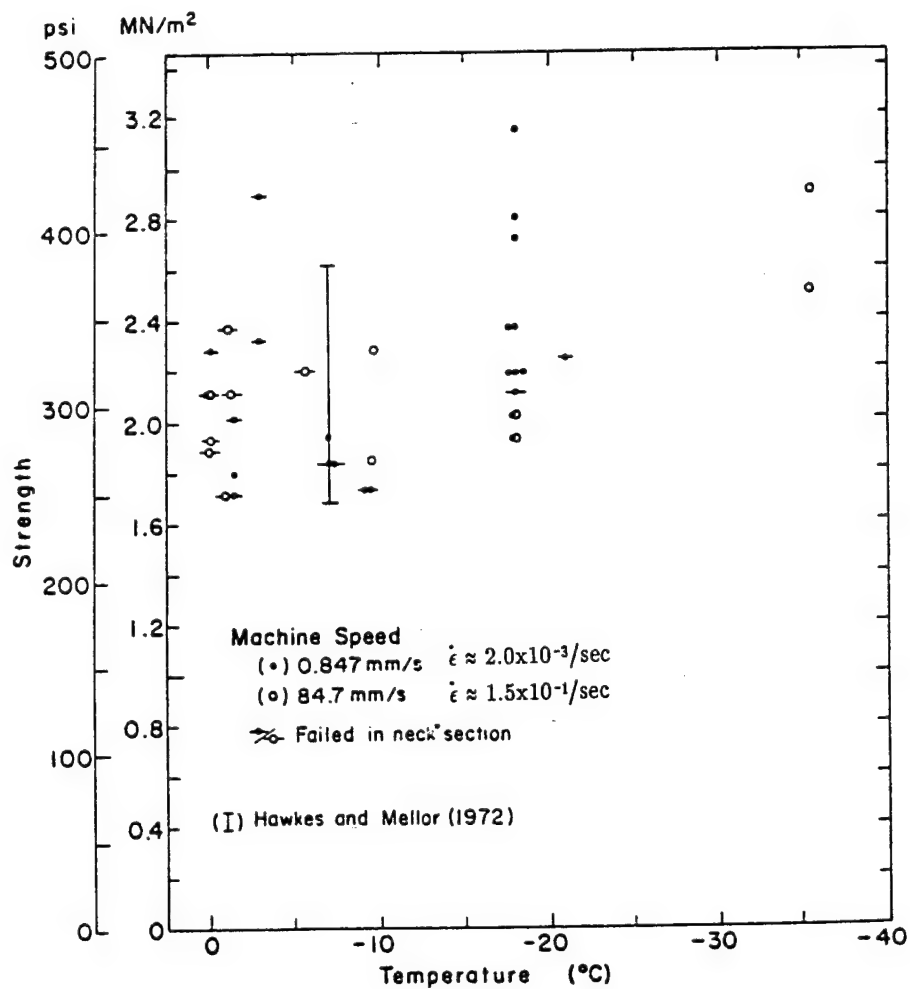


Figure 2.59

Uniaxial Tensile Strength versus Temperature for Granular Ice (from Haynes 1979)

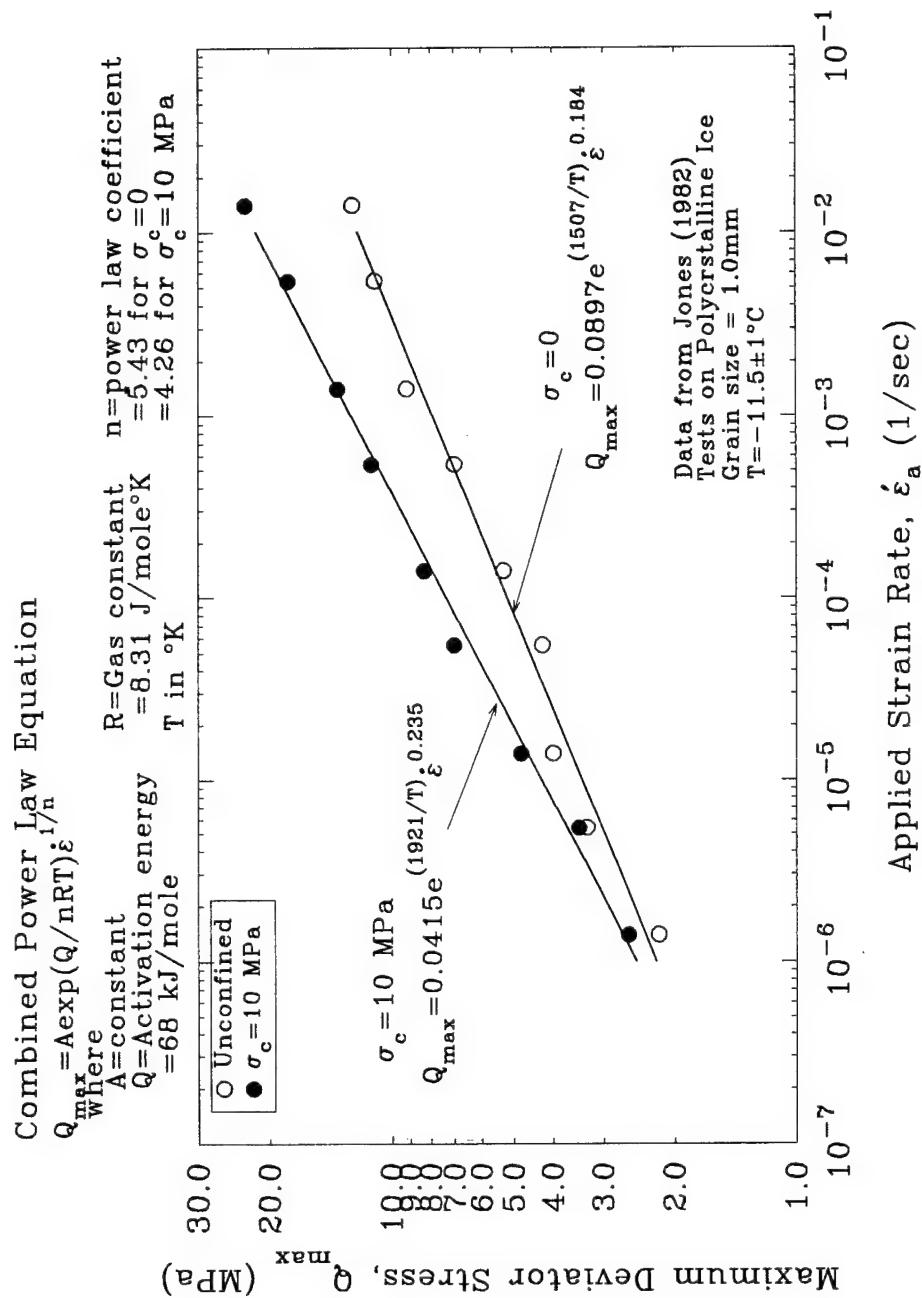


Figure 6.6 Peak Strength versus Strain Rate Equations for Polycrystalline Ice Developed from Results by Jones (1982)

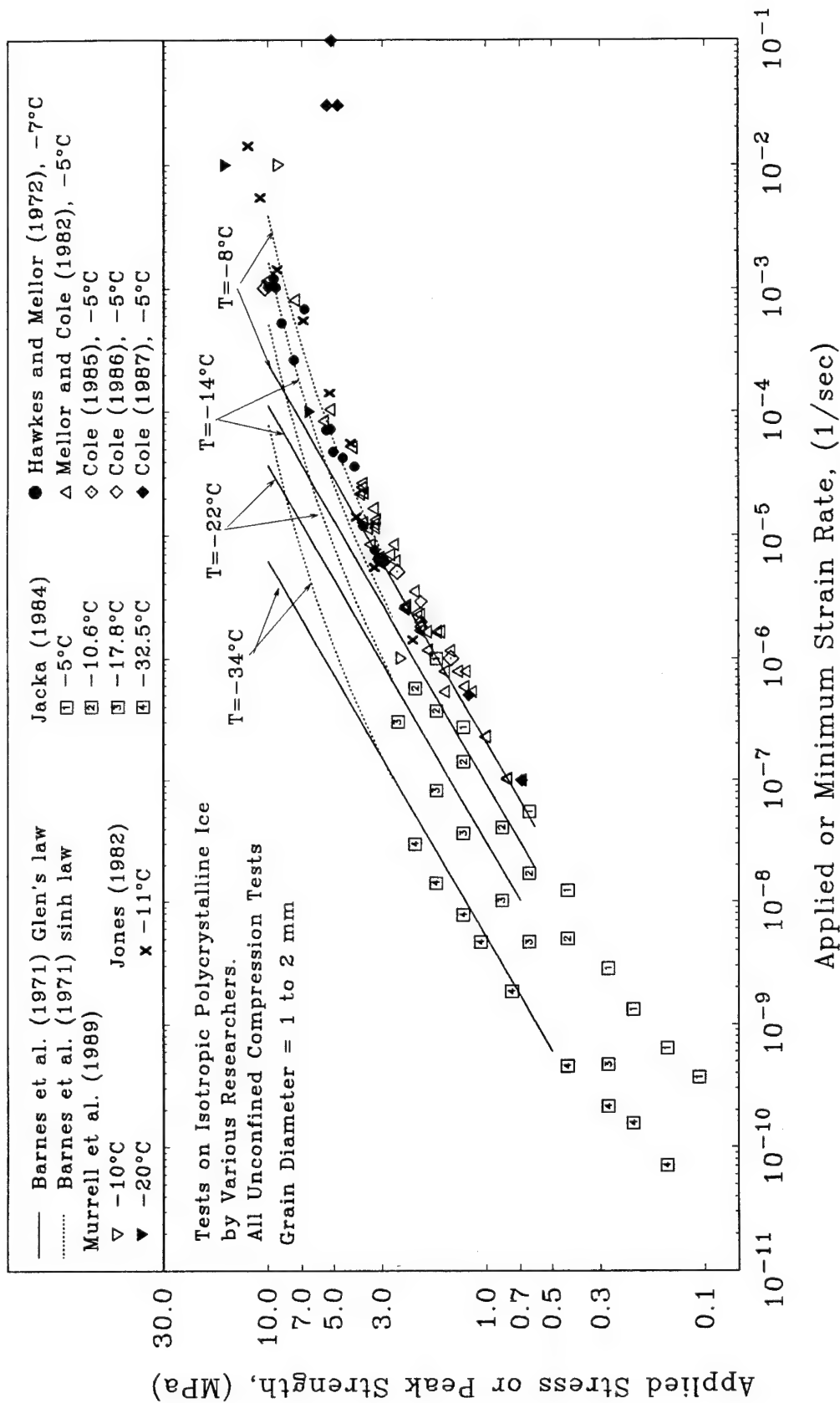


Figure 2.60 Stress versus Strain Rate for Creep and Strength Tests on Isotropic Polycrystalline Ice (Swan 1994)

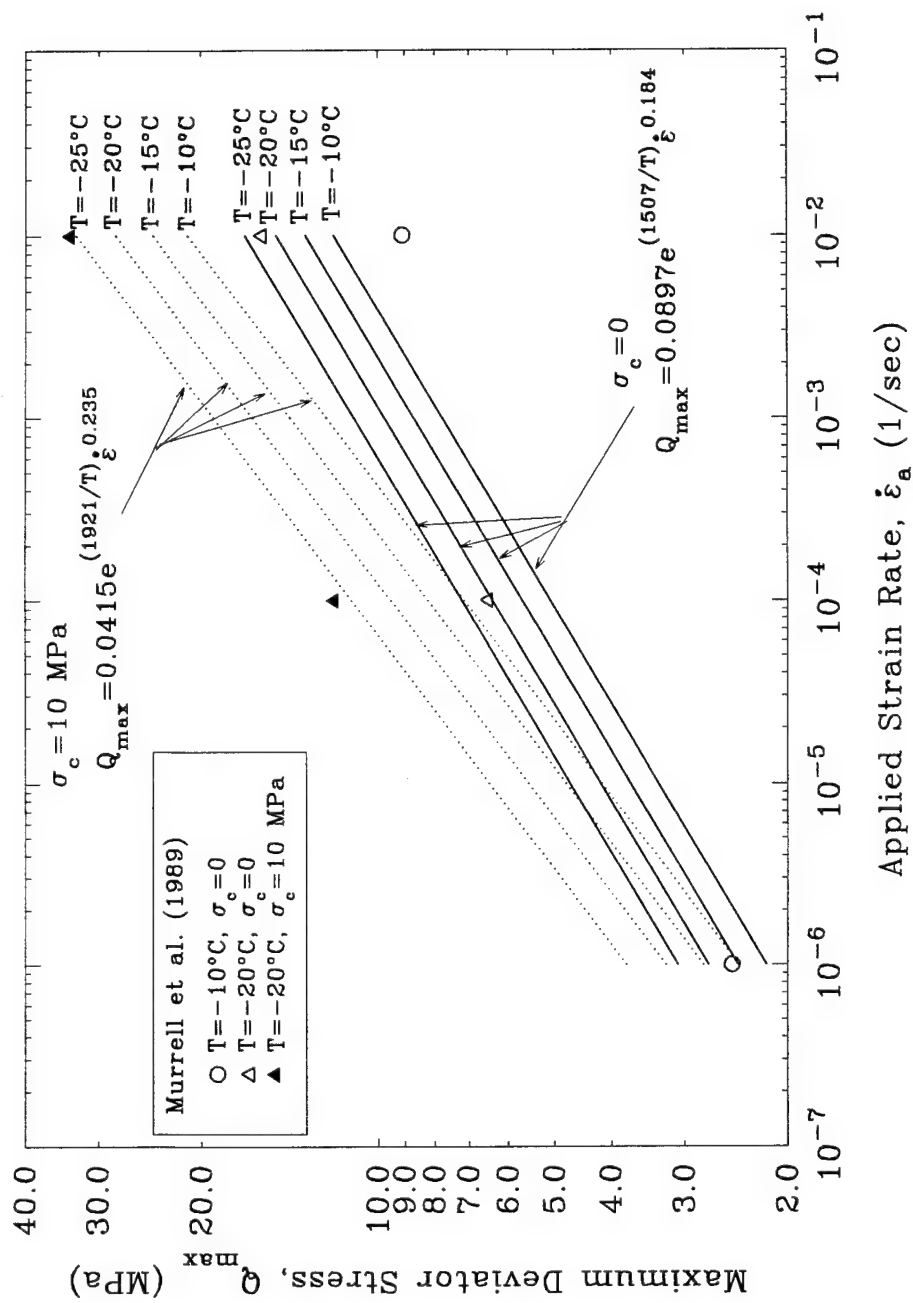


Figure 6.7 Calculated Peak Strengths of Polycrystalline Ice Used in the Dilatancy-Hardening Model Compared with Results by Murrell et al. (1989)

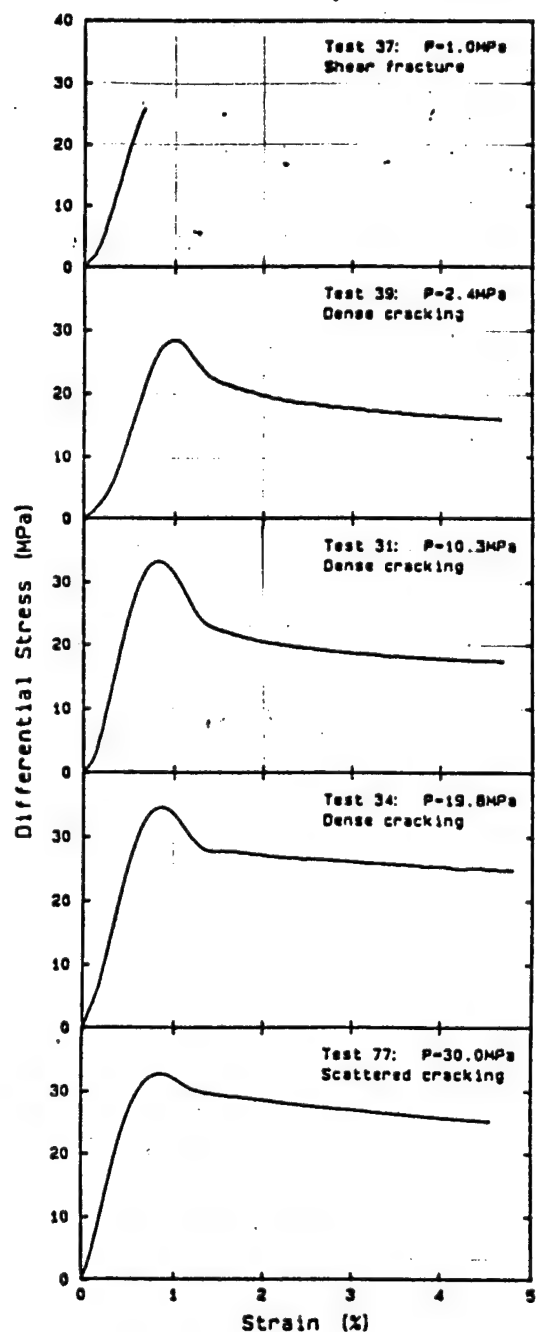
$T = -20^{\circ}\text{C}$ $\dot{\epsilon} = 10^{-2}\text{s}^{-1}$ Grain $\phi \approx 1\text{mm}$ 

Fig. 6. Stress-strain curves for pure ice specimens under triaxial compression at -20°C and a strain-rate of $10^{-2}/\text{s}$.

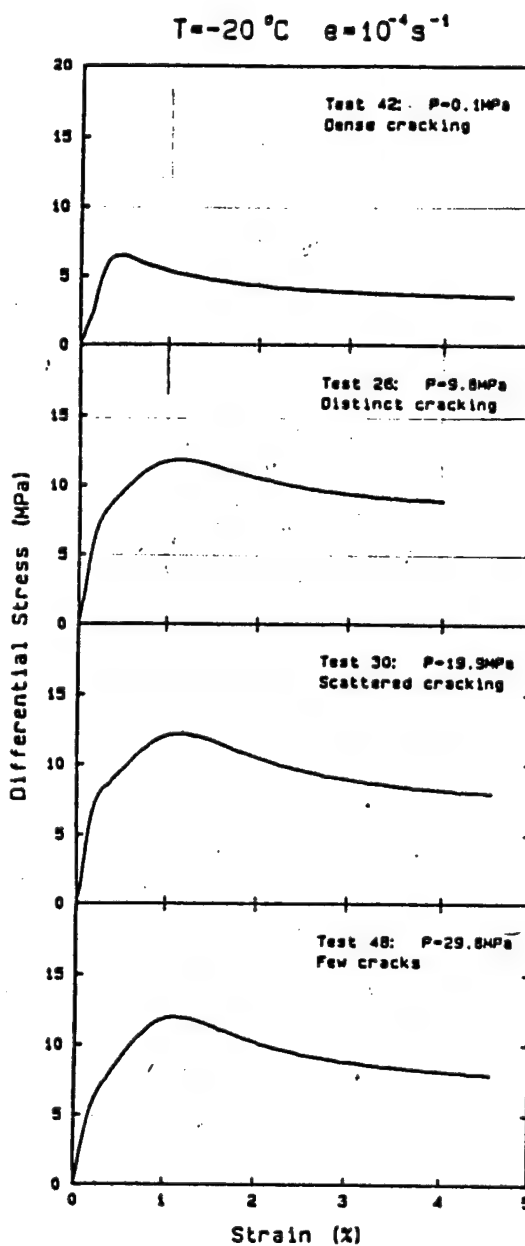


Fig. 7. Stress-strain curves for pure ice in triaxial compression at -20°C and a strain-rate of $10^{-4}/\text{s}$. P = confining pressure.

Effect of Confinement on Stress-Strain Behavior of Pure Ice
(preprint of Murrell et al. 1989)

σ_c (MPa)	Slow $\dot{\epsilon}$	Moder. $\dot{\epsilon}$	Fast $\dot{\epsilon}$
0.1	●	○	⊗
10	■	□	⊕

Note: Approximate ratios scaled from Fig. 5.15 to 5.18
 where $Q_{fs} = Q_{fs} + Q_i$ from D-H model and
 Q_p = peak strength from conventional tests.

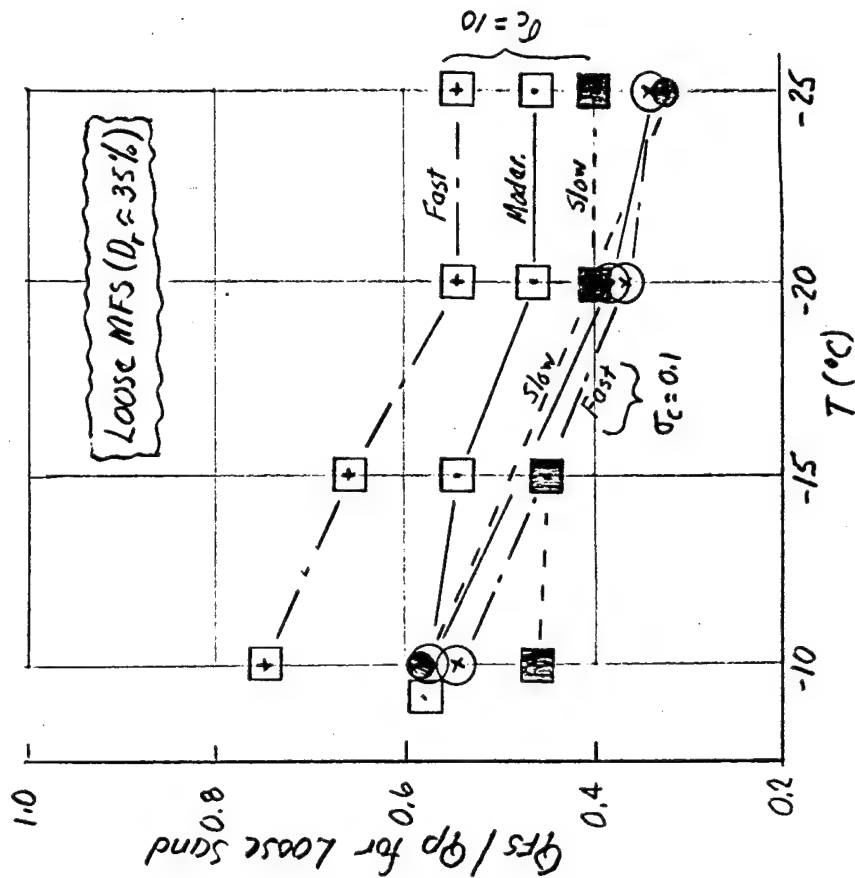
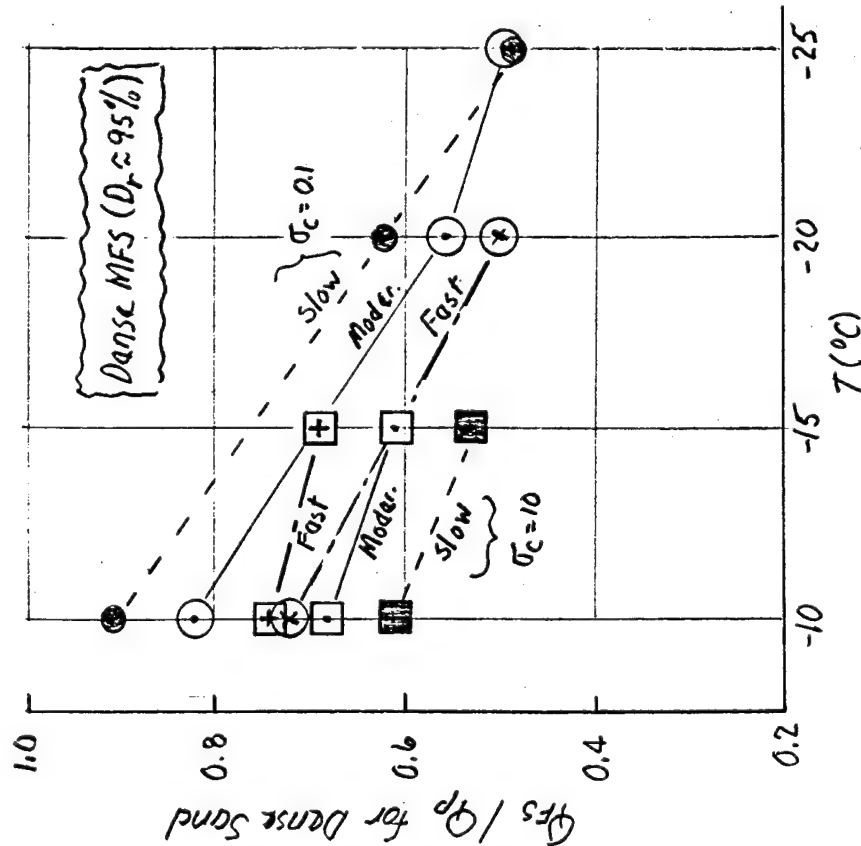


Fig. A2 Ratio of D-H Model Predicted to Measured Peak Strength vs. Nominal Temperature

CCL 2/18/95 ARO

4/95

NOTE: $T(^{\circ}K)$

$$Q_i(m_i^e) = 0.0897 e^{(1507/T)} (i)^{0.184}$$

$$Q_c(MPa) = 0.0415 \times (\dot{\epsilon})^{0.235} \quad (1921/7)$$

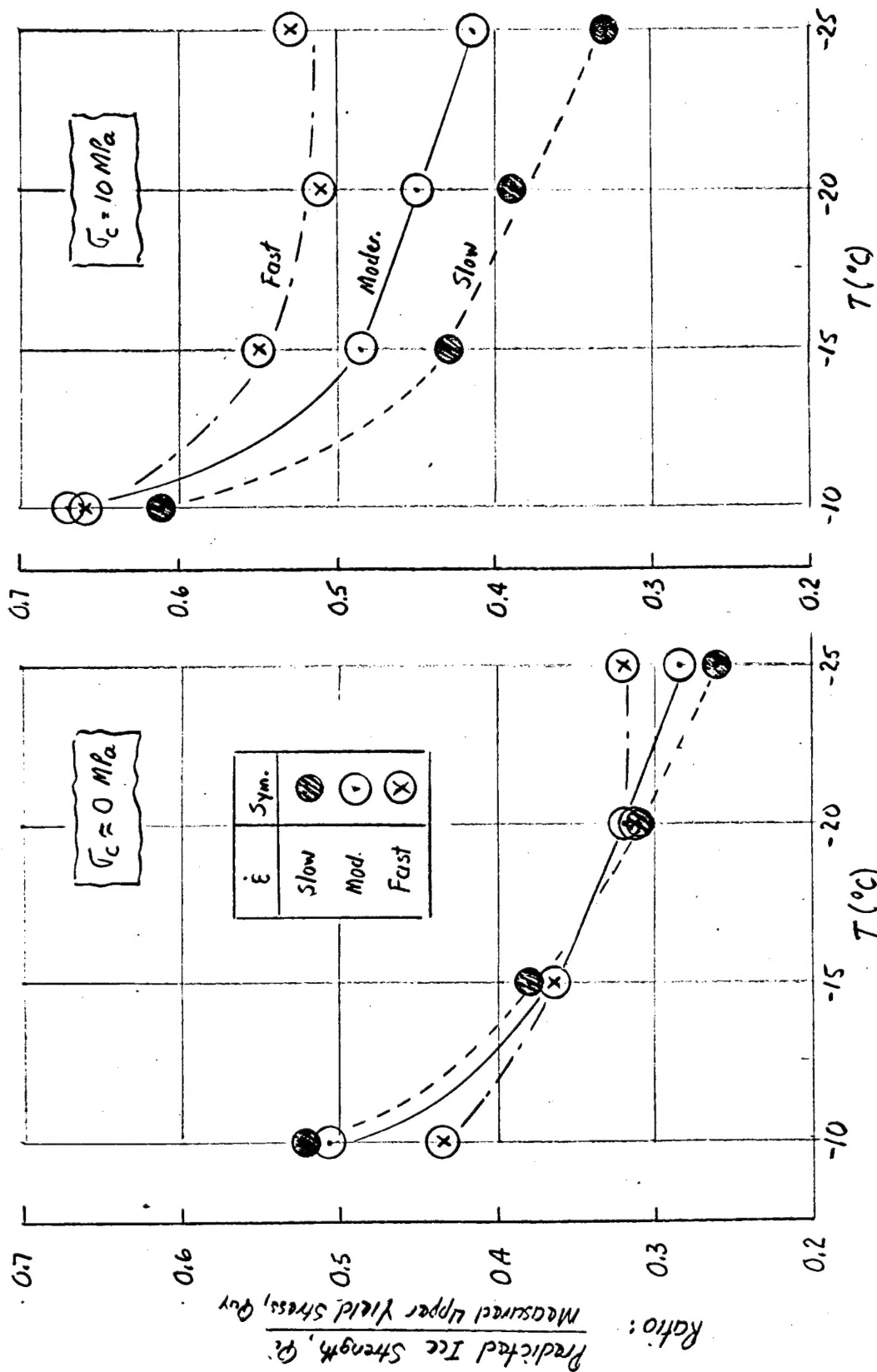


Fig. B1 Predicted Ice Strength (Q_i) / Meas. Upper Yield Stress (Q_U) vs. Nominal Temp. for Frozen MFS

Sheet E9

CEL 2/19/95 AKO

σ_c (MPa)	Slow	Mod.	Fast
0.1	●	○	⊗
.10	■	□	+

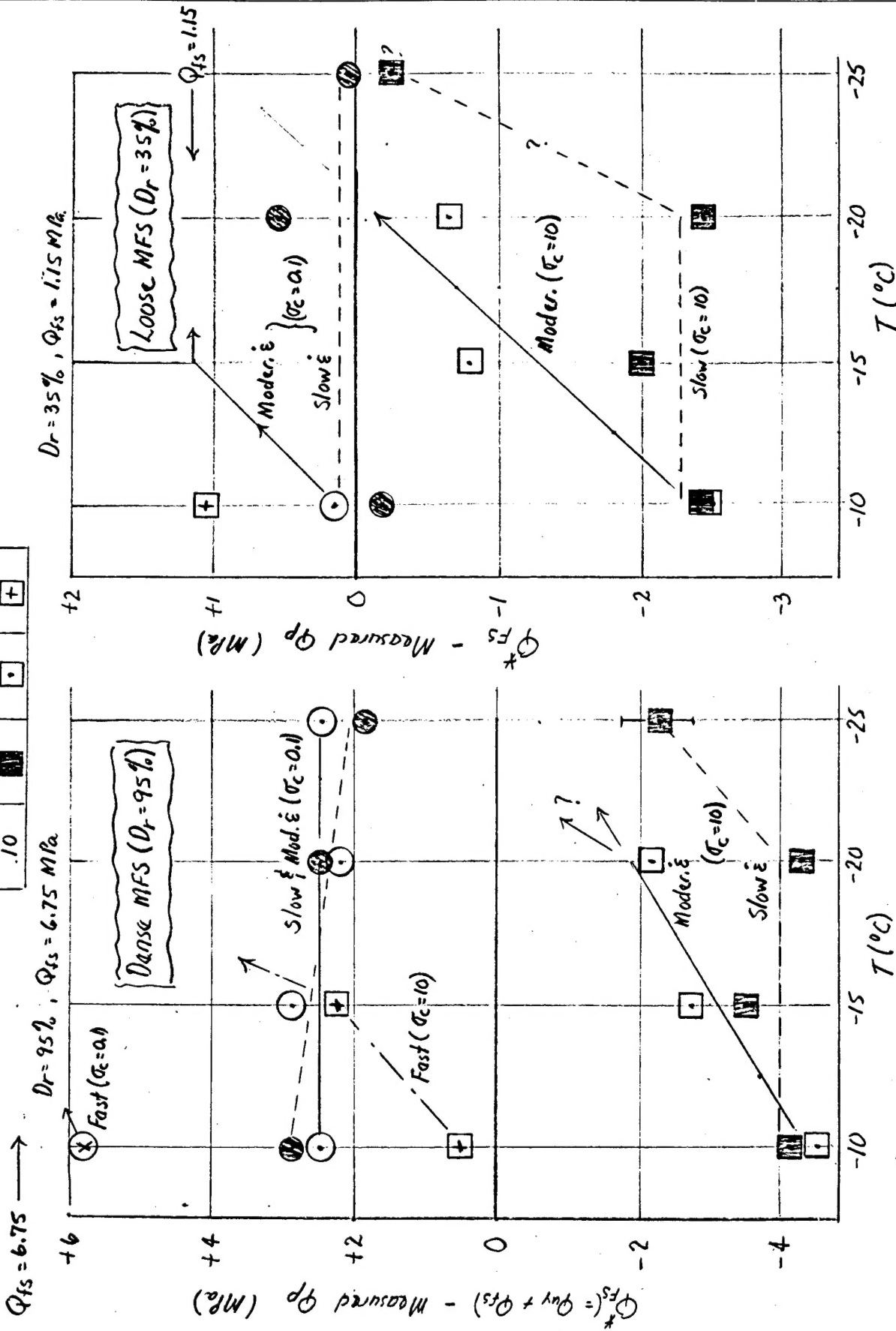
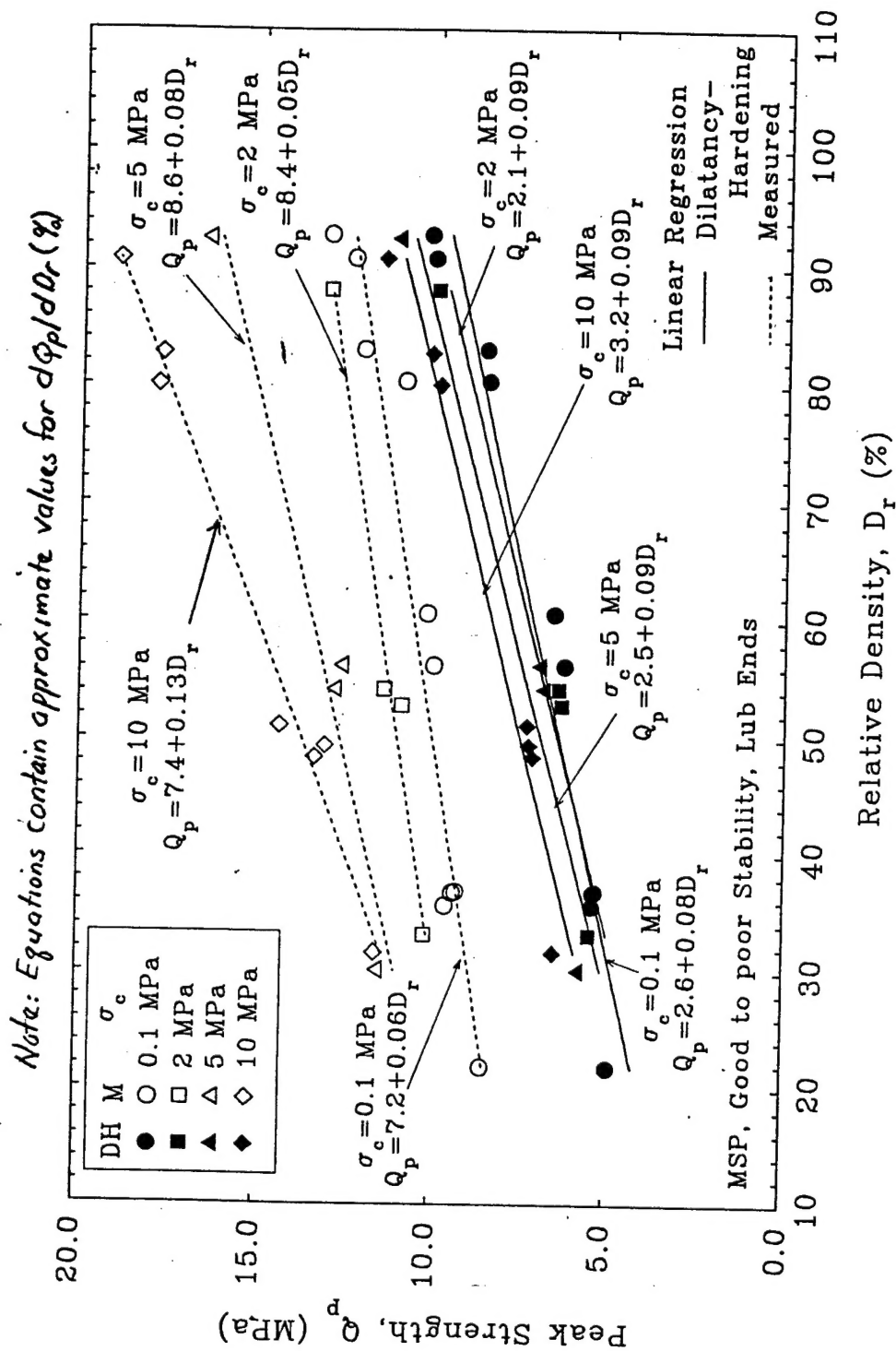


Fig B5 Modified D-H Model Predicted Q_{FS}^* minus Measured Peak Strength (Curve Types C & D)

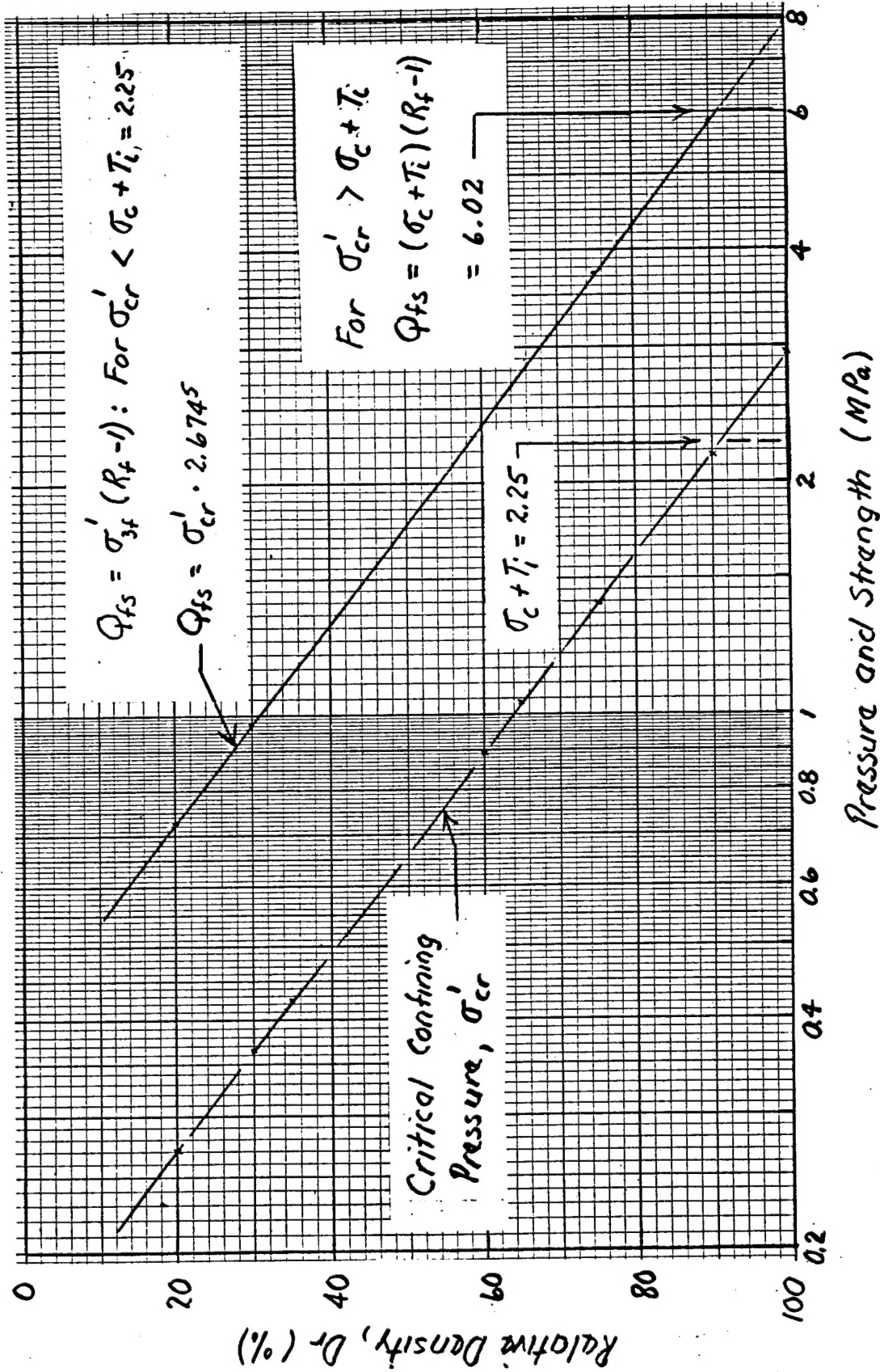
Sheet E10



Figure

Comparison of Peak Strength versus Relative Density Estimated from the Dilatancy-Hardening Model and Measured in Conventional Frozen MFS Tests at Moderate Strain Rate, $T = -10^\circ$ and Various Confining Pressures

Note: Drawn for $\sigma'_c = 0.1 \text{ MPa}$ and ice tensile strength $T_i = 2.15 \text{ MPa}$



Confining Pressures (σ'_{cr} and $\sigma'_c + T_i$) and Undrained Strength (Q_{fs}) vs. Relative Density (D_r) for Manchester Fine Sand